University of Bath

PHD

A study of the coefficient of thermal expansion of nuclear graphites

Hacker, Paul John

Award date:
2001

Awarding institution:
University of Bath

Link to publication

Alternative formats
If you require this document in an alternative format, please contact:
openaccess@bath.ac.uk

Copyright of this thesis rests with the author. Access is subject to the above licence, if given. If no licence is specified above, original content in this thesis is licensed under the terms of the Creative Commons Attribution-NonCommercial 4.0 International (CC BY-NC-ND 4.0) Licence (https://creativecommons.org/licenses/by-nc-nd/4.0/). Any third-party copyright material present remains the property of its respective owner(s) and is licensed under its existing terms.

Take down policy
If you consider content within Bath's Research Portal to be in breach of UK law, please contact: openaccess@bath.ac.uk with the details. Your claim will be investigated and, where appropriate, the item will be removed from public view as soon as possible.

Download date: 05. May. 2023

A STUDY OF THE COEFFICIENT OF THERMAL EXPANSION OF NUCLEAR GRAPHITES

submitted by

Paul John Hacker

for the degree of PhD of the University of Bath

February 2001

COPYRIGHT

Attention is drawn to the fact that the copyright of this thesis rests with the author. This copy of the thesis has been supplied on condition that anyone who consults it is understood to recognise that its copyright rests with its author and that no quotation from the thesis and no information derived from it may be published without the prior written consent of the author.

This thesis may be made available for consultation within the University Library and may be photocopied or lent to other libraries for the purposes of consultation.

Signed: 

Date: 22/02/01

UMI Number: U135821

All rights reserved

INFORMATION TO ALL USERS
The quality of this reproduction is dependent upon the quality of the copy submitted.

In the unlikely event that the author did not send a complete manuscript
and there are missing pages, these will be noted. Also, if material had to be removed,
a note will indicate the deletion.

UMI U135821
Published by ProQuest LLC 2014. Copyright in the Dissertation held by the Author.
Microform Edition © ProQuest LLC.
All rights reserved. This work is protected against
unauthorized copying under Title 17, United States Code.

ProQuest LLC
789 East Eisenhower Parkway
P.O. Box 1346
Ann Arbor, MI 48106-1346

UNIVERSITY OF BATH
LIBRARY
50
- 2 JUL 2001
Ph.D.

For My Wife, Joanne.

"Felix qui potuit rerum cognoscerne causas"

(Lucky is he who understands the causes of things)

Virgil 70-19 BC: Georgics

"Do or do not. There is no try"

The character "Yoda" in The Empire Strikes Back

ACKNOWLEDGEMENTS

The author is indebted to the following people for their helpful assistance, comments and encouragement:

Dr Gareth Neighbour and Professor Brian McEnaney (Supervisors)
Dr Angela Tomlinson (University of Bath)
Drs James Reed, Mark Hartley, Mark Bradford and Corinne Olivier (British Energy Generation Plc).

Also special thanks are due to the technical and support staff within the Department of Engineering and Applied Science at the University of Bath and to British Energy Generation Ltd for their financial support of this work.

ABSTRACT

This thesis presents the results of a study of the Coefficient of Thermal Expansion (CTE) of two grades of nuclear graphite that are used as the moderator in the Magnox and Advanced Gas-Cooled reactors operated in the UK. This work has two main aims, the first is to characterise those elements of the graphite microstructure that control CTE within these materials and to relate these to the effects induced within the reactor. The second is to develop a microstructural model, of general applicability, that can initially be applied to model the CTE changes within the graphites under reactor conditions (neutron irradiation and radiolytic oxidation). These aims have been met by study in three interlinked areas, theoretical, experimental and modelling.

Previous to this study, a loose assembly of single crystals together with changes in small scale nanometric porosity (Mrozowski cracks) were used to describe CTE behaviour of nuclear graphite both as-received and under reactor conditions. Within the experimental part of this thesis the graphite nanostructure was studied using, primarily, Transmission Electron Microscopy (TEM). This work concluded that structure on this scale was complex and that the loose assembly of single crystals was a poor microstructural approximation for modelling the CTE of these materials. Other experimental programmes measured the CTE of highly oxidised samples and simulated the effects of irradiation. The former discovered that CTE remained largely unaffected to high weight losses. This insensitivity was explained by "The Continuous Network Hypothesis" that was also related to classical percolation theory.

The final part of the thesis modelled an abstraction of the key microstructural features identified in the previous parts of the thesis. This approach has been applied to AGR moderator graphite where it has successfully modelled the thermal expansion behaviour of the as-received, irradiated and oxidised material.

PUBLICATIONS

In addition to this thesis, elements of this work have been published in the following:

JOURNAL PUBLICATIONS

Hacker, P. J., Neighbour, G. B. and McEnaney, B. (1999b). The Thermal Expansion Behaviour of AGR Moderator Graphite. *The Nuclear Engineer*, **40**[6], 229-235.

Hacker, P. J., Neighbour, G. B. and McEnaney, B. (2000). The coefficient of thermal expansion of nuclear graphite with increasing thermal oxidation. *Journal of Physics D: Applied Physics*, **33**, 991-998.

CONFERENCE PROCEEDINGS

Neighbour, G. B., Hacker, P. J. and McEnaney, B. The Effects of Oxidation on Thermal Expansion in a Polygranular Graphite. *Extended Abstracts, Eurocarbon '98, Strasbourg, France*, 715-716.

Hacker, P. J., Neighbour, G. B. and McEnaney, B. Microstructural Features That Control The Coefficient of Thermal Expansion of Nuclear Graphites. *24th Biennial Conference on Carbon, Charleston, South Carolina, USA*, 706-707.

Hacker, P. J., Neighbour, G. B. and McEnaney, B. The Microstructural Modelling of CTE in Nuclear Graphites. *1st World Conference on Carbon, Berlin, Germany*, 395-396.

TABLE OF CONTENTS

PART A: THEORETICAL

PART B: EXPERIMENTAL

PART C: MODELLING

INTRODUCTION

All except one of the UK's commercial nuclear power stations use graphite as the principal component of the reactor core. This graphite serves as both a moderator of neutrons and as a structural component. Throughout the life of a graphite moderated nuclear fission reactor the graphite undergoes changes in mechanical and physical properties, primarily due to radiolytic oxidation and dimensional changes due to fast neutron irradiation from the fuel. These effects reduce the ability of the moderator core to withstand external loads and cause the generation of internal stress.

The Coefficient of Thermal Expansion (CTE) plays an important role in the development of internal stress generated within the bricks of the moderator core due to the existence of neutron flux and temperature gradients. It is also important in the consideration of the effects of external loads that generate contact stresses. Although a detailed knowledge of CTE is an important requirement for the understanding of the behaviour of the graphite under reactor conditions, no theory exists to describe all the changes in CTE observed under reactor conditions to changes in the microstructure of the material.

This study has two main aims. The first is to identify and characterise those elements of the microstructure that are important in controlling CTE behaviour. The second is to develop an improved microstructural model of the thermal expansion behaviour of nuclear graphites that is generic. The intention is that it could eventually be applied to a range of graphites and other carbon materials but for the purpose of this study concentrates on moderator graphites used in the UK. After an introductory section, this thesis consists of three linked parts, Parts A, B and C, the contents of which are summarised in Figure 0.1. Part A, theoretical considerations, incorporates a review of work done on CTE of nuclear graphites in the reactor environment and also re-examines and extends this work. The second part, Part B, reports the experimental work undertaken, primarily to simulate the effects of the reactor environment on microstructure and CTE. In addition to the measurement of the CTE of highly thermally oxidised graphite samples, Part B also includes a microstructural study using, primarily, Scanning and Transmission Electron Microscopy (SEM and TEM) to characterise the microstructural elements controlling CTE. Experimental programmes

are also reported investigating the effects of pre-stress and relaxation in CTE as a function of time and to experimentally test hypotheses developed during the discussion of the experimental results.

The final part of this thesis, modelling of CTE, is given in Part C and draws on the results from Parts A and B to develop a microstructural model to account for CTE behaviour in nuclear graphites. A new approach to modelling CTE in these materials is presented that is modular so as to maintain an understanding of the complex microstructural interactions at each stage of the modelling process. The final chapter concludes the thesis and makes recommendations for further study.

0.1 NUCLEAR POWER GENERATION

In 1994 the nuclear industry celebrated the fiftieth anniversary of the first self-sustaining controlled nuclear chain reaction at the University of Chicago under the direction of Enrico Fermi. Since then the peaceful use of nuclear energy generation has spread to such an extent that over 30 countries operate nuclear power stations. Although the nuclear power industry is facing contrasting fortunes in different parts of the world, nuclear generating capacity is expected to grow by some 22% between 1992 and 2010. Globally, approximately 40 new reactors are under construction and a further 60 are in the planning stage (Hammond, 1996).

Within the UK, the Calder Hall Magnox reactors, opened in 1956, initiated the use of commercial nuclear power in the world. By 1997, in addition to the early Magnox reactors (with the exception of those at Berkley and Trawsfyndd), fourteen Advanced Gas-cooled Reactors (AGR) and one Pressurised Water Reactor (PWR) were in operation in the UK producing approximately 25% of the UK's electricity.

The basics behind nuclear fission and especially the conditions required for self sustaining nuclear fission reactions can be found from many sources (*e.g.* Wilets, 1964). Fermi was the first to realise that since neutrons have no charge they could induce artificial radioactivity more easily than protons or alpha particles. Although it was Otto Hahn who is credited with producing identifiable reaction products from neutron induced fission (see Benson, 1991) and he also proposed a mechanism to explain the

fission process based on the 'liquid-drop' model of the nucleus (Bohr and Wheeler, 1939) in which particles within the nucleus are assumed to move freely and randomly and interact only with their nearest neighbours. In this model, when a spherical uranium nucleus absorbs a neutron, it undergoes oscillations. If a neck forms the short range nuclear force between the two parts of the 'dumbbell' is greatly reduced. However, the long-range electrical repulsion diminishes only slightly and the nucleus splits into two roughly equal fractions. This process is summarised in the following nuclear equation where the short-lived ($\sim 10^{-14}$ s) compound nucleus in an excited state is denoted by an asterisk.

$$n + {}^{235}_{92}U \rightarrow {}^{236}_{92}U^{*} \rightarrow {}^{140}_{54}Xe + {}^{94}_{38}Sr + 2n + Energy \qquad [01]$$

Approximately 180 MeV of energy is released during the fission process and although ~160 MeV is carried away by the kinetic energy of the fission fragments, fast neutrons with energies of up to ~20 MeV are produced. Provided the energy of these neutrons can be moderated to thermal energies (< 1eV) a self-sustaining chain reaction can result. Moderation involves reducing the energy of fission neutrons by elastic collision processes thereby increasing their capture cross section by other uranium nuclei and continuing the fission chain reaction.

Although the broad principles remain the same, the design details evolved from the earlier Magnox reactors to the latest AGRs. For both reactors the source of the energy necessary to generate electricity is from nuclear fission. Within the Magnox reactor fissile natural uranium, inside a fuel cladding, is placed within vertical fuel channels into the core whereas for the AGR reactor pellets of UO_2 are used. The fission reaction, controlled by the raising or lowering of control rods, heats the core to several hundred degrees centigrade. Coolant gas (primarily CO_2) is circulated around the core which in turn is in thermal contact with the boilers. The boiler, turbine and condenser form a closed circuit the purpose of which is to extract the heat from the steam created at the top of the circuit via the turbines that are used to generate electricity.

In order to slow fast neutrons to thermal energies, a moderator is used. Graphite, used in both the Magnox and AGR designs, is a suitable material for such purposes due to its

low neutron capture cross section, relative abundance, the low atomic mass of carbon (required to ensure a high dissipation of neutron energy during each collision with a carbon atom (King, 1964)) and the relatively low cost of the material.

The AGR graphite moderator core, ~9 m in diameter and 8 m deep, is encased within a concrete pressure vessel approximately 20m in height, Figure 0.2, and is unique to the UK. In addition to the graphite core, the principal components of an AGR are a gas baffle cylinder and dome (to separate the inlet and outlet gas streams); a boiler shield wall; twelve boiler units (arranged in quadrants); and eight circulators (two per quadrant) (Neighbour, 1998). The core and gas baffle are mounted on a circular grillage (the diagrid) which is carried on an arrangement of columns. Boron steel is used for the control rods. The carbon dioxide coolant circulates at a pressure of 40 bar with typical outlet temperatures of the gas being ~650°C. The uranium dioxide fuel is enriched to about 3% U-235 (natural uranium is 0.7% U-235) and clad in stainless steel cans. The reactor and steam generators are housed within a concrete pressure vessel the walls of which are about 6 metres thick. The typical electrical output of an AGR is 660MW and it operates with a thermal efficiency of about 40%.

The AGR core itself is a cylindrical graphite structure assembled from bricks of cylindrical and square cross section, loosely keyed together, Figure 0.3. As the core serves as a structural component it is thereby submitted to load during operation of the reactor. Importantly, therefore, the structure of the core is of a radial-keying design that allows the lattice pitch to be maintained for continued insertion and removal of the fuel under the distortions that occur during the operational life of the reactor. Full descriptions of this 'keying concept' and the core structure are available elsewhere (*e.g.* Kelly, 1985).

0.2 THERMAL ANALYSIS AND THE COEFFICENT OF THERMAL EXPANSION (CTE).

Thermal analysis is the term applied to a group of methods and techniques in which thermal and physical properties of a substance are measured as a function of temperature as the substance is subjected to a controlled temperature programme (see

Brown, 1988). The determination of the thermal dilation of a solid material is one such analysis technique where the property of interest is the length of the substance.

The term 'solid material' is used here to specify materials that exhibit sufficient rigidity over the test temperature range such that the sensing probe does not produce indentation of the specimen. Measurement of the thermal expansion of liquids and gases present unique problems concerning confinement of the substance discussions of which can be found elsewhere (*e.g.* Charsley and Warrington, 1992).

For extremely precise (better than +/- 40 nm/m.K) determination of the linear thermal expansion of a solid material, interferometry is the preferred method (ASTM E289-94). This method involves placing a specimen of known geometry between two flat mirrors, in contact with at least one, Figure 0.4. Light (usually laser light) illuminates each mirror and interferes to produce a fringe pattern. As the sample dilates with temperature a change in the fringe pattern is detected corresponding to the length change of the specimen. In addition to the high accuracy attainable with this method the material remains stress free unlike most traditional methods based upon a mechanical technique. Although precise, interferometry is sensitive to external acoustic vibration and is expensive to set up and maintain. Therefore, if the detection of expansions of the order of 1μm/m.K are sufficient, dilatometry, using mechanical methods, is the preferred option (ASTM E 831-93). As the mechanical method is used in this work further details are contained in Part B. By way of introduction this method uses a pushrod, connected to a linear variable differential transducer, which is brought into contact with the sample. The expansion of the sample is therefore converted into a linearly varying voltage.

Introductory discussion of the CTE of materials is given in many textbooks (*e.g.* Atkins, 1994) therefore only a brief discussion is given here. Generally, materials change their dimensions with temperature due to the asymmetric nature of the inter-atomic potential of the substance (Austin, 1952). Consider Figure 0.5(a), which shows a schematic of the interatomic potential between two atoms. Position '1' represents the potential and separation at static equilibrium. Now as the temperature is raised the average energy of the system increases, however as the potential well is asymmetric the mean separation of the atoms increases, Figure 0.5(b), and thus the substance expands.

As the thermal expansion of a typical material is, in general, a continuous non-linear function of temperature, instantaneous and average coefficients over a temperature range can be derived. The differences between the two definitions are discussed below and are shown graphically in Figure 0.6. Strictly it should also be noted that the term "thermal dilation" is more precise than "thermal expansion", as contractions are included in the former. However, the latter is in common use with negative values taken to represent a contraction.

In order to arrive at a definition that is independent of the length of the sample, the first definition is known as the instantaneous or physical linear Coefficient of Thermal Expansion, α_i, measured at a temperature, T_1, and is defined as follows (Ibach and Luth, 1993).

$$\alpha_i = \frac{1}{L_0} \cdot \left(\frac{\partial L}{\partial T} \right)_{T_1} \qquad [02]$$

where L_0 is the length of the material at some initial temperature T_0 and L and T are continuous variables representing length and temperature respectively.

The second definition, and the one most often used in practice, is known as the average or technical Coefficient of Thermal Expansion where an average CTE, $\bar{\alpha}$, is calculated from the Relative Length Change (RLC) of the material over a particular temperature range as given by

$$\bar{\alpha} = \frac{\Delta L}{L_0} \cdot \frac{1}{\Delta T} \qquad [03]$$

where the change in length (ΔL) occurs over a temperature range (T_0 to $T_0+\Delta T$). For most solids the linear CTE is of the order of 10^{-5} K^{-1}. The implicit assumption in these definitions is that the CTE of a material can only be measured if the sample is kept in a stress free state. Thermodynamically this requires that the derivative of the free energy, with respect to volume (*i.e.* the pressure) is zero for all temperatures.

The second method of describing CTE (the average method) between the temperature range 20-120°C (termed the low temperature range in this thesis) has historically been used within the nuclear industry to characterise the expansion of nuclear graphites. Previous investigations at the University of Bath (Neighbour *et al.*, 1997) have suggested that the temperature range 20-600°C (termed the high temperature range in this thesis) should also be considered as this better represents the operating temperatures of AGR. Both of these averages will also be used here to enable swift comparisons to be made. However, the dilation curve (*i.e.* the thermal expansion plotted as a function of temperature) gives the most information on the expansion behaviour of a particular sample and should be considered the most complete method of describing CTE behaviour.

0.3 CARBON AND GRAPHITE

The carbon atom ground state configuration, $(1s^2)(2s^2 2p_x 2p_y)$, can form sp^3, sp^2 and sp^1 hybrid bonds as a result of promotion and hybridisation. Thus, although the natural valency of carbon is four, hybridisation can result in multiple bonds ranging in length from 118pm to 153pm for a pure single bond. In graphite, co-planar trigonal (sp^2) bonds are formed with neighbouring carbon atoms in a hexagonal net sheet structure to form the graphene plane. Detailed accounts of the chemical and physical nature of carbon can be found from many sources (*e.g.* Atkins, 1994).

The crystal structure of graphite, one of the classic allotropes of carbon (the other of course being diamond), has been fully documented (*e.g.* Kelly, 1981). Another major allotrope of carbon, the "Fullerenes", were only discovered in 1985 and are different from diamond and graphite in that they generally consist of carbon atoms arranged in the form of a geodesic spheroid and were thus named after the inventor of the geodesic dome, Buckminster Fuller. An introduction to Fullerenes is given by Pierson (1993).

The commonest crystal form of graphite is hexagonal and consists of a stack of layer planes (graphene planes) with the stacking sequence ABABAB..., Figure 0.7. The rhombohedral form of graphite with a stacking sequence ABCABC, is a minor component of well-crystallised graphites but can be increased substantially (from ~3% to ~20%) by deformation processes such as grinding. The proportion of rhombohedral

graphite can be reduced by high temperature heat treatment showing that the hexagonal form is more stable. The nature of the layer plane size, perfection and orientation are important elements in characterising the microstructure of graphite. For both forms of graphite the in-plane C-C distance is 142pm, mid way between a pure single and double carbon-carbon bond. Conversely, the inter-layer distance is 335 pm and results from a different type of chemical bonding from that found in-plane. The large interlayer spacing suggests that π orbitial overlap cannot account for the interlayer bonding so it is thought that the interlayer potentials result from van der Waals type interactions. Although there have been many attempts to calculate interplaner properties, a review by Kelly (1981) concluded that there is no satisfactory treatment of interlayer forces in graphite.

Natural graphite deposits are found all over the world but the quality of the material, in terms of purity, varies widely. These extensive deposits are generally classified as disseminated flake, crystalline 'plumbago' and amorphous 'blacklead'. The disseminated flake is a lamellar form occurring in metamorphic rocks such as limestone. One source of this kind, Ticonderoga, has provided perfect crystals used in many fundamental studies (*e.g.* Hennig, 1956). 'Plumbago' is mineral carbon found in well defined veins or pockets. Near amorphous graphite is found as fine particles in slates or shale. These beds are sometimes very extensive since they are created by metamorphosis of coal seams. Natural graphite generally contains impurities, which must be minimised in nuclear applications, however some unusually pure graphite sources do exist, for example, in Sri Lanka.

Artificial graphites are either polygranular or single crystal in nature with a wide range of crystallite perfection and properties. Single crystal graphites can be produced by pyrolitic deposition using an organic material, usually methane. Variation in the perfection and orientation of material can be obtained by varying the conditions and materials used in manufacture. Although the existence of these materials has been known for over 90 years, modern studies were initiated by Grisedale *et al.* (1951) and Brown and Watt (1958). In particular, the effects of deposition temperature have been studied by Bokros (1969).

0.4 POLYGRANULAR NUCLEAR GRAPHITES

Nuclear graphites are commonly formed from a coke and coal tar pitch blend. The proportion of materials used depends on the type of graphite being produced, but is typically ~80% coke and ~20% coal tar pitch. In the case of nuclear graphites a very high purity is required with the presence of elements with high neutron adsorption cross sections such as ^{10}B being particularly undesirable. Impurities are minimised by either using a very pure coke or by including a coke or graphite purification stage in the process which generally involves exposing the graphite to gaseous halides. The manufacturing process, summarised in Figure 0.8, varies in detail between different graphite manufacturers and graphite grades. Indeed polygranular graphite is sometimes considered a difficult material to study due to batch to batch variations that cannot be easily quantified.

After the coking process is complete the coke is broken and calcined at temperatures in the range 900-1300^{0}C to reduce the volatile content and prevent excessive shrinkage in later treatments. The coke is then crushed and milled before being sized in various fractions. The fine fraction (of dimensions less than about 0.4 mm) is known as 'flour'. The coarse fraction has a characteristic size of ~1-10 mm depending on the properties of the final artefact. The shape and properties of the coarse coke particles depend markedly on the coke source. Some cokes break into highly anisotropic 'needle cokes' whereas others produce more equi-axed shapes, *e.g.* those derived from Gilsonite ores. As will be discussed later, the properties of the final body are strongly dependent upon this aspect of the coke structure. The size fractions are mixed in proportions chosen to give the desired properties of the final material and then blended with the coal tar pitch. The mix is heated to ensure homogeneous mixing and formed into shape by extrusion or moulding. The shape of the coarse coke particles are important in the forming process since either extrusion or moulding will tend to orient particles with the long axis preferentially aligned parallel to the extrusion or perpendicular to the pressing direction. Within this work, the coarse filler particles that can be defined in the final artifact will be termed the filler phase and the remaining material (predominantly the flour and coal tar pitch) will be termed the binder.

The body is then baked to coke the pitch binder at temperatures in the range 750-900^{0}C in a process known as carbonisation. The baking cycle volatilises approximately one-third of the pitch binder content which shows a loss in density and increased permeability. The density of the artefact after baking can be increased by impregnation with coal tar pitches, which usually have a lower melting point than the binder pitches. This is required to ensure that the impregnant is fluid at the impregnation temperature. The bodies are then rebaked to pyrolise the impregnant carbon in the pores. Although two to three impregnation cycles are normal, for nuclear graphites there can be as many as six impregnations to increase the density by several percent to the required level, typically 1.6-1.7 g.cm^3 (Kelly, 1981).

Final graphitisation of the carbon artefacts is conducted at temperatures in the range 2600-3000^{0}C. The carbon blocks are stacked in a conducting coke bed buried under insulating material. The heating is provided by a large electric current being passed through the bed via water cooled electrodes at the ends of the furnace. The length of a heating cycle varies, but it is approximately two weeks after which the graphitised blocks are unpacked from the surrounding coke bed.

Two types of graphite are used as the moderator material in UK civil reactors. Pile Grade A (PGA) graphite is used in the earlier Magnox reactors and Gilsonite based graphites are used in the AGRs. Within this thesis, these materials will be referred to as Magnox or AGR graphites respectively. Although it is recognised that different grades of graphite are used to reflect neutrons back into the core and as fuel sleeves these are not discussed specifically here.

Magnox graphite is an extruded, medium-textured, nuclear graphite developed specifically for use as the moderator in the Magnox reactors made either by Anglo Great Lakes Ltd. (AGL) or British Acheson Electrodes Ltd (BAEL). The samples used in this work originate from archive material used to construct the Bradwell reactors. Unfortunatly, one of these reactors contained material manufactured by AGL and one manufactured by BAEL, therefore the unique identity of the samples cannot be confirmed. Magnox graphite is formed from a needle coke resulting in preferential alignment of the coke grains during extrusion and hence anisotropic properties. The elongated filler particles range in size up to ~2mm long by ~0.5 mm wide and are

surrounded by smaller coke particles, flour grains and a coarse textured coal tar pitch. The virgin material has a typical density of about 1.6 $g.cm^{-3}$. The virgin material contains a high percentage of porosity (~25-30% by volume). Typical thermo-mechanical properties of Magnox graphite are given in Table 0.1 in the directions parallel and perpendicular to extrusion (referred to as Parallel and Perpendicular within this thesis). These values were derived from various sources contained in the International Database on Irradiated Nuclear Graphite Properties (Hacker *et al.*, 1998).

The manufacturing process results in Magnox graphite having an extremely complex microstructure, originating from the graphitisation of several carbonaceous phases, as shown by optical microscopy, Figure 0.9. The material contains large, elongated petroleum coke filler particles (F) (Shell H-100), surrounded by smaller filler particles, flour grains and a coarse-textured coal-tar binder phase (B). It has ~25-30% porosity (by volume) of which the majority (~21%) is open (*i.e.*, accessible to oxidising gases). The filler particles contain shrinkage cracks (parallel to the basal planes) indicating a common basal plane alignment within crystallites. The microstructure of the binder phase contains mostly gas-evolution pores of different size.

PROPERTY	DIRECTION	VALUE
Compressive Strength (MPa)	Parallel	25
	Perpendicular	30
Dynamic Young's Modulus. (GPa)	Parallel	11
	Perpendicular	5.5
Thermal Conductivity ($Wm^{-1}K^{-1}$)	Parallel	190
	Perpendicular	120
CTE (Low Temperature Range)(10^{-6} K^{-1})	Parallel	0.91
	Perpendicular	3.01

TABLE 0.1 Typical Properties of Magnox graphite.

The anisotropy exhibited by Magnox graphite was unacceptable for the higher irradiation fluences and temperatures that are attained in AGRs (Davies, 1996). After development and testing stages, the final material chosen for use in AGRs is a near-

isotropic, moulded graphite developed from Gilsonite coke. Named GCMB graphite it was first produced by BAEL and then its successor company UCAR Ltd (AGL also manufactures a Gilsonite graphite, called IM1-24). The use of Gilsonite coke results in a near-isotropic material consisting of quasi-spherical grains up to ~1mm in diameter. These exist in a matrix that originated as flour coke and a smooth coal tar pitch binder before graphitisation at ~3000 °C. Impregnation during the baking cycle raises the density to ~1.8 $g.cm^{-3}$ and the material has a total pore volume of ~20%. Typical properties of virgin AGR moderator graphites are shown in Table 0.2. It should be noted that the CTE is higher than in both of the directions of Magnox graphite.

Although the bulk properties of AGR graphites are more isotropic than the Magnox material, the manufacturing process also results in AGR graphites having an extremely complex microstructure, as shown using optical microscopy, Figure 0.10. There are spherical Gilsocarbon filler particles, originating from the coarse Gilsonite coke particles (G), ~0.9 mm in diameter, enclosed in a thin mosaic region (S). Also present are large fragments of Gilsocarbon particles (F). The Gilsocarbon filler particles consist of small contiguous crystallites, which are slightly misaligned to form a circumferential pattern that contributes substantially to the near-isotropy of the graphite. Within the filler particles are calcination cracks (C) resulting from volumetric shrinkage during calcination and are mostly closed pores. The Gilsocarbon filler particles are bound together within the fine-textured, binder phase (B), derived from coal tar pitch and the fine 'flour', and containing open and closed porosity. In the intermediate regions between filler particles, there are regions of fine mosaics (S), indicating the presence of graphite crystallites of size <10 μm. The mosaic texture of the binder phase also contributes to the bulk isotropy of moderator graphite. There are also large gas-entrapment pores in the binder phase, resulting from bubble percolation of volatile gases during the baking stage of manufacture that are open to the atmosphere. Within some open pores, areas of impregnation can be identified, Figure 0.10. For this work, samples of AGR graphite (GCMB grade) obtained from archive material from the Heysham II reactor are used, unless stated otherwise.

PROPERTY	VALUE
Compressive Strength (MPa)	90
Dynamic Young's Modulus (GPa)	11
Thermal Conductivity ($Wm^{-1}K^{-1}$)	119
CTE (Low Temperature Range) 10^{-6} K^{-1})	4.84

TABLE 0.2: Typical properties of AGR graphite.

The complex microstructures of both graphites present significant difficulties in describing the behaviour of these materials with reference to their constituent elements. The influence on properties of the graphite microstructure at the resolution of the optical microscope has been discussed extensively elsewhere (*e.g.* Neighbour, 1993). Because of these difficulties in interpretation, the microstructural influences can be simplified by viewing polygranular graphites as an assembly of single crystals. At its simplest, a two dimensional array can be constructed where each element of the array behaves as single graphite crystal. Due to the limited understanding of microstructural influences on property changes in polygranular graphites, this approach has been used extensively in the past and is discussed in Part A.

0.5 INTRODUCTION TO THE MEASUREMENT AND THE EFFECTS OF THE REACTOR ENVIRONEMNT

The graphite core suffers from two principal damage mechanisms during the lifetime of the reactor. The first is due to neutron irradiation which causes changes to the component graphite crystals. The second is radiolytic oxidation that gasifies carbon atoms into the circulating gas stream. Both of these damage mechanisms will be discussed in detail in Part A in relation to CTE. The first purpose of this introductory section is to give a brief summary to the way in which irradiation conditions are

measured and reported within the UK. The second purpose is to give an overview of the effects of the reactor environment on properties other than CTE with emphasis on how these can interact with changes in CTE.

In order to compare the amount of damage that occurs to the graphite lattice when the material is irradiated in different reactors (with different neutron spectra), irradiation neutron fluence should be expressed on a common scale. Within the UK, this scale is based upon the activation of a piece of nickel foil that would occur in a given reactor, against that which would occur if the foil were placed at a standard reference position in the DIDO materials testing reactor. Hence, graphite damage by neutron irradiation expressed in this fashion is based on the Equivalent DIDO Nickel (EDN) scale. Similarly, Equivalent DIDO Temperature (EDT) is used to relate irradiation temperatures to those at a standard reference position in the DIDO rector. The methods involved in converting the fluence and temperatures measured in a particular reactor to EDND and EDT respectively are complex and open to debate, as has been discussed by many authors *e.g.* Neighbour (1999) and Kelly (1994).

The net effect of radiolytic oxidation is to change the pore structure of the graphite that is open to the oxidising gas by gasifying carbon atoms from the pore surface. Neutron irradiation alters the atomic structure of the component crystallites thereby changing their dimensions, which in turn alters the surrounding pore structure and also changes the crystallites properties. These changes interact to produce a composite change to the bulk behaviour of the material.

With reference to thermo-physical properties other than CTE *e.g.* Young's modulus and thermal conductivity, the effects of radiolytic oxidation have been shown to result in an approximately exponential decrease in the property (for example, Figure 0.11). This decay is usually described by the Knudsen equation (Knudsen, 1959) as described by

$$X=X_0 exp(-bx) \qquad [04]$$

where X is the property of interest, X_0 is the value of the property before oxidation, x is the fractional weight loss of the graphite and b is an empirically derived parameter based upon a fit to the data.

The initial effects of neutron irradiation however result in an increase in Young's modulus, Figure 0.12. The combination of simultaneous neutron irradiation and radiolytic oxidation therefore result in an initial increase in modulus followed by a subsequent exponential decrease.

Of particular importance is the relationship between CTE and dimensional change. Initially, the effect of neutron irradiation is to cause nuclear graphites to decrease in dimensions. This is commonly known as irradiation shrinkage, with subsequent irradiation resulting in net pore growth and bulk expansion, *e.g.* Figure 0.13 for AGR graphite (Kelly, 1985). The fluence corresponding to the shrinkage maximum is often referred to as 'turnaround' and it is known that turnaround is delayed (*i.e.* occurs at a higher fluence) as a result of radiolytic oxidation. Knowledge of both irradiation shrinkage behaviour and CTE is important in order to understand fully the resultant shape change of graphite core components under different flux and temperature gradients. Therefore, although it is not an aim of this work to study dimensional change, elements of this study are relevant to an understanding of the relationship between dimensional change and CTE and will be discussed in Part A of the thesis.

A fundamental understanding of CTE and its interaction with other thermo-physical properties under neutron irradiation and radiolytic oxidation is therefore important in ensuring the mechanical stability of graphite moderated fission reactors and hence the continued safe generation of electrical power by this means.

0.6 SUMMARY

Within this chapter, an introduction to the thesis, the aims and structure of the work have been described. The first aim is to characterise the microstructural features controlling CTE and the second is to develop a microstructure based model of CTE in these materials. This has been followed by a review of the nuclear fission process and a description of the graphite moderated nuclear reactors used in the UK.

An introduction to the properties of graphite was then given that continued with a description of the manufacture of polygranular nuclear graphites. The specific type of

graphite used as moderator materials in the UK were then introduced with reference to structure observed by optical microscopy. The key carbonaceous phases, filler binder and impregnant were identified in each. Also, typical thermo-physical properties for each material were given. In order to provide the background to the following work an introduction to the measurement and effects of the reactor environment on moderator graphite was given with a particular emphasis on the relationship between CTE and dimensional change.

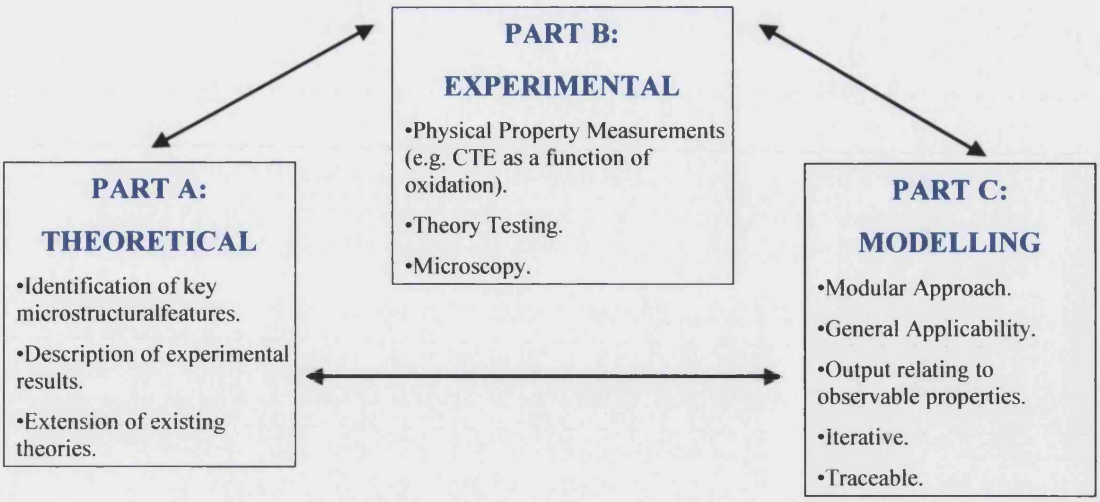

Figure 0.1. Outline of the interlinked structure of the thesis.

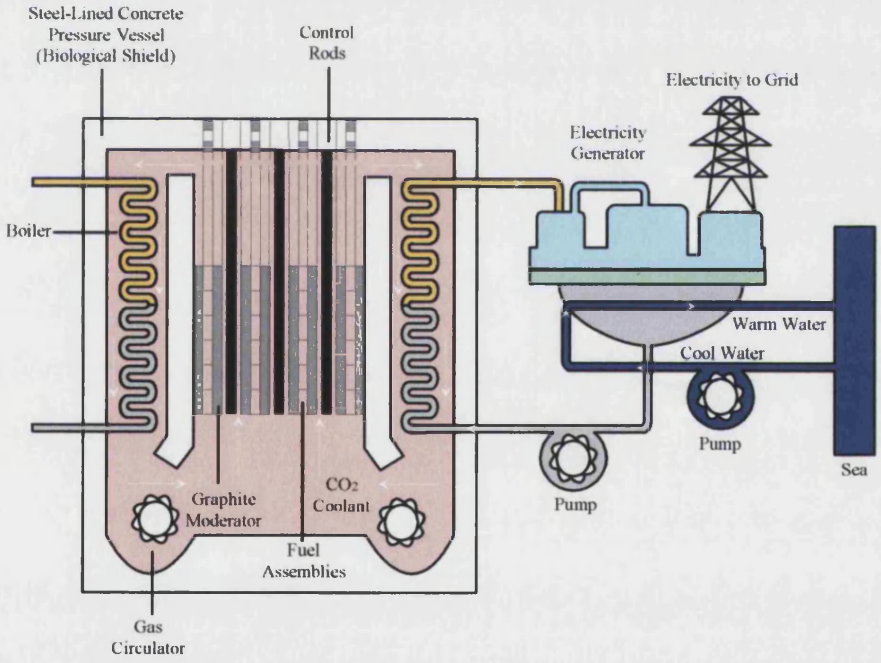

Figure 0.2. Schematic of the Advanced Gas Cooled Reactor.

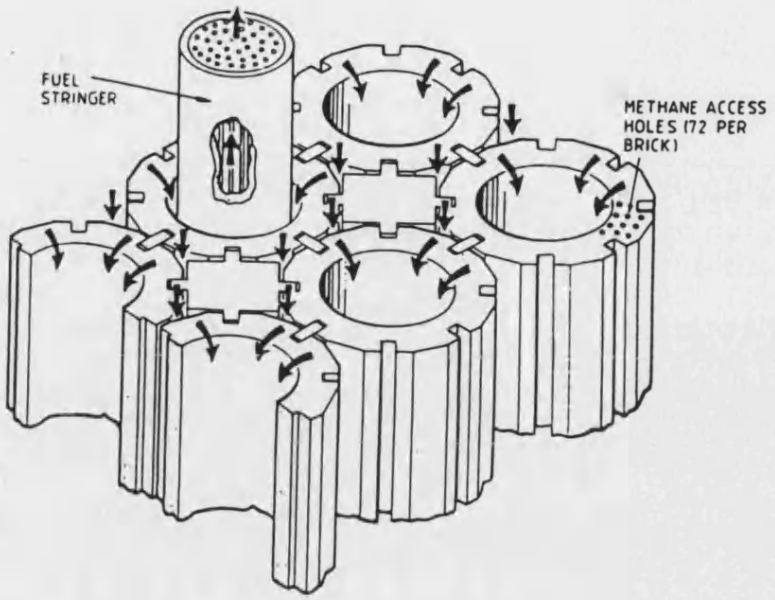

Figure 0.3. The 'keying' structure of the bricks in the AGR core (Kelly, 1985).

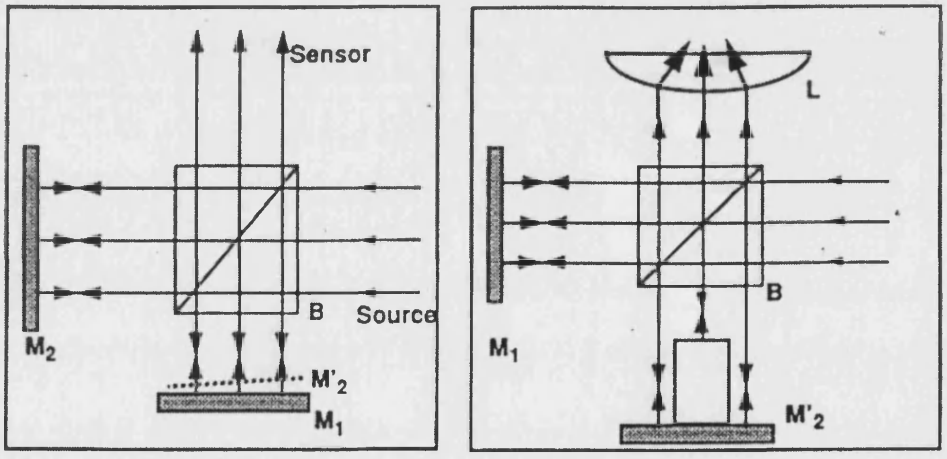

(A) (B)

Figure 0.4. Schematic diagram of the principle of interferometry, showing (a) the principles of interferometer (b) a typical measurement system with specimen (ASTM E289-94).

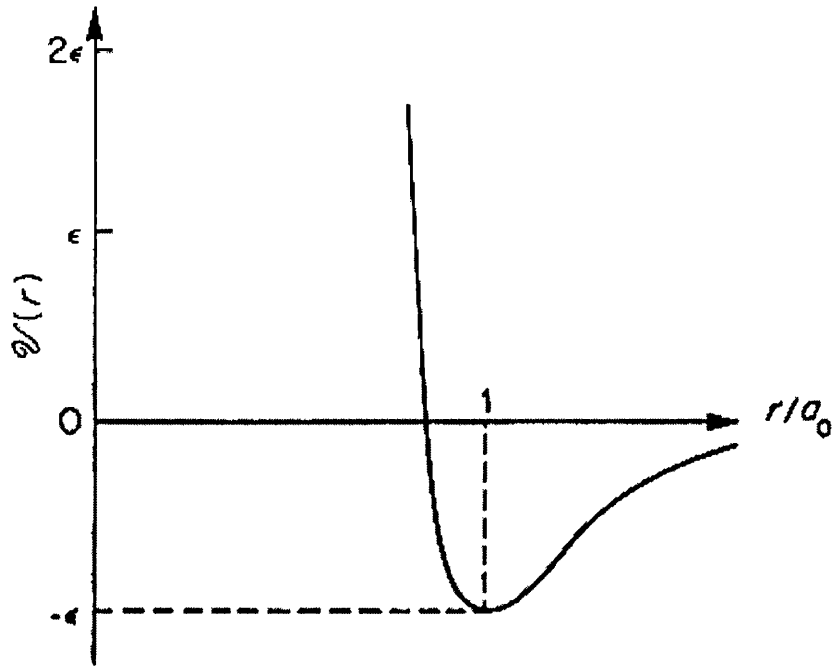

Figure 0.5(a). Schematic of an inter-atomic potential plotted in arbitrary units of ε and the atomic separation, r, plotted in units of a_0, the position of static equilibrium.

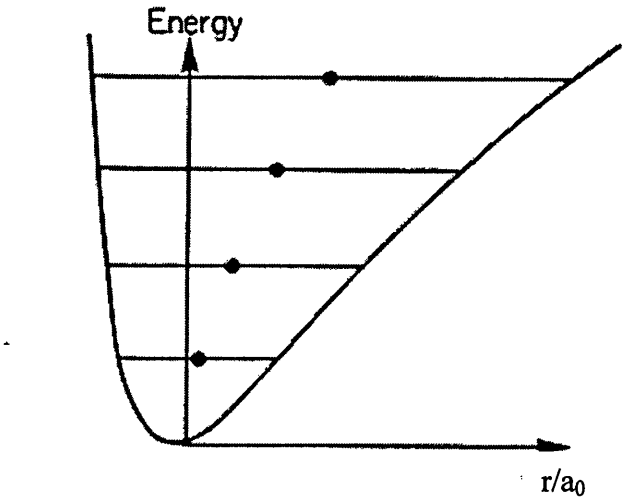

Figure 0.5(b). Schematic of the increase in the mean position of an atom in an asymmetric potential well as the energy of the system increases.

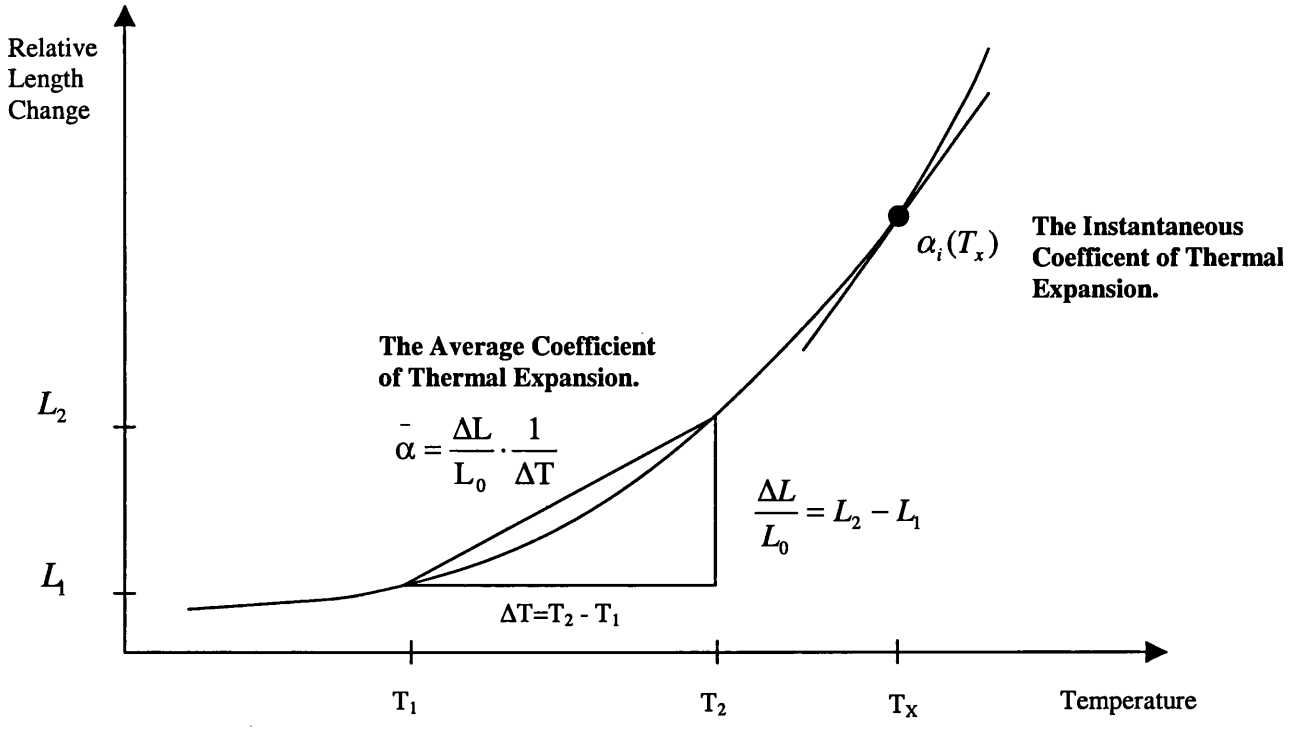

Figure 0.6. The different definitions of the Coefficient of Thermal Expansion. Where L_o is the initial sample length, L_2 and L_1 are the sample length at temperatures T_2 and T_1 respectively ($T_2 > T_1$).

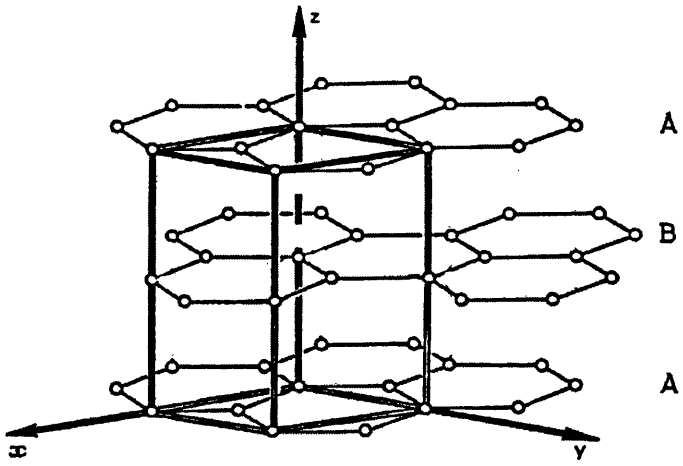

Figure 0.7. The graphite crystal structure (Mantell, 1968).

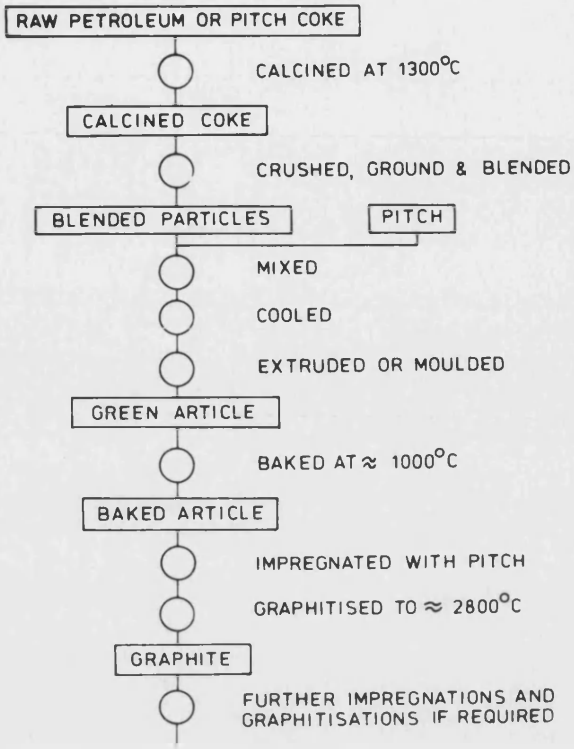

Figure 0.8. The nuclear graphite manufacturing process (Kelly, 1981).

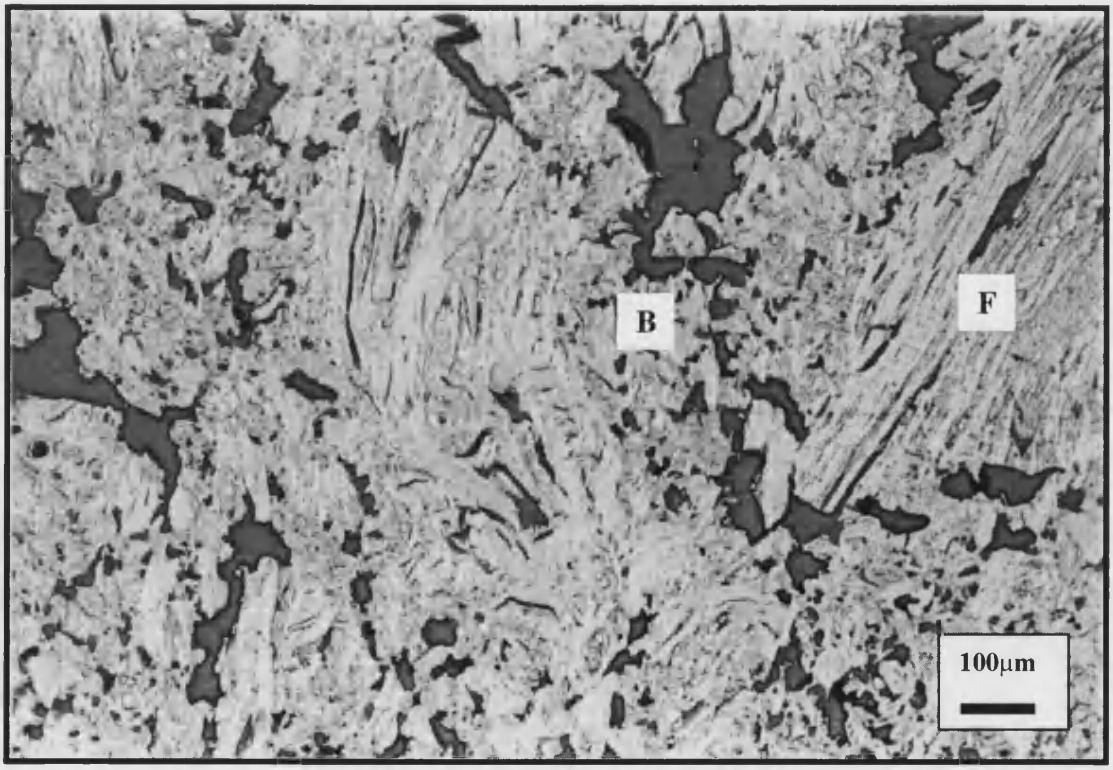

Figure 0.9. An optical micrograph of PGA graphite showing (F) filler particle and (B) binder phase.

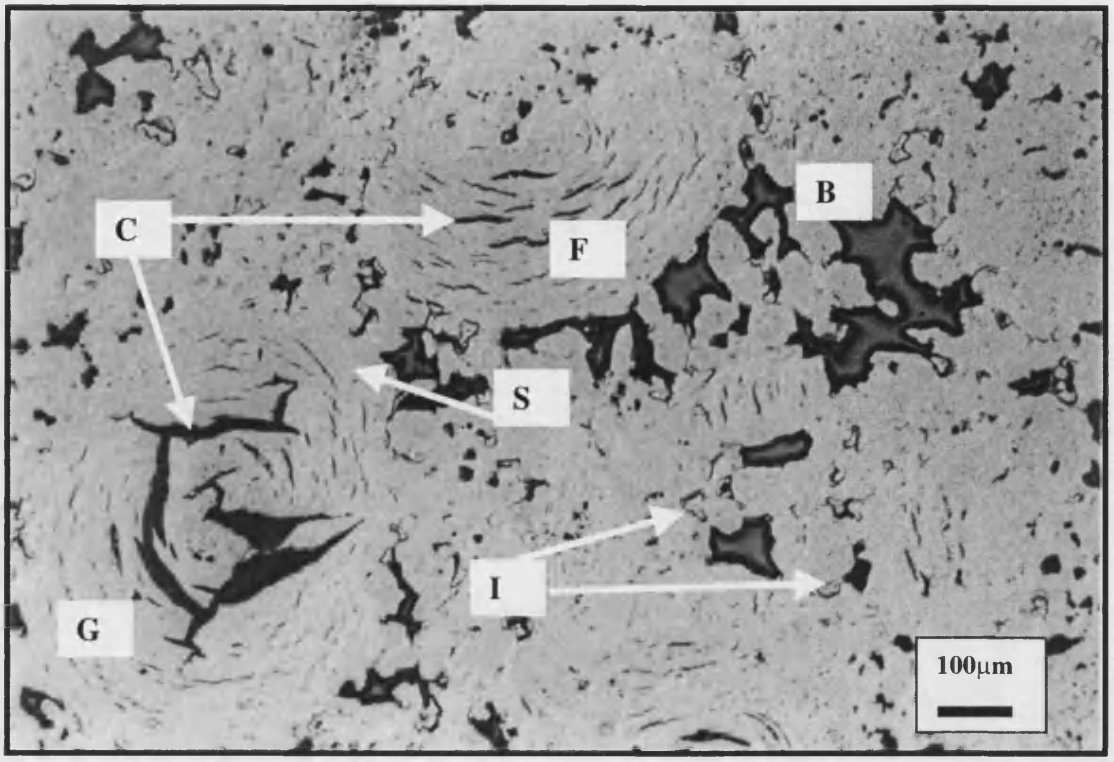

Figure 0.10. An optical micrograph of AGR graphite showing (G) Giloscarbon filler particle (F) gilsocarbon fragments (C) calcination cracks, (B) binder phase, (I) impregnant (pitch injected during baking) and (S) thin mosaic region.

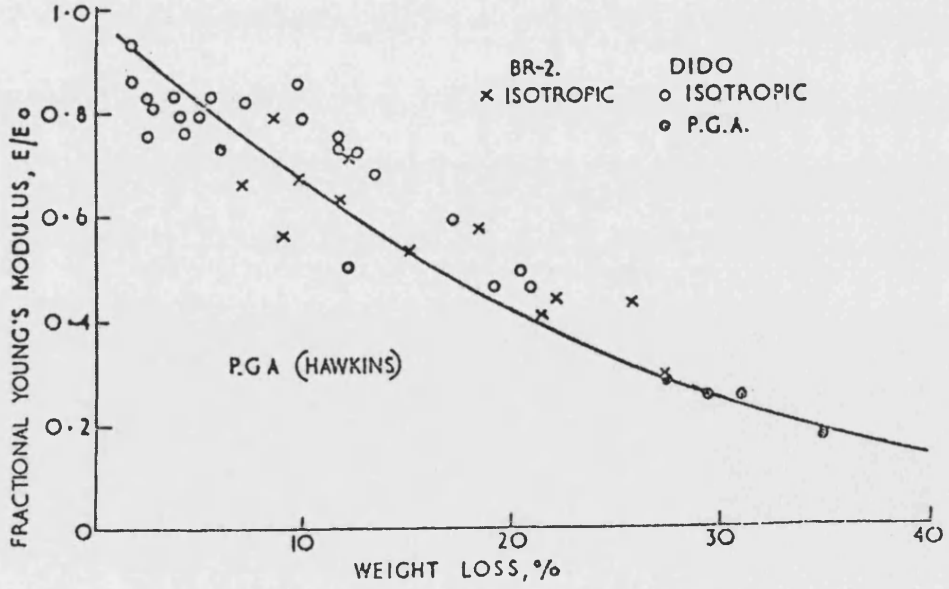

Figure 0.11. Young's modulus as a function of radiolytic oxidation for AGR (isotropic) and PGA moderator graphite (Brocklehurst *et al.*, 1968).

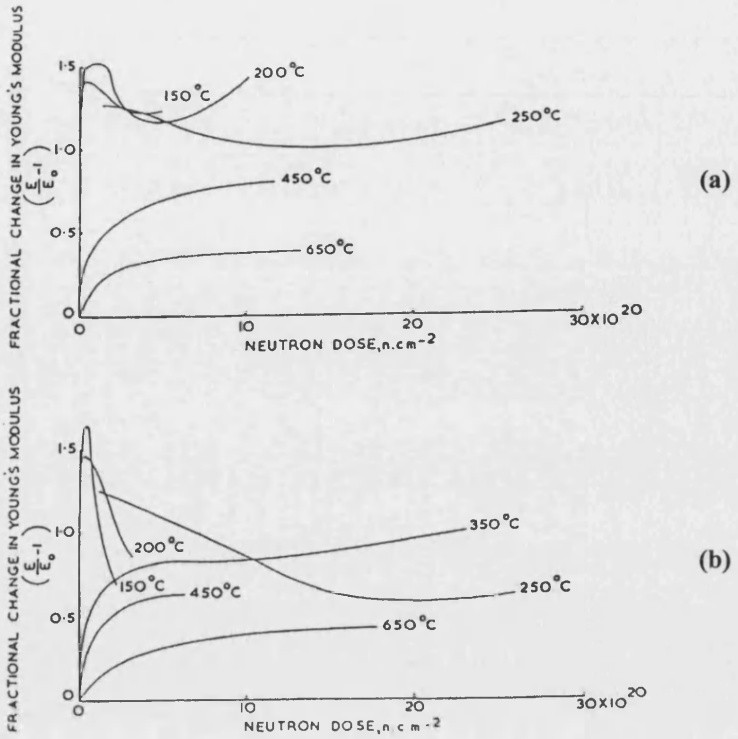

Figure 0.12. The effect of neutron irradiation on the Young's modulus of PGA graphite in the directions (a) perpendicular to extrusion and (b) parallel to extrusion (Birch and Brocklehurst, 1986).

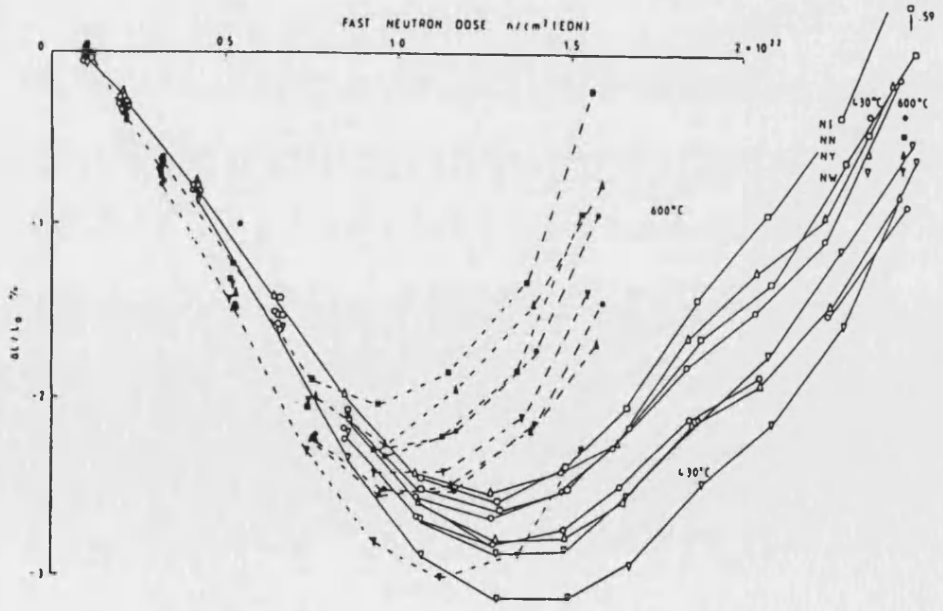

Figure 0.13. The dimensional change of AGR graphite under neutron irradiation (irradiated at 430 and 600°C EDT) (Brocklehurst and Kelly, 1993).

PART A: THEORETICAL CONSIDERATIONS.

OBJECTIVES

This part of the thesis has two main objectives. The first is to review the existing work on single crystal and polygranular graphites in relation to CTE. This review concentrates on the behaviour of the property under reactor conditions and also considers thermal oxidation effects with a view to characterising the important elements of microstructure that control CTE behaviour. The second objective is to critically review and extend (from a theoretical perspective) the description of the microstructural processes controlling CTE. Within the discussion, Chapter 3, new work is presented that will be used as a basis for the experimental investigations described in Part B.

"Pooh looked at his two paws. He knew that one of them was right,
and he knew that when you had decided which one of them was right,
then the other was left, but he could never remember how to begin"

A. A. Milne 1882-1956

CHAPTER 1
THE THERMAL EXPANSION OF UNIRRADIATED NUCLEAR GRAPHITES

In order to develop an understanding of CTE in irradiated and oxidised material, the thermal expansion of unirradiated graphites must first be discussed. This chapter begins with a review of existing information on the CTE of the unirradiated graphite single crystal before discussing the polygranular material.

1.1 GRAPHITE SINGLE CRYSTALS

During the 1980s, The International Committee for the Characterisation and Terminology of Carbon published the definitions of around 40 terms related to carbon science (Kochling *et al.*, 1982). Notably absent from these definitions is one for the single crystal itself and as such this term is used loosely in the literature (Alain *et al.*, 2000). In this work, the term Graphite Single Crystal should be taken to describe a material with the crystallographic properties discussed in the introduction and where the long range order and crystallographic perfection is extensive enough such that the effects of grain boundaries and imperfections are negligible. Natural graphites, such as Ticonderoga, are examples of such materials.

There have been numerous studies of the CTE of natural graphite single crystals and the class of materials called Highly Oriented Pyrolytic Graphite, HOPG, in which the degree of crystalline perfection approaches that of natural single crystals. Alain *et al.* (2000) conclude that for CTE and dimensional change, the behaviour of HOPG materials closely resemble those of single crystals. Work up to 1980 on the CTE of these materials has been reviewed in detail by Kelly (1981) and so only a summary is presented here.

In a graphite single crystal, there are two principal expansion coefficients: α_c, the CTE parallel to the hexagonal *c*-axis, and α_a, the CTE parallel to the basal planes (*a*-axis). Figure A.1 shows some measurements of α_c values for graphite single crystals (Nelson

and Riley (1945), Matuyama (1955), and HOPG Entwisle (1962)) measured in the temperature range 0-2000°C. These values were obtained from the variation in the position of x-ray diffraction peaks with temperature.

Nelson and Riley (1945) found the increase in interlayer spacing, d, with temperature, T (K), could be fitted to

$$d = 3.345 + 90.35 \times 10^{-6} (T - 273) + 6.315 \times 10^{-9} (T - 273)^2, (\text{Å}). \qquad [A1]$$

Given that $\alpha_c = (1/d)\, \partial d / \partial T$, differentiation of Equation [A1] gives

$$\alpha_c = 27.00 \times 10^{-6} + 3.05 \times 10^{-9} (T - 273), (\text{K}^{-1}) \qquad [A2]$$

Nelson and Riley found negative values of α_a that decrease to a minimum and then increase with temperature; $\alpha_a = 0$ at ~ 400°C and values of α_a become positive at higher temperatures. The room temperature values for graphite single crystals are $\alpha_c = 27.0 \times 10^{-6}$ K^{-1} and $\alpha_a = -1.5 \times 10^{-6}$ K^{-1}. The small values of α_a at all temperatures result from the strong C-C bonds in the basal plane while the negative values of α_a at low temperatures are due to the Poisson's contraction (following the large c-axis expansion) dominating the small thermal expansion of basal plane C-C bonds (Nelson and Riley, 1945). Riley (1945) gave the first theoretical description of thermal expansion in graphite single crystals. The theory is based upon the assumption that the thermal lattice vibrations can be separated into modes polarised parallel or perpendicular to the basal planes and is derived in detail and extended by Kelly (1981).

When considering the thermal expansion of natural and man-made graphites, deviations from perfect crystallinity also have to be considered. The extent of disorder within graphite crystallites can be described using the parameter p which is the probability of a stacking error between adjacent planes. For perfect graphite $p = 0$ and the interlayer spacing, d, is 0.3354 nm while for turbostratic carbon $p = 1$ and d ~ 0.344 nm (Bacon, 1951). Steward *et al* (1960) measured c-axis expansion over the temperature range -220-2600°C for graphites with $p = 0$, 0.2 and 0.7. For the graphite with $p = 0.2$ they found

$$d = 3.357 + 91.9 \times 10^{-6}(T - 273) + 5.3 \times 10^{-9}(T-273)^2, (\text{Å}) \qquad [A3]$$

which on differentiation gives

$$\alpha_c = 27.38 \times 10^{-6} + 3.16 \times 10^{-9}(T - 273), (\text{K}^{-1}). \qquad [A4]$$

For the graphites with $p = 0$ and $p = 0.7$ Steward *et al* (1960) found curves of d versus T that were similar to Equation [A3], but translated parallel to the temperature axis, *i.e.* at a given temperature the interlayer spacing had shifted by a constant amount. Therefore, although the absolute value of interlayer spacing may depend upon crystallite perfection, the thermal expansion behaviour remains similar.

1.2 POLYGRANULAR GRAPHITES – THE ASSEMBLY OF SINGLE CRYSTALS

Historically, polygranular nuclear graphites have been widely modelled as an "assembly of single crystals". However, within this model different approaches have been used to derive expressions of the CTE of the bulk material as a function of the CTE of component crystallites. Sutton and Howard (1962) described polygranular graphite as consisting of an assembly of unrestrained single crystals and derived an expression for CTE based upon expressions for crystallite orientation. Therefore, in general, the CTE values parallel and perpendicular to the direction of extrusion or moulding, $\alpha_{\parallel}$ and $\alpha_{\perp}$, are related to the single crystal values by the following equations

$$\alpha_{\parallel} = K_1\alpha_c + K_2\,\alpha_a, \qquad \alpha_{\perp} = K_3\,\alpha_c + K_4\,\alpha_a \qquad [A5a,b]$$

where the constants K_1 - K_4 are defined by the Bacon orientation functions (Bacon, 1956). For example, K_2 is defined as:

$$K_2 = \frac{\int I(\phi).\sin^3\phi.d\phi}{\int I(\phi).\sin\phi.d\phi} \qquad \text{(integrals between 0 and } 0.5\pi), \qquad [A6]$$

where ϕ is the angle between the c-axes of the graphite crystallites and the extrusion or moulding direction and $I(\phi)$ is the density of basal plane poles per unit solid angle ϕ. The other constants are related to K_2 as follows:

$$K_1 + K_2 = 1; \quad K_2 = 2K_3; \quad K_3 + K_4 = 1. \qquad \text{[A7a,b,c]}$$

In the case of a randomly orientated array of single crystals (that could be used to model, say, an isotropic graphite), $K_2 = 2/3$, therefore in such a model the CTE in any arbitrary direction, α_x, is given by the following

$$\alpha_x = \frac{1}{3}\alpha_c + \frac{2}{3}\alpha_a \qquad \text{[A8]}$$

Kelly (1981) states that, in general, the volumetric CTE of a polycrystal is given by the trace of the tensor of the individual thermal expansion coefficients, relative to an arbitrary axis of the sample *i.e.*

$$\alpha_v = Trace\begin{pmatrix} \alpha_{xx} & \alpha_{xy} & \alpha_{xz} \\ \alpha_{yx} & \alpha_{yy} & \alpha_{yz} \\ \alpha_{zx} & \alpha_{zy} & \alpha_{zz} \end{pmatrix} = \alpha_{xx} + \alpha_{yy} + \alpha_{zz} \qquad \text{[A9]}$$

Expressed using the notation of Equation [A5], with $\alpha_{\|}$ and $\alpha_{\perp}$ representing the expansion of the sample relative to the direction of extrusion or moulding, Equation [A9] can be re-written as follows

$$\alpha_v = 2\alpha_{\perp} + \alpha_{\|} \qquad \text{[A10]}$$

In the isotropic case, the volumetric CTE is equal to three times the linear CTE (Ibach and Luth, 1991) enabling the following relationship to be derived.

$$\alpha_v = 2\alpha_a + \alpha_c \qquad \text{[A11]}$$

Measurements of CTE on both isotropic and anisotropic polygranular graphites show that $\alpha_v < 2\alpha_a + \alpha_c$. This inequality is usually attributed to accommodation of expansion in porosity in the graphites, specifically in Mrozowski cracks that form parallel to the basal planes during manufacture as a result of anisotropic shrinkage on cooling from graphitisation temperatures. Although Mrozowski (1956) postulated the existence of these cracks, it was Sutton and Howard (1962) who claimed to have observed them (using replica Transmission Electron Microscopy) as being ~25-30 nm in width with a periodicity of 500 nm. Mrozowski cracks are believed play a vital role in the understanding of CTE in nuclear graphites and, as such, are discussed extensively throughout this thesis.

Sutton and Howard (1962) adapted Equation [A5] to account for accommodation effects such that

$$\alpha_{\parallel} = K_1\gamma\alpha_c + K_2\beta\,\alpha_a, \text{ and } \alpha_{\perp} = K_3\gamma\alpha_c + K_4\,\beta\alpha_a \qquad \text{[A12a,b]}$$

where γ and β are accommodation coefficients for CTE in the c and a directions respectively. They also introduced an "orientation parameter", x, given by $K_2=1/3(2 + x)$, with subsequent relationships to the other K-values. Numerical values of x and γ were obtained by measuring $\alpha_{\parallel}$ and $\alpha_{\perp}$ at 400°C where $\alpha_a \approx 0$ (Nelson and Riley, 1945). At this temperature

$$x = (R - 1)/(R - ½) \text{ and } \gamma = (\alpha_{\parallel} + 2\alpha_{\perp})/\alpha_c, \qquad \text{[A13a,b]}$$

where $R = \alpha_{\perp}/\alpha_{\parallel}$. Values of $\gamma = 0.36$ to 0.39 and $x = 0.28$ to 0.40 were found for various blocks of a "British reactor grade A" graphite (presumably, Magnox graphite, PGA grade). Using x-ray methods, the constants K_1-K_4 were determined and hence values of the factor $\beta = 1.03$ and 1.45 were obtained for two blocks of the graphite. Sutton and Howard (1962) note that values of $\beta > 1$ are meaningless as pure accommodation coefficients and suggest that the measurement of values > 1 in the Magnox graphite may be due to the existence of intercrystalline stresses.

In a similar approach to that of Sutton and Howard, Price and Bokros (1965) investigated the CTE of a range of graphites and pyrocarbons. Adapting their notation to that used above, they employed a simplified version of Equation [A12]

$$\alpha_{\|} = K_1 \gamma \alpha_c + K_2 \alpha_a, \text{ and } \alpha_{\perp} = K_3 \gamma \alpha_c + K_4 \alpha_a \qquad [A14]$$

The assumption that $\beta = 1$ was justified on the grounds that Mrozowski cracks lie parallel to the c axis and only act to accommodate expansions perpendicular to the basal plane. Morgan (1967) showed that Equation [A14] could be written as

$$\alpha_{\|} = K_1 \gamma_{\|} \alpha_c + (1 - K_1 \gamma_{\|}) \alpha_a \text{ and } \alpha_{\perp} = K_3 \gamma_{\perp} \alpha_c + (1 - K_3 \gamma_{\perp}) \alpha_a \qquad [A15a,b]$$

and stated that the assumptions by Sutton and Howard that $\gamma_{\|} = \gamma_{\perp}$ and $\beta_{\|} = \beta_{\perp}$ and by Price and Bokros that $\beta_{\|} = \beta_{\perp} = 1.0$ are neither necessary nor correct as the degree of accommodation provided parallel and perpendicular to extrusion is a function of crystallite orientation. He suggested that accommodation could be accounted for by a single coefficient whose value varied with the direction of measurement of CTE. Morgan also noted that Equation [A15] is of the same form as one derived on general thermodynamic grounds by Simmons (1959)

$$\alpha_{\|} = A_{\|} \alpha_c + (1 - A_{\|}) \alpha_a \text{ and } \alpha_{\perp} = B_{\perp} \alpha_c + (1 - B_{\perp}) \alpha_a \qquad [A16]$$

where $A_{\|}$ and $B_{\perp}$ are parameters related to the stress distribution in the polygranular graphite. This equation is often written in terms of α_x, the CTE in a generalised direction, x, such that

$$\alpha_x = A_x \alpha_c + (1 - A_x) \alpha_a \qquad [A17]$$

A difficulty with Equations [A16] and [A17] is in relating the parameters to measurable properties of the graphite. In an attempt to overcome this problem Jenkins (1964) derived a similar expression for α_x ,

$$\alpha_x = (M_x/\mu_x)\alpha_c + [1 - (M_x/\mu_x)]\alpha_a \qquad [A18]$$

where M_x is a complex function of the degree of preferred orientation, the extent of cracking and the crystallite elastic compliances, and μ_x is the elastic modulus of the polygranular graphite in the x-direction. This model assumes that there is a boundary restraint acting on the graphite crystallites and that the average strain of each crystallites is the same as the average strain in the matrix that provides the boundary restraint. However, M_x still contains free parameters that account for "structural effects".

Martin and Entwisle (1963) measured the CTE of PGA graphite heat-treated to different temperatures over the temperature range -196 to 700 °C; they also studied pressed natural graphite and an isotropic graphite (but no details of the type of isotropic graphite were given). They analysed their results using Equation [A17] expressed as

$$A_x = \frac{\alpha_x - \alpha_a}{\alpha_c - \alpha_a} \qquad [A19]$$

and demonstrated that CTE values measured over two temperature ranges were linearly related to each other, so offering some justification for their assumption that A_x is independent of temperature. Mason and Knibbs (1964) measured the CTE of several graphites including Magnox moderator graphite over the range -196-2000°C and analysed their results using Equation [A16]. For the reactor grade graphite at 400°C they found $A_{\|}$ = 0.084 and $B_{\perp}$ = 0.160; the low values were attributed to accommodation in 'microvoids'. The two parameters were constant up to 800°C, in agreement with the findings of Martin and Entwisle (1963), but increased progressively at higher temperatures and were ~30% greater than their initial values at 2000°C; this may be attributed to a progressive closure of microvoids as a result of c-axis expansion.

In summary, three different approaches have been used to relate the thermal expansion of an assembly of graphite single crystals to the thermal expansion of single crystals. The first approach described by Sutton and Howard (1962) uses a geometrical argument for crystallite orientation to determine the expansion of the assembly in an arbitrary direction. The second uses a therodynamic argument (Simmons, 1959) and the third is

based upon a constant stress or strain criterion (Jenkins, 1964). In each case, the models contain free parameters that incorporate most, if not all, microstructural influences. For example, the expression derived thermodynamically by Simmons, Equation [A17] uses the free A_x parameter to contain *all* microstructural effects, *e.g.* accommodation, orientation internal stress *etc.* This has resulted in an expression that resembles a "rule of mixtures" description that could be derived intuitively, containing no microstructural information.

1.3 THE EFFECTS OF MANUFACTURING ON CTE

In order to be able to improve on the existing microstructural descriptions of CTE in polygranular nuclear graphites their microstructures have to be further discussed and the key features controlling CTE need to be identified. Polygranular graphites differ in several respects from those of pyrolytic or single crystal graphites. As discussed in the introduction, the material can be characterised by the presence of two or more carbonaceous species (originating as the binder filler or impregnant phases), a wide range of crystallite sizes and orientations in different parts of the microstructure which are dependent upon raw materials and manufacturing processes. A complex pore network of different types is present that is created at different stages in the manufacture of the graphite and the filler. As a consequence of the simplicity and widespread use of the expressions presented in the previous section, only a small number of studies have investigated the effects of altering the manufacturing process on CTE and microstructure and these are discussed here.

Okada (1960) studied the influence of binder proportion, size of coke filler particles and type of binder pitch on the CTE of experimental carbons. He also studied the effects of subjecting the coke filler to different calcination temperatures. Okada showed that curves of CTE as a function of binder content exhibit maxima, whose positions change with particle size distributions of the filler coke. The positions of the maxima for CTE measured in the parallel direction were different from those for the CTE measured in the perpendicular direction. To investigate the dependence of CTE on particle size distributions of the coke filler, the ratio of coarse grain to fine powder was varied. Okada (1960) showed that CTE increased with increasing content of fine powder.

Further, Okada (1960) argued that the filler particles play the main role in controlling thermal expansion. As many of the filler particles contact each other directly, or they are connected to each other by very thin binder bridges around the contact points, most of the binder coke is present on the surface of the filler particles. Okada (1960) argued, therefore, that that the binder does not affect the thermal expansion of the main framework of the carbon.

Platonov *et al.* (1979) studied the CTE of a range of reactor graphites subjected to different heat-treatment temperatures. They found that in all cases the values of CTE increased as the final heat-treatment temperature is raised from 1000 to 2000 °C. However, values of CTE decrease sharply as the final heat-treatment temperature is increased above 2000 °C. This was attributed to the generation of Mrozowski cracks on cooling from the higher heat treatment temperatures. Values of the accommodation factor, A_x, were estimated using Equation [A17] and, in agreement with work described previously, the values of A_x varied with graphite type and increased with measurement temperature above 750 °C due to closure of Mrozowski cracks. However, in contrast with the work of Martin and Entwisle (1963) and Mason and Knibbs (1964) they found that A_x decreased progressively with measurement temperature up to 700 °C.

Kelly (1992a) suggested that the relatively high thermal expansion coefficients found for Gilsocarbon graphites and graphites containing Santa Maria cokes may be because large local differential strains do not develop or that cracks have been suppressed by isostatic moulding. He recognised that the extent of accommodation will depend upon the extent of cracking, which in turn depends upon coke structure, but that no detailed models relating crack formation to coke structure exist.

1.4 EFFECTS OF THERMAL OXIDATION

For many thermo-physcial properties of nuclear graphites, thermal oxidation has been found to represent a pessimistic bounding case for the effects of radiolytic oxidation (Pickup, 1996). In general, gaseous oxidation of graphite occurs in depth throughout a nuclear graphite specimen due to the existence of open and transport porosity. Interpretation of the results from any oxidation programme requires the oxidation

conditions to be such that the rate of attack is uniform within the samples. Within this section, the microstructural effects of oxidation on graphite single crystals are first presented, followed by the kinetics of oxidation of polygranular nuclear graphite.

The detailed study of the microstructural effects of thermal oxidation, in single crystals, began with the works of Hennig (1959, 1960, 1961, 1966) and Thomas (1965) on Ticonderoga natural graphite. Both Hennig (1961) and Griesdale (1963) noted that the ratio $R_{(a/c)}$ of the rates of oxidation by molecular oxidation in the *a* and *c* direction respectively, was greater than 15. Also, the oxidation mechanism produced distinctive pits on surface sites in the basal plane. Feates (1970) describe the oxidation mechanism under conditions of minimal reaction as occurring by diffusion of active species across basal surfaces to reactive sites, such sites being either vacancies or edge sites (Hennig and Kanter, 1960). When simulating the effects of radiolytic oxidation on nuclear graphites, thermal oxidation using CO_2 under conditions of minimal reaction is preferred (Alain *et al.* 2000). Glenda-Hughes and Thomas (1962) studied the reaction of carbon dioxide on natural graphite at temperatures between 800 and 900°C and report that the only attack mechanism is parallel to the basal planes with no evidence of in-plane pitting.

The kinetics of thermal gasification of polygranular graphite by carbon dioxide is well documented (*e.g.* Strange and Walker, 1976). The rate of gasification of heterogeneous, porous materials such as nuclear graphites can occur under one or more of three regimes, the dominance of each regime being dependant, primarily, on reaction temperature. The first regime, Zone I, considers the oxidation process to be under chemical control, *i.e.* the reaction rate is controlled by the reaction of active sites within the bulk of the solid. The second, Zone II, occurs when the rate controlling mechanism is determined by in-pore diffusion of reactant gas molecules from the external surface to reactive sites within the pores and subsequent transport of products from reactive sites to the exterior. The final regime, Zone III, occurs when external boundary layer diffusion is controlling the reaction, *i.e.* the rate is controlled by the transport of gas molecules to the external surface of the solid from the gas. Wood *et al.* (1980) state that for uniform (or homogeneous) oxidation within a specimen oxidation should proceed

slowly, to the extent that the concentration gradient of the reactant gas to the sample interior is insignificant, *i.e.* the reaction should proceed under Zone I conditions.

Some information on the effects of thermal oxidation on the CTE of nuclear graphites and carbons is also available. From studies on pitch-bonded carbons Okada (1960) reports that the influence of low temperature (Zone I) oxidation on CTE is small. He found that CTE decreases in the earlier stages of oxidation and then becomes constant for oxidation greater than ~18% weight loss. He attributes this to the fact that the macropore structure which is developed upon oxidation does not affect the thermal expansion of carbon. Zhao *et al.* (1981) studied the effects of the thermal oxidation of commercial petroleum coke graphites in dry air at 773 K and noted that, following a small decrease (~5%) in CTE between 0 and 0.7% weight loss, the CTE of these materials remained unaltered until at least 15% weight loss.

Neighbour *et al.* (1997) undertook a scoping exercise to determine if a significant change in the CTE of AGR moderator graphite occurs as a result of thermal oxidation up to ~40% weight loss. Two measurements of mean CTE were used: (i) between 20-120 °C and (ii) between 20-600 °C. A significant difference (95% confidence) was not found between the mean values of CTE for the as-received and oxidised graphites in either case.

1.5 THE EFFECTS OF PRE-STRESS

Due to the existence of loading and internal stresses within a reactor core the effects of pre-stress on CTE is of engineering importance and can also be used to further probe the nature of CTE within nuclear graphites. An increase in the CTE of polygranular graphite after compressive pre-stress was first observed by Gazda (1970) and later by Hart (1972). Matsuo and Sasaki (1981a) studied the variation with temperature of the CTE for H-327 grade nuclear graphite (an isotropic nuclear material, similar to AGR graphite) in the unstressed condition and in the presence of applied compressive stresses ranging from ~45% to ~95% of the failure stress. Their results showed that thermal expansion increased linearly with applied compressive stress, similar results were found by Geurin (1998). In both cases, this was attributed to stress induced closure of

microcracks thereby reducing the available internal crystallite accommodation. However, in later work Matsuo and Sasaki (1982) report that a tensile pre-stress also increases CTE. As a tensile stress would be expected to increase the available accommodation, a reduction in CTE was expected.

Neighbour *et al.* (1997) attempted to determine if a significant change in the CTE of AGR moderator graphite occurs as a result of compressive pre-stressing (at ~80% of the failure stress) compared with graphites in the as-received condition. Two measurements of mean CTE were used: (i) between 20-120 °C and (ii) between 20-600 °C. A significant difference (95% confidence) was not found between the mean values of CTE for the as-received and pre-stressed graphite between 20-120 °C, but a significant increase was found for 20-600 °C. In the latter case, the difference in the means of CTE was small.

Additional studies of the effects of both tensile and compressive pre-stress on CTE were conducted as part of the study of irradiation induced creep (see following chapter). Here, it is noted that the creep results support those given here. In particular, the anomalous increase in CTE under a tensile pre-stress has again been observed, although the magnitude is reported to be small.

1.6 THERMAL EXPANSION IN OTHER SIMILAR MATERIALS

For many ceramics and other polycrystalline and polygranular aggregates, thermal expansion is usually described as not being influenced at all by porosity and is simply controlled by the expansion of the constituent crystals (*e.g.* Euler, 1957 and Rice, 1993). Although the size and nature of the 'porosity' being considered is not discussed, it is likely that these discussions concern micrometric porosity.

Experimental studies have also been conducted using controlled porosity. For example, Coble and Kingery (1956) added naphthalene to an alumina casting slip to vary porosity from 5 to 50% by volume. The samples were produced in a manner that ensured comparable grain development, thereby eliminating structural variables other than porosity. Coble and Kingery (1956) concluded that the CTE of isotropic ceramic bodies

was unaffected by changes in porosity. In anisotropic ceramic bodies the effect of porosity upon CTE is not known, but Coble and Kingery (1956) state that it is expected to be small.

In his review of thermal expansion of non-metallic crystals Austin (1952) also discusses the thermal expansion of aggregates and how these differ from those of single crystals. Considering the effects of porosity on expansion, two limiting cases are considered, A and B in Figure A.2. The first is that in which there is a continuous matrix of solid material which contains holes, A in Figure A.2, the second is a bonded group of solid grains surrounded in part by porosity, B in Figure A.2. Austin shows that in the first case the observed expansion of the solid is simply that of the matrix material. In the second case it is difficult to make generalisations since the net expansion is influenced, primarily, by the degree of bonding and by the anisotropy and the size of the grains. In many cases (as is observed in nuclear graphites) the expansion of the aggregate appears to be less than that of the single crystal but this is not always the case.

The expansion of polycrystalline and polygranular aggregates often displays hysteresis between heating and cooling curves and between thermal cycles (behaviour which is not exhibited by the single crystal). Sosman (1928) has discussed the general situation, Figure A.3. If an aggregate of isotropically orientated crystals is heated at a rate slow enough to avoid the creation of a large temperature gradient, each grain expands equally. On cooling, the aggregate returns to its original size and shape. If, however, the rate of heating is rapid enough to produce a large temperature gradient some grains expand more rapidly than others, disrupting the structure.

The second row of Figure A.3 represents the behaviour of anisotropically orientated grains. When such a material is heated the grains expand differently in different directions, creating porosity. Resultant changes in localised stresses also partially re-orientate the structure such that when the aggregate is cooled some porosity remains unfilled and the structure is partially disrupted. Thus, subsequent cooling and expansion curves result in a hysteresis, shown in the third row of Figure A.3.

1.7 SUMMARY

Within this chapter the CTE of as-received graphite has been reviewed beginning with the single crystal and continuing by consideration of polygranular nuclear graphites. The CTE of single crystals and HOPG materials is well understood and can be described *ab initio* based upon the theoretical work of Riley (1945). However, due to the structural complexity of nuclear graphites a different approach is required. Historically, a simple abstraction of the microstructure has been made. This considers the polygranular material to consist of a loose assembly of graphite single crystals and this approach has been used extensively to describe the properties of nuclear graphites in relation to those of the single crystal. With respect to the objectives of this work, however, the model of an assembly of single crystals contains no provision for relating microstructural elements to CTE. In general, microstructural effects are contained within empirically derived parameters.

Although the focus of many previous works has been on the assembly of single crystals model, some considerations of the microstructural influences controlling CTE have been made. Many of the microscopical studies are discussed in relation to irradiation and radiolytic oxidation changes and are to be reported in the next chapter. In this chapter, those works that relate microstructure specifically to unirradiated graphites are reported. Okada (1960) considered the effects of altering the pitch content and the proportion and size of filler particles used in the manufacture of a range of graphites and carbons. He concludes that filler particles play the main role in determining thermal expansion and increasing the content of fine particles in the coke mix increases the CTE of the artefact. Also, evidence was presented for Russian moderator graphites supporting the hypothesis that Mrozowski cracks begin to close as temperature is raised from 1000 to 2000°C but annealing above 2000°C results in a rapid decrease in CTE. The use of thermal oxidation was discussed as a method of simulating radiolytic oxidation and previous studies (one to ~40% weight loss) on the effects of thermal oxidation on CTE have found no large differences in CTE under thermal oxidation. The effects of compressive and tensile pre-stressing on CTE were also reviewed and the CTE was reported to increase in both cases.

The thermal expansion of other polycrystalline and polygranular materials has been considered and it has been generally concluded that porosity changes have little effect in influencing CTE. The general discussion of the thermal expansion behaviour of a polygranular aggregate was discussed by Sosman (1928) and indicates that differences in dilation between heating and cooling curves and thermal cycles are to be expected.

CHAPTER 2

THERMAL EXPANSION AND THE REACTOR ENVIRONMENT

The aim of this chapter is to document the effects of neutron irradiation on CTE in nuclear graphites followed by a discussion of the effects of radiolytic oxidation. As much of the existing literature on this subject is discussed relative to the corresponding bulk dimensional changes, this property is also considered. In a similar manner to the previous chapter, the discussion of neutron irradiation and radiolytic oxidation commences with the microstructural effects of each on natural graphites and HOPG materials before considering moderator graphites. The chapter continues with a description of how the irradiation data of HOPG has been applied to polygranular graphites, by extension of the "assembly of single crystals" model discussed in the previous chapter.

2.1 FAST-NEUTRON DAMAGE IN HOPG GRAPHITE

The effects of neutron irradiation and irradiation temperature on the graphite structure at the atomic scale are reasonably well understood. However, the relationship between these microstructural changes and the behaviour of CTE and dimensional change within polygranular nuclear graphites are less well known. This section therefore begins with a discussion of the basic fast-neutron displacement mechanism in graphite, followed by the effect of this mechanism on the CTE and dimensional change of natural graphites and HOPG materials. The effects of neutron irradiation on nuclear graphites are then presented which focuses on a microstructural description of these effects on CTE.

The fast neutrons produced in fission have energies of about 2 MeV. Moderation of these neutrons to thermal energies of <1 eV in graphite-moderated reactors is caused by elastic collisions with carbon atoms. Neutrons with energies in the range 25-60 eV are required to displace carbon atoms from the graphite lattice creating vacancies and interstitials; a large fraction of them will recombine with lattice vacancies. Others will coalesce and eventually may form dislocation loops or new graphitic planes. The interstitial clusters, on further irradiation, may be destroyed by fast neutrons or by

displaced carbon atoms (radiation annealing). The formation of interstitial clusters, dislocation loops and new graphitic planes will cause an expansion of the graphite crystal in the c direction. Adjacent lattice vacancies in the same graphite layer are believed to collapse parallel to the layers and form sinks for other vacancies, causing shrinkage parallel to the graphite layers, *i.e.*, in the a-direction (Burchell and Oku, 1994). There is a balance between displacement rate and defect mobility, which is related to temperature (Carpenter and Norfolk, 1984). Kelly (1992a) confirms that, at irradiation temperatures below ~300 °C (EDT), large bulk volume increases occur on neutron irradiation that are associated with high stored energy levels, so called "Wigner energy". At temperatures above 300 °C there is low Wigner energy due to a high defect mobility. At these temperatures, interstitials are so mobile that they aggregate to form large areas of new graphene planes and changes occur at constant volume. Dislocation loops have been observed in graphites (Amelinckx *et al.*, 1965), and it has been suggested that these loops are formed by the collapse of adjacent lattice planes into vacancy clusters (Kelly, 1982).

The effects of irradiation temperature are shown clearly in the data of Kelly *et al.* (1966a) who reported the effects of neutron irradiation on CTE and dimensional change. These were measured parallel and perpendicular to the deposition plane of a HOPG heat-treated to 2900 °C, and denoted as type β. The effects of neutron irradiation up to 15 x 10^{20} n/cm^2 (EDN) in the temperature range 150-200 °C on CTE are in Figure A.4(a); similar data for irradiations to higher fluences (up to 30 x 10^{20} n/cm^2 (EDN)) and at higher temperatures (250-650 °C) are in Figure A.4(b). The corresponding dimensional changes are in Figures A.5(a) and A.5(b), respectively. After irradiation at low temperatures the values of CTE in the *c*-direction generally decrease with initial irradiation fluence before becoming almost constant at doses greater than ~7 x 10^{20} n /cm^2 (EDN), Figure A.4(a). The CTE in the *a*-direction changes from negative values to positive values at an irradiation dose that depends upon temperature. At higher irradiation temperatures, Figure A.4(b), the values of CTE in the *c*-direction is nearly independent of neutron fluence and slightly lower than the unirradiated single crystal value; similar results are found for CTE in the *a*-direction with the value being slightly less negative than the unirradiated single crystal value. This behaviour is in agreement

with the mechanism of aggregation of interstitials to form new graphitic planes and a restoration of good graphitic structure at high temperatures.

A consideration of the respective dimensional changes shows that at low irradiation temperatures, Figure A.5(a), there are large expansions in the *c*-direction and smaller contractions in the *a*-direction, with a large net increase in volume. At a given neutron fluence the extent of the dimensional changes decrease with increasing irradiation temperature. Similar, but smaller, changes are seen at higher irradiation temperatures, which occur at nearly constant volume, Figure A.5(b). Both the CTE and dimensional change measurements are confirmed by other studies, *e.g.* Platonov *et al.* (1981) and are again in agreement with the irradiation damage mechanism described previously.

The irradiation work was continued to higher neutron fluences by Kelly and Brocklehurst (1971) who irradiated HOPG to 2.5 x 10^{22} n/cm^2 EDN at temperatures between 270 and 710 °C. CTE and dimensional change measurements were again made parallel and perpendicular to the deposition planes, Figures A.6(a,b) and A.7(a,b) respectively. Figure A.6 confirms that the *c*-axis and *a*-axis CTE values remain unchanged even at these high neutron fluences. Figure A.7 also confirms a continuation of the effects at low fluences for dimensional change *i.e.* a linear increase in dimensional change at temperatures >300°C. These are essentially linear extrapolations of the results obtained for HOPG at lower fluences in the earlier studies, Figure A.5 (Kelly *et al.*, 1966a).

2.2 IRRADIATION INDUCED STRUCTURE CHANGES IN POLYGRANULAR NUCLEAR GRAPHITES

The application of the HOPG data to an understanding of irradiation induced changes in nuclear graphites has largely focused upon an extension of the "assembly of single crystals" model described in the previous chapter. In particular, Equation [A17] has been adapted and used extensively. The details of this approach are presented later in section 2.4. Within this section, the CTE behaviour of AGR and Magnox moderator graphites are presented and compared to other nuclear graphites. This is followed by a

review of information relating to microstructural and CTE changes observed within nuclear graphties as irradiation damage increases with neutron fluence.

The CTE changes within AGR and Magnox moderator graphites as a function of neutron fluence are very different. Figure A.8 shows the irradiation behaviour an of AGR moderator graphite, irradiated at 430 and 600°C EDT. At the lower temperature CTE rises at low doses from ~4.2 x 10^{-6} K^{-1} to ~5 x 10^{-6} K^{-1} at 30 x 10^{20} n/cm^2 (EDN) before falling to ~1.5 x 10^{-6} K^{-1} at ~200 x 10^{20} n/cm^2 (EDN). During this decrease a "hump" in CTE is observed at ~100 x 10^{20} n/cm^2 (EDN). These data have been analysed by Neighbour *et al.* (1998) who could find no statistical justification for this feature (also, no physical evidence exists for this feature). At the higher irradiation temperature, the initial peak is lower and the rise more gradual followed by a rapid fall in CTE to ~1.5 x 10^{-6} K^{-1} at ~150 x 10^{20} n/cm^2 (EDN). The behaviour of Magnox graphite is more complex due to its anisotropy and is therefore different in the directions parallel and perpendicular to the extrusion direction. Figure A.9 shows the CTE of Magnox graphite at 600^{0}C. In both the Parallel and Perpendicular directions Magnox graphite exhibits an initial small rise in CTE upon irradiation which then remains constant until a fluence ~100 x 10^{20} n/cm^2 (EDN). At higher fluences the CTE values rise sharply. Although not given on Figure A.9, Brocklehurst and Kelly (1993) also show that irradiation at lower temperatures (<300°C) results in rapid increases in CTE (up to ~10 x 10 10^{-6} K^{-1}) and that these saturate at modest doses (~ 20 x 10^{20} n/cm^2 (EDN)).

The behaviour of AGR and Magnox graphites under irradiation is similar to those of other nuclear graphites. For example, Burchell and Eatherly (1991) found for the isotropic GraphNOL N3M nuclear graphite, subjected to irradiations between 600 and 875 °C and to fluences between 420 x 10^{20} and 200 x 10^{20} n/cm^2, that the CTE initially increases before decreasing well below the unirradiated value. For a Russian anisotropic nuclear graphite, Virgilev (1981) concluded that the CTE of GMZ graphite was independent of neutron fluence in both parallel and perpendicular directions for all heat-treatment temperatures from 2400-3000 °C. In an attempt at generalisation, Platonov *et al.* (1979) noted that under low temperature irradiation (< 250 °C) the CTE of most graphites first increases and then decreases to the initial or lower value. However, at a

high irradiation temperature, the changes in CTE of various grades of graphite are substantially different in both absolute magnitude and sign. The most general conclusion seems to be that graphites with a low initial CTE show an increase in the CTE when irradiated, while high-density, isotropic materials with a large initial CTE show a decrease upon irradiation.

The changes in CTE as a function of neutron fluence have been attributed to irradiation induced changes in Mrozowski cracks. Burchell and Eatherly (1991) proposed that the initial increase in CTE is due to the closure of fine porosity by irradiation induced c-axis crystal expansion. The size of the initial increase is determined by the irradiation temperature. At higher temperatures, the magnitude of the initial increase in CTE is less since the available internal porosity for c-axis growth is reduced due to greater closure of the fine porosity by thermal expansion. Subsequent reductions in CTE are caused by the generation of new porosity with continued neutron damage. This is supported by other workers with different graphites, *e.g.* Virgilev (1981). Similarly, the dimensional change behaviour of AGR graphites (see Figure 0.13) has also be described as being controlled by "small scale" porosity changes as Simmons (1959) correlated CTE and dimensional changes.

In an attempt to further understand irradiation induced porosity changes Kelly *et al.* (1974) report the effect of neutron irradiation up to 1.5 x 10^{22} n/cm^2 (EDN) upon the development of porosity in AGR graphite, Figure A.10. Total porosity gradually decreases with increasing irradiation. They sub-divided the porosity into four pore size bands and showed that the contribution of the largest class of pores (100-10 μm) remained almost constant after an initial increase, whereas the volumes of smallest class of pores (<0.1 μm) showed a progressive decrease with irradiation. Concentrating solely on small porosity, Martin and Caisley (1977) studied the effect of irradiation of nuclear graphites at ~1035 °C on porosity of size 2.5-10 nm using small angle neutron scattering. This technique considers both open and closed porosity, although scattering can also occur from small crystallites and disordered regions. Included in their study were production batches of IM1-24 and GCMB grades of AGR graphite from AGL and BAEL, respectively. After a fluence of ~5 x 10^{21} n/cm^2 EDND, there was a reduction of 40% in pores with a radius of gyration of 10 nm. However, for pores of radius 2.5 nm,

there was an increase of 200% after the same fluence. In both cases, the rate of change of pore size due to irradiation decreased monotonically with increasing neutron fluence. The authors concluded that changes in the 10 nm porosity cannot be correlated with the onset of turnaround (in dimensional change) and suggest that there may be a correlation with pores which are larger than 10 nm. Thus small porosity is strongly altered by neutron irradiation whilst larger scale porosity remain unaltered.

In order to further understand the microstructural origins of changes in both CTE and dimensional change microscopical studies relating microstructural changes to relevant properties have to be undertaken. Due to the complex nature of the material it is difficult to obtain quantitative information, however several studies have been conducted with the aim of linking microstructure and property changes.

One of the earliest microscopial studies of a range of nuclear graphites under irradiation was conducted by Engle (1971). He used optical microscopy in combination with the measurement of CTE and dimensional change of a range of graphites irradiated at elevated temperatures (950-1280 °C) to develop a semi-quantitative model of the effects of irradiation on microstructure. He began by classifying elements of the microstructure as follows.

V_b bulk volume

V_c volume of the crystallites

V_y volume of the filler particles including closed microporosity (filler particles were denoted by Engle (1971) as sink-float particles)

V_{p1} closed microporosity within the filler particles (extra-crystallite porosity)

V_{p2} closed porosity within the filler particles (intra-grain porosity)

V_{p3} open porosity

Engle (1971) then linked the bulk volume changes following irradiation to microstructural changes, Figure A.11(a-e). He noted the following common features during initial bulk contraction.

For needle-coke graphites, closed intra-grain porosity (V_{p2}) is eliminated during the initial densification up to the maximum contraction, but for near-isotropic graphites, a large portion of V_{p2} is not filled by c-axis expansion and volumetric turnaround occurs before V_{p2} is depleted, Figure A.11(d). The median volume of the filler particles increases with fluence. The open porosity V_{p3} decreases up to volumetric turnaround, but thereafter new porosity is generated and appears predominantly in V_{p3}.

Engle (1971) states that the volumetric changes of the filler particles combined with the changes in V_{p2} and V_{p3} represent the average contribution of the crystallite volume changes and show the internal re-arrangements that occur within the microstructure so that the bulk volume changes are related to the crystalline and porosity changes by:

$$\Delta V_b = \Delta \overline{V_y} + \Delta V_{p2} + \Delta V_{p3} \qquad [A19]$$

At maximum contraction there was some micrographical evidence of crack closure. After expansion, pores and cracks formed at the boundaries between filler particles and there was some disintegration of the binder phase between filler particles.

Engle (1971) also suggests a correlation between volumetric CTE and the mean apparent crystallite size, L_c (= 5.35nm for H-315-A graphite). After irradiating a range of needle coke graphites, the crystallite size distribution was observed to shift to higher values with a corresponding increase in CTE. In contrast, near-isotropic graphites with small crystallite sizes in a narrow size range showed a decrease in CTE after irradiation. Engle (1974) also states that a conclusion by some workers is that increasing crystallite size of a polygranular graphite reduces the extent of retained irradiation damage.

More recently other workers have attempted to describe the microstructural changes that influence CTE and dimensional change under irradiation using Scanning Electron Microscopy. Virgilev and Grigoreva (1986) discuss the dependence of the CTE of a Russian reactor graphite upon neutron fluence at various irradiation temperatures. They report that the number of initial slit like pores and cracks formed from processing stresses (*i.e.* Mrozowski cracks) decreases to accommodate lattice expansion. As

irradiation proceeds, the dimensions and volumes of these pores and cracks increase and so the capacity for accommodation increases with a corresponding decrease in CTE. Similar observations were made by Platonov *et al.* (1981) and Shtombakh *et al.* (1996). The former also concluded that rapid increases in stresses and intense cracking begin after turnaround and noted that the new cracks are mainly oriented in a direction normal to the basal planes. Shtrombakh *et al.* (1996) report detailed studies of radiation-induced structural changes in Russian graphite (GR280) and noted the destruction of the filler-binder interface as turnaround is approached.

The current description of the effects of neutron irradiation on dimensional changes in AGR graphites was reviewed by Tucker and Wickham (1990) and is similar to the description for changes in CTE. However, in contrast to CTE behaviour, neutron irradiation of polygranular reactor graphites results in initial bulk shrinkage at low neutron fluences followed by expansion at higher doses, leading eventually to a net expansion of the graphite (see Figure 0.13). The reversal of shrinkage, *i.e.* 'turnaround' begins when the shrinkage cracks are unable to accommodate new irradiation-induced crystallite growth. Turnaround occurs at lower fluences at higher irradiation temperatures. This is attributed to a reduction in the extent of accommodation available for irradiation-induced c-axis expansion as a result of closure of Mrozowski cracks by thermal expansion (Burchell and Oku, 1994). The irradiation dose at which turnaround takes place is also believed to depend upon the extent of radiolytic oxidation that has occurred (Brocklehurst, 1984). With further crystallite growth and net bulk expansion internal stresses develop to the point where new microcracks and pores begin to appear. For AGR graphites turnaround usually occurs around 125 x 10^{20} n/cm^2 (EDN) (Norfolk *et al.,* 1986) at an irradiation temperature of 530 (EDT), with a shrinkage greater than 3%.

CTE and dimensional change under irradiation are therefore often loosely associated with the closure of Mrozowski crack porosity. This is discussed further in the following chapter. Here, it is noted that the behaviour of each is different under irradiation, indicating the requirement for further explanation.

2.3 RADIOLYTIC OXIDATION

The second major damage mechanism to which the graphite within the cores of UK nuclear reactors are subjected is radiolytic oxidation. Within this section the radiolytic oxidation process is described and this is followed by a review of information on the changes that occur within the pore structure of the graphite as radiolytic oxidation proceeds. Finally, the effects of radiolytic oxidation on the CTE of AGR and Magnox graphites are described.

Radiolytic oxidation is initiated by radiation energy (principally from γ rays). CO_2 is broken down to CO plus a range of short-lived oxidising ions and free radicals, sometimes denoted collectively as "Ox". "Ox" recombines to reform CO_2 unless it impinges on a graphite surface, in which case it gasifies a carbon atom as CO. "Ox" diffuses into the surface of graphites, at most, a few micrometres before annihilation. Radiolytic oxidation therefore occurs as fast in pores of width from a few micrometres upwards as it does on an external surface. Moreover, because it enlarges the pores, which then contain more gas and accessible surface, corrosion tends to accelerate with time eventually approaching three times the original rate (Best *et al.*, 1985 and Murdie *et al.*, 1986). The rate of reaction is determined by gamma flux, gas pressure and open pore volume in the graphite. This corrosion can be inhibited to an acceptable level by the use of methane (~0.02% volume) and carbon monoxide (~1% volume) in the coolant gas. As Kelly (1992a) reports, a full understanding of radiolytic oxidation is difficult to achieve because it requires a good description of the size and shape of the open porosity and of the porosity opened to gas by oxidation.

Martin and Caisley (1978) studied the effect of thermal and radiolytic oxidation on the pore structure of two nuclear graphites by small angle neutron scattering. One graphite was derived from a petroleum coke and the other from Gilsocarbon coke. They concluded that an observed difference in scattering between thermal and radiolytic oxidation was due to thermal oxidation attacking all pores and radiolytic oxidation attacking small pores. The authors compared the results with their studies discussed previously on the effects of neutron irradiation on porosity (Martin and Caisley, 1977) and concluded that greater changes in the size distribution of very small pores occur

after neutron irradiation than after radiolytic oxidation. In the case of thermal oxidation, pores of initial sizes 2.5 and 10 nm (radius of gyration) were more affected in the petroleum coke graphite, than in the isotropic material. By contrast, radiolytic oxidation to a given percentage weights loss results in comparable fractional changes in the 10 and 2.5 nm porosity within the two graphites. Martin and Caisley (1978) note that, as the porosity is measured by the radius of gyration concept, long fine pores are not observed.

Microscopy and image analysis techniques were used by Murdie *et al.* (1986) to study the changes in porosity of AGR graphite caused by radiolytic gasification in carbon dioxide. Graphite samples with a range of weight losses (0-22.8%) were examined by optical and scanning electron microscopy. In virgin graphite, open porosity was located entirely within the binder phase, whereas the closed porosity was predominantly (83%) contained in the Gilsocarbon filler particles. The closed porosity was made up of 5μm wide crack-like pores orientated concentrically around the central pores. Their results suggested that as much as 4.4% of the pore volume of the virgin graphite was composed of pores less than 7×10^{-4} μm^2 cross sectional area (c.s.a.) (this being the resolution of the SEM). After radiolytic oxidation, it was noted that the apparent open pore volume increased from 6.6 to 33.8% and the apparent closed pore volumes decreased from ~3% to 0.1%. The increases in apparent open porosity resulted from gasification within the original open porosity (mainly in coarse grained mosaics) and, to a lesser extent, by the opening and development of closed porosity.

Murdie *et al.* (1986) also attempted to identify the pore size range within which radiolytic oxidation was occurring and deemed these to be pores of <100 μm^2 c.s.a. and in particular within pores <2 μm^2 c.s.a., initially within the binder coke. There was no evidence for creation of new porosity, but existing fine porosity was developed. New open pores ($<2\mu m^2$ c.s.a) were developed by gasification of existing open porosity into the closed porosity (<2 μm^2 c.s.a) within the binder phase. The structure of pores >100 μm^2 c.s.a. showed little change, due to the inhibition of oxidation by CH_4 in the oxidising gas, and they are only developed at weight losses >17% by coalescence of open porosity <100 μm^2 c.s.a. By 12.1 %wt loss the closed porosity within the Gilsocarbon filler has opened.

Consideration of the effects of radiolytic oxidation on the thermo-physical properties of AGR and Magnox graphites was made by Brocklehurst (1984). In order to determine the effect of oxidation only, the changes produced by fast neutron irradiation were removed by thermal annealing. They reported CTE measurements on both Magnox and AGR graphites that were oxidised in flowing CO_2 at high pressure. These experiments produced samples of up to 20% weight loss for isotropic graphites and up to 30% weight loss for Magnox graphites. Figure A.12 shows the CTE of AGR graphite as a function of radiolytic oxidation in 2% CO / 0.02% CH_4 / CO_2 coolant. Although there is some scatter in the measurements of CTE, the authors stated that there was no marked effect due to radiolytic weight loss. Similarly, for Magnox reactor graphites oxidised under the same conditions but to 30% weight loss no significant change in CTE was reported to occur. Kelly (1992a) states that, although the experiments are complex, radiolytic oxidation has no effect on the CTE of AGR or Magnox graphites.

2.4 DESCRIBING THE CTE AND DIMENSIONAL CHANGES OF IRRADIATED POLYGRANULAR GRAPHITE USING THE "ASSEMBLY OF SINGLE CRYSTALS" MODEL.

Due to the complexity of the structural changes occurring under neutron irradiation and radiolytic oxidation within nuclear graphites, the assembly of single crystals has been adapted as the simplest way to incorporate irradiation and oxidation effects. As such, this approach has been used extensively to help understand the effects of the reactor environment on CTE and dimensional change and is discussed here, together with inherent limitations and recent advances.

In early work, based upon their experimental observations of HOPG graphites, Kelly *et al.* (1966b) discuss the dimensional changes in polygranular graphites under fast-neutron irradiation. By extension of the "assembly of single crystals" approach they proposed that the strain in the direction x in a polycrystalline aggregate, after fluence γ, is related to strains in the crystals by

$$g_x = A_x(\gamma)g_c + (1-A_x(\gamma))g_a \qquad [A20]$$

where $g_x = (1/l_x)(dl_x/d\gamma)$ is the fractional increase in length l_x in the direction x in the aggregate per unit dose (the dimensional change rate), $g_c = (1/X_c)(dX_c/d\gamma)$ is the fractional increase in length in the c-direction of a crystal per unit dose, and $g_a = (1/X_a)(dX_a/d\gamma)$ is the fractional increase in length in the a-direction of a crystal per unit dose. $A_x(\gamma)$ is a structure factor that is dependent upon the irradiation dose and temperature.

Similarly, the CTE, α_x of the polycrystalline aggregate in the direction x, in the same irradiated state, is related to the crystal CTE values, α_c and α_a, by an adaptation of Equation [A17]

$$\alpha_x = A_x(\gamma)\alpha_c + (1-A_x(\gamma))\alpha_a \qquad [A21]$$

Thus another "structure factor" (now a function of neutron fluence) incorporating all microstructural effects is used. Kelly (1981) states that the parameter $A_x(\gamma)$ may change for a number of reasons such as the different relative changes of the crystallite elastic constants with temperature or irradiation or changes in the pore structure due to crystallite thermal expansion (*e.g.* closure of Mrozowski cracks) or oxidation.

Kelly (1981) noticed that for both AGR and Magnox graphites, at low fluences (< 25 x 10^{20} n/cm^2 (EDN), the first maxima in CTE which is temperature dependant) and irradiated below ~600°C the dimensional change rate, g_x, is linearly related to the thermal expansion coefficient α_x:

$$g_x = a\alpha_x + b \qquad [A22]$$

the coefficients a and b varying with irradiation temperature. Kelly showed that Equations [A19], [A21] and [A22] can be combined to give

$$g_x = \left(\frac{\alpha_x}{\alpha_c - \alpha_a}\right)(g_c - g_a) - \left(\frac{\alpha_a}{\alpha_c - \alpha_a}\right)(g_c - g_a) + g_a \qquad [A23]$$

As irradiation proceeds the linear relationship between CTE and dimensional change rate ceases to be valid. Kelly (1992a) states, therefore, that for doses greater than a temperature-dependent threshold value, γ^*, new porosity is created that renders Equation [A23] invalid. To account for pore generation at large doses, a new relationship (the Brocklehurst/Kelly model) was defined. For irradiations at constant temperature it can be summarised in an adaptation of Equation [A21]:

$$g_x = A_x(\gamma)g_c + [1 - A_x(\gamma)]g_a + \frac{dF_x(\gamma)}{d\gamma} \qquad [A24]$$

where $F_x(\gamma)$ is the contribution to the total strain per unit fluence, g_x, due to pore generation. Kelly (1992a) states that $F_x(\gamma)$ is dependent upon the "crystal shape change parameter", X_T, which is defined as

$$X_T = (\Delta X/X_c - \Delta X/X_a) \qquad [A25]$$

where $\Delta X/X_c$, $\Delta X/X_a$ are the dimensional changes of the component crystals measured perpendicular and parallel to the basal plane. However, both Kelly (1992a) and Arai (1996) state that the change in the "structure factors" *i.e.* $A_x(\gamma)$ as a function of X_T are different for different graphites, being dependent on the detailed structures of the coke grains and binder/impregnant phases. Therefore, the key parameter that relates the single crystal behaviour to that of the aggregate, $A_x(\gamma)$, remains poorly understood in relation to microstructural changes occurring within the material.

Kelly (1992a) extended his argument to incorporate the effects of pore generation due to radiolytic oxidation. He proposed that the influence of weight loss due to radiolytic oxidation on observed dimensional changes will be that of the created porosity if the fractional volume change of the graphite, $\Delta V/V_0$, is the sum of changes occurring in the crystallites and in the porosity $\Delta V_P/V_0$. Kelly showed that if ρ_B and ρ_C are the apparent and crystal densities and x is the weight loss then

$$\frac{\Delta V_P}{V_0} = \frac{\Delta V}{V_0} + \left(\frac{\rho_B}{\rho_C}\right)x - \left(\frac{\rho_B}{\rho_C}\right)(1-x)X_T\left[\frac{1+2\delta}{1-\delta}\right] \qquad \text{[A26]}$$

where $\delta = g_a/g_c$. Since the porosity term due to oxidation is positive, it offsets the shrinkage due to irradiation and so turnaround is delayed.

In an attempt to add some microstructural information Neighbour (2000) has developed a generalised model for dimensional change as given by Equation [A27].

$$\frac{\Delta L}{L_0} = \sqrt[3]{n_1 x\left(\frac{\rho_0}{\rho_c}\right) + \left(\frac{\Delta V_p}{V_0}\right)_{IRR} + \left(\frac{\rho_0}{\rho_c}\right)\left[(1-n_2 x)(1+G_a)^2(1+G_c) - 1\right]} \qquad \text{[A27]}$$

Where ρ_0 and ρ_c are the initial bulk and single crystal densities respectively, x is the weight loss and G_a and G_c are derived from g_a and g_c as given by

$$G_a = \int_0^{\gamma} g_a d\gamma \qquad \text{and} \qquad G_c = \int_0^{\gamma} g_c d\gamma \qquad \text{[A28 a,b]}$$

The factor n_1 describes the amount of the porosity generated by oxidation that is subsequently filled by irradiation growth. In addition, the individual crystallite strain upon irradiation is affected by external oxidation (*i.e.* its dimensions change), therefore another factor n_2 is required to describe the degree of oxidation that occurs within the crystallite. Neighbour (2000) argues that n_2 can be approximated to 0.67 if crystallite dimensions during oxidation are reduced only by attack along the basal planes and pitting within the basal planes does not change the crystallite size. Neighbour (2000) showed that the model results compared well with pre-oxidised samples obtained from Materials Test Reactors (MTRs).

Although the assembly of single crystals approach can be applied semi-empirically to dimensional change and CTE it does not supply a consistent description. As Kelly (1992a) acknowledges, A_x and F_x are also defined as structure sensitive parameters, therefore these should be affected by radiolytic oxidation with a resulting change in

CTE. As CTE appears to be insensitive to oxidation, he suggests that this may be due to oxidation initially taking place in pores that are open to the coolant gas and whose effect on thermal expansion has already occurred. However, this situation cannot persist in the later stages of radiolytic oxidation as pores enlarge substantially.

In summary, extensions of the "assembly of single crystals" model recognise that some relationship exists between CTE and dimensional change under irradiation and oxidation and that it is strongly influenced by Mrozowski cracks. However, these processes cannot be described by exactly the same mechanisms as their behaviours under irradiation differ significantly, *i.e.* the minima in dimensional change do not occur at the same dose as the initial maxima in CTE and the latter appear to be unaffected by oxidation. This is discussed further in the following chapter.

2.5 THE EFFECTS OF IRRADIATION INDUCED CREEP

In addition to the main structural disruption processes of neutron irradiation and radiolitic oxidation the CTE of nuclear graphites can also be altered by the process of irradiation induced creep. As this compensates dimensional changes (to some extent) it is of a practical importance within the reactor.

Graphite exhibits a remarkably high creep ductility under irradiation due to a mechanism identified by Kelly and Foreman (1986) as dislocation pinning unpinning. They suggest that dislocations present in the basal planes of unirradiated graphite are constrained by pinning points (consisting of clusters of interstitial atoms). During irradiation these pinning points are annealed (Gray *et al.*, 1967) thus each only provides a temporary barrier to dislocation movement. As a result the crystal creeps by basal slip at a rate determined by the pinning and unpinning of the dislocations.

The original definition of creep strain is the difference in length between a stressed specimen and a control and this is only correct if the dimensional change component in the stressed specimen is the same as that of the control. In fact creep produces significant modification to the dimensional change component of stress compared to that of the control and also causes changes in other properties (including CTE). Thus

the correct definition of creep strain is the difference in dimensions between a stressed sample and a sample with the same properties as the stressed sample, but irradiated in the unstressed state (Kelly and Burchell, 1994).

Creep strain has been shown to effect CTE of Gilsocarbon based graphites parallel to the stress axis as shown in Figure A.14 (Kelly and Burchell, 1994) where the unstressed CTE values are taken from control samples irradiated to the same dose as the stressed sample. Brocklehurst and Brown (1969) showed that annealing such samples (at 2000°C) irradiated to low fluences (below 50 x 10^{20} n/cm^2 (EDN)), results in the CTE recovering to that of the unstressed and unirradaited control specimens, but the creep strain is not fully recovered. The partial recovery of creep strain after annealing was also confirmed by Gray *et al.* (1967). However, data provided by Thrower and Reynolds (1963) on samples irradiated to higher neutron fluences under stress show that neither the unstressed or unirradiated CTE values were recovered on annealing. Gray (1973) also noticed that the differences in CTE values of samples irradiated unstressed and samples irradiated stressed is not large for both needle coke graphites (with a difference of ~1 x 10^{-6} K^{-1} at a dose of 10 x 10^{21} n/cm^2, E>0.18 MeV) and Gilsocarbon graphites (with a difference of ~0.5 x 10^{-6} K^{-1} at the same dose.)

Only limited data are available on the CTE changes perpendicular to the stress axis and this work was reported by Kelly (1992b). Kelly shows that, for Gilsocarbon based graphites in compression, the CTE perpendicular to the stress direction decreases compared to the irradiated control and is attributed to changes in crystallite orientation in addition to porosity changes. Kelly (1992b) also reports changes due to tensile applied stresses, in this case the results contradict his earlier work with a slight increase in CTE (from 4.01 to 4.51 x 10^{-6} K^{-1} between 20 and 120°C) and the transverse expansion coefficient is lower than that of the unirradiated and irradiated controls and is also lower than the result parallel to the applied stress. Kelly (1992b) points out that in this case the results are the opposite of what would have been expected from both the effects of crystallite re-orientation and porosity changes and are difficult to explain.

2.6 SUMMARY

This chapter has reported the effects of neutron irradiation and radiolytic oxidation on both graphite single crystals and polygranular nuclear graphites with respect to corresponding changes in CTE and dimensional change. For irradiation temperatures above 300°C the CTE of HOPG remains largely unchanged and dimensional changes increase linearly, both as a function of neutron fluence. In an attempt to understand the effects of irradiation on CTE and dimensional change an extension to the assembly of single crystals model was proposed and has been reviewed in this chapter. Within the modified model it was still found to be necessary to incorporate irradiation dependent structure terms that act to modify the amount of accommodation available to expanding crystallites. In addition, dimensional change and CTE behaviour under irradiation and oxidation are both attributed to changes in "small scale porosity" in this model. However, this chapter has shown that this description is not complete as the behaviour of CTE and dimensional change under irradiation and oxidation are very different.

The microscopy studies conducted on irradiated and oxidised nuclear graphites have been reviewed in order to further understand these small scale porosity changes. One of the most extensive microscopical studies of irradiated graphites was conducted by Engle (1971) who developed a model of microstructural changes during irradiation. Some important observations from his model on the effects of irradiation on the structure of polygranular graphites are that micropores are closed during irradiation. Although in isotropic graphites, turnaround in dimensional change occurs before such porosity is depleted. The effects of radiolytic oxidation have also been reviewed and this has been shown to attack a preferential range of open porosity in comparison to thermal oxidation that is non-specific. Similar to thermal oxidation, at <20% weight loss, CTE appears to be unaffected by radiolytic oxidation.

CHAPTER 3
MICROSTRUCTURAL FEATURES AND MODELS - A DISCUSSION

This discussion chapter begins by identifying the important microstructural features controlling CTE within the unirradiated material by consideration of the reviewed literature on UK nuclear graphites, other nuclear graphites and similar materials. A discussion on the validity of the "assembly of single crystals" model as a method of describing CTE is also presented. This includes a more detailed discussion on the inconsistencies within this model as currently applied to CTE and dimensional change under irradiation and radiolytic oxidation. The generation of a simple model of Mrozowski crack closure that includes the effects of irradiation is also presented. Based upon these works, a qualitative description of the behaviour of CTE in AGR and Magnox graphites, with respect to microstructural changes, is given. The discussion concludes by considering the effects of irradiation creep and places the thermal expansion behaviour of moderator graphites in context with other materials.

3.1 UNIRRADIATED POLYGRANULAR GRAPHITES

There is much evidence to support the view that the low values of CTE for polygranular graphites are due to accommodation in Mrozowski cracks. Other than the information provided by Sutton and Howard (1952) giving a crack size and periodicity, there appears to be little direct observational evidence of Mrozowski cracks and their specific size and location within the material.

The microstructure of nuclear graphites is much more complex than the abstraction used within the assembly of single crystals model and, as a consequence, this model is of limited value in this work. The studies pioneered by Engle (1971) and extended more recently by Russian workers *e.g* Shtrombakh *et al.* (1996), have linked changes in CTE to changes in microstructure revealed by optical and electron microscopy and this seems to be a more beneficial approach to improving the understanding of these phenomena.

3.1.1 Thermal Oxidation

The scoping study conducted by Neighbour *et al.* (1997) supports the hypothesis that thermal oxidation to weight losses up to ~40% has little or no effect on the CTE of AGR graphite. At first sight this is surprising since thermal oxidation has a marked effect on thermal conductivity of graphites and on other properties such as strength and elastic modulus. The most reasonable explanation is that, at low weight losses, thermal oxidation does not attack those parts of the microstructure that are critical in controlling CTE. However, without detailed observation of graphitic structure on the crystallite size scale (300 Å) it is impossible to provide any further support for these hypotheses.

Studies on other polygranular materials, such as sintered ceramics, have also concluded that oxidation has little or no effects on CTE (*e.g.* Coble and Kingery, 1956). The consensus appears to be that the pore structure that is developed by oxidation is distinct from that which provides accommodation for CTE and that thermal expansion is controlled, primarily, by crystallite structure

It is also useful to note here that radiolytic oxidation also appears to have little effect on CTE, although this has only been shown to ~20% weight loss (Kelly, 1985). Although the two mechanisms are different, the net effect of both radiolytic and thermal oxidation is the removal of solid material and this appears not to effect CTE, at least to low weight losses. It therefore appears reasonable to also conclude that the mechanism of oxidation (and in particular the subset of open porosity that may be developed differently in each case) has no effect on CTE changes at low weight losses. This result again supports the view that the macroscopic structure of the material in general, but specifically porosity developed by oxidation, is of little importance in controlling CTE.

These explanations are, however, incomplete. Intuitively, it is expected that some change in CTE will occur at very high weight loss due to extreme disruption of the structure and this has not been addressed, either experimentally or theoretically. As an objective of this work is to describe CTE behaviour with reference to microstructural changes, this must be considered. An experimental programme to investigate the behaviour of CTE at very high weight losses is therefore required. As well as providing

important information on when CTE becomes affected by oxidation, this may also provide a more general insight into the nature of CTE within these materials.

3.1.2 The Effects of Pre-Stress

The effects of compressive pre-stress, presented in chapter 1, section 1.5, are consistent with the description of the increase in CTE being caused by a corresponding reduction in accommodation available to expanding crystallites. Conversely, one may intuitively expect a reduction in CTE for samples that have suffered a tensile pre-stress. However, the works of Matsuo and Sasaki (1981) and Kelly (1992a) indicate that this is not the case with either no change or a small increase in CTE being reported. This appears to be incompatible with the explanation for the increase in the CTE of compressively pre-stressed samples *i.e.* Mrozowski crack closure leading to a reduction in accommodation. Conversely, application of a tensile pre-stress might be expected to lead to an increase in accommodation and so a reduction in CTE.

3.2 MICROSTRUCTURAL OBSERVATIONS ON IRRADIATED POLYGRANULAR GRAPHITES

The standard method for analysing the influence of irradiation upon the CTE and dimensional changes of irradiated reactor graphites is the Kelly-Brocklehurst model represented by Equations [A20] and [A23]; CTE is analysed using Equation [A21] that expands upon the "assembly of single crystals" model of unirradiated graphites.

Although there are similarities between the effects of irradiation on dimensional change and CTE, as discussed in chapter 2, section 2.4 the two processes are not identical, since the maximum values of CTE and dimensional shrinkage occur at different fluences. Typically, for AGR graphite irradiated at 430-450 °C (EDT), the maximum values of CTE and shrinkage occur at 25 x 10^{20} and 125 x 10^{20} n/cm^2 (EDN), respectively. Both processes are thought to be influenced by changes in "small scale" porosity, although the difference between porosity influencing CTE from that influencing dimensional change remains unclear.

Further progress can be made by making simple estimates of the requirements for Mrozowski crack closure by thermal expansion and by neutron irradiation and then applying these to the behaviour of CTE and dimensional change under irradiation. Figure A.15 shows a simple model of Mrozowski cracks of width, w, formed by cracking of a single crystal parallel to the a-axis and with a crack spacing, S. The temperature increase, ΔT, required to close the crack is given by the following:

$$\Delta T = \frac{w}{(S-w)\alpha_c} \qquad [A29]$$

Considering thermal expansion, from Equation [A2] a mean value of α_c = 29.64 x 10^{-6} K^{-1} may be assumed over the temperature range 20-2000 °C. Also, Sutton and Howard (1962) observed Mrozowski cracks in the size range 20-30 nm with a frequency of ~2 cracks per micron. Therefore taking an average value of w to be 25 nm and S to be 500 nm, ΔT = 1776 K. This is a reasonable estimate as it is thought that Mrozowski cracks begin to form at ~1800 °C on cooling from graphitisation temperatures when creep relaxation of thermal stresses cease to operate (Kraus and Semmler, 1978).

This simple model may be applied to estimate the neutron dose at 460°C needed to close cracks by c-axis expansion. After a dose of 250 x 10^{20} n/cm^2 (EDN) the fractional c-axis expansion is 0.46, Figure A.7(a). The relationship between expansion and dose is approximately linear, so the gradient, m_d, can be approximated as 1.84 x 10^{-23} cm^2 n^{-1}. If the effects of thermal expansion on crack closure are ignored, then the dose required to close a Mrozowski crack, D, is given by the following

$$D = \frac{w}{(S-w)m_d} \qquad [A30]$$

using the parameters given previously, D = 28.6 x 10^{20} n/cm^2 which is in good agreement with the experimental observation of the initial maxima in CTE for both AGR and Magnox graphites, Figures A.8 and A.9. This supports the conjecture that irradiation induced closure of Mrozowski cracks results in the initial increase in CTE. Interestingly, one would expect Mrozowski cracks to continue to form on cooling to

room temperature, giving a range of crack sizes. Therefore a crack spacing of w = 25 nm may be regarded as an upper bound for a whole family of crack sizes.

Considering dimensional change (at 460 °C EDT), maximum shrinkage occurs after a fluence of 125 x 10^{20} n/cm^2 (EDN), Figure 0.13, which from Figure A.7 corresponds to a c-axis expansion of 23% and 8.5% shrinkage in the a axis. Thus the total volume increase in graphite crystallites is ~3%. For AGR graphite, a reduction in linear dimensions of 3% is observed, Figure 0.13, which corresponds to a volumetric reduction of ~8.7%. The porosity required to accommodate such changes must be in the micron size range, since the majority of porosity in virgin graphite is greater than 100 nm equivalent diameter (*e.g.* see Best *et al.*, 1985). This is consistent with the hypothesis that it is large pores (> 100 nm width) that influence turnaround and that CTE is influenced by pores of width < 50 nm. Thus, dimensional change and CTE are influenced by different sub-classes of porosity.

3.3 QUALITATIVE DESCRIPTION OF CTE IN AGR AND PGA GRAPHITES UNDER IRRADIATION.

Although it is difficult to be conclusive at this stage, the evidence presented in this part of the thesis allows for a description of the changes in CTE under neutron irradiation to be made, especially in the case of AGR graphites, Figure A.8, where more evidence on irradiation behaviour is available. The small rise in CTE at low fluences can be explained by the reduction in *c*-axis accommodation for Mrozowski cracks, as shown by the simple model constructed above. This magnitude of this rise is dependant on the irradiation temperature due to a partial reduction in the size of Mrozowski cracks as temperature increases.

The subsequent decrease in CTE has been attributed to a 'jacking apart' of the structure by several authors (*e.g.* Jenkins, 1964) after the *c*-axis expansion provided by Mrozowski cracks has been exhausted. The disruption to the microstructure, in someway, inhibits the transfer of thermal strains probably by the progressive destruction of the "binder bridges" linking the "filler" grains together. At the point of maximum damage, the CTE value of the AGR graphite tends to reach a plateau at a low value, ~1

x 10^{-6} K^{-1}. The plateau implies that continued pore generation as a result of irradiation ceases to have any effect on CTE. Similar low values have been observed for various graphites in different studies, *e.g.* Pitner (1971). Previous investigations (*e.g.* Jenkins, 1964) support the suggestion that the low value of CTE is due to a total disruption of structure that results in a reduced ability to transmit thermal strains.

The CTE of Magnox graphite in both directions, at 600^{0}C, exhibits an initial small rise upon irradiation and then remains constant until a fluence ~100 x 10^{20} n/cm^2 (EDN) is reached. At higher fluences the CTE values rise sharply, Figure A.9. Although the experimental work conducted on the CTE of PGA graphite under neutron irradiation is less extensive than that for AGR graphite, a tentative extension of the argument made for AGR can be applied to PGA graphites. The first small rise in CTE occurs around the same fluence as the peak in CTE for UCAR GCMB graphite, ~25 x 10^{-20} n/cm^2 (EDN). Thus, this rise probably corresponds to a reduction in accommodation for irradiation-induced crystallite growth in the same fashion as that described for AGR graphite. The intermediate plateau seems to imply that, although structural disruption is occurring, the transmission of thermal strains is unaffected. PGA graphite is a coarser material than AGR graphite at manufacture and so it may be able to withstand more irradiation damage before the effects of localised structural disruptions are transmitted to the bulk. The work of Engle (1971) has shown a much wider pore size distribution in needle coke graphites compared with isotropic materials. Thus, it is also reasonable to assume that a greater amount of porosity will be oriented favourably within needle coke graphites. This porosity acts to accommodate a greater crystallite expansion, than AGR graphites, before appreciable transmission of strains to the bulk. The second rise in CTE at ~90 x 10^{20} n/cm^2 (EDN) can be compared to the turnaround in dimensional change of PGA graphite at ~100 x 10^{20} n/cm^2 (EDN).

The CTE of PGA graphite at low temperatures can be explained by reference to the large crystal dimensional changes that occur below ~300^{o}C (Figure A.7(a)). In this case, the space available to expanding crystallites before transmission of thermal strains to the bulk occurs is rapidly decreased and the CTE saturates at a low fluence.

3.4 THE EFFECTS OF IRRADIATION INDUCED CREEP

From the mechanism described by Kelly and Foreman (1974) the origins of irradiation induced creep are intra-crystalline and the imposition of creep is stated by many authors to affect CTE (*e.g.* Kelly and Burchell, 1994). On further investigation it is clear that, for the polygranular material, the situation is much more complex as the imposition of stress and irradiation each alone change CTE and other properties, such as Young's modulus, which in turn alter the elastic-plastic response of the material. Therefore, as Kelly (1994) proposes, an apparent creep rate will be observed that is a combination of the effects of a 'true' linear creep behaviour of the graphite crystals combined with changes in Young's modulus and CTE which are themselves affected by irradiation and by the imposition of a pre-stress.

The recovery of the CTE (Gray *et al.*, 1967) of annealed samples stressed and irradiated at low fluences implies that until this point the CTE behaviour is acting independent of the effects of creep strain (which does not recover) and therefore simple reversible porosity changes are likely to be occurring which do not significantly alter the connectivity of the structure. At higher fluences, original CTE values cannot be recovered by annealing (Thrower and Reynolds, 1963). Therefore, the combined effects of CTE changes due to irradiation and stress are likely to be coupled with the stress and irradiation induced changes in other properties and the linear irradiation creep of the single crystals. At this stage significant crystallite rearrangement is probably occurring, permanently altering the connectivity of the structure as suggested by Kelly (1992).

3.5 THE NATURE OF THERMAL EXPANSION IN OTHER RELATED MATERIALS

This review has shown that for many polygranular or polycrystalline aggregates the thermal expansion effects of the single crystals are modified by the existence of small scale porosity or the degree of structure connectivity. It is clear that, for the most part, the expansions of aggregates are insensitive to micrometric porosity changes.

Of particular interest is the description of the hysteresis behaviour described by Austin (1952). It follows that if this mechanism exists in nuclear graphites the process of measurement of thermal expansion alters the very property that is being measured. In addition, the manufacture of nuclear graphites results in an aggregate that contains internal stresses which could be partially relieved on heating, again resulting in a structural disruption and a change in expansion behaviour. It is possible, therefore, that the thermal expansion of nuclear graphite is not a fundamental property, but a complex function of the history of the sample.

3.6 SUMMARY OF DISCUSSION AND THE IMPLICATIONS FOR AN EXPERIMENTAL PROGRAMME

The behaviour of small-scale (nanometric) closed porosity appears likely to strongly influence the CTE behaviour of nuclear graphites. A simple model of Mrozowski crack closure has shown that these can account for the initial rise in CTE observed in AGR and Magnox graphites as a function of neutron fluence and also indicates that a different class of porosity is responsible for controlling dimensional change. Clearly, an aim of the experimental programme should be to identify and characterise this porosity together with the structure of the material on the nanometric scale. Such a programme should also be extended to measure the effects of thermal oxidation, to high weight losses, on CTE.

The reduction in CTE in AGR graphite as dose increases has been attributed to structural disruption, however it is unclear as to what scale such disruption is occurring and how such behaviour differs in Magnox graphite. The experimental programme should also attempt to explore this area by the disrupting the structure of samples in an attempt to simulate the effects of irradiation on CTE.

In addition to providing aims for the experimental programmes, this discussion section has also raised some subtle points concerning the nature of thermal expansion within these materials. For example, although the CTE of compressive and tensile pre-stress has been measured in the past the effects of time or temperature recovery have not been fully explored. More fundamentally, the experimental programme will first need to

characterise the expansion behaviour of these materials in the as-received condition, over successive thermal cycles and relate this to the results presented here on the thermal expansion of polygranular aggregates in general.

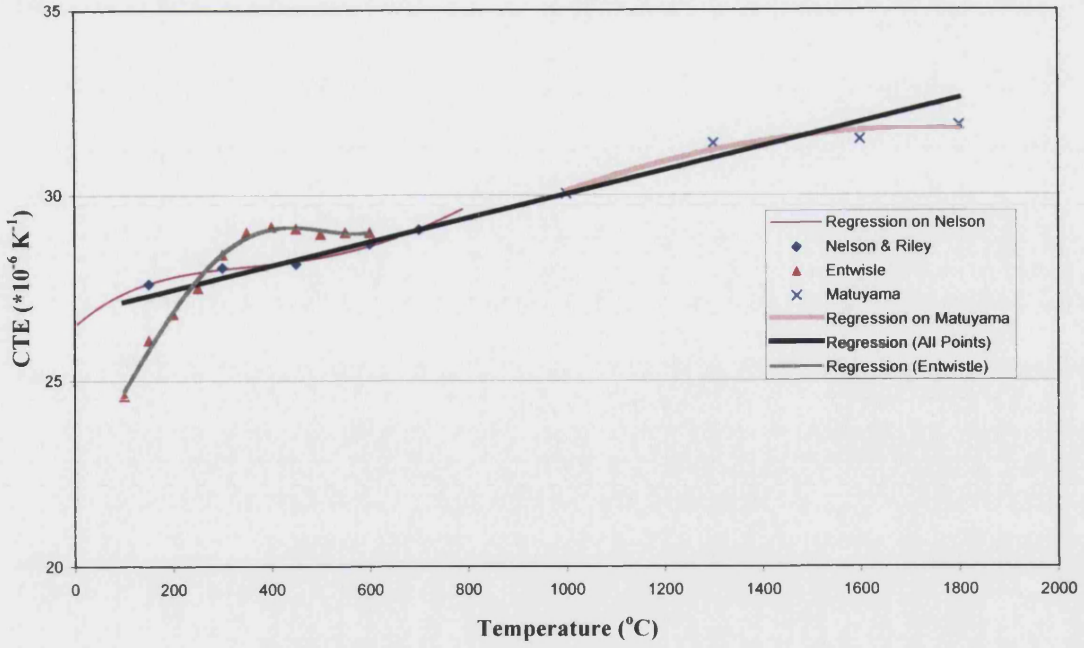

Figure A.1. Graphite single crystal CTE perpendicular to the basal planes, α_c as a function of temperature.

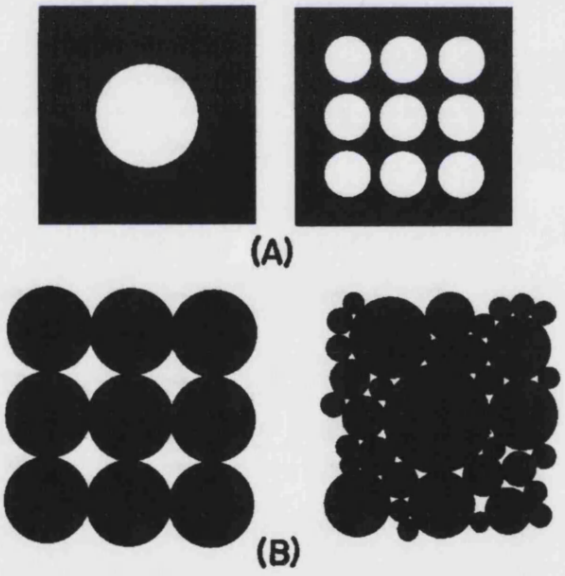

Figure A.2. Schematic showing different types of porosity within a solid (Austin, 1952).

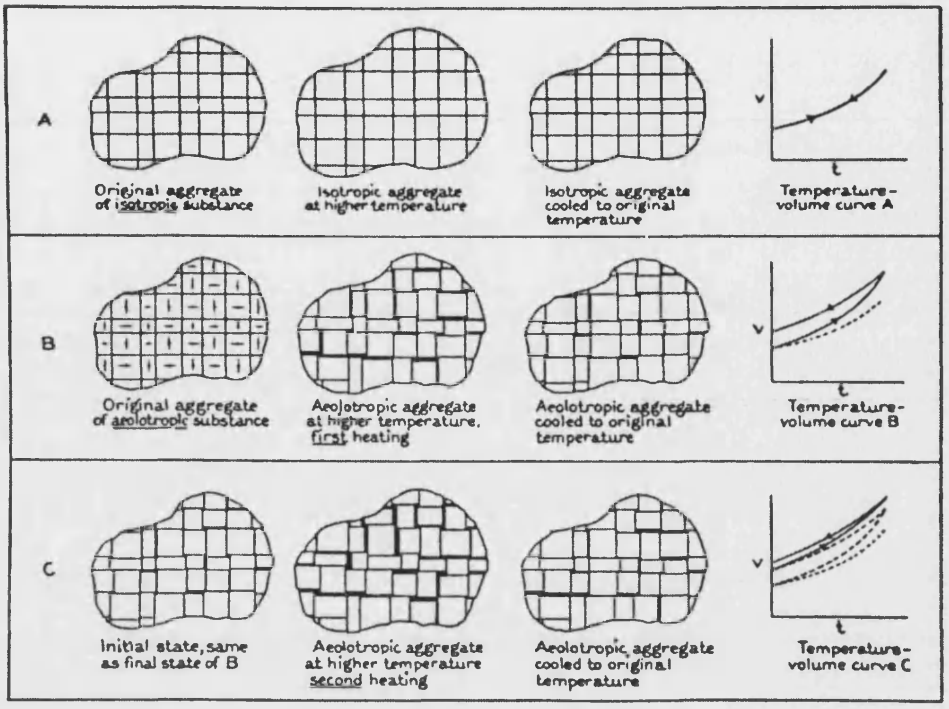

Figure A.3. Schematic showing the expansion behaviour of aggregates (Sosman, 1923)

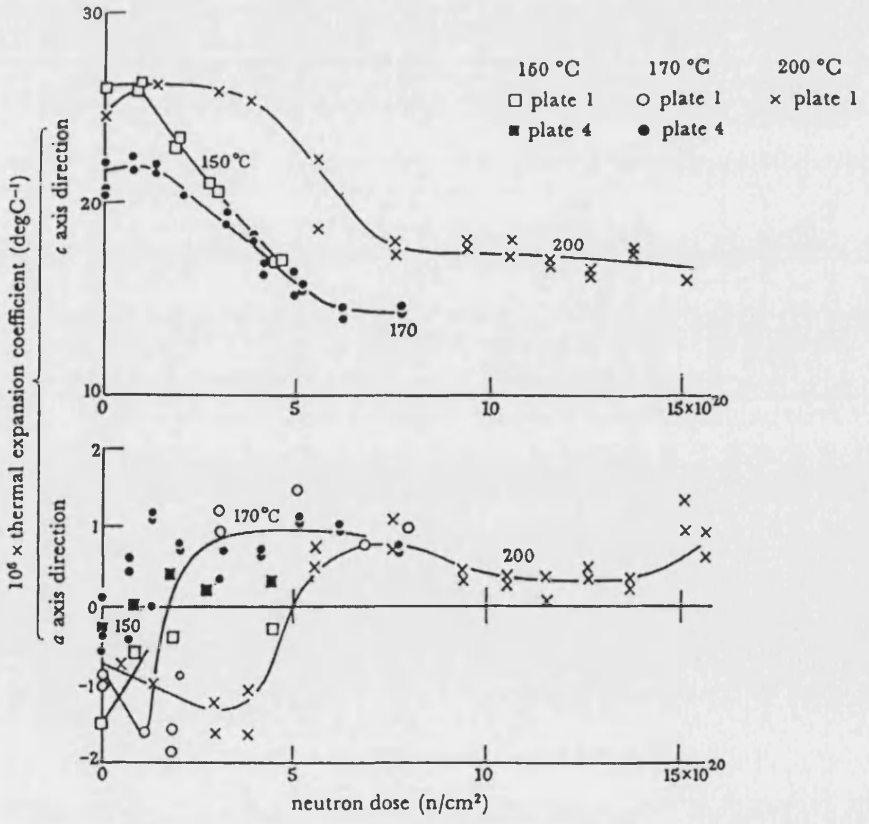

Figure A.4(a). CTE of pyrolytic graphite irradiated at 150, 170 and 200°C in the a and c directions (Kelly, 1966).

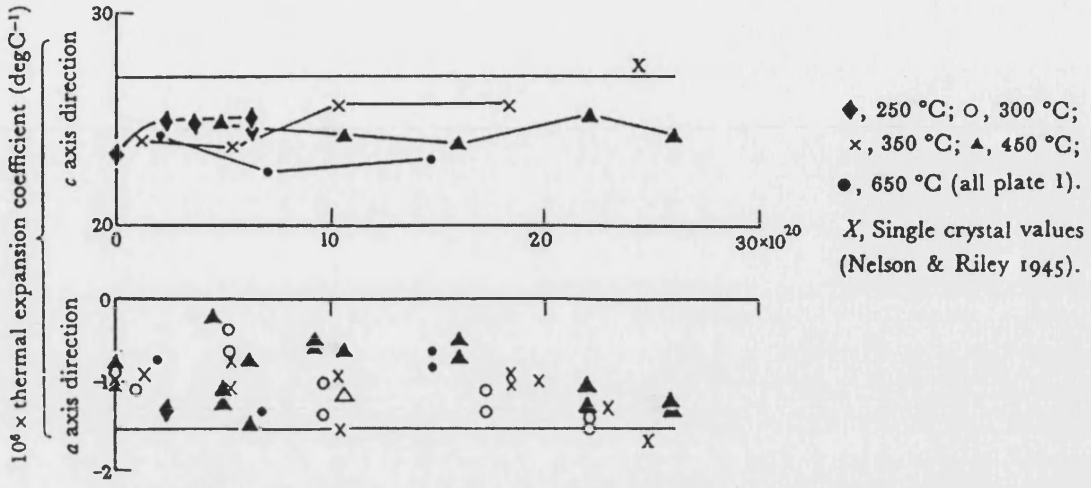

Figure A.4(b). CTE of pyrolytic graphite irradiated at 250, 300, 350, 450 and 650°C in the a and c directions (Kelly, 1966).

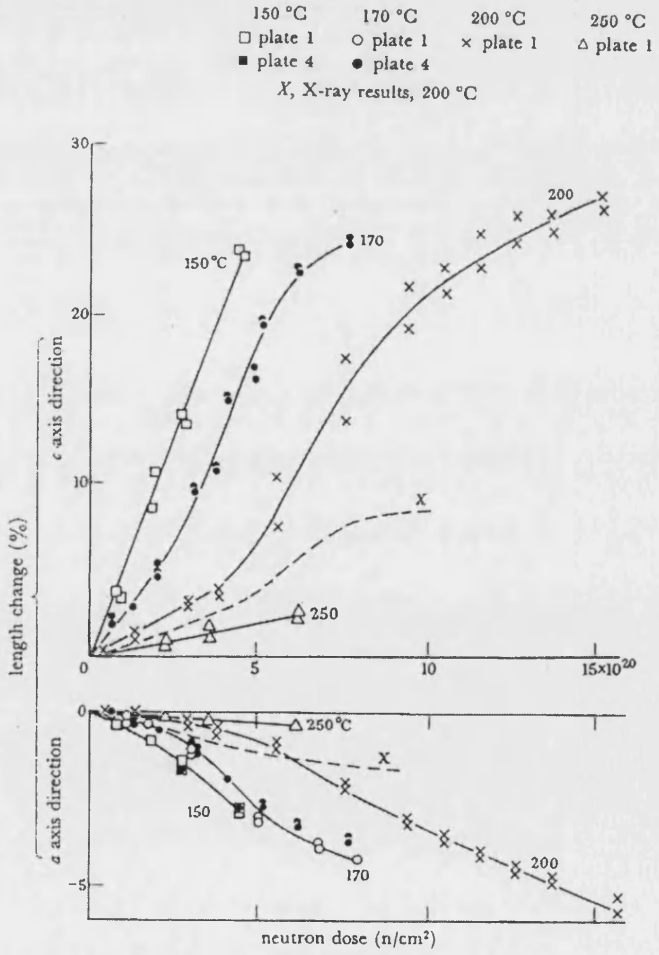

Figure A.5(a). Dimensional changes of pyrolytic graphite irradiated at 150, 200 and 250°C perpendicular (c axis direction) and parallel (a axis direction) to the deposition plane (Kelly, 1966).

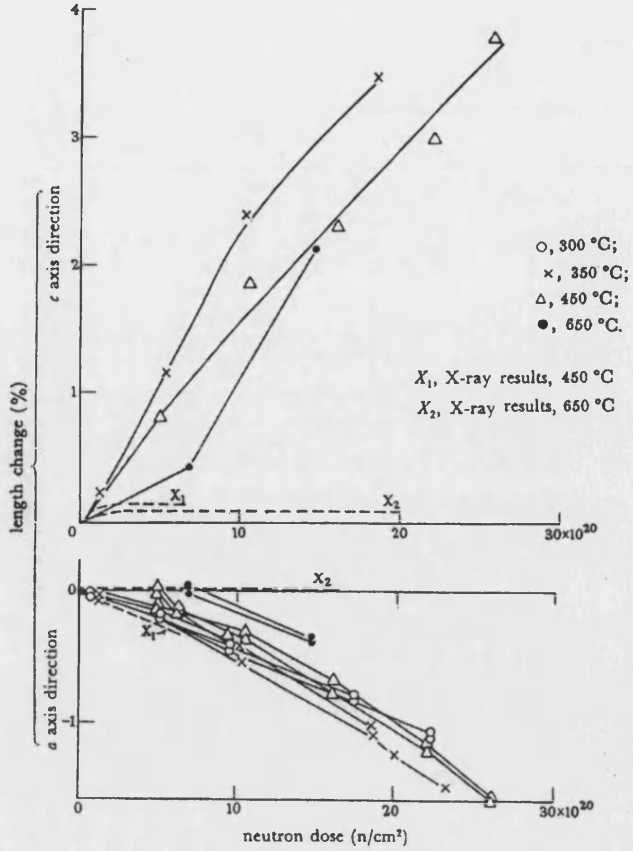

Figure A.5(b). Dimensional change of pyrolytic graphite irradiated at 300, 350, 450 and 650^{0}C perpendicular (c axis direction) and parallel (a axis direction) to the deposition plane. (Kelly, 1966).

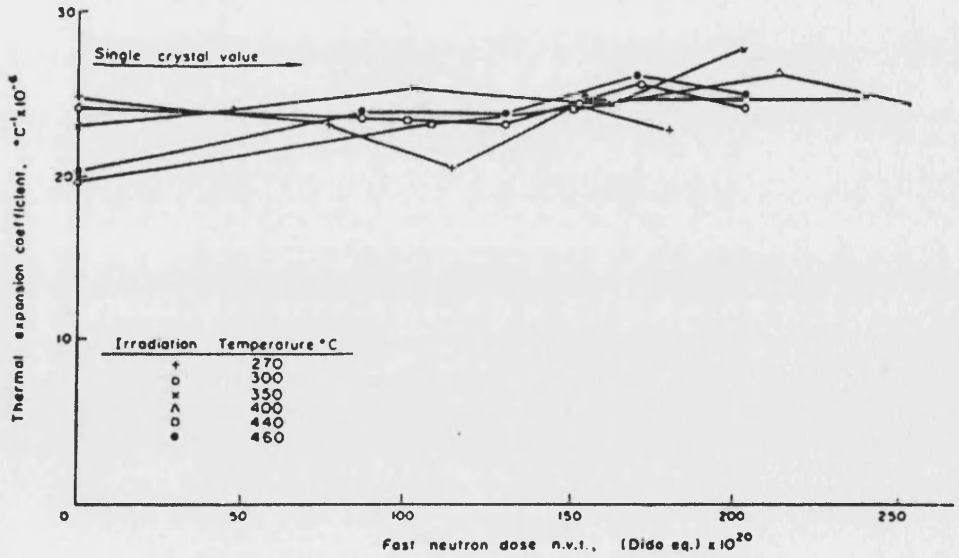

Figure A.6(a). CTE of pyrolytic graphite in the c direction irradiated to high dose in the temperature range 270-460°C (Kelly and Brocklehurst, 1971).

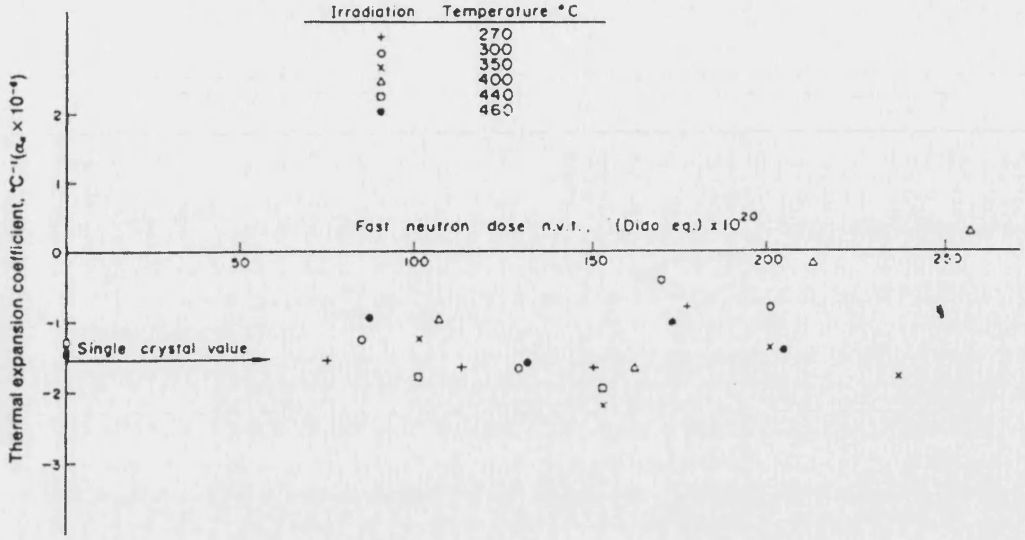

Figure A.6(b). CTE of pyrolytic graphite in the a direction irradiated to high dose in the temperature range 270-460°C (Kelly and Brocklehurst, 1971).

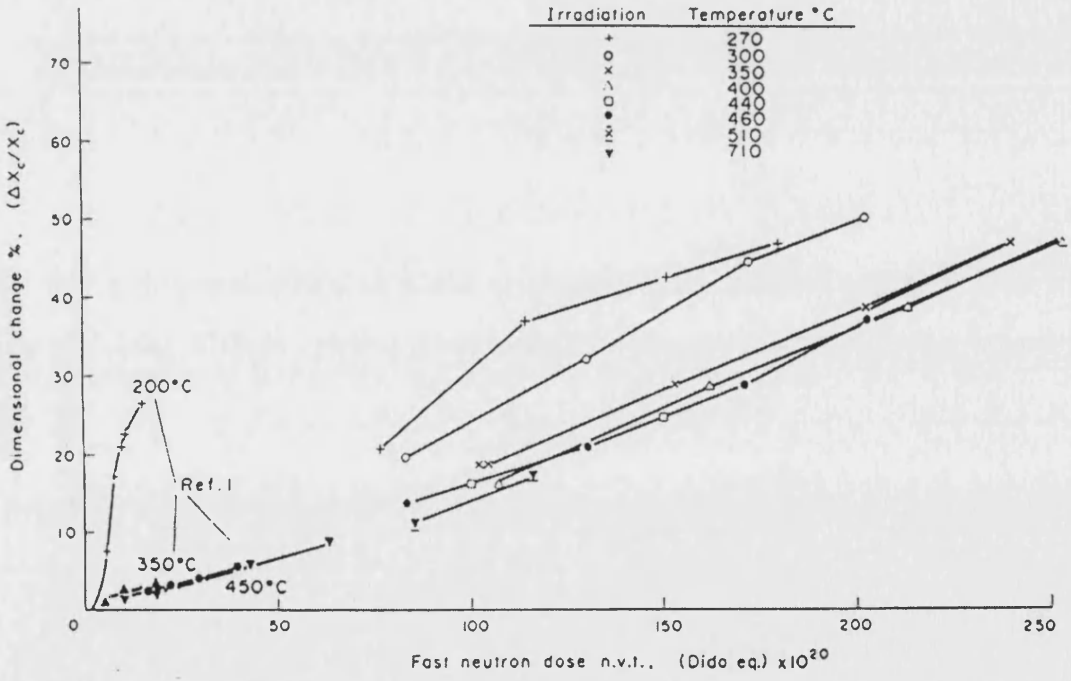

Figure A.7(a). Dimensional changes of pyrolytic graphite in the c direction irradiated to high dose in the temperature range 270-710°C (Kelly and Brocklehurst, 1971).

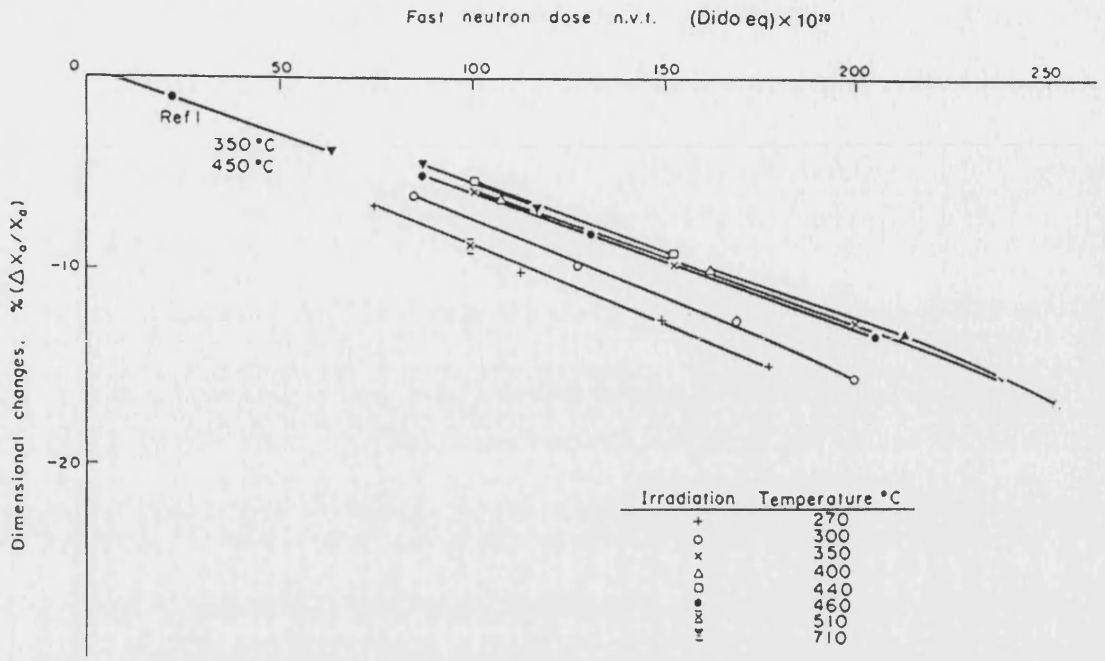

Figure A.7(b). Dimensional changes of pyrolytic graphite in the a direction irradiated to high dose in the temperature range 270-710°C (Kelly and Brocklehurst, 1971).

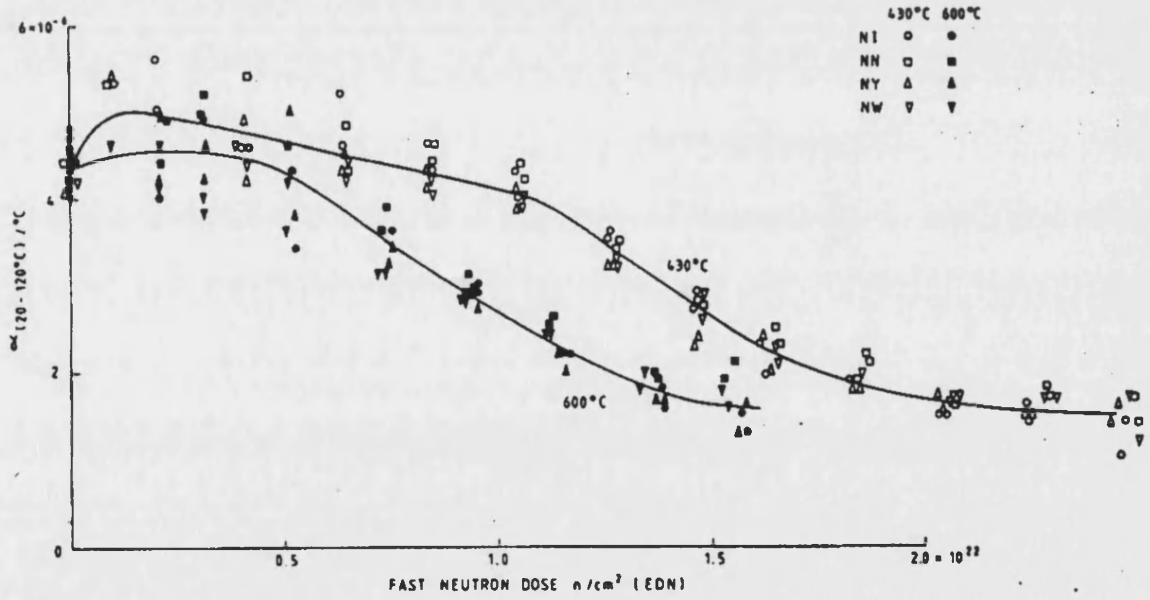

Figure A.8. CTE of AGR graphite under neutron irradiation at 430°C and 600°C (Brocklehurst and Kelly, 1993).

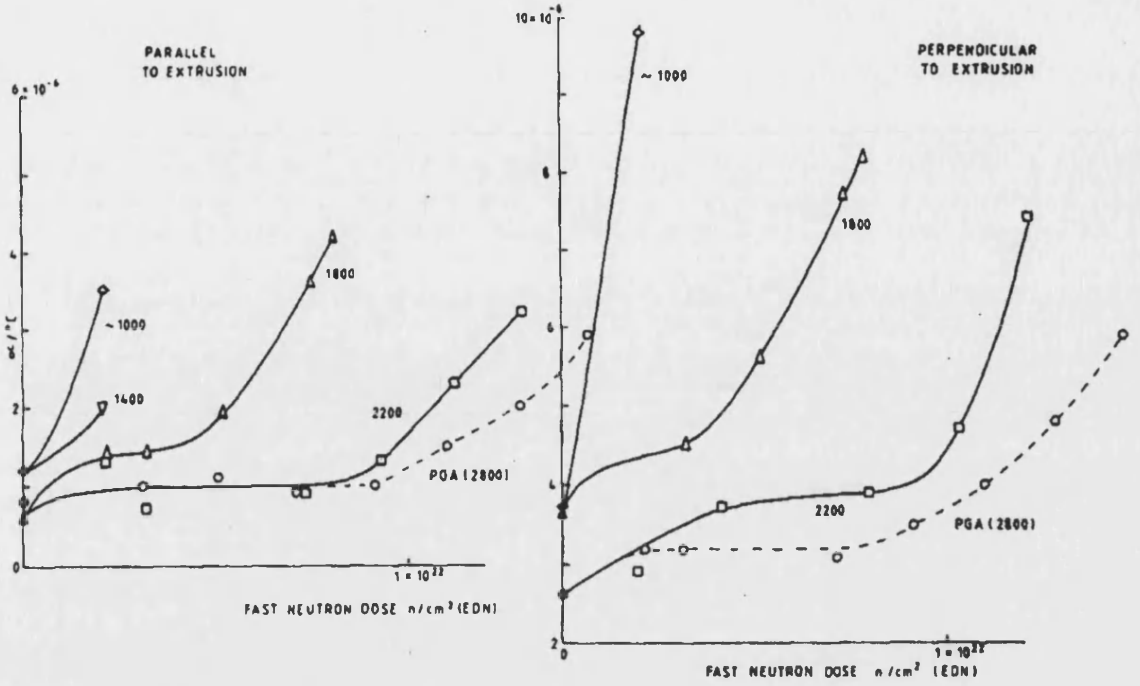

Figure A.9. CTE of Magnox moderator graphite under irradiation. The Magnox material is the dashed line in the Figure. (Brocklehurst and Kelly, 1993).

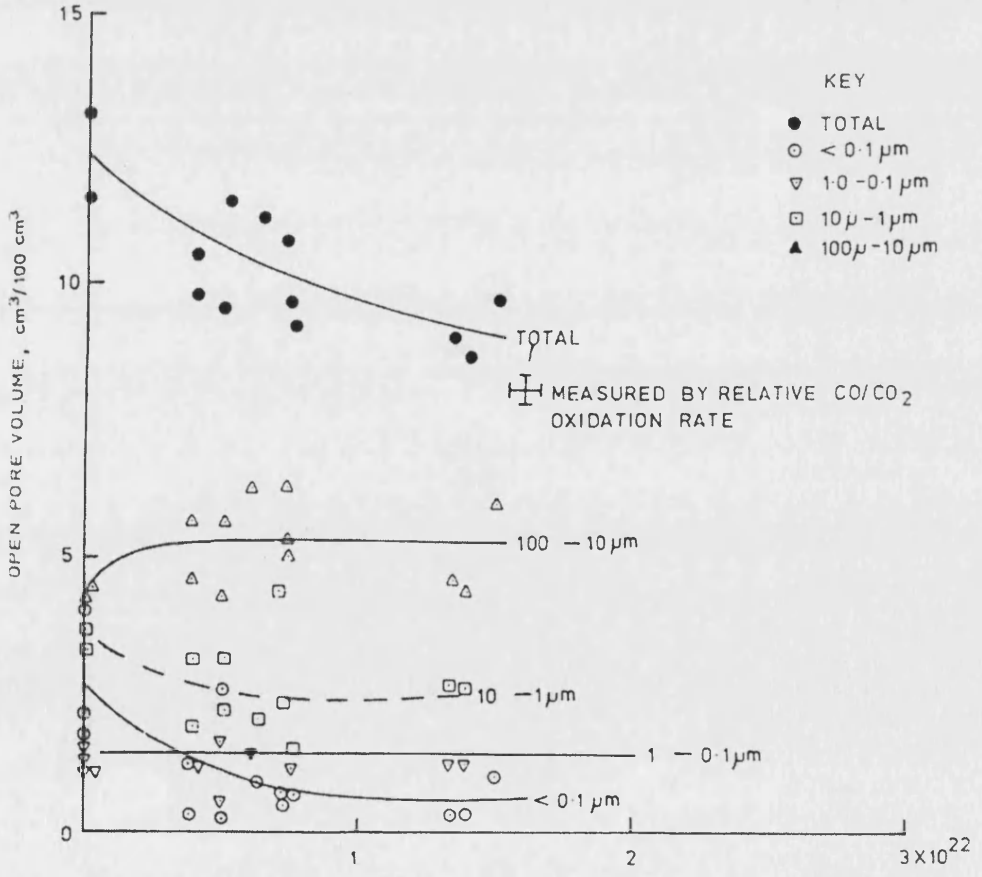

Figure A.10. Variation of pore volume with fast neutron irradiation for AGR graphite (Kelly *et al.*, 1974)

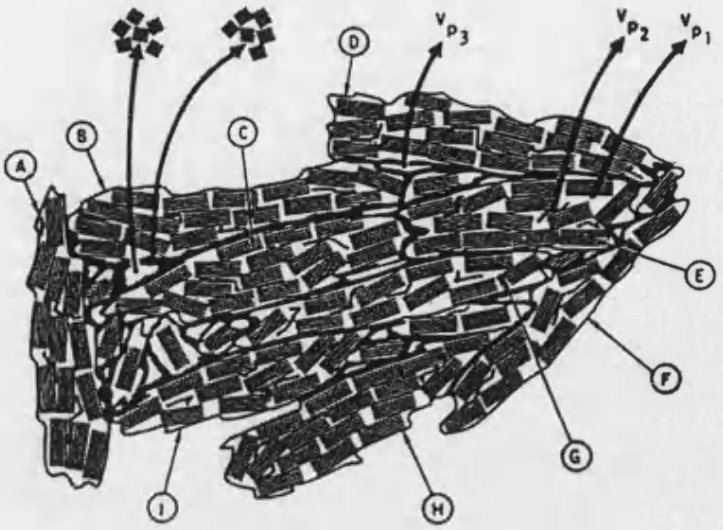

Figure A.11(a). Schematic of changes in graphite microstructure - Unirradiated material (Engle, 1971).

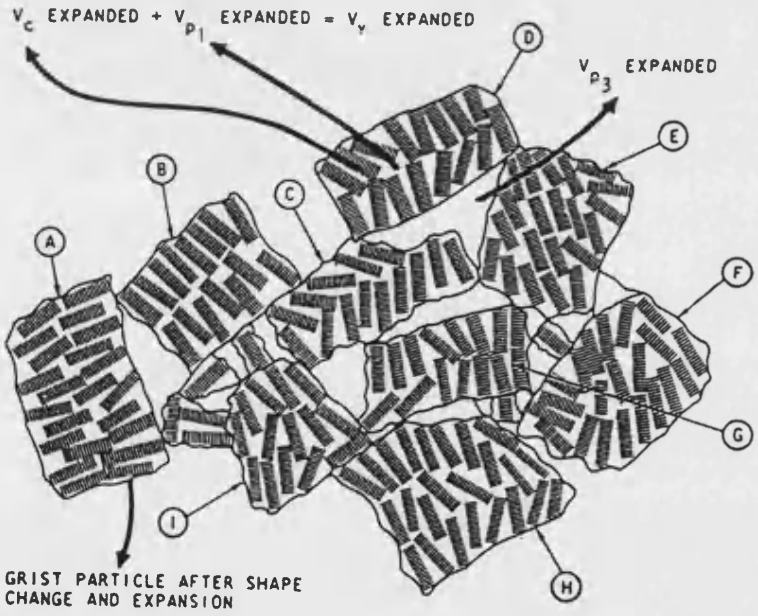

Figure A.11(b). Schematic of changes in graphite microstructure – Irradiated and expanded material (Engle, 1971).

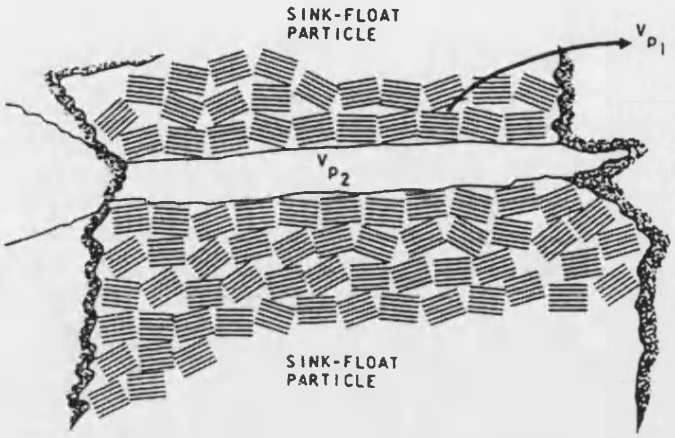

Figure A.11(c). Schematic of changes in graphite microstructure – Unirradaited material showing intra-grain porosity (V_{p2}) and extra-crystallite porosity (V_{p1}) (Engle, 1971).

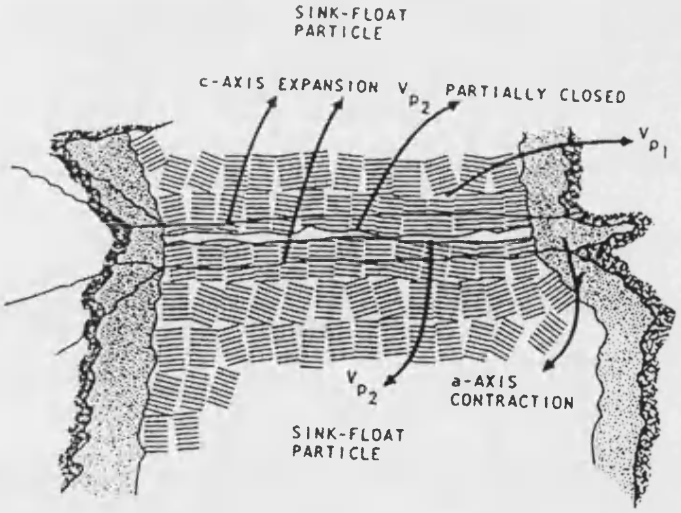

Figure A.11(d). Schematic of changes in graphite microstructure – Irradiated material showing partial closure of intra-grain porosity (V_{p2}) and extra-crystallite porosity (V_{p1}), together with stress induced cracking caused by a-axis contraction (Engle, 1971).

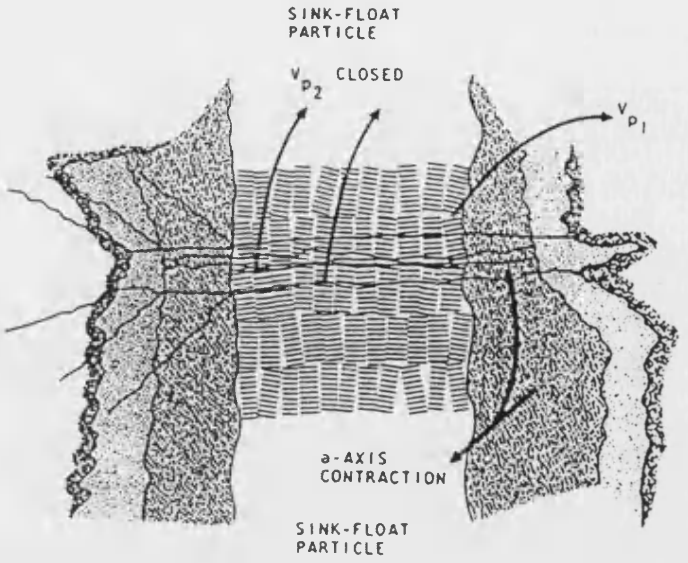

Figure A.11(e). Schematic of changes in graphite microstructure – Highly irradiated material showing full closure of intra-grain porosity (V_{p2}) and almost complete closure of extra-crystallite porosity (V_{p1}), together with extensive stress induced cracking caused by a-axis contraction (Engle, 1971).

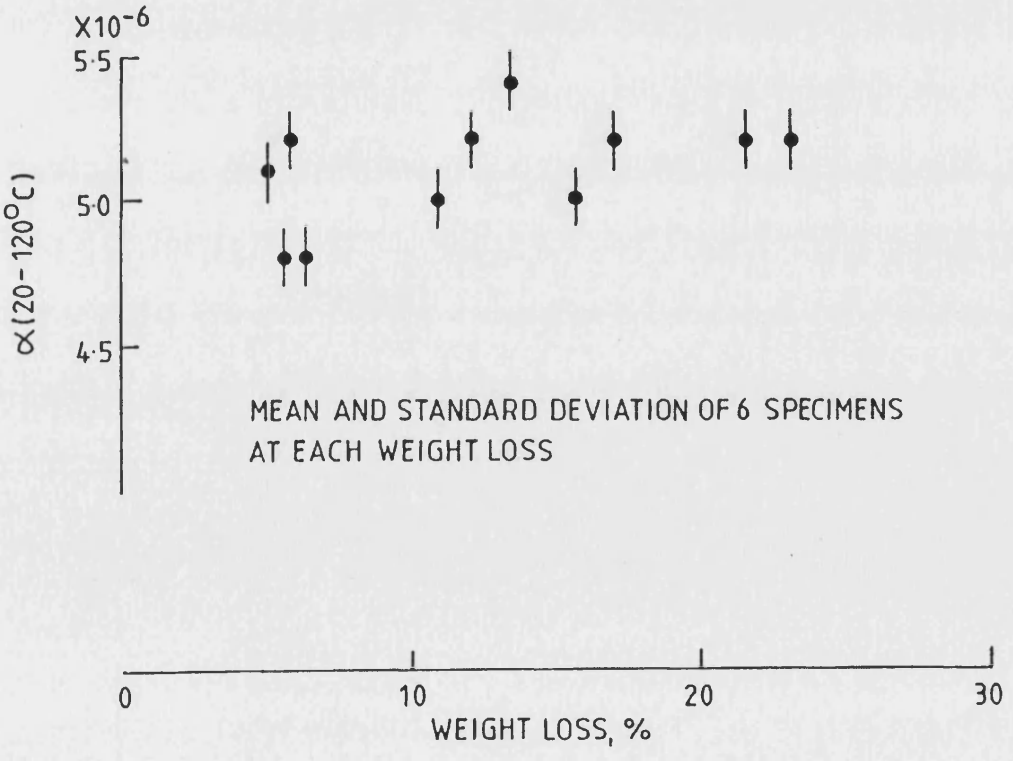

Figure A.12. The CTE of AGR graphite radiolytically oxidised to ~20% (Brocklehurst, 1984).

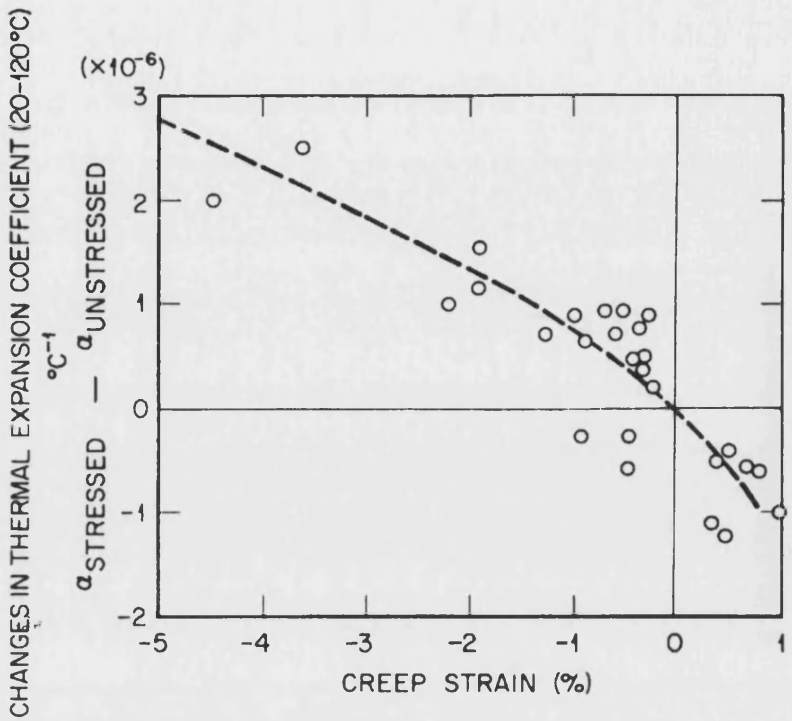

Figure A.14. The effects of irradiation induced creep on the CTE of AGR graphite (Kelly and Burchell, 1994).

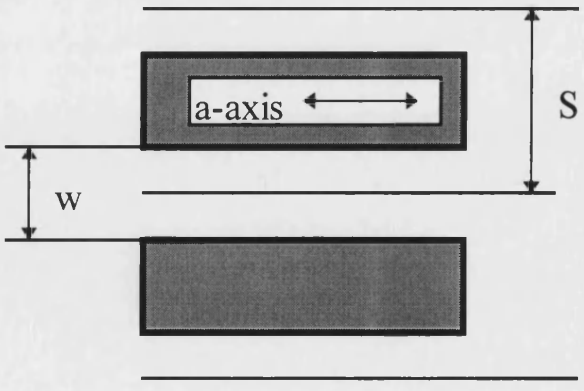

Figure A.15. A model of a Mrozowski crack within a crystallite of width, w, and spacing, S.

PART B: EXPERIMENTAL

OBJECTIVE

From Part A it is clear that only a limited understanding of the critical microstructural features that control CTE behaviour is currently available. The objective of this part of the thesis is to describe the purpose and structure of an experimental plan with reference to the work developed in Part A and with a view to the modelling requirements for Part C. The results from the implementation of the developed experimental programmes are then presented and discussed.

"It is a capital mistake to theorise before you have all the evidence.
It biases the judgement"
Sir Arthur Conan Doyle 1859-1930: A Study in Scarlet

CHAPTER 4

THE EXPERIMENTAL PROGRAMMES

There are three key experimental objectives that need to be satisfied in order to further characterise the nature of thermal expansion in nuclear graphites under reactor conditions and to allow the creation of a model. The first is the identification and characterisation of the small scale (<1μm) microstructure that is believed to control CTE. The second objective concerns possible changes in CTE at high weight losses. This also includes an analysis of the Closed Pore Volume (CPV) of graphite samples (of which porosity controlling expansion is believed to be a sub set). The third objective is to experimentally test the validity of the structural disruption hypothesis for describing the reduction in CTE seen in AGR moderator graphites as a function of neutron irradiation. This Chapter describes the structure and purpose of these experimental programmes.

Most of the existing microstructural studies of nuclear graphites have been made using optical microscopy. These studies were able to resolve detail of the order of a micron (around 200 times magnification) and are presented elsewhere (*e.g.* Neighbour, 1993). Apart from the work of Sutton and Howard (1956) who originally identified Mrozowski type porosity using replica Transmission Electron Microscopy, no detailed programme of work has been conducted to study the nanometric scale structure of these materials. This microscopical programme first aims to directly image Mrozowski cracks using a Scanning Electron Microscope. A secondary objective is to show the features of virgin and thermally oxidised nuclear graphites in the binder, filler and interface regions of the material. As the practical resolution of the SEM when studying nuclear graphites is being approached at ~30,000 times magnification a further attempt has been made to resolve detail to the crystallite level using Transmission Electron Microscopy.

Kelly (1985) reports that the CTE of AGR graphite radiolytically oxidised to ~20% weight loss shows no change in CTE. However, other thermo-physical properties show an exponential decrease with weight loss. Significant disruption to the structure of both AGR and Magnox moderator graphite has already occurred at weight losses around 20%

as viewed by optical microscopy, Figures B.1(a) and (b), so it remains unclear as to why CTE should remain unaffected. Although it is reasonable to assume that the microstructural elements that control CTE are unaffected by oxidation to low weight losses these features are unknown as are the effects of higher weight losses on CTE. A more satisfying explanation is therefore required. Within this experimental programme samples of AGR and Magnox moderator graphites shall be thermally oxidised up to the highest weight losses practically possible and their CTE measured.

The decrease in the CTE of AGR graphite at high neutron fluences (Figure A.8) has been described by Jenkins (1967) who attributed it to a structural disruption process that occurs when the porosity available to accommodate expansion is exhausted. However, the effects of direct structure disruption on these materials have not been experimentally studied. In particular, how does the disruption mechanism apply to the plateau observed during the irradiation of Magnox graphite? This issue is explored experimentally by a thermal disruption technique. Following the work of Platinov (1981) who subjected Russian graphites to high temperatures, samples of AGR and Magnox graphite shall also be subjected to high heat treatment temperatures (~2000°C) and cooled at varying rates. This is conducted with a view to causing microscopic structural disruption via differential contraction of crystallites and possible structural rearrangement.

4.1 THE THERMAL OXIDATION REGIME

Both the microscopical and dilatometry programmes require the production of oxidised graphite specimens. Thermally oxidised samples of AGR graphite (grade GCMB) and Magnox graphite (grade PGA) were prepared using established techniques (Neighbour and McEnaney, 1997) to encourage homogeneous oxidation under chemical control.

For Magnox graphite, ~40 cylindrical specimens, 18 mm length by 12 mm diameter, were machined with the long axes perpendicular and parallel to extrusion. Another 40 specimens were cut in random directions for AGR (GCMB grade) graphite (as this material is assumed to be a near isotropic material). Unless stated otherwise, this is the standard graphite sample geometry used throughout the experimental programme. Prior to use, each sample was ultrasonically cleaned in distilled water and dried for at least

two hours in an oven at 120 °C. Each sample was uniquely identified according to the following nomenclature where n is the number of the sample.

PBB n	Magnox moderator graphite (PGA from the Bradwell archive) cut parallel to the extrusion direction, denoted 'PGA Parallel'.
PBA n	Magnox moderator graphite (PGA from the Bradwell archive) cut perpendicular to the extrusion direction, denoted 'PGA Perpendicular'.
GH n	AGR graphite (GCMB grade, from the Heysham 2 archive) cut randomly.

Samples were heated in a tube furnace at 1.5 °C per minute to 900 °C in CO_2 with a low flow rate (~10cc/min) until the required weight loss was achieved. Prior and post oxidation, each sample was measured and weighed. Oxidation times were determined empirically. In order to oxidise AGR moderator graphite samples to ~60% weight loss, ~4.5 weeks were needed and to oxidise Magnox moderator graphite samples to ~50% weight loss, ~3 weeks were needed. After a specified period of oxidation samples with a range of weight losses were produced. In this work, the maximum weight losses obtained were ~60% and ~50% for AGR and Magnox graphites, respectively, Tables B.1(a-c). Samples oxidised to higher weight losses were unusable because they tended to disintegrate either in the furnace or on handling. As high weight losses were desired up to a third of samples within each batch disintegrated or were unusable. Although higher weight losses have been obtained in previous studies, *e.g.* >70% for AGR graphite (Neighbour and McEnaney, 1997), the specimens obtained were larger than in this work. Producing usable samples with high weight losses becomes progressively more difficult as the specimen dimensions decrease. The highly oxidised samples produced in this work tended to have irregular dimensions and occasionally were friable on handling.

Although careful control of the oxidation regime reduces the amount of external burn off, the total weight loss of the sample also consists of a fraction lost from the sample surface. Therefore, in contrast to measuring bulk weight loss, *i.e.* M_0-M (where M_0 is the initial sample mass and M is the mass after oxidation) a more appropriate measure of the corrected fractional weight loss, x', of the remaining material can be given by

$$x' = 1 - \frac{\rho}{\rho_0} \qquad [B1]$$

where ρ and ρ_0 are the final and initial bulk densities respectively.

The quality of the oxidised samples can also be judged microscopically by the retention of sharp edges, minimal reductions in dimension and the absence of extensive surface pitting.

Sample No.	Grade	Oxidation Time (Hours)	Initial Length (mm)	Final Length (mm)	Initial Diameter (mm)	Final Diameter (mm)	Initial Weight (g)	Final Weight (g)	Corrected Wt Loss (%)	
UCAR GCMB										
GH-01	GCMB (Hey. II)	0	18.09		12.07		3.76		0.00	
GH-02	GCMB (Hey. II)	0	18.04		12.04		3.66		0.00	
GH-03	GCMB (Hey. II)	640	17.98	17.85	12.02	11.79	3.6749	2.4304	29.38	
GH-04	GCMB (Hey. II)	640	18.09	18.09	12.05	11.7	3.711	1.5079	53.64	
GH-05	GCMB (Hey. II)	640	18.02	17.47	12.05	11.16	3.6912	1.6497	38.46	
GH-06	GCMB (Hey. II)	640	18.02	17.77	12.03	11.7	3.6807	2.2986	30.83	
GH-07	GCMB (Hey. II)	640	17.9	17.88	12.06	11.37	3.7506	1.5752	46.79	
GH-08	GCMB (Hey. II)	640	18.12		12.09		3.733	DISINTEGRATED		
GH-09	GCMB (Hey. II)	640	18.01		12.01		3.6915	DISINTEGRATED		
GH-10	GCMB (Hey. II)	640	18.08		12.06		3.7868	DISINTEGRATED		
GH-11	GCMB (Hey. II)	640	18.01	17.9	12.05	11.93	3.7163	2.8808	19.90	
GH-12	GCMB (Hey. II)	640	18.02	17.78	12.01	11.72	3.6802	2.1147	36.50	
GH-13	GCMB (Hey. II)	640	18.11	17.96	12.02	11.83	3.7648	1.6902	51.17	
GH-14	GCMB (Hey. II)	640	18.04	15.52	12.09	11.23	3.7892	0.5042	60.92	
GH-15	GCMB (Hey. II)	640	18.1	18.04	12.07	11.96	3.6709	3.1076	13.21	
GH-16	GCMB (Hey. II)	640	17.81	17.8	12.12	12.05	3.6814	3.3887	6.74	
GH-17	GCMB (Hey. II)	640	18.08	18.03	12.09	12.02	3.7723	3.4347	7.52	
GH-18	GCMB (Hey. II)	640	18.03	17.99	12.04	12.02	3.7602	3.1679	15.20	
GH-19	GCMB (Hey. II)	672	18.02	17.85	12.04	11.41	3.7328	1.2416	55.70	
GH-20	GCMB (Hey. II)	672	17.89		12.06		3.6846	DISINTEGRATED		
GH-21	GCMB (Hey. II)	672	17.75	17.66	11.97	11.71	3.7121	1.898	44.09	
GH-22	GCMB (Hey. II)	672	18.1		11.98		3.7851	DISINTEGRATED		
GH-23	GCMB (Hey. II)	672	17.8		12.1		3.7939	DISINTEGRATED		
GH-24	GCMB (Hey. II)	672	17.4	17.29	12.15	11.79	3.7049	1.3104	58.20	
GH-25	GCMB (Hey. II)	672	17.64		11.95		3.7421	DISINTEGRATED		
GH-26	GCMB (Hey. II)	672	17.99	17.8	12	11.44	3.7336	1.5017	49.70	
GH-27	GCMB (Hey. II)	672	18.2	18.07	11.89	11.8	3.7386	2.4544	32.14	
GH-28	GCMB (Hey. II)	672	18.4	18.24	12.07	12.02	3.7018	2.7044	25.25	
GH-29	GCMB (Hey. II)	672	18.2	17.96	12.11	12	3.6981	2.9368	17.48	
GH-30	GCMB (Hey. II)	672	18.15		12.18		3.7147	DISINTEGRATED		
GH-31	GCMB (Hey. II)	672	17.85	18.02	12.12	11.97	3.7391	2.4014	34.25	
GH-32	GCMB (Hey. II)	672	17.9	17.95	12.02	11.92	3.6997	1.7714	50.74	
GH-33	GCMB (Hey. II)	672	18.1	17.99	12.15	12	3.7465	3.4553	4.73	
GH-34	GCMB (Hey. II)	672	18.07	17.99	12.04	12.03	3.706	3.6828	0.02	
GH-35	GCMB (Hey. II)	700	18.02		12.06		3.6822	DISINTEGRATED		
GH-36	GCMB (Hey. II)	700	18.04		11.99		3.7287	DISINTEGRATED		
GH-37	GCMB (Hey. II)	432	17.88		11.99		3.6686	DISINTEGRATED		
GH-38	GCMB (Hey. II)	432	18.02		12		3.7573	DISINTEGRATED		
GH-39	GCMB (Hey. II)	432	17.96		11.96		3.7223	DISINTEGRATED		
GH-40	GCMB (Hey. II)	0	18	18	12.04	12.04	3.76	3.76	0.00	

TABLE B.1(a): The thermal oxidation of AGR moderator graphite samples.

Sample No.	Grade	Oxidation Time (Hours)	Initial Length (mm)	Final Length (mm)	Initial Diameter (mm)	Final Diameter (mm)	Initial Weight (g)	Final Weight (g)	Corrected Wt Loss (%)	
PGA Perpendicular										
PBA-1	PGA Perp (Brad)	672	17.6		12.1		3.4125	DISINTEGRATED		
PBA-2	PGA Perp (Brad)	672	17.55		12.08		3.407	DISINTEGRATED		
PBA-3	PGA Perp (Brad)	672	17.65	17.64	11.95	11.94	3.47	3.1269	9.66	
PBA-4	PGA Perp (Brad)	672	17.7	17.7	11.97	11.98	3.4516	2.2564	34.79	
PBA-5	PGA Perp (Brad)	672	17.68	17.66	12.12	12.13	3.4528	2.6699	22.73	
PBA-6	PGA Perp (Brad)	672	17.77	17.73	12.14	12.15	3.4151	3.3466	1.95	
PBA-7	PGA Perp (Brad)	0	17.68	17.68	12.02	12.02	3.4037	3.4037	0.00	
PBA-8	PGA Perp (Brad)	504	17.69		11.87		3.4335	DISINTEGRATED		
PBA-9	PGA Perp (Brad)	504	17.65		11.87		3.4069	DISINTEGRATED		
PBA-10	PGA Perp (Brad)	504	17.62	17.1	11.92	11.54	3.5276	1.8398	38.81	
PBA-11	PGA Perp (Brad)	504	17.65		11.85		3.5491	DISINTEGRATED		
PBA-12	PGA Perp (Brad)	504	17.67		11.87		3.4289	DISINTEGRATED		
PBA-13	PGA Perp (Brad)	504	17.62	17.54	11.85	11.48	3.5199	2.0822	34.27	
PBA-14	PGA Perp (Brad)	504	17.69	17.6	11.96	11.63	3.4427	2.391	24.63	
PBA-15	PGA Perp (Brad)	504	17.67	17.68	11.94	11.92	3.462	2.8312	17.94	
PBA-16	PGA Perp (Brad)	504	17.7	17.7	11.96	11.9	3.4435	2.9845	12.33	
PBA-17	PGA Perp (Brad)	504	17.7	17.68	11.94	11.91	3.4567	3.1859	7.22	
PBA-18	PGA Perp (Brad)	504	17.66		11.97		3.4079	DISINTEGRATED		
PBA-19	PGA Perp (Brad)	504	17.72		12.06		3.4258	DISINTEGRATED		
PBA-20	PGA Perp (Brad)	504	17.74		12.03		3.4909	DISINTEGRATED		
PBA-21	PGA Perp (Brad)	504	17.7		11.98		3.3813	DISINTEGRATED		
PBA-22	PGA Perp (Brad)	504	17.62	17.65	11.99	11.37	3.4354	2.5341	16.31	
PBA-23	PGA Perp (Brad)	504	17.68		11.98		3.4301	DISINTEGRATED		
PBA-24	PGA Perp (Brad)	504	17.63	17.6	11.88	11.66	3.477	2.5256	23.53	
PBA-25	PGA Perp (Brad)	504	17.84	17.2	11.96	11.6	3.4765	2.1996	27.43	
PBA-26	PGA Perp (Brad)	576	17.76	17.68	12	11.9	3.3845	2.3694	27.89	
PBA-27	PGA Perp (Brad)	576	17.74	17.66	12.04	11.96	3.4186	1.6852	48.94	
PBA-28	PGA Perp (Brad)	576	17.77	17.6	12.06	11.96	3.337	2.164	32.56	
PBA-29	PGA Perp (Brad)	576	17.7	17.61	12.04	11.94	3.481	2.022	39.76	
PBA-30	PGA Perp (Brad)	576	17.77	17.58	12.03	11.88	3.5011	1.952	40.73	
PBA-31	PGA Perp (Brad)	576	17.7	17.59	12.01	11.92	3.4214	2.279	31.28	
PBA-32	PGA Perp (Brad)	576	17.72	17.69	12.03	12	3.4118	2.638	22.01	
PBA-33	PGA Perp (Brad)	576	17.66	17.61	12	11.87	3.4345	3.1265	6.54	
PBA-34	PGA Perp (Brad)	576	17.7	17.66	12.1	11.97	3.505	3.23	5.49	
PBA-35	PGA Perp (Brad)	576	17.73	17.64	12.06	12	3.4714	3.372	1.37	
PBA-36	PGA Perp (Brad)	0	17.68	17.68	12.1	12.1	3.4707	3.4707	0.00	
PBA-37	PGA Perp (Brad)	0	17.74	17.74	12.06	12.06	3.4765	3.4765	0.00	
PBA-38	PGA Perp (Brad)	0	17.72	17.72	12.04	12.04	3.462	3.462	0.00	
PBA-39	PGA Perp (Brad)	711	17.74	17.64	11.96	11.45	3.3765	2.0369	30.81	
PBA-40	PGA Perp (Brad)	711	17.74	17.46	12.01	11.47	3.5188	2.0026	32.86	

TABLE B.1(b): The thermal oxidation of Magnox moderator graphite samples in the direction perpendicular to extrusion.

Sample No.	Grade	Oxidation Time (Hours)	Initial Length (mm)	Final Length (mm)	Initial Diameter (mm)	Final Diameter (mm)	Initial Weight (g)	Final Weight (g)	Corrected Wt Loss (%)	
PGA Parallel										
PBB-1	PGA Par (Brad)	504	17.77	17.66	12.04	11.61	3.40	2.09	30.99	
PBB-2	PGA Par (Brad)	504	17.77	17.74	12.03	11.96	3.40	1.96	40.98	
PBB-3	PGA Par (Brad)	504	17.77		12.02		3.39		DISINTEGRATED	
PBB-4	PGA Par (Brad)	504	17.82	17.60	12.05	11.70	3.50	2.27	28.26	
PBB-5	PGA Par (Brad)	504	17.75	17.60	12.01	11.81	3.50	2.53	23.53	
PBB-6	PGA Par (Brad)	504	17.75	17.68	11.99	11.64	3.46	2.30	27.34	
PBB-7	PGA Par (Brad)	504	17.71		11.98		3.38		DISINTEGRATED	
PBB-8	PGA Par (Brad)	504	17.76	17.67	12.01	11.93	3.44	2.53	24.48	
PBB-9	PGA Par (Brad)	504	17.75	17.68	12.02	12.04	3.37	2.47	26.73	
PBB-10	PGA Par (Brad)	504	17.80	17.67	12.02	11.94	3.51	3.11	9.32	
PBB-11	PGA Par (Brad)	504	17.75	17.71	12.03	11.98	3.49	3.28	5.07	
PBB-12	PGA Par (Brad)	504	17.75	17.70	12.01	11.91	3.52	3.42	0.91	
PBB-13	PGA Par (Brad)	0	17.76	17.76	11.99	11.99	3.45	3.45	MACHINE ERROR	
PBB-14	PGA Par (Brad)	0	17.74	17.74	12.05	12.05	3.38	3.38	0.00	
PBB-15	PGA Par (Brad)	0	17.79	17.79	12.03	12.03	3.51	3.51	0.00	
PBB-16	PGA Par (Brad)	0	17.73	17.73	12.03	12.03	3.50	3.50	0.00	
PBB-17	PGA Par (Brad)	0	17.70	17.70	12.05	12.05	3.44	3.44	0.00	
PBB-18	PGA Par (Brad)	0	17.73	17.73	12.02	12.02	3.50	3.50	0.00	
PBB-19	PGA Par (Brad)	336	17.74		11.97		3.38		DISINTEGRATED	
PBB-20	PGA Par (Brad)	336	17.72		12.02		3.42		DISINTEGRATED	
PBB-21	PGA Par (Brad)	336	17.70		11.99		3.34		DISINTEGRATED	
PBB-22	PGA Par (Brad)	336	17.71	17.68	11.95	11.89	3.38	2.76	17.19	
PBB-23	PGA Par (Brad)	336	17.71	17.68	12.00	11.96	3.48	3.16	8.49	
PBB-24	PGA Par (Brad)	336	17.74	17.70	11.88	11.80	3.39	3.00	MACHINE ERROR	
PBB-25	PGA Par (Brad)	336	17.67	17.62	11.96	11.90	3.37	2.99	10.04	
PBB-26	PGA Par (Brad)	504	17.72	17.02	12.04	11.07	3.52	2.15	20.08	
PBB-27	PGA Par (Brad)	504	17.76		12.04		3.42		DISINTEGRATED	
PBB-28	PGA Par (Brad)	504	17.70	14.62	12.05	7.32	3.48	0.60	TOO FRIABLE	
PBB-29	PGA Par (Brad)	504	17.75	16.24	11.98	10.18	3.43	1.35	TOO FRIABLE	
PBB-30	PGA Par (Brad)	504	17.73	17.34	11.98	11.35	3.56	2.29	23.32	
PBB-31	PGA Par (Brad)	504	17.75	16.96	12.03	10.17	3.47	1.50	TOO FRIABLE	
PBB-32	PGA Par (Brad)	504	17.76		12.00		3.37		DISINTEGRATED	
PBB-33	PGA Par (Brad)	504	17.74	17.76	12.02	11.87	3.50	2.84	16.34	
PBB-34	PGA Par (Brad)	504	17.87	17.81	12.05	11.88	3.41	2.68	18.19	
PBB-35	PGA Par (Brad)	504	17.77	17.76	11.99	11.99	3.56	3.44	3.52	
PBB-36	PGA Par (Brad)	504	17.73	17.79	12.02	12.05	3.49	3.45	1.86	
PBB-37	PGA Par (Brad)	657	17.80		12.02		3.56		DISINTEGRATED	
PBB-38	PGA Par (Brad)	657	17.78		11.99		3.45		DISINTEGRATED	
PBB-39	PGA Par (Brad)	657	17.79		12.05		3.52		DISINTEGRATED	
PBB-40	PGA Par (Brad)	657	17.76		12.07		3.48		DISINTEGRATED	

TABLE B.1(c): The thermal oxidation of Magnox moderator graphite samples in the direction parallel to extrusion.

CHAPTER 5

MICROSTRUCTURAL CHARACTERISATION OF AGR AND MAGNOX MODERATOR GRAPHITES

The discussion in Part A suggests that CTE behaviour is controlled primarily by small-scale structure, most likely at the crystallite level. Therefore, in order to improve the understanding of thermal expansion in these materials it is necessary to explore the structure of material at the nanometric scale level. Ultimately, this will require the use of transmission electron microscopy to obtain the resolution required. However, the use of a range of microscopical techniques from optical to transmission electron microscopy allows a continuum of microstructural information to be obtained across a range of magnifications from ~50 times to ~100,000 times magnification. Some optical micrographs have previously been presented in the introduction and have also formed the basis of previous studies which have been discussed, therefore this section focuses on Scanning and Transmission Electron Microscopies (SEM and TEM) as methods for examination of differences in small scale structure between Magnox and AGR moderator graphites and as a tool for examining the effects of thermal oxidation on the structure at these scale. The primary aim is to first identify Mrozowski cracks within graphite. This is followed by a general SEM study of AGR and Magnox moderator graphites and continues with a TEM study of each material both before and after thermal oxidation.

5.1 SCANNING ELECTRON MICROSCOPY

The instrument used in this study was a T330 Scanning Electron Microscope manufactured by Japanese Electron Optics Ltd. (JEOL), with a beam voltage of 15kV. An initial technique involved gold sputter coating of samples, however this was found to be unsatisfactory as the detail and porosity of the specimen became hidden by the gold coating. All samples were therefore studied after oxidation with no further mounting or treatment other than the use of diamond paste to remove, by polishing, the machining marks left on unoxidised samples. Where indicated a razor blade was used to cut the sample to produce an observable surface within the body of the sample. Due

to the low electron backscattering of graphite, the practical resolution from this technique occurred at a magnification of ~30,000 times. At this resolution porosity of ~25 nm in width (including Mrozowski cracks) are just resolvable. Such porosity was identified in the binder region of unoxidised AGR moderator graphite, often occurring around a larger pore, Figure B.2(a). Magnification of an area to the right of the pore, Figure B.2(b), identifies what appears to be slit shaped porosity of the width identified with Mrozowski cracks. Interestingly, these cracks appear to exist in a family of different crack sizes ranging from ~15 nm to ~100 nm in accordance with the discussions in Part A (chapter 3, section 3.2).

5.1.1 SEM Observations of Magnox Graphite

Further observations at lower magnification of Magnox and AGR moderator graphite were conducted to achieve the secondary aim of microstructural characterisation of each material at SEM magnifications and to identify oxidation effects. Figure B.3 shows the general structure of unoxidised Magnox moderator graphite. Gas entrapment porosity is visible and filler and binder regions can be identified. Figure B.4 shows in more detail a filler particle within a coarse binder region at the edge of a gas entrapment pore in the unoxidised graphite. Close examination of Figure B.4 shows that the filler particle contains many slit shaped pores (probably arising from the calcination process during manufacture), however few features of the filler or binder regions can be identified. Also, in the unoxidised state, the demarcation between filler and binder regions is not clear and good structural continuity exists between these regions. An example of the existence of fine cracks and the sub-micron platelet structure observed throughout the unoxidised material is given in Figure B.5.

At modest levels of oxidation, the binder phase is observed to oxidise preferentially to the filler phase. This is demonstrated in Figure B.6, which is of Magnox moderator graphite oxidised to 23% weight loss and clearly shows a filler particle with limited attack along the basal planes. Surrounding this filler particle are large pores within a region of disrupted binder structure. The rapid isolation of filler particles as oxidation proceeds may, in this instance, be due to poor wetting of the binder pitch during manufacture. The limited nature of attack on the filler phase is demonstrated in Figure

B.7, where the filler particles have maintained their planar and continuous shape with no evidence of disintegration. This has resulted in a striking difference in structure between the filler (F) and binder (B) phases with easy identification of the interface between the two (FB). Even at this modest weight loss, the integrity of the filler-binder interface has suffered with a loss of continuity. Possible effects of the thermal oxidation mechanism can be seen at higher magnifications, Figure B.8, where both in-plane pitting and attack along basal planes are observed. The random folds within the binder phase and the fine pore structure, also observed throughout the structure are presented in Figure B.9.

As oxidation proceeds, extensive disruption to the binder phase continues with minimal structural effects on the filler particles, Figure B.10 (Magnox moderator graphite oxidised to ~30% weight loss). The filler particle is easily identified and although opening of the large calcination cracks in the centre of some of the filler particles is occurring they remain largely intact in a severely disrupted binder phase. At weight losses above 40%, thermal oxidation is shown to be attacking most parts of the structure of the material. Large interconnected porosity networks are being created, Figure B.11, with the material becoming more particulate in character. Areas of structure are also observed consisting of disparate regions, Figure B.12. At some of the highest achievable weight losses in these samples, ~45%, filler particles are seen with large central cracks (likely to be pre-existing calcination cracks) and further cracking between layer planes, Figure B.13. Extensive crack development occurs from existing gas entrapment porosity, Figures B.14 and B.15, due to the creation of a large continuous porosity network, however the structure continues to have integrity.

5.1.2 SEM Observations of AGR Graphite

Similar (but generally less obvious at a given weight loss) microstructural observations are evident upon oxidation of AGR moderator graphite. Figure B.16 shows the platelet structure in the binder phase near an emergent gas-entrapment pore at the surface of as-received AGR graphite. In particular the extent of gas entrapment porosity is shown spanning the field of view and therefore extending over more than 100μm. At 30% weight loss, filler and binder regions are easily identified with large scale destruction of

the binder evident as well as an opening of the concentric "onion" layers within the Gilsocarbon filler particles, Figure B.17. This indicates that 'breakthrough' from open porosity in the binder phase has occurred into the closed porosity (calcination cracks) in the filler particles. In many cases, and in contrast to Magnox moderator graphite, the filler-binder interface remains largely intact, Figure B18, although the effects of oxidation are readily observed in the binder phase itself, Figure B.19.

At very high weight losses (~70%), and at low magnifications, the material is disorganised and disrupted and appears discontinuous in places. In general, the structure is composed of large voids and areas of highly-interconnected, fine porosity with some recognisable areas of filler (F) and binder (B) phases, Figure B.20. Identification of original porous features, such as gas-entrapment pores, is difficult due to the large amount of new porosity generated. Only at these very high weight losses is there any evidence for attack of the filler/binder interface, Figure B.21, and this appears less extensive than in Magnox moderator graphite oxidised to ~30% weight loss. In many places at the filler particle boundary there is evidence of fine pits and voids, Figure B.22 although structural connectivity continuous to be maintained. In both Figures B.21 and B.22, the attack on the filler-binder interface is shown by the generation of fine porosity within the interface. This may be due to selective removal of the fine mosaic binder pitch observed as a thin layer surrounding filler particles in optical microscopy, as suggested by Okada (1960).

5.2 TRANSMISSION ELECTRON MICROSCOPY

Five samples were prepared for Transmission Electron Microscopy (TEM); two as-received AGR moderator graphite samples, one oxidised AGR moderator graphite sample with ~30% weight loss, one as-received Magnox moderator graphite sample and one oxidised Magnox moderator graphite sample also with ~30% weight loss. The practical difficulties involved in preparing graphite specimens for TEM are not trivial. Electron transmission, and hence the generation of an image, can only occur through sample regions of less than ~1000 atomic radii, so maintaining the integrity of porous and non-homogeneous samples such as polygranular graphite is difficult. In addition, it

is very difficult to specify a particular region to study as this depends very much on the areas that happen to become thin enough to allow transmission.

Each sample was prepared by cutting a 0.5 mm slice from a 12 mm sample of material. These samples were then mounted on glass slides and hand ground on silicon carbide papers of decreasing grit size to a thickness of ~80 μm. Discs of 3 mm diameter were cut from this material and mounted on the specimen platen of a VCR Dimple Grinder using hot wax. Dimples were ground into each sample using a diamond impregnated wheel, followed by final fine polishing until a calculated sample thickness of ~5 μm was achieved. These samples were further thinned to perforation using a Gatan Duomill Ion Miller inclined at 11° to the sample surface. The ion miller removes material atomically by energetic collision between argon ions and the material surface. The ion milled samples were then studied in a JEOL 2000FX Transmission Electron Microscope operating with a beam voltage of 200 kV.

Sample 1 – Binder Region of Unoxidised AGR Moderator Graphite

Sample 1 appeared to be predominantly binder material although this is difficult to show conclusively. The principal features of the microstructure revealed by TEM, Figures B.23, B.24, are lamellar ribbons of graphitic stacks separated by fine lenticular cracks. These cracks are between 20-100 nm in width separating graphitic ribbons that are up to ~35 nm in height by up to ~75 nm in length. The structure is fibrous along these stacks (Figure B.25), with continuous ligaments of material joined together along the *a*-axis direction. This continuity of structure shows that the material is not the loose aggregate of single crystals that is assumed in some microstructural models used to describe CTE in graphites. More extended linear fibrous structures with common basal plane orientations can be seen at higher magnification, Figure B.26. These appear to be examples of extended 'Local Molecular Ordering' described by Oberlin (1989). At this scale it is difficult to differentiate between the filler and binder regions.

Figures B.24 and B.25 contain spiral features containing graphitic ribbons oriented in spirals several hundred nanometers in diameter. The spirals have more porosity close to their periphery with finer ribbons at their centre. These may be relics of disclinations,

which have been described by White (1975) using polarised light microscopy. Disclinations are formed by coalescence of mesophase during carbonisation of binder or during coking of filler particles. Alternatively, these regions could be the relics of the graphitisation of quinoline insoluble fractions. These were identified as 'carbon black like inclusions' in the pitch bonded graphites studied by Jones and Woodruff (1970). Indeed the folding of ribbons around the core of these objects is accompanied by 'polygonisation', similar to that seen in TEM of graphitised carbon blacks (Oberlin, 1989). Polygonisation is indicated by sharp changes in orientation of the layer planes along the ribbons.

All micrographs show a large amount of porosity on the nanometer scale with the lenticular cracks lying parallel to the graphitic ribbons being plentiful. These lenticular cracks may be identified with Mrozowski cracks. The TEM observations are in broad agreement with those of Sutton and Howard (1962) who found ~30 nm sized cracks with a periodicity of 500 nm. However, estimates from Figures B.25 and B.26 indicate a periodicity of ~50-100 nm. In addition, cracks can be found with widths much less than 25 nm. For example, Figure B.26 shows some cracks with widths less than 5 nm. Interface regions are found throughout the structure, *e.g.* Figure B.27. These may mark a fold boundary between domain or mosaic structures formed during carbonisation of the binder phase, Menendez *et al.* (1997). However, close inspection of Figure 27 also indicates that region A may have thinned to a greater extent than region B, hence the interface may be an artefact of the relative relief between these two regions. In either case, there is no evidence for crystallographic registers across the interface that might be indicative of a twin boundary.

Sample 2 – Filler Particle in Unoxidised GCMB Graphite

Fortuitously, Sample 2 perforated within a filler particle and was thin enough around the exposed edge to allow a study of the structure within a Gilsocarbon filler particle at six positions. The region of the thinned and visible area is smaller here than in the positions studied in Sample 1. At the edge of the sample, Figure B.28 shows a large circular feature several hundred nanometers in diameter that is similar to those found in Sample 1, Figure B.25. These circular structures are maintained when the area is viewed at

higher magnifications, Figure B.29. Within the filler particle, a coarser structure of ripple-like or folded graphitic stacks is also observed, Figure B.30. Also, rapid changes in crystallographic orientation between, say, regions A and B in Figure B.30 are apparent together with abrupt boundaries (indicated as C) that may represent individual crystallite stacks. 'Ridge' regions, similar in size and form to the replica TEM images given by Sutton and Howard (1962) and identified by them as Mrozowski cracks are visible. However, in Figure B.30 these appear to be step edges of graphitic planes. While microstructural features could be identified that are similar to those in Sample 1, the overall amount of porosity appeared to be less, *e.g.* Figure B.30. Although difficult to characterise, the periodicity and widths of cracks appear to be similar to those seen in Sample 1 of AGR moderator graphite.

Sample 3 - Oxidised AGR moderator Graphite (~30% Weight Loss)

Preparation of AGR graphite samples oxidised to 30% weight loss for the TEM proved to be difficult, possibly due to weakening of the material by oxidation. There was evidence of artefacts at the edge of the TEM samples possibly due to removal or pull out of graphite during sample preparation. The most common observation was that the edge of the graphitic stacks tended to end abruptly in splays of graphitic fibrils, Figure B.31. Comparison between the unoxidised graphite and the oxidised material suggests that there may be a widening of the porosity between ligaments. However, the extent and size of very fine porosity (width less than 20 nm) remains unaltered.

Sample 4 - Unoxidised Magnox Moderator Graphite

The principal microstructural features found in Magnox moderator graphite are similar to those seen in AGR graphite. These include the ribbons of graphitic stacks separated by fine lenticular cracks and the circular objects, Figure B.32. More disorganised structures were also observed, Figure B.33. Also a wider range of stack sizes ranging up to 60 nm in height by 1000 nm in length was observed, Figure B.34. Extended regions of Local Molecular Ordering are also seen, Figure B.35, similar to those seem in AGR moderator graphite, which are most probably within filler particles. Closer inspection at higher magnification within the same region shows that the structure still contains

ligaments seen in the previous samples, Figure B.36. The small-scale porosity is also of similar shape to that found in the AGR moderator samples, *i.e.* thin and lenticular. Pore sizes range from up to ~50 nm in width and more than 300 nm in length and with a high periodicity of ~20-50 nm. The nature of the ligament structure however, makes quantification of the porosity difficult. Within the planar regions, the porosity is much more ordered following the direction of the surrounding material, as shown in Figures B.35 and B.36.

Sample 5 - Oxidised Magnox Moderator Graphite (~30% Weight Loss)

The microstructure of oxidised Magnox moderator graphite was more easily observed than was the case for oxidised AGR moderator graphite. In the former, the voids between the graphite stacks and ribbons are more sharply delineated than in the unoxidised material *e.g.* Figures B.37 and B.38. Figure B.38 also shows an interfacial fold boundary with a large amount of porosity on both sides which has a characteristic width of ~100nm with a periodicity of ~100nm. At the edge of samples the microstructure appears to splay into small tendrils, Figure B.39. This is shown most dramatically in Figure B.40 where the material resembles a fern leaf that is apparently formed by splays about a fold boundary. These features are likely to be the result of selective oxidation removing material from more reactive regions.

5.3 SUPPORTING EVIDENCE FOR THE EXISTENCE OF FINE POROSITY

The TEM, results have provided much evidence to support the existence of plentiful amount of nanometric scale porosity. However, it is also impossible to exclude the possibility that the structure viewed by TEM is an artefact of the sample preparation route. To explore this possibility the surface of unprepared samples (simply washed) of AGR moderator graphite were also viewed using Atomic Force Microscopy (AFM). The principle of the AFM is discussed by Cohen *et al.* (1993). An atomically fine tip is first brought into contact with the sample. As this tip is moved across the sample surface, under a constant force, it deflects in response to the surface topology. This deflection is detected by the displacement of a laser beam reflected from the back of the tip, enabling a map of the surface topology to be generated. For this work a Digital

Instruments III AFM was used with a silicon tip. As the graphite surface consists of loose flakes the instrument was operated in the tapping mode (Binning *et al,* 1986). This technique involves oscillating the tip to and from the sample surface with an amplitude of 10-100 nm such that the tip "taps" the sample at the bottom of each oscillation. This method has the advantage of minimising contact induced distortion of the sample surface and prevents the tip becoming trapped (by capillary forces) in surface contaminants.

A typical AFM result is shown in Figure B.41. The image shown in the bottom left corner of the figure has been analysed along the indicated line. Thus, qualitative topographical information along this line is presented in the graph in the top left corner of the image. The horizontal and vertical distances, between each set of markers displayed on the image and on the line analysis, are also displayed. These red and green markers indicate features that can be identified as cracks ~10 and 18 nm wide respectively, and with a spacing of ~160 nm, in support of the TEM findings.

5.4 SUMMARY OF MICROSCOPY STUDY

As viewed by optical microscopy the structures of AGR and Magnox moderator graphites show marked differences. The constituent components used in manufacture, the large filler coke particles and the finer flour and binder pitch are visible as different carbonaceous phases. As viewed by SEM, structural differences are also apparent between the phases and differences also appear when the samples are oxidised. At the TEM scale, however, very few differences exist between both grades of graphite. The general structure is fibrous and continuous with small circular features visible in both materials. Large amounts of nanometric scale porosity, of different sizes, exist within each material. The existence of this fine porosity has been confirmed by the imaging of the unprepared surface of AGR moderator graphite by AFM.

These microscopy results are discussed further in chapter 9 where they are used in the generation of a description of the effects of thermal oxidation on the microstructure of AGR and Magnox graphites with respect to changes in CTE.

CHAPTER 6

THE MEASUREMENT OF THERMAL EXPANSION

This chapter contains a discussion of the measurement technique, mechanical dilatometry that was identified in the introduction as the most suitable method for measurement of CTE in these materials. Due to the extensive use of this technique in the work that follows, a comprehensive commissioning, calibration and evaluation process has been conducted to ensure the quality of the experimental output. The process has been developed with reference to relevant British and American test standards, the primary reference being ASTM E 228-85 "Standard Test Method for Linear Thermal Expansion of Solid Materials With a Vitreous Silica Dilatometer". These processes will be discussed here in detail and have resulted in the production of an experimental method statement for the measurement of these materials by mechanical dilatometry (Hacker and Neighbour, 1999).

The basic principle behind mechanical dilatometry is the measurement of a linear length change of a sample as it is being heated (or cooled) by the use of a push-rod in contact with the sample, the movement of which can be recorded. The recorded measurement, therefore, is of the length change (or dilation) as a function of the sample temperature.

6.1 THE INSTRUMENT

The instrument used in this work is a Netzsch Instruments Dilatometer, Model 402C, Figure B.42. The experimental layout is shown schematically in Figure B.43 and consists of the dilatometer main measurement unit, a power unit and controller, a thermostat, vacuum pump and a computer. The measurement unit, Figure B.44, consists of the sample holder (containing the push-rod and thermocouple), the measurement system (to which the push rod is attached) and the furnace, the latter is free to slide over the sample holder by being positioned on runners.

The sample holder and pushrod are manufactured from fused silica, and are pictured in Figure B.45 and shown schematically in Figure B.46. The push-rod extends axially along the length of the sample holder. The sample is placed in the end of the sample

holder as shown in Figure B.45. A schematic of the measurement system is shown in Figure B.47. The pushrod is bought into contact with the sample automatically and a small constant force (~1cN) is applied via the contact spring. Subsequent linear motion of the pushrod is converted to a voltage by the inductive length measurement system. The instrument allows a maximum sample length of 30mm and a practical maximum sample width of ~15mm to avoid fouling the thermocouple.

The controller acts as an interface between the computer, the software of which controls the operation of the furnace and receives data from the measurement unit. The controller powers the furnace to ensure that the temperature programs are followed and also displays the status of the instrument.

The thermostat maintains the temperature of the water circulating around the housing of the measurement unit. This ensures that the thermal expansion of elements within the measurement system, that could affect the measured dilation, is kept to a minimum as the experiment is conducted. The vacuum pump is used to conduct measurements under vacuum by connection to the measurement unit end of the sample holder.

6.1.1 Operation Overview

Operation of the instrument commences with placing of the sample (of an appropriate size) in the sample holder. Samples are machined to ensure that the ends are parallel to minimise movement of the sample perpendicular to the push-rod during measurement. For samples of small diameter (< 10 mm) fused silica sample rests can be placed within the sample holder to ensure that the sample and push-rod assembly is maintained in its axial orientation during measurement. The push-rod is then bought into contact with the sample automatically using the command switches on the front of the instrument. The furnace is then positioned over the push-rod and screwed on to the instrument body at the measurement end. Air is evacuated using the vacuum pump that remains on during the experiment and the vacuum is allowed to stabilise (at ~3mbar) before measurement commences. Before sample measurement, a calibration run is conducted on a known reference material, the results from which are used by the computer software to correct

the measured expansion in subsequent measurements, as discussed in the following section.

The remaining operation is now conducted using the computer software. First the measurement and sample information is input and the type of measurement (calibration or sample) is chosen. Finally, the temperature profile is specified as a series of segments. Each segment is either dynamic (*i.e.* a temperature ramp) or isothermal (*i.e.* a hold at temperature), Figure B.48. The determination of an appropriate temperature profile for accurate yet expedient measurements of CTE in nuclear graphites is discussed in a following section.

6.2 CALIBRATION

A discussion of the errors associated with the measurement of thermal expansion by thermomechanical techniques is given by Riga *et al.*(1991). They conclude that the total error on an average CTE measurement ($\delta\alpha$) is given by the following relationship

$$\frac{\partial\alpha}{\alpha} = -\frac{\partial L_0}{L_0} + \frac{\partial(\Delta L)}{\Delta L} - \frac{\partial(\Delta T)}{\Delta T} \qquad [B2]$$

which corresponds to the errors on the measurements of initial length, L_0, the sample expansion, ΔL and the temperature measurement ΔT.

The measurement of L_0 with a micrometer can be conducted with an error of less than 10μm when L_0 is >10mm. Riga *et al.* (1991) conclude that the error on CTE in this case is less than 0.1% and is deemed insignificant by them in comparison to the other sources of error. This assumes that the sample geometry is regular and that the sample is machined with flat, parallel faces perpendicular to the axis of the sample holder. The effect of an error on ΔT is also generally less than that of ΔL. In the case of the current instrument, the temperature measurement had been calibrated by the manufacturer before shipment and during commissioning.

The error on ΔL can be minimised by calibration using a crystallographically cubic certified material whose relative expansion and length are similar to that of the test material (ASTM E 228-85). The details of the calibration methods used in the Netzsch software are described in Appendix 1. Within this work, either an alumina (or quartz for Magnox moderator graphite in the parallel direction as the instantaneous CTE of quartz at 600°C is 0.5 x 10^{-6} K^{-1}) standard was used. Sapphire and tungsten standards were also supplied and used as additional reference materials for initial commissioning purposes. These standards were certified by the supplier to be at least 99.96% pure. Each standard (with the exception of quartz) was supplied as a cylinder 6mm ∅ by 25 mm length.

The quartz standard was originally supplied as a 6mm ∅ by 50mm length sample and as a certified standard material. That is, the piece of quartz was individually measured by a standards authority in Germany (at the "*Physikalisch-Technische Bundesanstalt*", Braunschweig) and a certified expansion table supplied. Unfortunately, the length of this standard was too great for the current instrument. Therefore, the standard was carefully cut to maintain parallel edges. One of these pieces was subsequently tested by Netzsch in Germany and the expansion compared to the original certified expansion tables with negligible differences.

The alumina and sapphire standards were supplied as "secondary standards". That is, samples from the same manufacturing lot were tested by the supplier and the expansion tables of such samples supplied with the material. The tungsten standard was supplied as a "normal standard", whose expansion is referenced to expansion tables provided as a part of the computer software.

The dilatometer control software ensures that the calibration run is conducted using the same heating profile as that of the specimen. Once a calibration run has been undertaken the software allows the calibration curve to be used to calibrate any subsequent sample measurement. Calibration was undertaken regularly to ensure that the accuracy of the instrument was maintained.

6.3 COMMISSIONING

In order to measure the accuracy and reproducibility of the instrument a commissioning programme was undertaken. However, before the start of such a programme it is necessary to first determine the temperature profile to which samples should be subjected. The relevant standards (*e.g.* ASTM E 228-85) dictate that the sample heating (or cooling) rate should not exceed 3^0C per minute and also specifies maximum tolerances for transducer variation (<±2.6 μm), the specimen temperature variation (±2°C) and the temperature gradient in the specimen (0.5°C) per centimetre. Practically, this requires that thermal equilibrium is attained at isothermal stages and quasi-static thermal equilibrium is maintained during the heating and cooling phases, *i.e.* temperature gradients across the sample are not created and that sample heating/cooling rates follow furnace heating/cooling rates.

In order to decide upon a suitable heating profile, the quartz standard was measured over two thermal cycles (only corrected by the native sample holder correction term) with heating rates of 1, 3 and 5°C per minute. Each rate was also tested with different hold times at temperature. The resulting dilations curves were compared by smoothness and accuracy to the tabulated value of the quartz standard. From this information, heating/cooling rates of 3°C per minute with a hold at temperature of 30 minutes and a hold between thermal cycles of 120 minutes were chosen, Figure B.48. Each heating segment of the dilation curves produced by the dilatometer are readily identified as follows.

- Green Curve - First Heating Segment.
- Blue Curve - Second Heating Segment.
- Red Curve - First Cooling Segment
- Purple Curve - Second Cooling Segment

The set of standards obtained enabled the accuracy of the instrument to be determined with confidence by the testing of standards by calibration with each other and referencing the output to given expansion tables. In these cases, the average CTE values were derived from the second heating cycle, although the difference between heating

cycles for these materials was negligible *e.g.*, Figure B.49. The expansion of sapphire, tungsten and alumina were therefore measured by calibration with alumina. In each case, the difference in average CTE of the measured and tabulated values over the temperature range 20-600°C was small (Table B.2). An example dilation curve for the measurement of the alumina sample (corrected with an alumina calibration) is shown in Figure B.50, compared to the supplied expansion data.

Material	**Measured CTE (x 10^{-6} K^{-1})**	**CTE from expansion tables (x 10^{-6} K^{-1})**	**Difference (%)**
Sapphire	8.125	8.281	1.92
Tungsten	4.805	4.874	1.44
Alumina	7.887	7.798	1.12
Quartz	0.578	0.566	2.12

TABLE B.2: Measurement of CTE standards.

Thus, over the temperature range 20-600°C the dilatometer can be characterised as producing results to an accuracy of greater than ~2%, even for samples with low expansions. By studying Figure B.50, this inaccuracy reduces substantially as the temperature increases and is negligible above ~150°C. Further, the reproducibility of the instrument was tested by repeating the above measurements three times and extracting the average CTE over the same temperature range (20-600°C), the results and standard deviations are shown below in Table B.3 which demonstrates the good reproducibility of the dilatometer in the measurement of CTE values.

Material	CTE (1) ($x\ 10^{-6}\ K^{-1}$)	CTE (2) ($x\ 10^{-6}\ K^{-1}$)	CTE (3) ($x\ 10^{-6}\ K^{-1}$)	Mean	Standard Deviation (%)
Sapphire	8.1253	8.1355	8.1252	8.1286	0.07
Tungsten	4.8053	4.8212	4.8050	4.8105	0.19
Alumina	7.8872	7.8879	7.9073	7.8941	0.14
Quartz	0.5781	0.5792	0.5686	0.5753	1.01

TABLE B.3: Instrument Reproducibility.

During the course of the experimental programme the instrument was recalibrated after approximately ten measurements. Negligible differences were found between each calibration measurement, both in the nature of the calibration curve and in the average values of CTE obtained.

In summary, the commissioning programme demonstrated the satisfactory performance of the dilatometer in the measurement of materials with a wide range of CTEs. Thus, for all samples, the temperature profile shown in Figure B.48 was adopted for all subsequent CTE measurements.

CHAPTER 7

THE MEASURMENT OF CTE AND PORE VOLUMES OF AS RECEIVED AND OXIDISED NUCLEAR GRAPHITES

Within this chapter, the dilation response of as received graphite samples of Magnox and AGR moderator graphites over two thermal cycles are presented followed by the effects of thermal oxidation on the CTE of these materials. Due to the suggested relationship between small scale porosity and CTE, the effects of oxidation on the pore volume of AGR moderator graphite specimens are also presented with particular emphasis placed upon the behaviour of closed porosity. In addition to the effects of oxidation, the Closed and Open Pore Volume (CPV and OPV) of a range of different grades of as received AGR moderator graphite has been measured and correlated to CTE.

The dilation curve provides the most complete description of the thermal expansion behaviour of a particular sample. Although computation of an average CTE value from such curves is often desirable as it allows rapid comparisons to be made. However, differences are often observed between the first and second heating cycles in these materials (*e.g.* Slagle (1969)). In these cases, questions remain such as: from which cycle should CTE values be derived? The first objective of the dilatometry programme is to characterise experimentally the thermal expansion behaviour of as-received samples of AGR and Magnox moderator graphites. The CTE values derived from such curves can also be used as references for later aspects of the experimental programme.

From the literature review in Part A, CTE is shown to be insensitive to radiolytic and thermal oxidation to weight losses up to ~20%. However, as discussed, one may intuitively expect some change at very high weight losses. A study examining changes in CTE to high weight losses will not only present new and useful data on the behaviour of CTE at high weight losses but should also provide information enabling a deeper understanding of CTE in these materials to be made.

7.1 THERMAL EXPANSION OF AS-RECEIVED NUCLEAR GRAPHITES

The thermal expansion of five samples of AGR moderator graphite and five each of Magnox moderator graphite in the directions Parallel and Perpendicular to extrusion were prepared. Their expansions were measured over two thermal cycles using the procedure discussed in the previous Chapter. Two dilation curves are shown in each of Figures B.51(a and b), B.52(a and b) and B.53(a and b) for AGR and Magnox moderator graphites, the latter in the directions Parallel and Perpendicular to extrusion, respectively. These figures are those curves with the smallest and largest difference between thermal cycles respectively. The average CTE values for each segment over the low and high temperature ranges (as defined in the Introduction, section 0.2) are shown in Table B.4 and the corresponding mean values (and spread) are shown in Table B.5.

Sample	CTE (Low Temp Range) $*10^{-6}$ K^{-1}				CTE (High Temp Range) $*10^{-6}$ K^{-1}			
Number	1st Heat	1st Cool	2nd Heat	2nd Cool	1st Heat	1st Cool	2nd Heat	2nd Cool
Magnox								
Parallel								
PGA Para 1	0.6908	1.2381	0.7654	1.2596	1.9091	2.1734	2.0841	2.1986
PGA Para 2	1.1635	1.313	0.7567	1.3295	2.2425	2.2426	2.1659	2.2708
PGA Para 3	1.2723	1.3824	0.8891	1.4583	2.2819	2.3355	2.2799	2.3598
PGA Para 4	1.1334	1.3162	0.8223	1.3611	2.2722	2.2487	2.1799	2.2737
PGA Para 5	1.1138	1.3657	0.835	1.4006	2.3364	2.3467	2.256	2.36
Magnox								
Perpendicular								
PGA Perp 1	3.4109	2.4757	3.5166	2.5619	4.5548	4.1977	4.2759	4.1812
PGA Perp2	3.3121	2.2899	3.441	2.4051	4.3182	4.1332	4.1677	4.1711
PGA Perp3	3.201	2.3197	3.4224	2.3874	4.2983	4.0427	4.113	4.0072
PGA Perp4	3.286	2.2793	3.4018	2.3652	4.3166	3.9998	4.066	3.9745
PGA Perp5	3.2991	2.2877	3.412	2.3712	4.3211	4.0112	4.096	4.0101
AGR								
AGR 1	5.413	5.82	5.414	5.877	6.404	6.503	6.3768	5.509
AGR 2	5.306	5.403	5.072	5.459	6.192	6.402	6.2291	6.378
AGR 3	5.022	5.68	5.181	5.724	6.203	6.677	6.424	6.638
AGR 4	4.973	5.46	5.142	5.505	6.043	6.282	6.147	6.302
AGR 5	4.019	5.63	5.256	5.683	6.274	6.64	6.3975	6.564

TABLE B.4: The CTE of as received graphites over two heat cycles.

Graphite	CTE (High Temperature Range, Second Heat Segment) x 10^{-6} K^{-1}			CTE (Low Temperature Range, Second Heat Segment) x 10^{-6} K^{-1}		
	Mean CTE	Lowest CTE	Highest CTE	Mean CTE	Lowest CTE	Highest CTE
AGR	6.315	6.147	6.424	5.202	5.073	5.412
PGA Parallel	2.193	2.084	2.280	0.814	0.757	0.889
PGA Perpendicular	4.144	4.066	4.276	3.439	3.402	3.517

TABLE B.5: Average CTE of as received graphites (second heating segment).

The difference in dilation behaviour, both between heating and cooling cycles and between thermal cycles, is fully discussed in Chapter 9. Here it is noted that, for the AGR moderator samples, if a difference between segments exists, it is between the first heating segment and the remaining segments. The remaining segments are generally bunched closely together. When considering the segment from which to derive average CTE values, from the perspective of reproducibility, the second heating segment should be selected, at least in the case of AGR graphite. For Magnox moderator graphite, the situation is less clear as significant differences are shown between both heating curves. However, the cooling curves are generally closely related for samples in both the Parallel and Perpendicular directions. The average CTE values in the low temperature range compare closely to those given in the introduction (Tables 0.1 and 0.2), with the exception of AGR moderator graphite which is ~0.7 x 10^{-6} K^{-1} higher. For the Magnox moderator graphite samples measured in the parallel direction, the initial expansion between room temperature and ~120°C is also extremely low resulting in the dilation curve deviating significantly from linearity.

7.2 THE CTE OF THERMALLY OXIDISED GRAPHITE

For each of the samples prepared by thermal oxidation (as discussed is chapter 4, section 4.1) thermal dilations were measured using the established procedure detailed in the previous chapter. For this work, it is changes in CTE with oxidation that are of interest. Therefore Figures B.54(a-c) show plots of the average CTE ($\alpha(20,600)$), normalised by the average unoxidised CTE, versus corrected weight loss after thermal oxidation for AGR and Magnox moderator graphites in the Parallel and Perpendicular directions,

respectively. For both AGR and Magnox moderator graphite in the Parallel direction, values of $\alpha(20,600)$, remain essentially constant over the weight loss range considered with the scatter of data being greater for the Magnox graphite. However, for Magnox moderator graphite measured in the Perpendicular direction, values of $\alpha(20,600)$ show a rise with increasing weight loss. In order to confirm this effect, CTE values for a selection of these samples were re-measured. Overall, the results were consistent with the first set of measurements, except that in every case the repeated measurements were greater than the first by approximately 10%.

Further consideration of the CTE of oxidised Magnox graphite in the perpendicular direction (Figure B.54(c)) reveals that, if the samples below 10% weight loss are excluded, there appears to be no further change in CTE at weight losses > 10%. That is, a step increase exists between the CTE of samples oxidised below 10% and those oxidised above 10%. To test this difference statistically, the data in Figure B.54(c) were split into two populations, those below and above 10% weight loss respectively. Hypothesis testing was then used to compare the two datasets (the method is given in Appendix 3). This concluded that, at the 5% significance level, the two datasets were from different populations.

An increase in CTE with oxidation is difficult to explain. As oxidation proceeds, porosity is being developed therefore a decrease is expected as more accommodation is offered to expanding crystallites before transmission of expansion to the bulk. It is more likely that the apparent increase in CTE is an artefact of the experimental process. After oxidation to weight losses > 10% samples of Magnox graphite are extremely friable and shed material readily on handling, altering the sample geometry. Upon measurement of Magnox graphite it was also noticed that there were fragments of the material within the dilatometer. The loss of material from the sample is likely to reduce the initial length (L_0) from that measured before placement into the dilatometer, leading to an apparent increase in RLC ($\Delta L/L_0$), and hence CTE. This is also consistent with the observation that the CTE of re-measured samples increased from that measured initially. Re-measured samples, that have been handled extensively, are likely to have shed additional material, further reducing the L_0 value from that originally measured. In the case of Magnox samples measured in the parallel direction, the lack of an obvious similar

increase in CTE as a result of material shedding can be explained by such an increase being masked within the scatter of data. Also, material is more likely to be shed perpendicular to the long axis of the needle coke grains within Magnox graphite, preserving the length of sample orientated in the parallel direction.

7.3 THE MEASUREMENT OF THE PORE VOLUMES OF GRAPHITE SAMPLES

The closed and open pore volumes of the oxidised AGR graphite samples were measured using a Micrometics AcuPyc 1330 helium pycometer. The method of obtaining pore volume data via pycnometry is discussed in detail by Tomlinson *et al.* (1999). The sample is surrounded with helium gas in a closed cell that, under pressure, penetrates the entire open pore network (without being absorbed on the surface). The output from the pycnometer is the helium volume, V_{He}, required to fill the open porosity. As the sample mass is also measured the "helium density", ρ_{He}, (defined as *sample* mass divided by the displaced *helium* volume) can also be computed. In this case, it can be shown (Tomlinson *et al.*, 1999) that the CPV and OPV (as percentages of the sample volume) can be computed from the following

$$CPV = \left[\left(1-\frac{\rho_{He}}{\rho_c}\right)\left(\frac{\rho_B}{\rho_{He}}\right)\right]\times 100 \qquad OPV = \left[\left(1-\frac{V_{He}}{V_B}\right)\right]\times 100 \qquad \text{[B3 a,b]}$$

where ρ_B is the bulk density of the sample and ρ_c is the single crystal density (assumed to be 2.26 g.cm^{-2}). A plot of the CPV against sample weight loss is shown in Figure B.55, where an exponential fit is seen to be more appropriate than a linear one (lower R^2 value, Lyons (1993)). For completeness, the OPV is shown and this increases linearly with weight loss.

In addition to an examination of the effects of oxidation on CPV, the correlation between the CPV and CTE of as received AGR graphite samples was also studied. Ten different bricks of archive graphite were used (each of archived material from different reactor stations). From each brick, six samples (8mm ∅ by 12mm in length) were

machined. The CPV of each sample was measured as discussed previously and the CTE over two thermal cycles was obtained, as discussed in the previous Chapter with $\alpha(20,600)$ being computed for the second heating segment. Figure B.56 presents the correlation between CTE and CPV as a mean value for each block together with "error bars" representing the standard deviation of the CTE and CPV values for the six samples measured within that block. Although the "error bars" are wide, a decrease in CTE is observed with increasing CPV. The significance of this result is discussed in a wider context in chapter 9, but here it is noted that CTE appears to be sensitive to porosity created during manufacture rather than to porosity created during oxidation.

7.4 SUMMARY

Within this chapter, CTE measurements of both as-received and oxidised AGR and Magnox moderator graphites have been made. Within the as-received materials differences were observed between heating and cooling segments. These differences were small for AGR moderator samples, where, in general, the largest difference occurs between the first heating segments and the remaining segments. For Magnox moderator graphites these differences are usually much larger. The dilation response of Magnox moderator graphite in the parallel direction is also very low to ~120°C, resulting in a significant deviation from linearity in the dilation curve.

It has been found that oxidation does not effect the CTE of AGR graphite to weight losses up to ~60%. Also, the CTE of Magnox moderator graphite in the parallel direction appears to be unaffected by thermal oxidation to ~40% weight loss and the CTE of this material in the perpendicular direction only shows a small increase at low weight losses. The CPV of these samples was also measured and was found to decrease exponentially. In addition to the oxidised samples, the CTE and CPVs of as-received AGR graphite taken from different reactors has been measured. As CPV increases CTE broadly decreases. These results are discussed further in chapter 9.

CHAPTER 8

STRUCTURAL DISRUPTION AND RELAXATION EFFECTS

The decrease in the value of CTE as a function of neutron irradiation has been attributed to "structural disruption" (Jenkins, 1964) or, "crystallite re-arangement" (Kelly, 1992b). This is thought to occur when porosity in the locality of expanding crystallites can no longer contain localised stresses which then disrupt the bulk structure. It may be possible to test this theory experimentally by simulating this structural disruption by a process other than irradiation. As shown by Platonov *et al.* (1979) (and discussed in chapter 1, section 1.3) high heat treatment temperatures can be expected to alter the CTE of nuclear graphites by the reduction and subsequent reformation of accommodating porosity. Computing the temperature related crack closure for graphite heated to 2000°C (using the model given in chapter 3, section 3.2) suggests that this temperature increase may have the general effect of closure of porosity equivalent to a dose of ~50 x 10^{20} n/cm^2 (EDN). Therefore, some decrease in CTE from the as-received value could be observed.

8.1 THE EFFECTS OF HEAT TREATMENT

Five samples of AGR graphite (of the same type and dimensions as those described previously) were prepared in an Astro Industries furnace by heating to 2000°C in a helium atmosphere. The samples were heated at 20°C per minute and held at temperature for 30 minutes. Automatic temperature control of the furnace was not possible therefore for the first two samples the furnace was simply switched off after the hold time resulting in rapid cooling. These rapidly cooled samples exhibited a warped geometry and therefore the accuracy of the determination of initial length and the ability to seat the sample correctly in the dilatometer were reduced. An example dilation curve is shown in Figure B.57(a). For samples three, four and five the furnace power was reduced manually, resulting in a much lower cooling rate (estimated at about 10°C per minute to ~1000°C). An example dilation curve is shown in Figure B.57(b).

The results of the CTE values taken from the second heat cycle (high temperature range) are shown in Figure B.58 in comparison to the average of the as-received samples. The CTE results for heat treated samples cooled rapidly are within the scatter of results from the as received samples. However, the CTE values for the heat treated samples cooled more slowly are all below the lower bound of the CTE values of the as-received samples. In the case of the slowly cooled samples, this supports the hypothesis that some internal structural disruption has occurred that has affected CTE after thermal closure of accommodating porosity and is consistent with the description of the decrease in CTE under neutron irradiation (see Figure A.8 and chapter 3, section 3.3).

This experiment was repeated for Magnox graphite using samples in the perpendicular direction, Figure B.59. In this case, all of the results remained within the bounds of the as-received samples, indicating that any structural disruption that may occur does not alter CTE. This is also consistent with the behaviour of Magnox graphite under neutron irradiation where, after an initial rise at low doses, CTE is unaffected by neutron irradiation until high fluences (see Figure A.9 and chapter 3, section 3.3).

8.2 PRE-STRESS RELAXATION

Although the effects of pre-stress have been discussed in chapter 1, section 1.5, the possible relieving of these effects as a function of time or thermal cycles has not been fully addressed. The question of the permanency, or otherwise, of such effects is important in determining the behaviour of the material as it ages within the reactor core but also serves to further the understanding of the accommodating porosity within these materials.

An experimental programme has been conducted to explore the effects on CTE of pre-stressing samples that are allowed to relax over time. Samples of AGR graphite (18 mm length by 12 mm diameter) were pre-stressed to 90% of the failure load as determined by first measuring the failure load for three samples, an example load-deflection curve is shown in Figure B.60. An average failure load of 9.72 kN was found, corresponding to a 90% pre-stressed load of 8.75 kN. After pre-stressing 3 sets of 4 samples the CTE of each was measured after approximately 0, 10, 100 and 100 hours. Average CTE values

were determined for each segment of the thermal cycle between room starting temperature (~25°C) and 600°C.

In each case, the dilation over the first heating segment was significantly different from the expansion over subsequent heating and cooling cycles, *e.g.* Figure B.61. After the CTE measurement, a small increase in length was recorded (from that after pre-stressing) ranging from 0.01 to 0.06 mm, in rough agreement with the length changes observed between the first and second heating cycles in the dilatometer. A plot of the average CTE ($\alpha(20,600)$) for both the first and second heating segments as a function of time (on a log scale) is shown in Figure B.62 and indicates only a small recovery in CTE with time. However, a significant reduction in CTE is observed from the first to second heating cycles. These results imply that the effect of a large amount of the applied pre-stress is recovered during the first heating cycle, which is manifested as a strain recovery. This work extends, and the results are consistent with, the work of others, *e.g.* Gurein (1998), who showed qualitatively that CTE increases under a pre-stress. The results are also consistent with the crack closure theory describing an increase in CTE given by Matsuo and Sasaki (1981) and discussed in chapter 1, section 1.5.

8.3 SUMMARY

The structures of AGR and Magnox moderator graphites have been disrupted by high heat treatment in an attempt to simulate the effects of neutron irradiation on the CTE of these materials. After heating graphite samples to 2000°C and cooling slowly a decrease in CTE is observed for AGR graphite samples whereas Magnox graphite samples (in the Perpendicular direction) remain unchanged. This is consistent with the CTE behaviour of these materials as a function of neutron irradiation and supports the qualitative microstructural description of the effects of neutron irradiation on CTE given in chapter 3, section 3.3.

The results of the compressive pre-stressing experiment show that some recovery of CTE occurs over time. However, the observation of large differences between the first and second heating segment suggest that CTE, pre-stress and temperature induced recovery of strain are highly dependent upon each other.

The following chapter develops descriptions for these results and those of the entire experimental programme. These are used to identify the critical microstructural elements that control CTE in order to enable the generation of a new microstructural based model of CTE in nuclear graphites.

CHAPTER 9

THE EXPERIMENTAL RESULTS - A DISCUSSION

The theme of the experimental work described in this part of the thesis has been to examine changes in CTE in response to induced microstructural changes. This has been done with a view to simulating the effects of exposure of graphite to the reactor environment, *i.e.* neutron irradiation and radiolytic oxidation. This has been conducted in response to the theoretical work described in Part A and the need to define the nature of a microstructural model of CTE that is to be developed in Part C.

The purpose of this discussion chapter is to apply the observations obtained from the experimental work to produce microstructural descriptions of observed CTE behaviour under radiolytic oxidation and neutron irradiation. The discussion begins by generating a qualitative description of thermal oxidation in AGR and Magnox graphites. This section continues by discussing the structural changes observed as a result of thermal oxidation to those expected from radiolytic oxidation. Further, a new microstructural explanation of the insensitivity of CTE to oxidation is generated, the Continuous Network Hypothesis. Parallels are drawn between this description and percolation theory, the latter being generally applicable when studying issues of material connectivity. The discussion then turns to the simulation of the effects of irradiation by heat treatment, together with a discussion of relaxation effects over time and thermal cycles.

9.1 SEM AND TEM MICROSCOPY OF AS-RECEIVED AND OXIDISED GRAPHITES

For both Magnox and AGR moderator graphite thermal oxidation appears to disrupt the binder phase preferentially to the filler phase and this is in agreement with the conclusions of other workers using optical microscopy (*e.g.* Pickup *et al.*, 1986). This preferential disruption can be explained by the existence of smaller crystallographic domains being present in the binder regions of the material and therefore a greater number of reactive "edge-sites". As discussed in Part A, (chapter 1, section 1.4) Feates *et al.* (1970) studied the thermal oxidation of graphite single crystals (by various gases)

and identified the reaction mechanism as consisting of a certain amount of in-plane pitting with most of the gasification occurring at edge sites. Therefore, under conditions of minimal reaction, the diffusion of active species across basal planes to reactive edge sites limits the oxidation rate. Indeed, evidence for pitting and basal plane attack have been presented here, *e.g.* Figure B.8.

9.1.1 Qualitative Description of Thermal Oxidation in AGR and Magnox Graphites

These SEM studies allow a qualitative description of the thermal oxidation of AGR and Magnox moderator graphites to be made. The effects of thermal oxidation are similar for both materials with the identification of several key stages. In Magnox moderator graphite, oxidation up to 15% weight loss produced selective attack within the binder phase with evidence of etching along the graphitic planes and pitting within the planes. As oxidation proceeds the transport porosity is observed to open rapidly by attack along fissures from gas evolution pores. Small filler particles are attacked readily, leaving larger ones isolated. At weight losses >30%, filler particles reduce in size with enlargement of the calcination and shrinkage cracks, large scale disruption of the binder is apparent with the creation of a continuous porosity network. Above 40% weight loss, the connectivity of the structure is progressively destroyed. Although the oxidation mechanism in AGR moderator graphite is similar to that in Magnox graphite, differences are observed. In particular, significant enlargement of the calcination cracks in the filler particles did not occur until ~25% weight loss and these particles preserved their integrity until ~40% weight loss. Also, in general, the filler binder-interface remains intact to weight losses > 40%.

This description of thermal oxidation effects can also be extended to the structural changes occurring on the TEM scale. This study has shown that the nanometric microstructures of both graphites contain similar features. The predominant feature is an extended network of ribbons consisting of graphitic stacks separated by fine lenticular cracks. Also seen in both types of graphite are circular features, that exist in both filler and binder regions. The lenticular cracks may be identified with Mrozowski cracks. These TEM observations are in broad agreement with those of Sutton and

Howard (1962) who found ~30 nm sized cracks with a periodicity of 500 nm. However, the present work shows that this description is rather simplistic since Mrozowski cracks exist in a range of shapes and sizes and they are not confined to a small size distribution implied by the results of Sutton and Howard.

Historically, Mrozowski cracks have been defined by size and periodicity *i.e.* by following the suggestion of Sutton and Howard (1962). This microscopy work has shown that it may be better to define them based upon their *formation.* Indeed, this approach is based upon the original description given by Mrozowski (1956). Therefore, it is suggested that Mrozowski crack porosity be defined as porosity created *during manufacture* by virtue of the *differential thermal expansion and relative orientation of crystallites* and acts to accommodate local expansions, before transmission of strain to the bulk. This is also supported by the discussion of the Mrozowski crack closure model given in chapter 3, section 3.2 that suggests Mrozowski cracks should exist in a wide size range up to ~25 nm in width.

TEM has provided some indication that the size and density of Mrozowski cracks in AGR moderator graphite do not change during thermal oxidation. For Magnox moderator graphite the effects of thermal oxidation on the size and density of Mrozowski cracks are less clear. Importantly, the structure of nuclear graphites on the crystallite scale is continuous and far different from the loose assembly of single crystals model discussed in chapter 1, section 1.2.

9.1.2. Radiolytic Oxidation.

Only a limited amount of information on the effects of radiolytic oxidation on the microstructure of nuclear graphite is available, as discussed in chapter 2 section 2.3. For example, Murdie *et al.* (1986) showed that, for AGR graphite, gasification occurred in the pore size range <100 μm cross sectional area (csa) and, in particular within pores < 2 μm csa. Pores larger than this showed little change due to inhibition of the oxidation by CH_4 in the oxidising gas and were only developed at weight losses > 17%.

In contrast to the effects within the polygranular material, much information exists on the radiolytic oxidation mechanism on the atomic scale. Both Feates (1968) and Henning (1966) suggest that the primary mass loss mechanism in the radiolytic oxidation of graphite is via diffusion of the active species (suggested by Best *et al.* (1985) to be the reactive CO_3^- ion) to the reactive edge sites facilitated by a small amount of in plane pitting. This view has been reinforced by the molecular simulations of Leary *et al.* (2000) who have modelled the radiolytic oxidation process using molecular dynamics and quantum theory.

Thus, it appears that on the atomic scale both thermal and radiolytic oxidation proceed via similar mechanisms. *i.e.* a small amount of basal plane pitting followed by diffusion of the active species to the reactive edge sites. In this case, the differences between the microstructural effects of radiolytic and thermal oxidation are due, primarily, to the effects of the inhibition of the active species by CH_4, in the case of radiolytic oxidation. This has the net effect of restraining the size of porosity that is developed with corresponding differences in the degradation of mechanical properties between thermal and radiolytic oxidation. Indeed, these views have been supported by the work of Alain *et al.* (2000) and Neighbour *et al.* (1998) who also suggest that thermal and radiolytic oxidation proceed via similar mechanisms.

9.2 THE NATURE OF INTERNAL ACCOMMODATION CONTROLLING THERMAL EXPANSION

Following from the definition of Mrozowski cracks given in section 9.1.1, it is reasonable to assume that they should form part of the porosity closed to oxidising gases, *i.e.* part of the CPV of the material. As such, CTE should be sensitive to the amount of initial closed porosity present in the material, a proportion of which is Mrozowski cracks. This view is consistent with Figure B.56 that indicates an inverse correlation between CPV (of the as-manufactured samples) and CTE. Further, Figure B.55 indicates that even at high weight losses some closed porosity remains. Thus, by implication, it is also likely that Mrozowski cracks also remain.

The presence of Mrozowski cracks within closed porosity is also consistent with CTE being unaffected by oxidation. By implication, if it is assumed that porosity closed to thermal oxidation is also closed to radiolytic oxidation, CTE will remain unaffected in both cases. In this instance, the precise nature of the oxidising mechanism is irrelevant as far as the effects of oxidation on CTE are concerned. Therefore, any microstructural description of the insensitivity of CTE to thermal oxidation is likely to be valid in the radiolytic case and *vice versa.*

From the microscopy presented in chapter 5 it has become apparent that it is not useful to attempt to attribute the thermal expansion behaviour of these materials to constituent elements of the material such as binder, filler or impregnant. The TEM study has shown that, for structure on the nanometric scale, these manufacturing elements can no longer be discerned. In this sense, it may be more fruitful to consider the thermal expansion of a graphite sample to be some complex summation of the thermal response of localised connected assemblies of crystallites. However, the suggestion by Okada (1960) that the filler particles play the main role in determining thermal expansion remains reasonable. Filler particles are likely to be the only assemblies that contain a significant amount of crystallite ordering so that their collective behaviour dominates the thermally induced strain of the aggregate.

9.3 THE CONTINUOUS NETWORK HYPOTHESIS

The microscopy study has identified Mrozowski cracks within both AGR and Magnox moderator graphites and the discussion in the previous sections also suggests that Mrozowski cracks are different from the porosity created by oxidation. Further, the former provides accommodation for crystallite *c*-axis expansion and controls CTE. However, on oxidation to high weight losses some Mrozowski cracks must be removed from the material by oxidation due to the massive disruption of the structure (Hacker *et al.* (1999a)). Therefore, if Mrozowski cracks are largely responsible for the low CTE values of nuclear graphites, then it may be proposed that upon oxidation there must remain an excess of Mrozowski cracks present above those required to control CTE. The TEM study presented previously has shown that lenticular (Mrozowski) cracks between graphitic ribbons are ubiquitous in both AGR and Magnox moderator graphite.

There is also no evidence that the density and width of these cracks is altered by thermal oxidation to at least 30% weight loss.

Jenkins (1964) proposed a constant strain model to describe the change in CTE with irradiation for a material without any porosity and assumed that the strain experienced by constituent crystallites is the same as that of the bulk. Jenkins (1964) showed that if localised tensions within the material (caused by anisotropic dimensional changes on irradiation) cannot be relieved by plastic flow, individual crystals will fracture and 'remove' their effectiveness from the expansion of the aggregate. Importantly, Jenkins also showed that in this case, the constant strain approximation continued to apply and that the CTE will not change until the material falls apart.

Extending Jenkins (1964) argument to the case of thermal oxidation, it may be proposed that there are two requirements for CTE to be unaffected by oxidation. The first requirement is one continuous "path" for transmission of thermal strains throughout the sample. The second requirement is that a sufficient density of Mrozowski cracks remains to provide the same amount of accommodation as in the unoxidised material, *i.e.* the accommodation aspects of strain transmission paths remain unaltered. Of course, one may expect a sample to collapse long before the network has been reduced to a single path. This hypothesis is illustrated schematically in Figure B.63 (Hacker *et al.*, 1999b) that represents the unoxidised graphite with many paths in a network connecting both sides of the material. The oxidised graphite is represented with large pores present, and therefore a reduced number of paths available, but still a number of paths survive to transmit thermal strains from one side to the other. As long as one or more paths exist, the same thermal strain can be transmitted through the material. In summary, the continuous network hypothesis assumes that if a sample has retained its integrity after oxidation, it must also have retained a sufficient number of paths through which thermal strains are transmitted and so the CTE remains constant.

This Continuous Network hypothesis can be tested experimentally. The sample size used in the CTE measurement programme for this work was 18 mm x 12 mm diameter. Consider an oxidised sample of the same geometry, but with all the continuous network paths destroyed apart from a thin slab of effectively unoxidised material in the middle,

as shown in Figure B.64(a). The CTE of a thin 'slab' of AGR moderator graphite (15 x 6 x 1.1mm thick), measured along the long axis, was 6.14 x 10^{-6} K^{-1} between ~20 to 600 ^{0}C. This is in close agreement with that measured for the samples of standard geometry. If this thin slab sample represented a continuous network within a sample of standard geometry, then the sample could be said to have an apparent weight loss of ~93%. Imagine further that this thin slab sample is cut into a "S" or "zig-zag" shape so that there was not a direct, linear path between its two end faces, as shown in Figure B.64(b). This sample geometry should exclude the possibility of direct transmission of thermal strains across the sample. The CTE of such a thin "S" shaped thin slab of AGR moderator graphite, measured along the length axis, was 6.16 x 10^{-6} K^{-1} between ~20 to 600 ^{0}C. This is, again, in close agreement with that measured previously for the samples of standard geometry. These simple experiments provide some supporting experimental evidence for the concept of a continuous network for the transmission of thermal strains.

9.4 CONSIDERING THE CONTINUOUS NETWORK HYPOTHESIS AS A PERCOLATION PHENOMENON

A comparison can be made between the Continuous Network hypothesis and percolation theory which describes the connectivity or otherwise of a system (Stauffer, 1984). Percolation theory can be used to describe changes in thermal and electrical properties and is especially powerful in exploring critical phenomena, *i.e.* property step changes. Although the Coefficient of Thermal Expansion (CTE) in nuclear graphites has been shown to be invariant to thermal oxidation, until at least 60% weight loss, the physical relationship between thermal expansion and thermal conductivity can be exploited to link the two and develop a percolation limit that is relevant in both cases (Hacker *et al.*, 2000).

Many introductions to percolation theory can be found in the literature (*e.g.* Stauffer, 1984 and Sahimi, 1983) so only a brief introduction is given here. Consider a lattice (square in this case) where each site is randomly populated, with a probability p, Figure B.65(a). Percolation theory deals with the nature of clusters of occupied sites thus formed. Here, a cluster is a defined as a set of occupied sites in mutual contact.

Physically, these sites can be taken to represent properties of interest, for example the conducting regions of material in a porous solid.

In order to address the critical change problem, the concept of a percolation threshold needs to be introduced. Consider further the square lattice of Figure B.65(a). There will exist some critical probability, p_c , at and above which a continuous network (or a percolating cluster) of sites in mutual contact will exist from one side of the lattice to the other, Figure B.65(b). For all $p>p_c$, a cluster extends from one side of the lattice to the other, whereas for all $p<p_c$ no such cluster exists, Figure B.65(c). However, if a percolating cluster exists, this does not mean that any *particular site* belongs to the percolating network. Another probability, the strength of the percolating network, P, is therefore defined as the probability that a particular site is connected to the percolating cluster. Obviously P is zero when $p < p_c$. If p approaches p_c from above (*i.e.* from a strongly percolating network to the percolation threshold) a general result from percolation theory states, for all lattice types and dimensions, that

$$P \propto (p - p_c)^{\beta} \qquad [B5]$$

where β is a lattice parameter that is related to the nature of the lattice. Currently, the values of both p_c and β can only be determined analytically for a few lattice types (Essam *et al.,* 1987). For other lattice types these values can be approximated by numerical computation on a finite lattice.

Irrespective of the lattice type, Equation [B5] can be applied to existing graphite data to obtain the percolation threshold of the network. This can be done by relating P directly to the physical property of interest. Although this approach cannot be directly applied to the CTE data, percolation theory has been used extensively as a method of modelling both thermal and electrical conduction in different systems (Family and Landau, 1984).

The thermal and electrical conductivities of nuclear graphites can both be shown to follow the same functional relationship to the porosity volume fraction (Neighbour *et al.*, 1999). Therefore, a percolation limit chosen for one must be equally valid for the

other. As no data are readily available for the change in thermal conductivity with thermal oxidation of AGR moderator graphite, the following percolation threshold is derived for data on the electrical resistivity of thermally oxidised AGR moderator graphite (Neighbour *et al.*, 1999).

The material property of interest is the Conducting Volume Fraction of the graphite, (*i.e.* one minus the Total Pore Volume (TPV) of the graphite, the porosity is assumed to be a perfect insulator). This value can be used as a value for p in Equation [B5], the probability that a particular site will be filled with the conducting phase of the material. Therefore,

$$p = (1 - TPV) \qquad [B6]$$

Below p_c no percolation cluster exists, therefore the conductivity is zero. However, above p_c the electrical conductivity, σ, across the network can be shown to be proportional (although not directly) to the probability of an individual site being connected to the percolating cluster (Stauffer, 1985), such that

$$\sigma \propto P^n \qquad [B7]$$

where n is a scaling parameter. Equation [B5] can now be rewritten in a physically more useful way whilst also normalising by the initial conductivity to remove the constant of proportionality as

$$\frac{\sigma}{\sigma_0} = \left(\frac{(1 - TPV) - p_c}{(1 - TPV)_0 - p_c} \right)^{\mu} \qquad [B8]$$

where μ is a parameter dependent on the dimensionality of the lattice. The theoretical relationship between μ and the lattice parameter β of Equation [B5] is unknown (Sahimi, 1984). However, extensive numerical modelling on large lattices has empirically calculated μ to be close to 2.0 for three-dimensional lattices. (Derrida *et al.*,

1984, Zabolitzky, 1984 and Lobb and Frank, 1984). P_c can now be deduced by fitting Equation [B8] to data of resistivity as a function of conducting volume fraction.

The result of fitting Equation [B8] to the electrical resistivity data described earlier is shown in Figure B.66 (with $\mu = -2$), resulting in a percolation threshold at 0.01674 of the conducting volume fraction. This volume fraction can be converted to an approximate weight loss following the method described by Feng and Bhatia (1999). Ignoring any ash component, the following relationship between Conducting Volume Fraction, V and weight loss was given

$$V = (1 - \varepsilon_0)(1 - x) \qquad [B9]$$

where ε_0 is the initial total fractional porosity of the graphite (~0.17) and x is the weight loss. Therefore, for the electrical resistivity data of AGR graphite, Equation [B9] estimates a percolation threshold of ~98% weight loss. This indicates that the graphite must be almost completely oxidised before the percolation threshold for electrical resistivity is reached.

Within this work, the CTE of nuclear graphites has been shown to be insensitive to thermal oxidation to at least 60% weight loss. Percolation theory itself, however, cannot be directly applied to the CTE data. As there is no evidence of a change in property, there can be no calculation of a percolation threshold. However, the results obtained for the percolation threshold for electrical conductivity are relevant for CTE, due to the direct relationship between electrical and thermal conductivities. A constant CTE implies that a constant thermally induced strain is being transmitted across the sample. If the electrical, and hence thermal conductivity, of the graphite has stepped to zero (*i.e.* its percolation threshold has been passed) it is difficult to see how a constant CTE can continue to be obtained. Conversely, a high percolation threshold for electrical conductivity supports the hypothesis that thermal strains can continue to be transmitted and CTE is expected to remain unchanged.

9.5 SIMULATED STRUCTURAL DISRUPTION

The results from the measurement of heat treated samples cooled slowly gives some support to the hypothesis that structural disruption, on the crystallite scale, is responsible for the decrease in CTE as a function of irradiation for AGR graphite, Figure B.58. Slagle (1968) also discusses what is expected to be observed when samples of polygranular graphite are cooled from an annealing temperature of 1000°C. He reasoned that a greater stress build-up and increased internal cracking should be observed in specimens that have been cooled at high rates than those cooled slowly. Therefore, samples cooled at a high rate should exhibit a lower CTE than those samples cooled more slowly. The current experimental work suggests that the opposite is true when cooling from temperatures approaching those of graphitisation. In this case, the slow cooling rate may allow the structure to reorganise from that before annealing thus providing a greater amount of accommodating porosity than that originally available. This situation is shown schematically in Figure B.67.

Interestingly, the effects of high temperature heat treatment on Magnox graphite (Figure B.59) suggest that a thermally induced structural disruption does not have any effect on CTE. This can be attributed to the coarse structure of the material in comparison to AGR graphite and is consistent with the qualitative description of the effects of irradiation on this material given in chapter 3, section 3.3.

9.6 TIME DEPENDENCE AND RELAXATION EFFECTS

The results from the measurement of the pre-stressed samples have shown that the recovery of CTE of pre-stressed samples over time is small. However, there is a significant recovery of CTE and a length change between the first and second thermal cycles. This implies that stored strain is being released and the material makes a partial thermally induced recovery towards its initial state. The thermal and mechanical history of these materials may therefore be important in determining expansion behaviour and this is likely to contribute to the scatter associated with the measurement of thermal expansion. This also explains why, even after careful placement of samples in the dilatometer, a difference is sometimes observed between the first and second heating

cycles. These results are in agreement with the general discussion of polycrystals given by Austin (1952) who suggests that the process of measuring the CTE (*i.e.* heating the sample) may also disrupt the microstructure and alter the CTE behaviour measured on subsequent cycles. In this case, the acquisition of a reproducible dilation curve is not representative of the original material but one slightly altered by the heating process. These results are also in agreement with the conclusions of Slagle (1969) who studied the hysteresis in thermal expansion of TSX (needle coke) graphite over several thermal cycles. He concluded that the hysteresis was caused by the relief of thermal stress during heating.

From the results presented here and the work of Slagle (1969) on TSX (needle coke) graphite and the discussion by Austin (1956) it is suggested that differences between thermal cycles are likely to be caused by a combination of two effects. The first is the "settling in" of the sample during the initial stages of measurement, this is likely to be strongly influenced by the positioning and seating of the sample in the dilatometer. The second is the relaxation of internal stress created during manufacture with a related CTE sensitive structure disruption. From an engineering perspective, therefore, it would seem desirable to quote CTE values derived from the second heating cycle within which these effects have largely been removed. This approach would better represent the behaviour of the material in service. In any case, irrespective of the cycle from which average CTE values are computed, it is clearly incorrect to consider the CTE of these materials to be a fundamental material property as one may consider, for example, the thermal expansion of single crystals.

9.7 SUMMARY AND MODELLING REQUIREMENTS

From the microscopy work presented in this thesis and elsewhere, it is clear that the microstructure of nuclear graphites is extremely complex. However, at the nanometric scale, irrespective of the degree of oxidation or the graphite type, the microstructure appears to be similar. These are regions of spherical inclusions (*e.g.* Figure B.28) or arcs of connected ligaments (*e.g.* Figure B.25) each containing large amounts of porosity that have been created during manufacture. Within this part of the thesis, the importance of structural connectivity on CTE has been demonstrated. Also, 'as

manufactured' porosity has been shown to influence CTE as opposed to that created by oxidation which has been shown to have no effect. These concepts have been incorporated within the Continuous Network Hypothesis (which has also been supported by percolation theory).

Although the loose assembly of single crystals model provides a simplified abstraction of this structure the elements of as-manufactured' porosity and structural connectivity are not incorporated. If an abstraction is constructed that contains these basic elements of microstructure then it may be possible to model both the CTE behaviour of nuclear graphites under neutron irradiation and the insensitivity of CTE to oxidation. Due to the complexity of the problem, such a modelling approach should be modular. That is, each aspect of the problem is isolated and builds upon that solved previously such that the increasing complexity of the model can be understood and developed by iteration. This new modelling process is described and implemented in Part C.

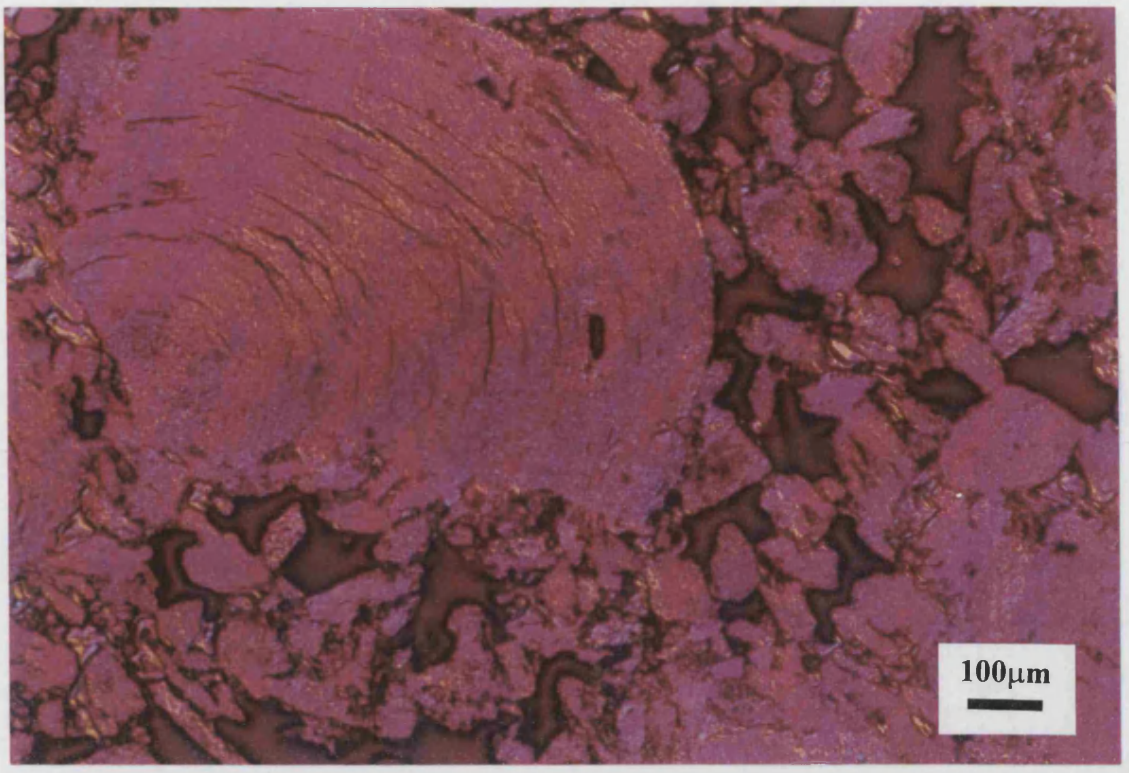

Figure B.1(a). Polarised light optical micrograph of oxidised AGR graphite to ~20% weight loss.

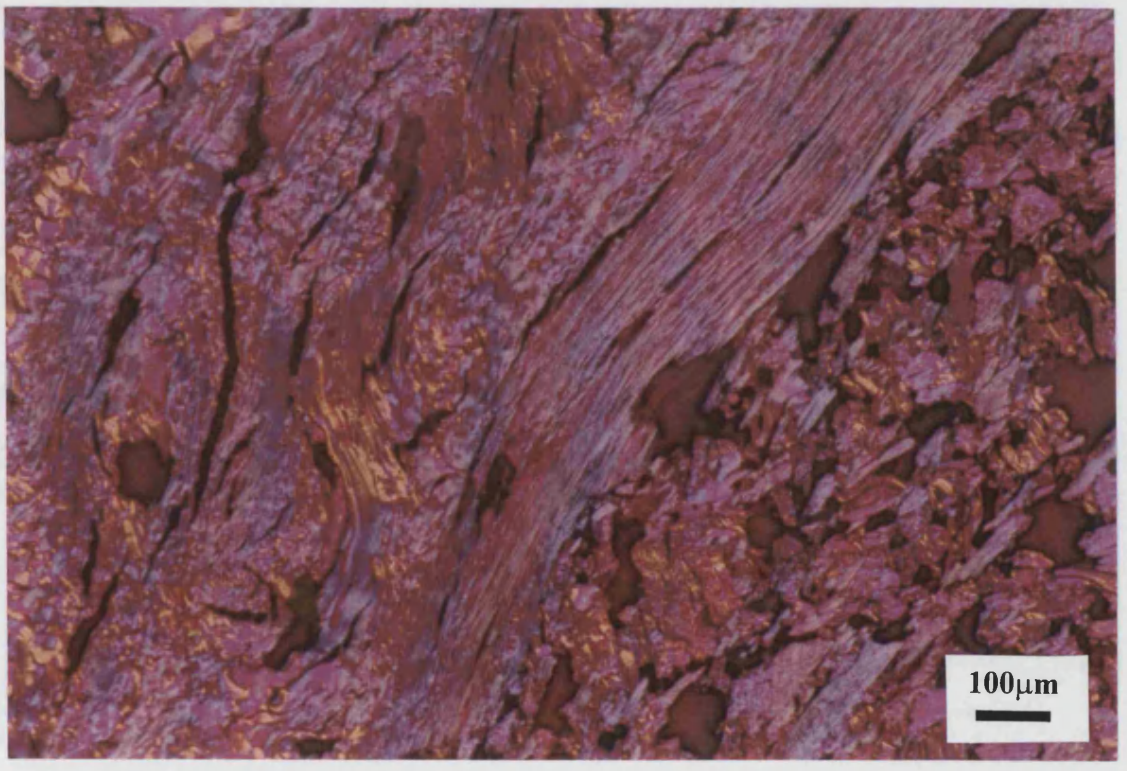

Figure B.1(b). Polarised light optical micrograph of Magnox moderator graphite oxidised to ~20% weight loss.

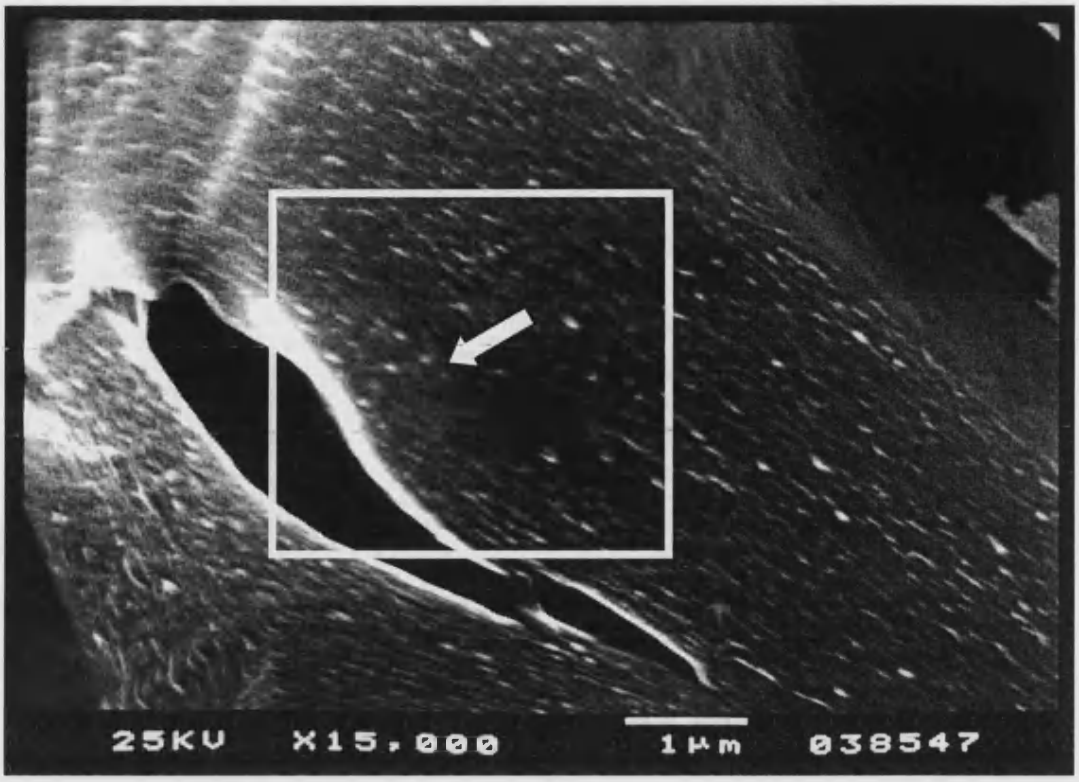

Figure B.2(a). SEM of AGR graphite showing Mrozowski crack porosity (as indicted) next to a larger gas entrapment pore.

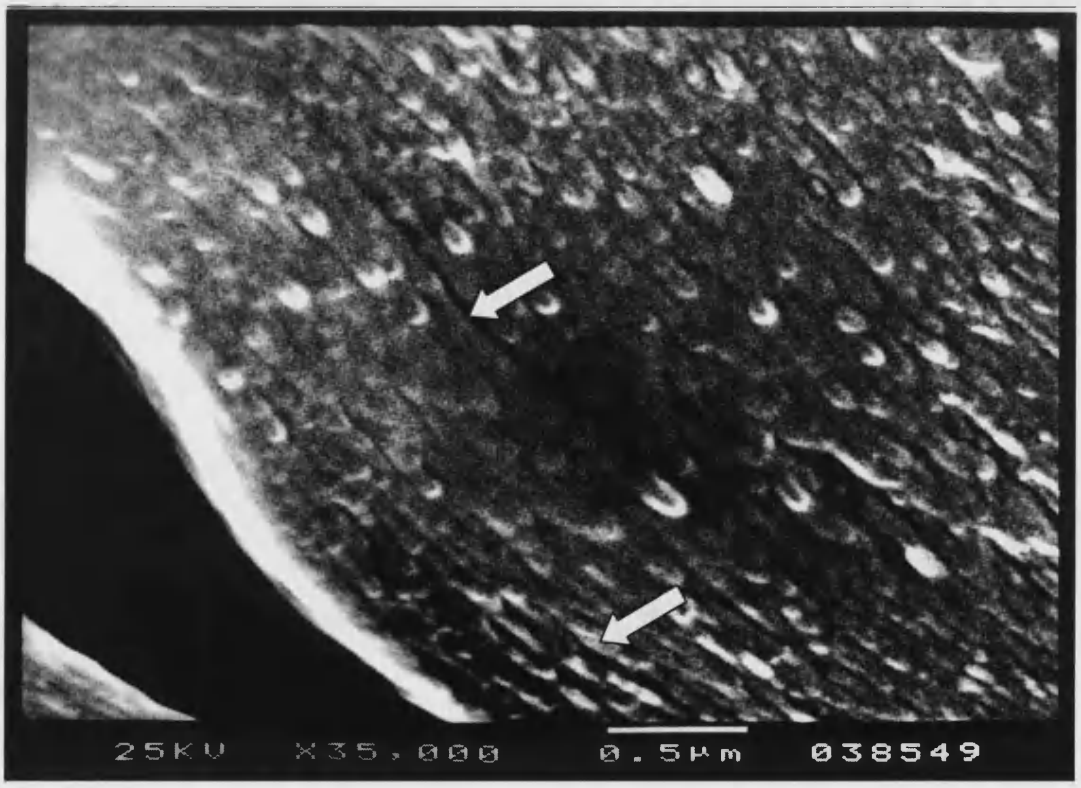

Figure B.2(b). Magnified area to the right of the large pore, as indicated in the framed area of Figure B.2(a), showing a range of crack sizes.

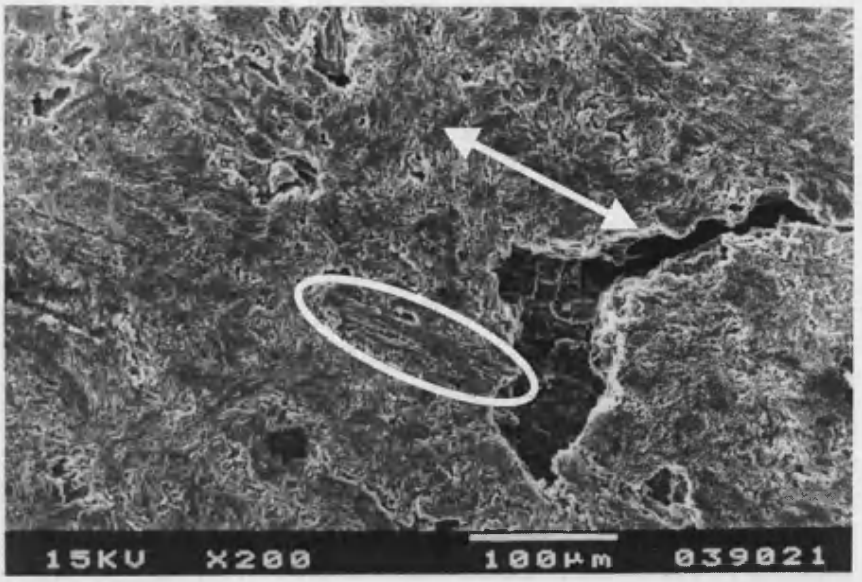

Figure B.3. The machined surface of unoxidised Magnox moderator graphite with a circled filler particle and the alignment (extrusion direction) indicted by the arrow.

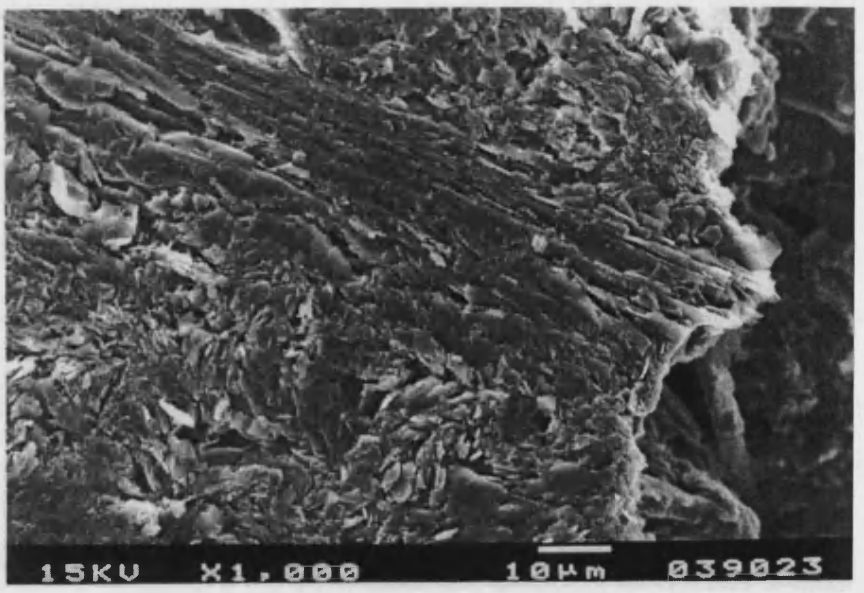

Figure B.4. An elongated filler particle within a coarse structure at the edge of a gas entrapment pore in unoxidised Magnox moderator graphite.

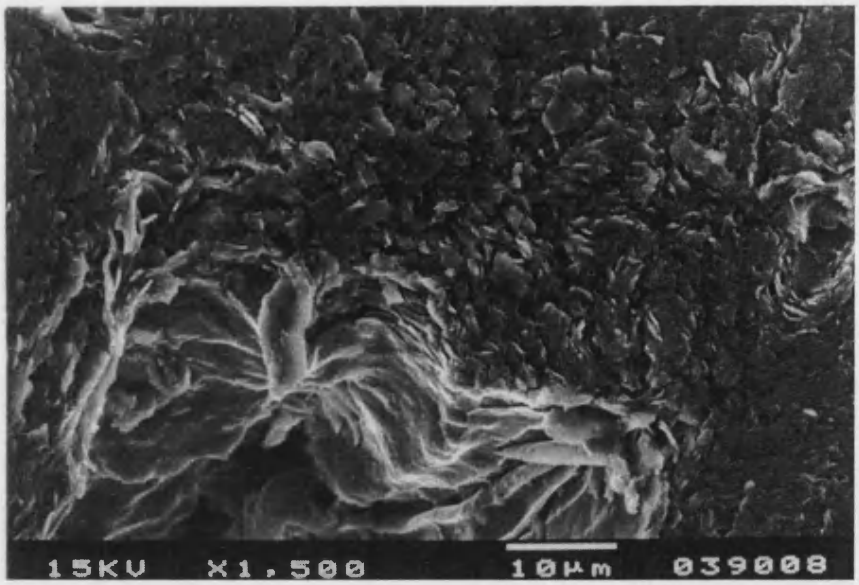

Figure B.5. Example fine cracks and general structure in the binder phase near gas entrapment porosity in unoxidised Magnox moderator graphite.

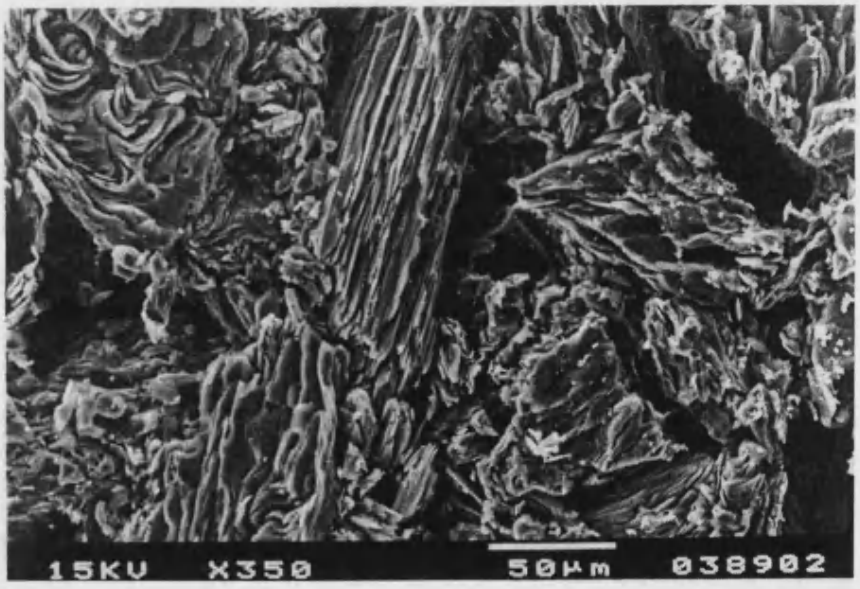

Figure B.6. Overview of oxidised Magnox moderator graphite (~23% weight loss) with preferential oxidation of the binder phase.

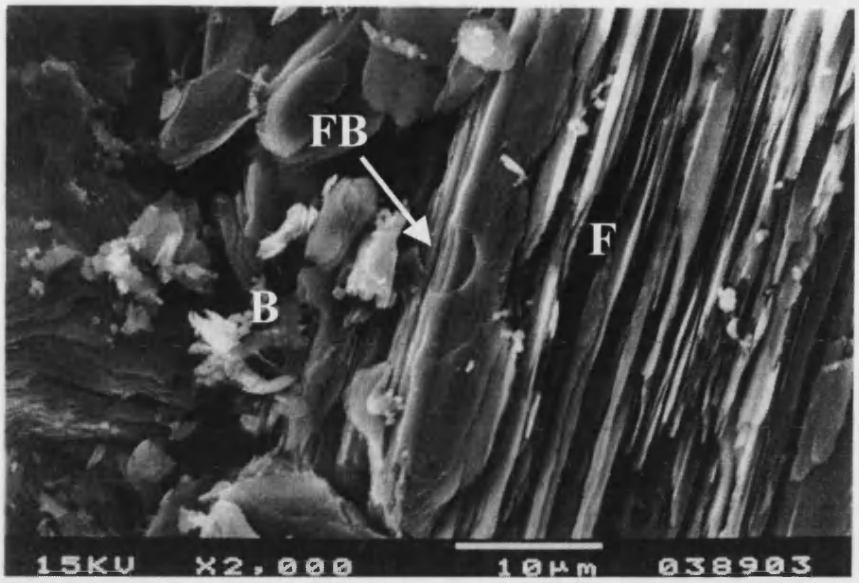

Figure B.7. The filler-binder interface in oxidised Magnox moderator graphite (~23% weight loss) showing F- Filler particle, B- Binder phase and FB- The filler/binder interface region.

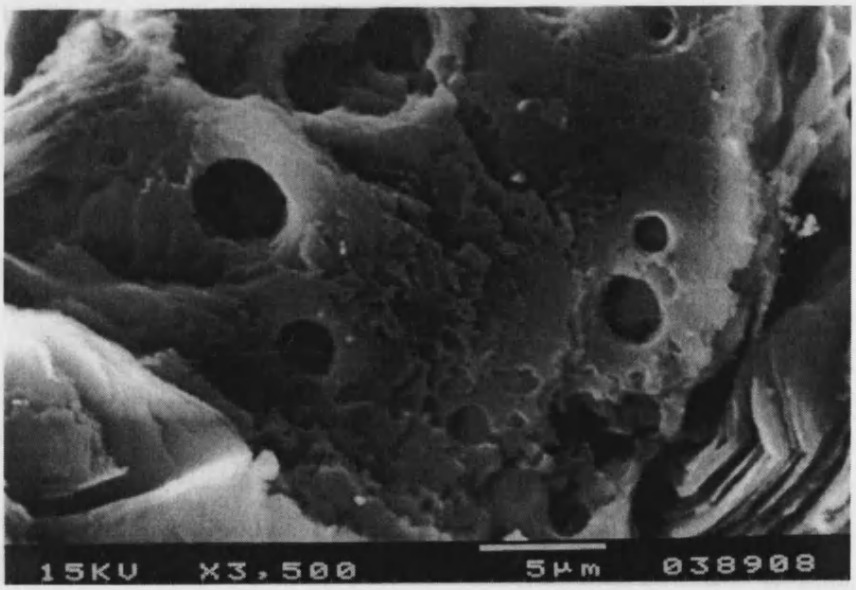

Figure B.8. Oxidation in Magnox moderator graphite (~23% weight loss) showing pitting.

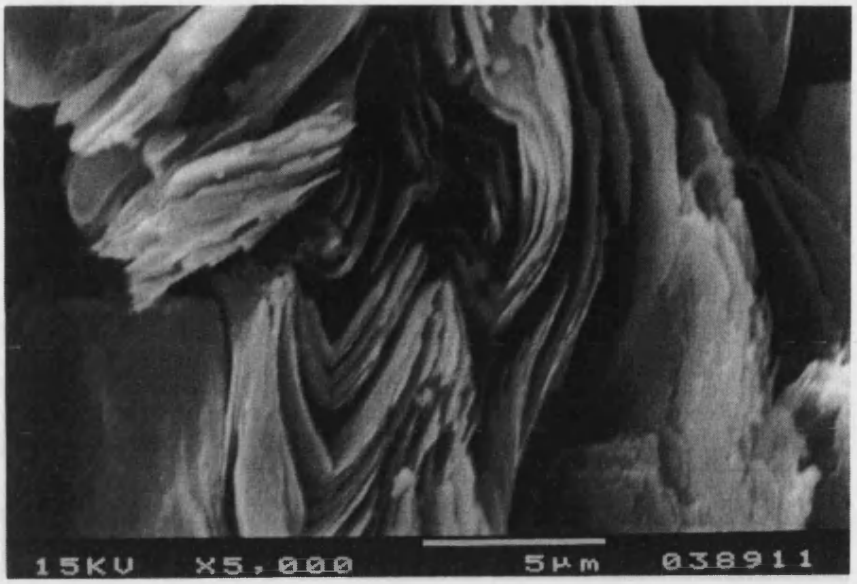

Figure B.9. Fine pore network between graphitic planes at the edge of a gas entrapment pore in Magnox moderator graphite oxidised to ~23% weight loss.

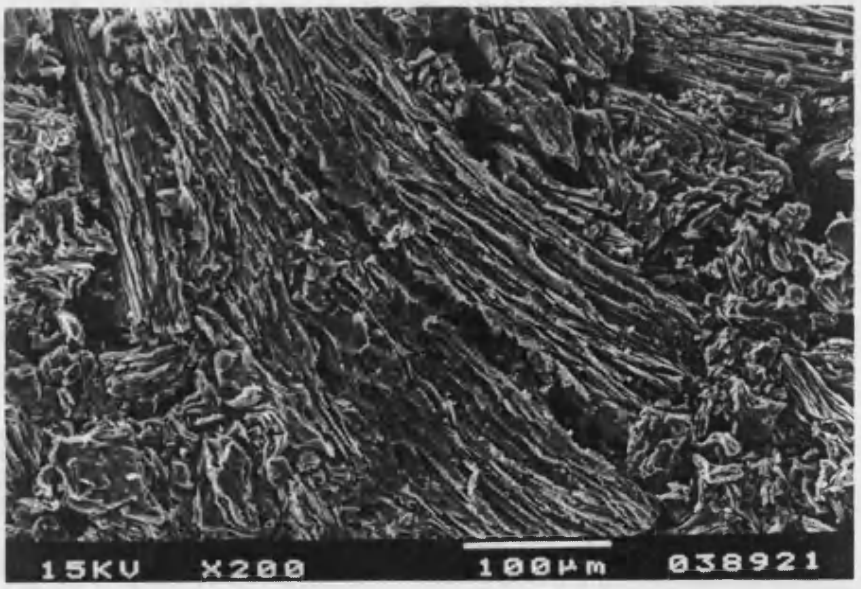

Figure B.10. Magnox moderator graphite (in the direction perpendicular to extrusion) oxidised to ~30% weight loss with preferential oxidation of the binder phase.

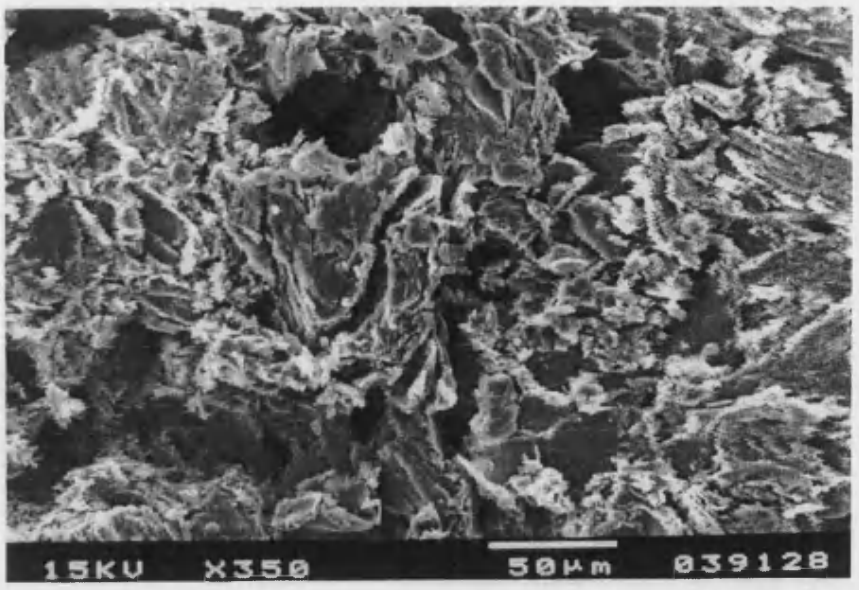

Figure B.11. An example of interconnected porosity in the binder phase in oxidised Magnox moderator graphite (~43% weight loss).

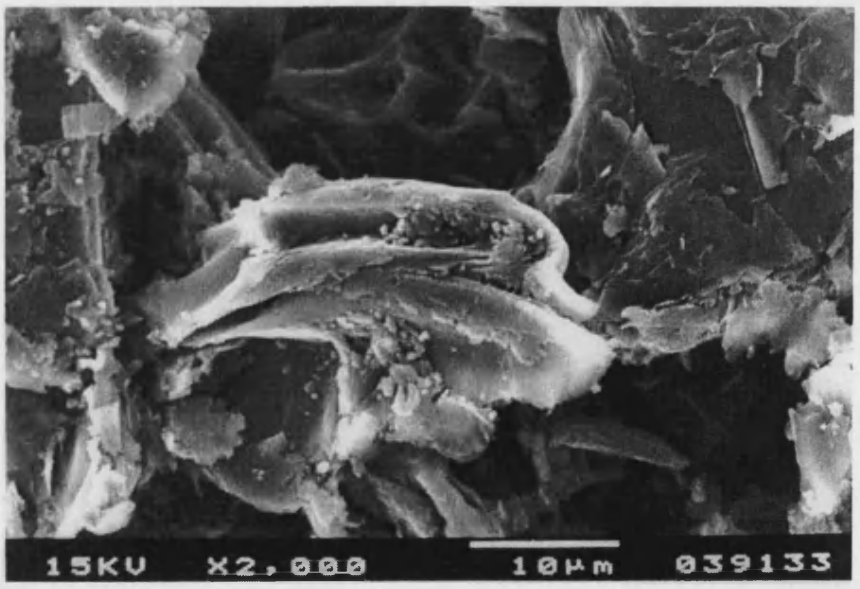

Figure B.12. An area of disrupted binder phase with a large amount of porosity and with small pores present in oxidised Magnox moderator graphite (~43% weight loss).

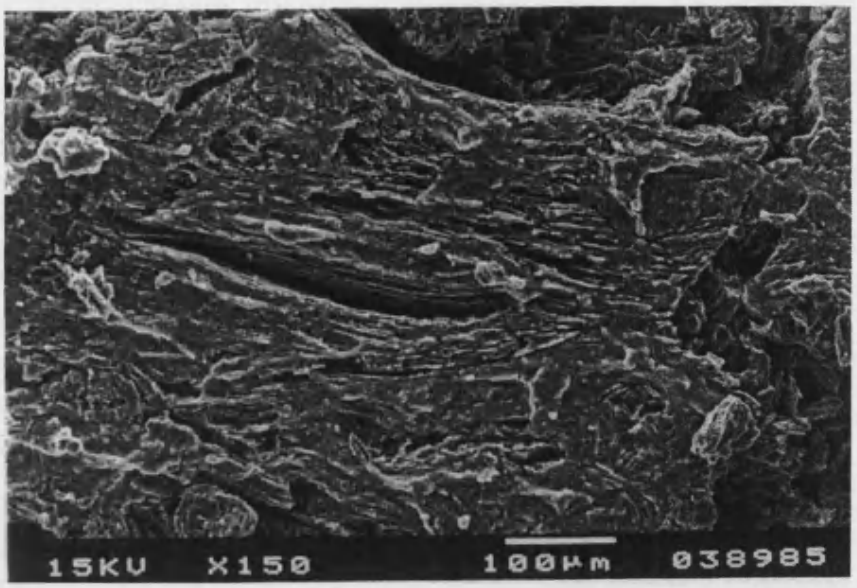

Figure B.13. Overview of oxidised Magnox moderator graphite (~45% weight loss).

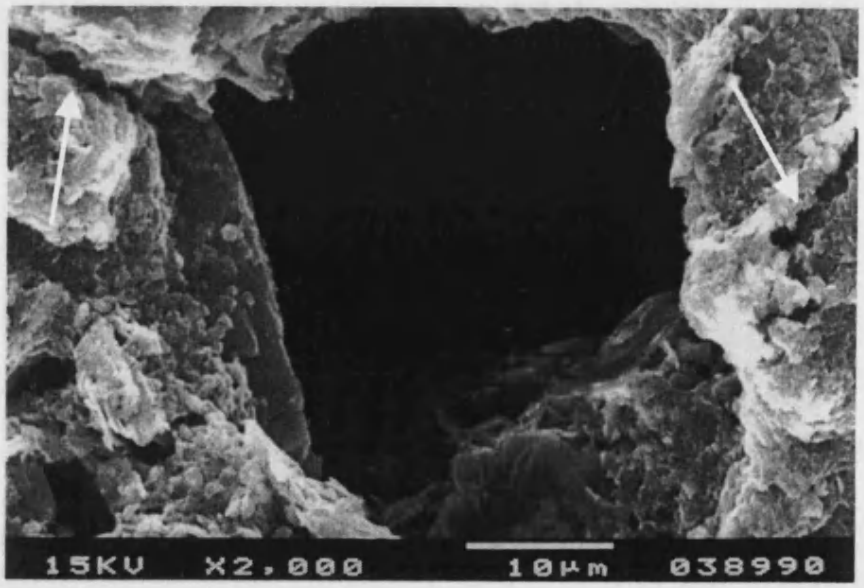

Figure B.14. Development of cracks by oxidation from a gas entrapment pore (indicated by arrows) in oxidised Magnox moderator graphite (~45% weight loss).

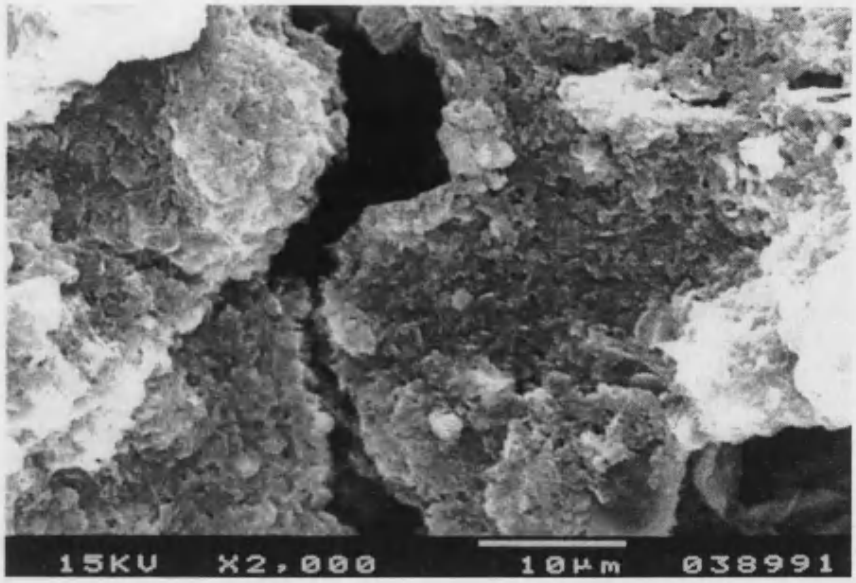

Figure B.15. Example of a branch crack from a gas entrapment pore in oxidised Magnox moderator (~45% weight loss).

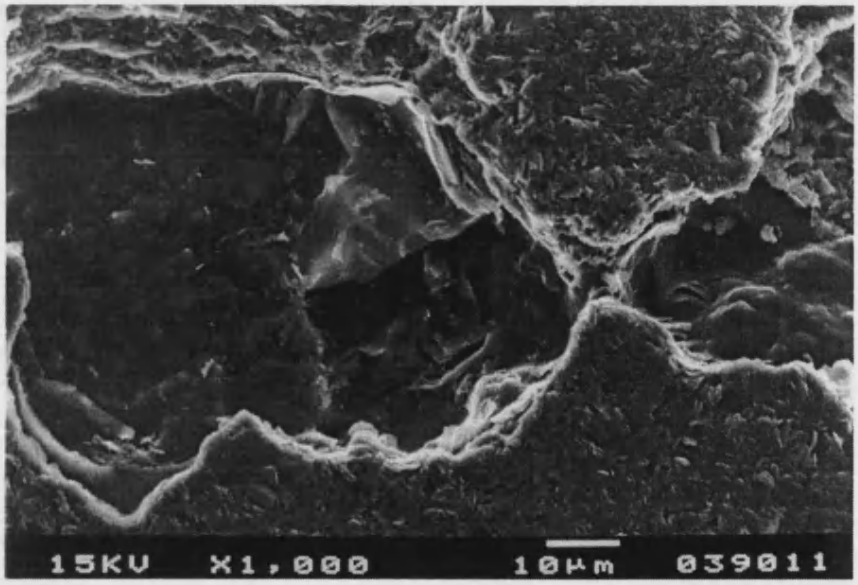

Figure B.16. Examples of fine cracks and general structure in the binder phase near gas entrapment porosity in unoxidised AGR moderator graphite.

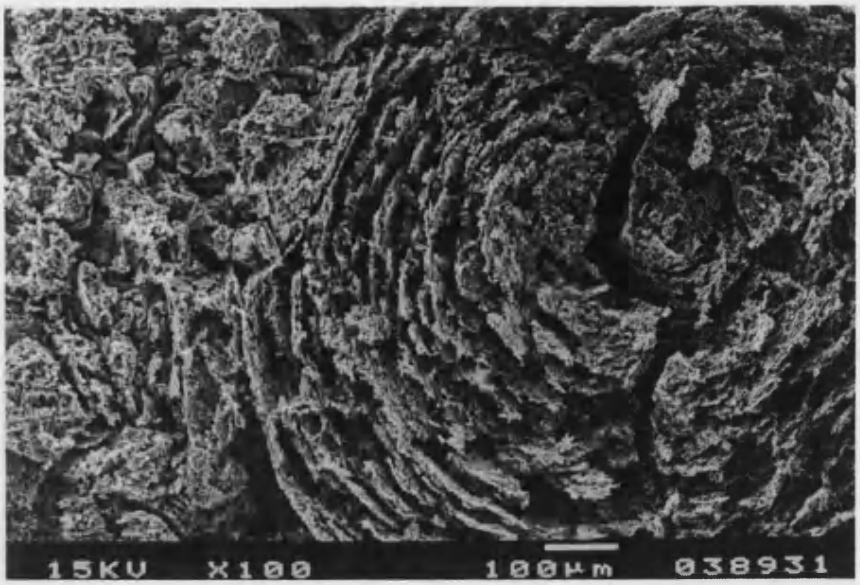

Figure B.17. Opening of the concentric layers within the Gilsocarbon filler in oxidised AGR graphite (~30% weight loss).

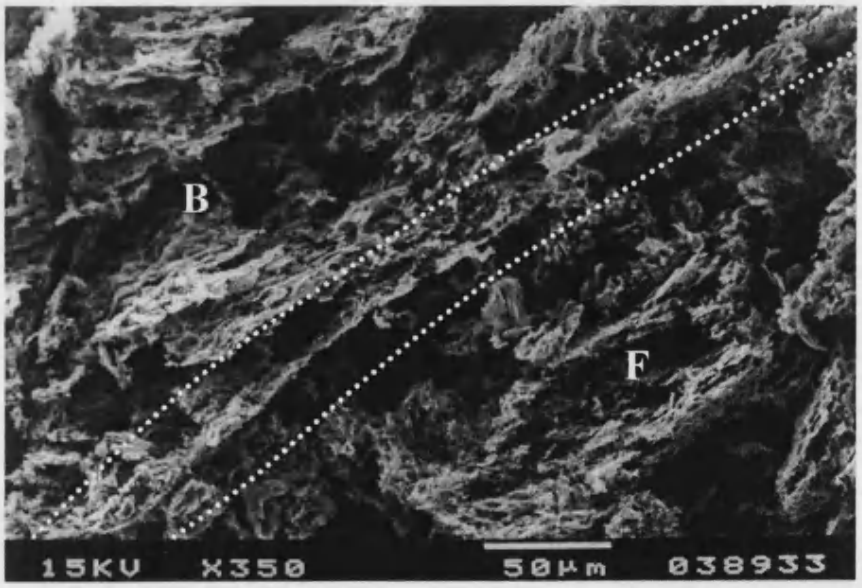

Figure B.18. Filler-binder interface (as indicted between the dotted lines) in oxidised AGR graphite (~30% weight loss) where F and B indicates the filler and binder regions respectively.

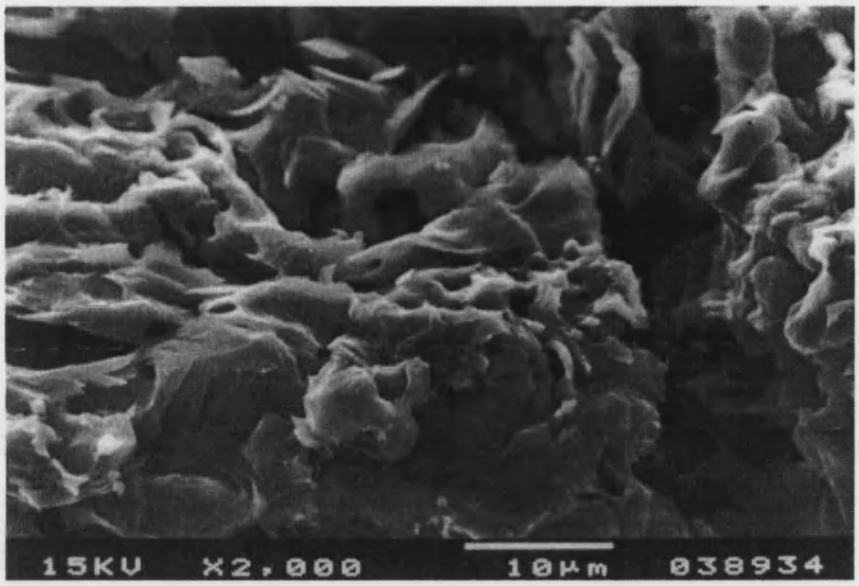

Figure B.19. Oxidation attack in the binder phase (visible along the edges of graphitic planes) in oxidised AGR graphite (~30% weight loss).

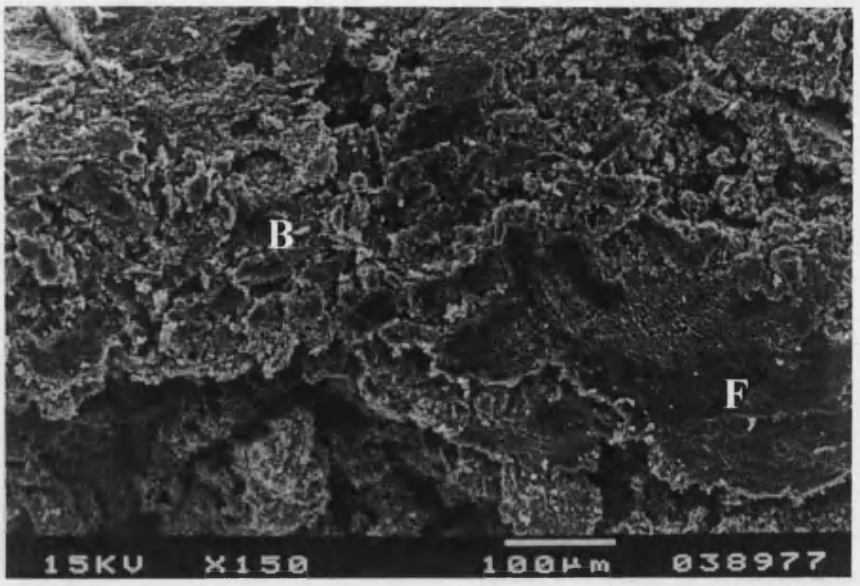

Figure B.20. Large voids and areas of highly interconnected fine porosity in highly oxidised AGR graphite (~70% weight loss) with the identification of filler (F) and binder (B) regions.

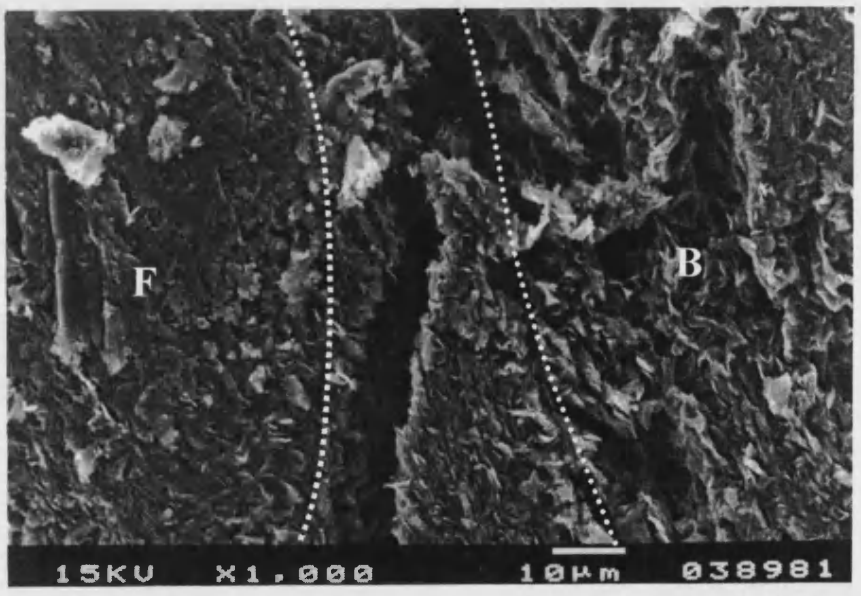

Figure B.21. Oxidation attack in the filler-binder interface (between the dotted lines) in highly oxidised AGR graphite where F and B represent regions of filler and binder, respectively. (~70% weight loss).

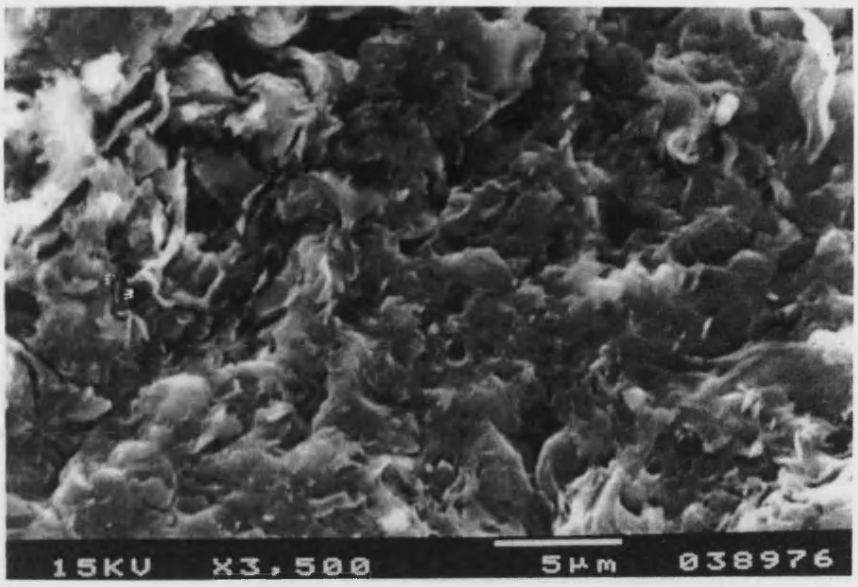

Figure B.22. Pits and voids within the filler particle boundary (the entire view) in highly oxidised AGR moderator graphite (~70% weight loss).

Figure B.23. Transmission electron micrograph of unoxidised AGR graphite (UCAR GCMB grade) in the binder phase (S1P1 x 70,000).

Figure B.24. Transmission electron micrograph of unoxidised AGR graphite (UCAR GCMB grade) in the binder phase (S1P4 x 35,000).

Figure B.25. Transmission electron micrograph of unoxidised AGR graphite (UCAR GCMB grade) in the binder phase (S1P4 x 140,000).

Figure B.26. Transmission electron micrograph of unoxidised AGR graphite (UCAR GCMB grade) in the binder phase (S1P5 x 280,000).

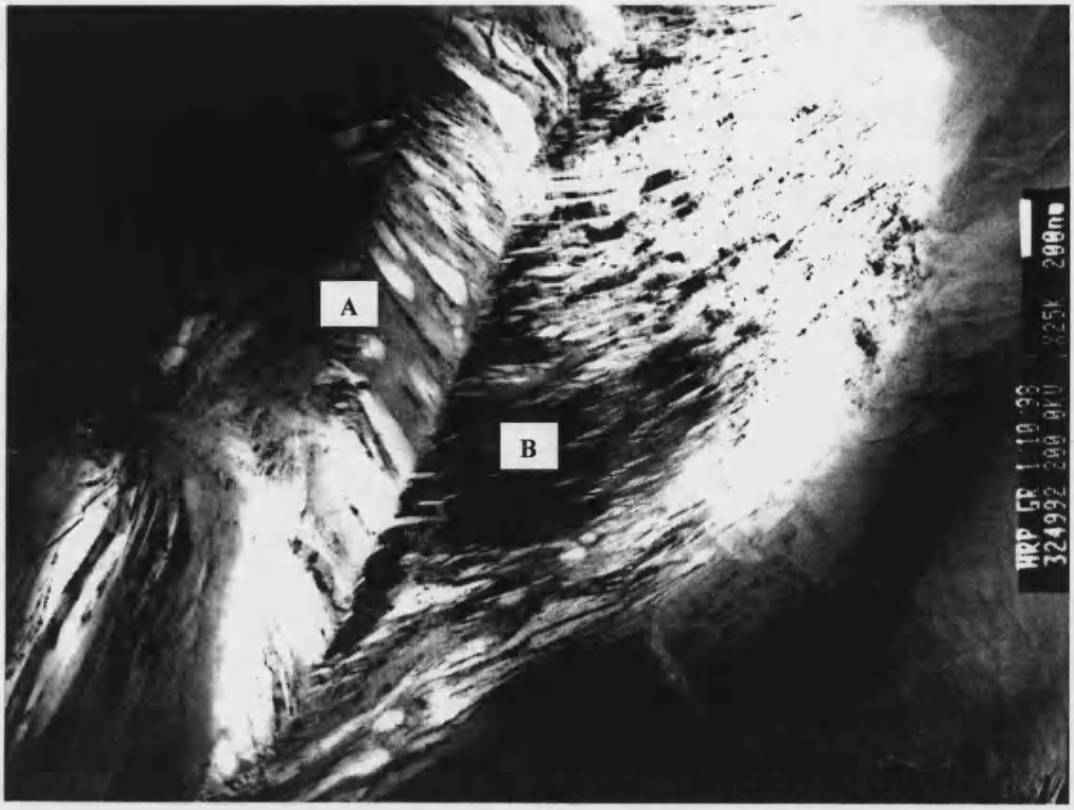

Figure B.27. Transmission electron micrograph of unoxidised AGR graphite (UCAR GCMB grade) in the binder phase (S1P3 x 35,000) showing two regions A and B.

Figure B.28. Transmission electron micrograph of unoxidised AGR graphite (UCAR GCMB grade) in the filler phase (S2P1 x 70,000).

Figure B.29. Transmission electron micrograph of unoxidised AGR graphite (UCAR GCMB grade) in the filler phase (S2P1 x 280,000).

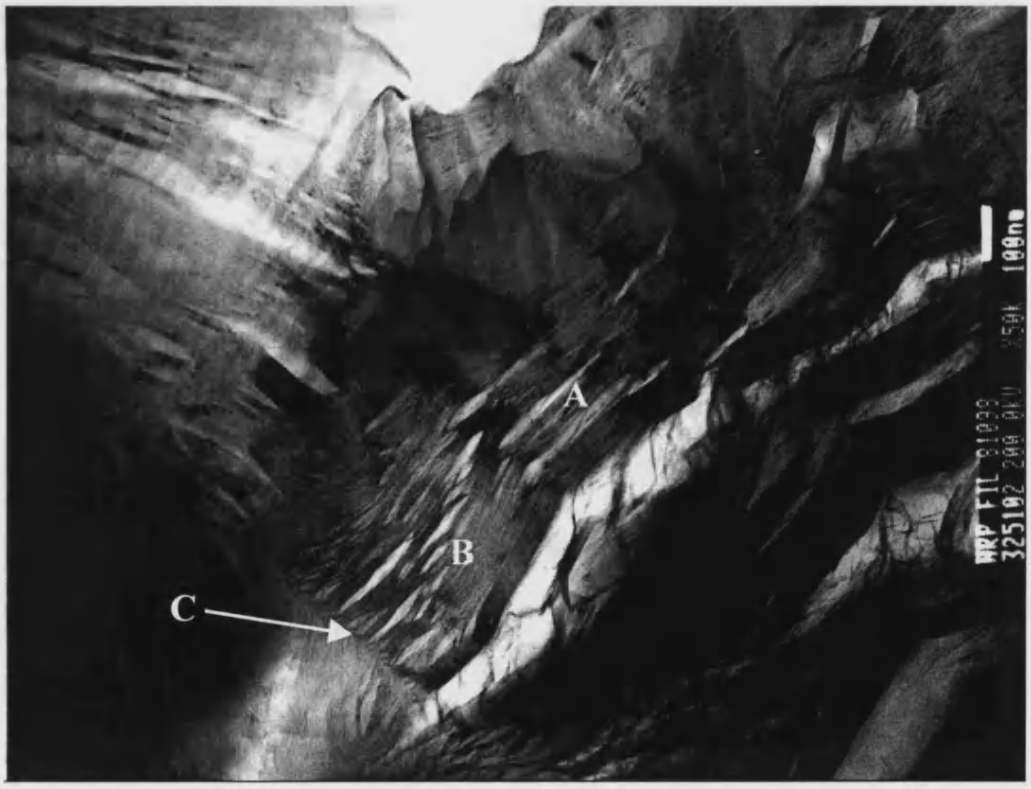

Figure B.30. Transmission electron micrograph of unoxidised AGR graphite (UCAR GCMB grade) in the filler phase (S2P2 x 70,000), indicating changes in crystallographic orientation between regions A and B and an abrupt boundary at C.

Figure B.31. Transmission electron micrograph of oxidised AGR graphite (UCAR GCMB grade) to 30% weight loss (S3P2 x 140,000).

Figure B.32. Transmission electron micrograph of unoxidised Magnox moderator graphite (S4P1 x 140,000).

Figure B.33. Transmission electron micrograph of unoxidised Magnox moderator graphite (S4P2 x 140,000).

Figure B.34. Transmission electron micrograph of unoxidised Magnox moderator graphite (S4P5 x 140,000).

Figure B.35. Transmission electron micrograph of unoxidised Magnox moderator graphite (S4P4 x 70,000).

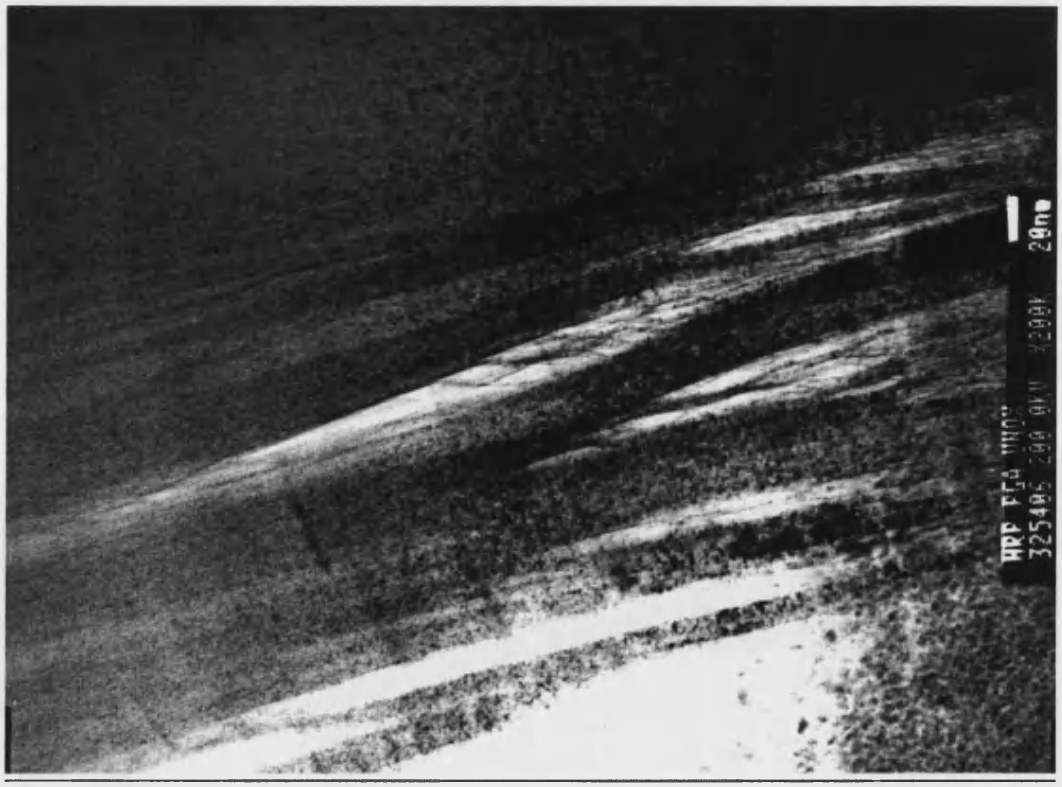

Figure B.36. Transmission electron micrograph of unoxidised Magnox moderator graphite (S4P4 x 280,000).

Figure B.37. Transmission electron micrograph of oxidised Magnox moderator graphite to 30% weight loss (S5P4 x 35,000). Note, scale bar is at 200 nm.

Figure B.38. Transmission electron micrograph of oxidised Magnox moderator graphite to 30% weight loss (S5P6 x 35,000). Note, scale bar is at 200 nm.

Figure B.39. Transmission electron micrograph of oxidised Magnox moderator graphite to 30% weight loss (S5P5 x 35,000).

Figure B.40. Transmission electron micrograph of oxidised Magnox moderator graphite to 30% weight loss (S5P1 x 35,000).

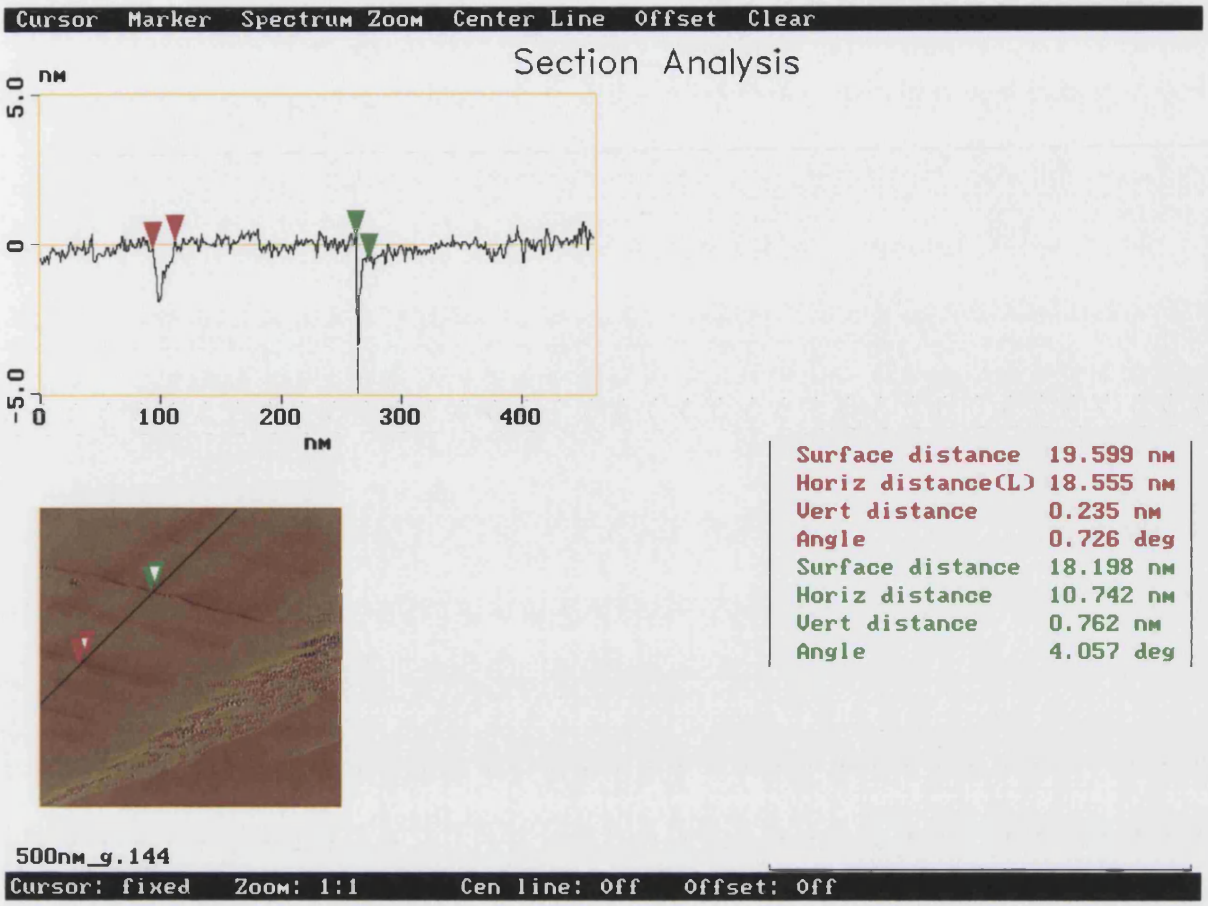

Figure B.41. AFM image of graphite surface including a qualitative line analysis.

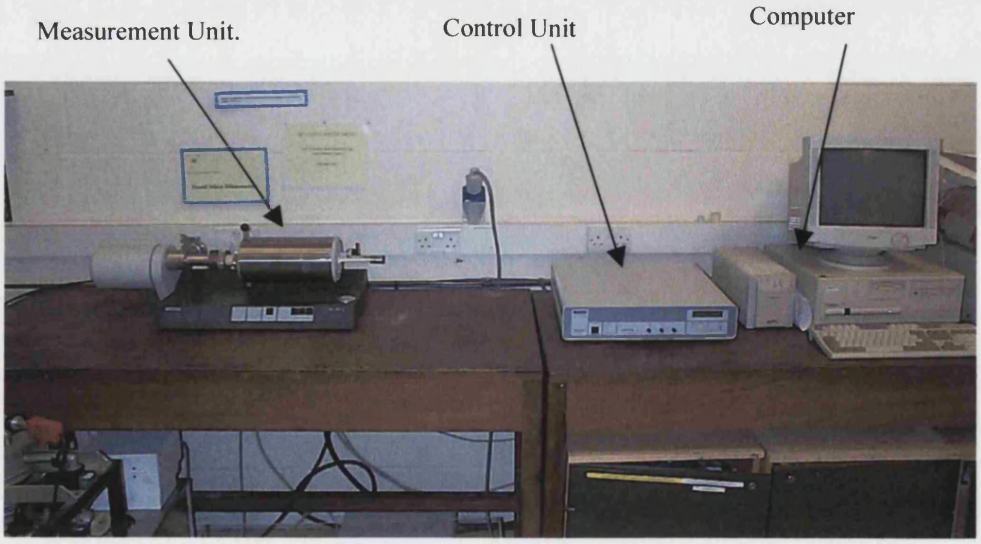

Figure B.42. Picture of the dilatometer system.

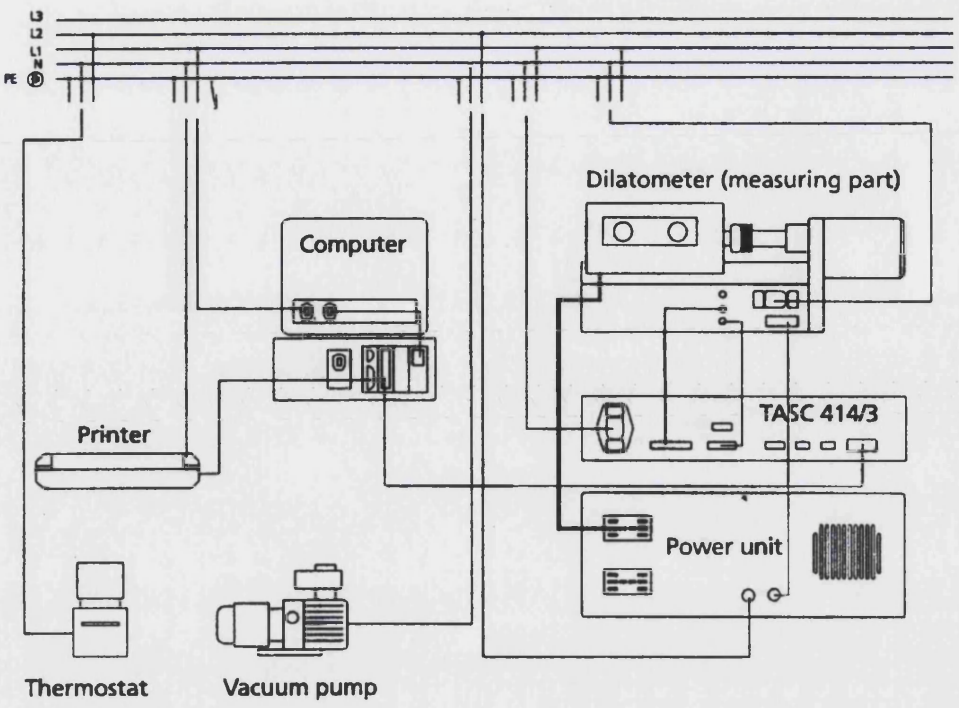

Figure B.43. Dilatometer setup schematic.

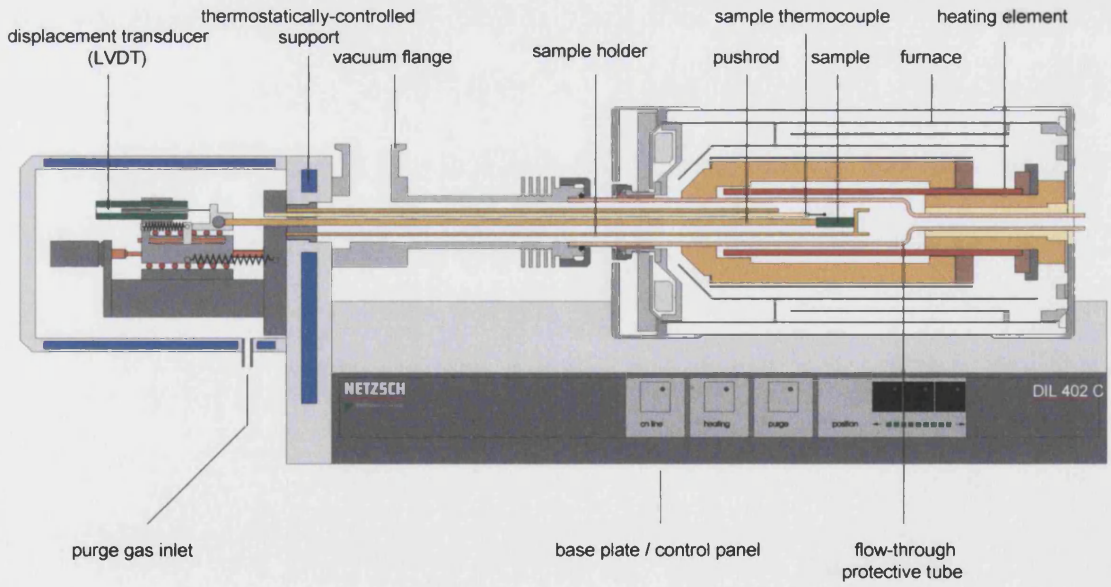

Figure B.44. Schematic of the measurement unit (courtesy of Netzsch Instruments Ltd.).

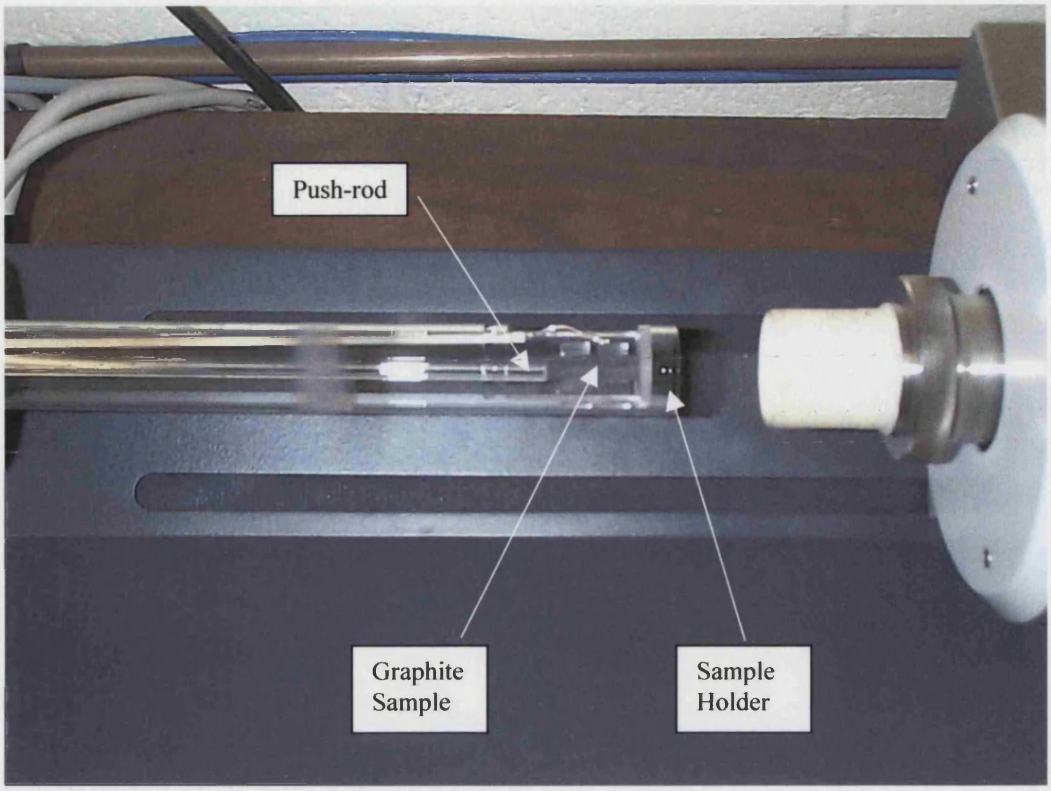

Figure B.45. Dilatometer sample holder and pushrod complete with graphite sample.

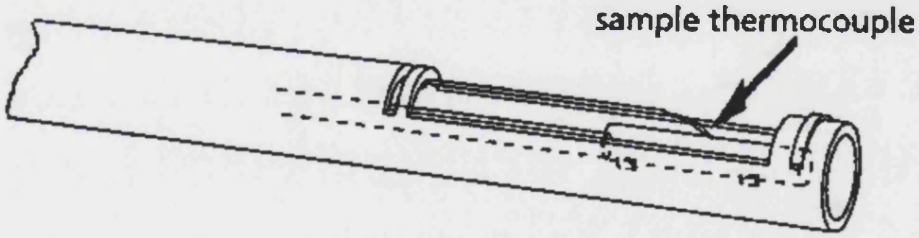

Figure B.46. Schematic of sample holder and pushrod (dotted line).

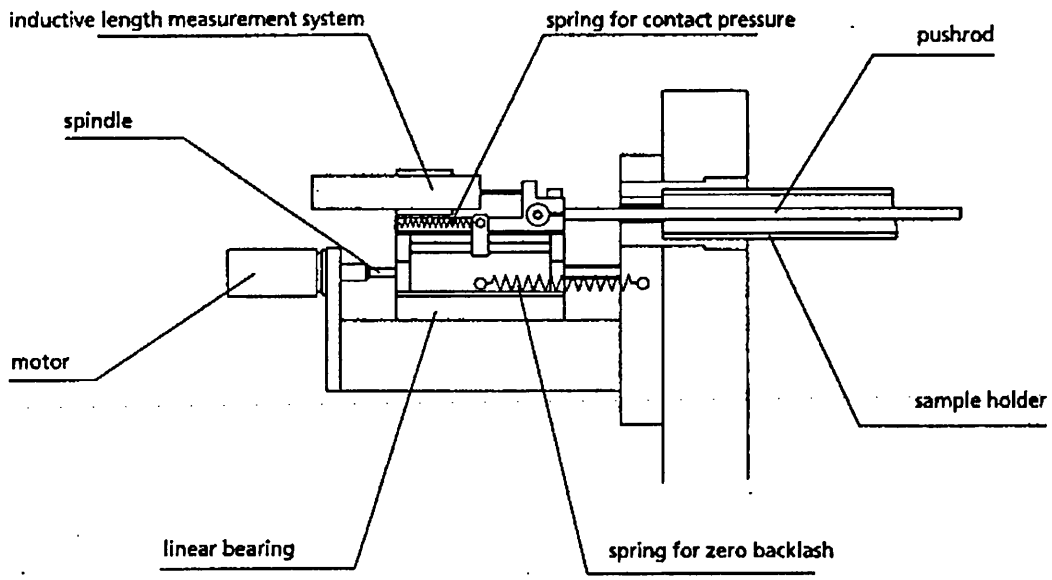

Figure B.47. Schematic of measurement system.

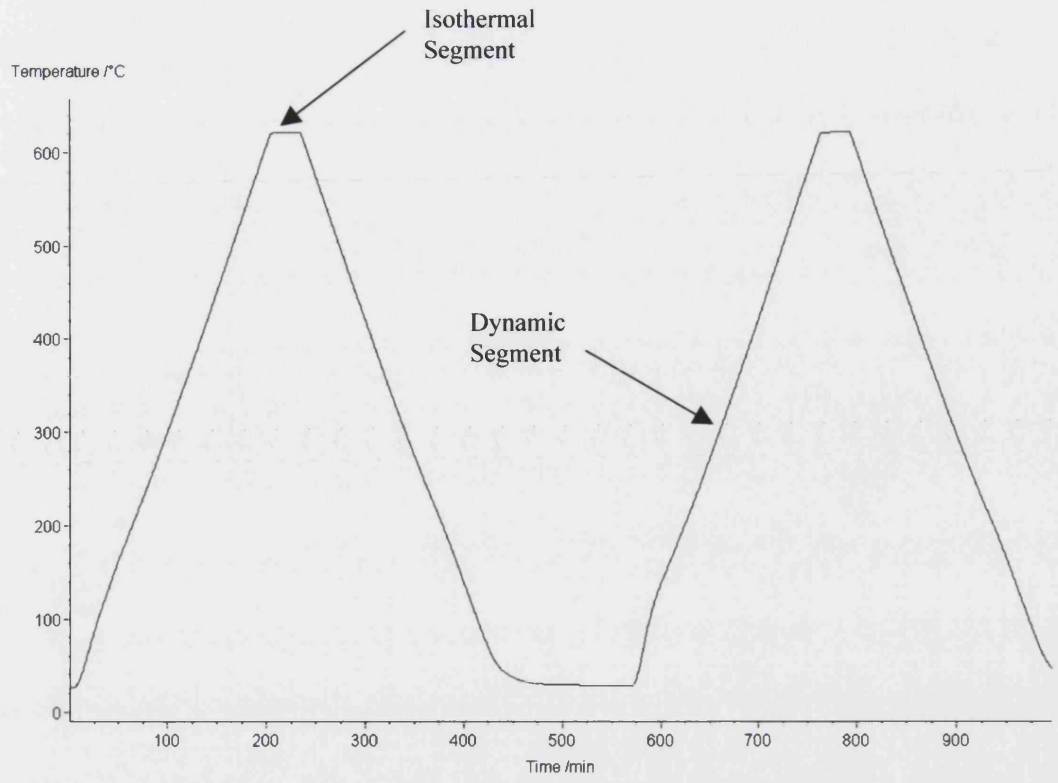

Figure B.48. Example temperature profile showing isothermal and dynamic segments over two thermal cycles.

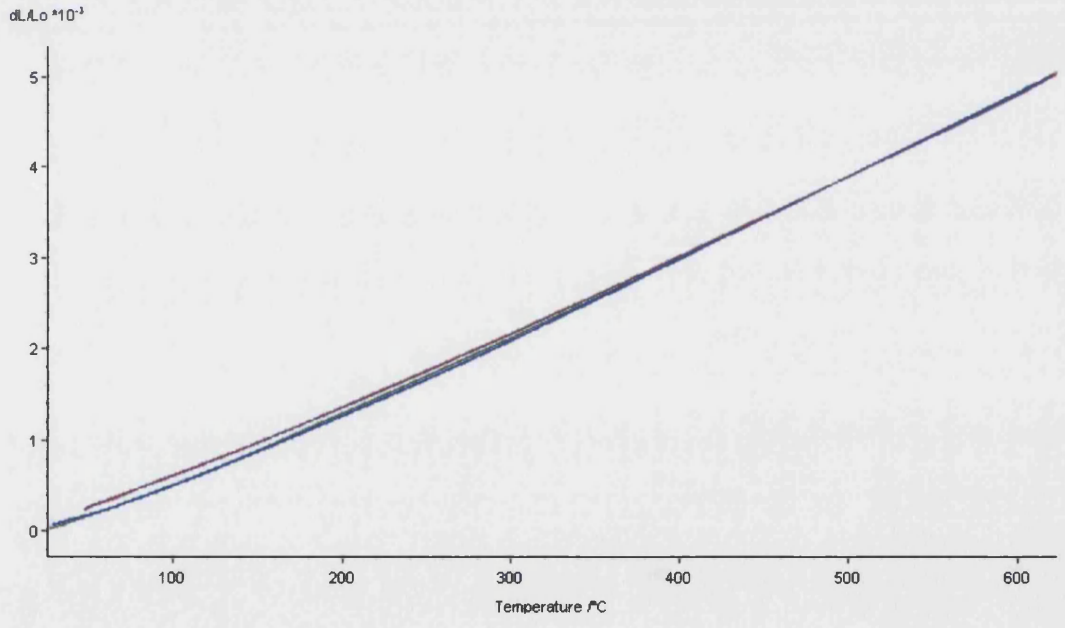

Figure B.49. Dilation curve showing the thermal expansion of the sapphire standard calibrated using Alumina.

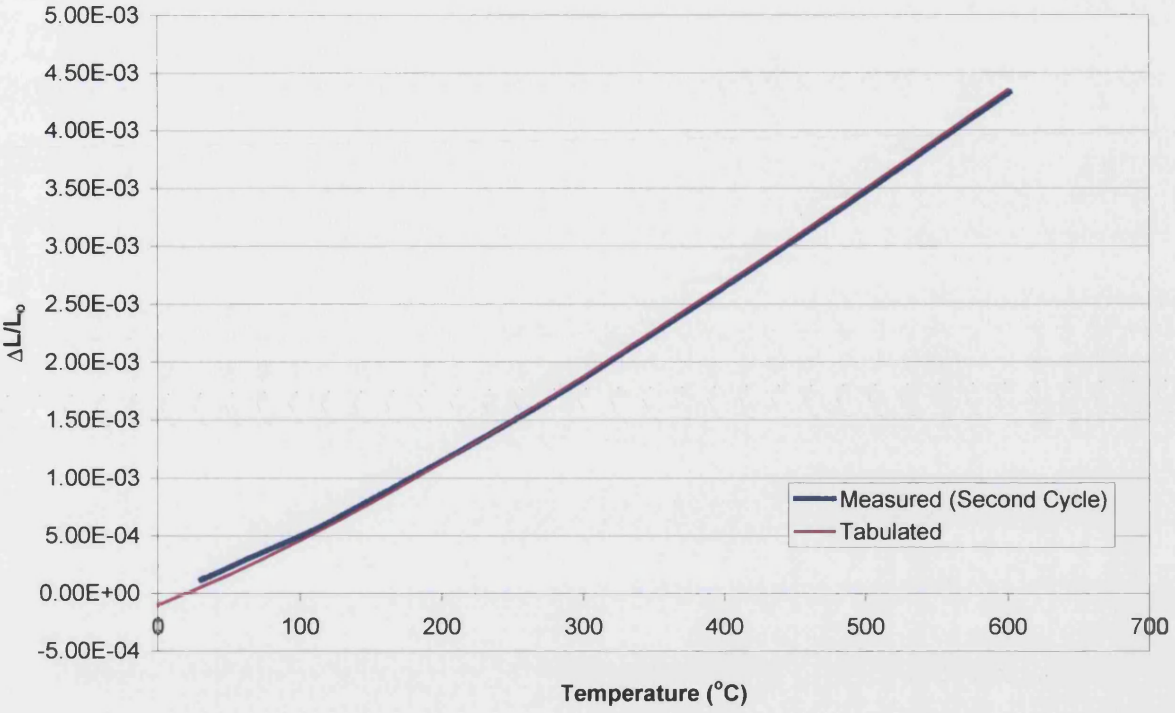

Figure B.50. The measurement of the dilation of the alumina standard in comparison to the tabulated standard data over the second thermal heating segement.

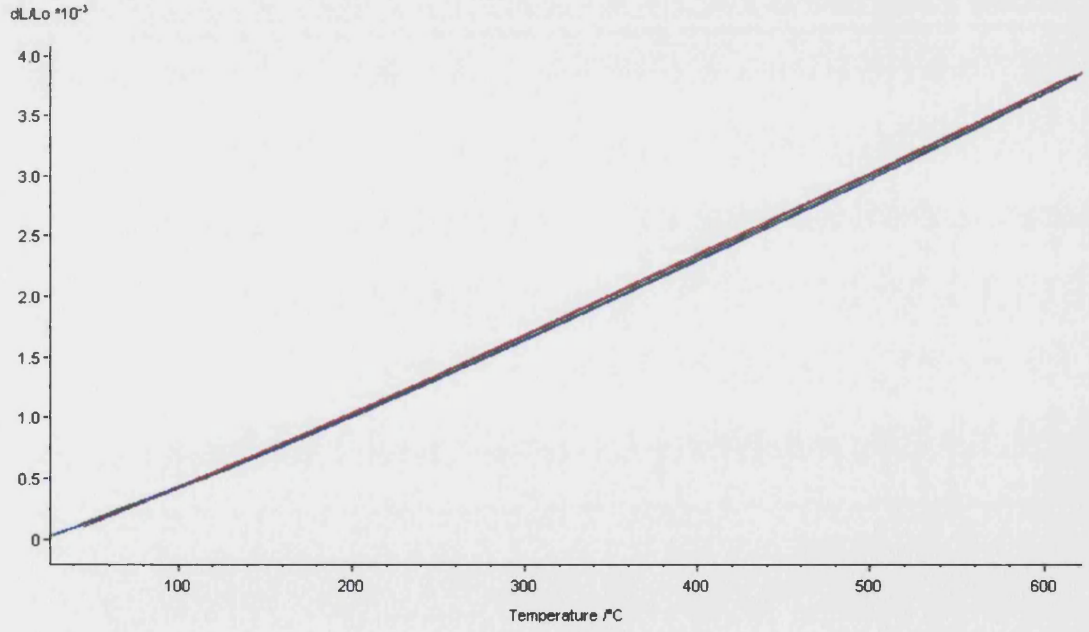

Figure B.51(a). The dilation of 'as received' AGR graphite sample over two heating cycles.

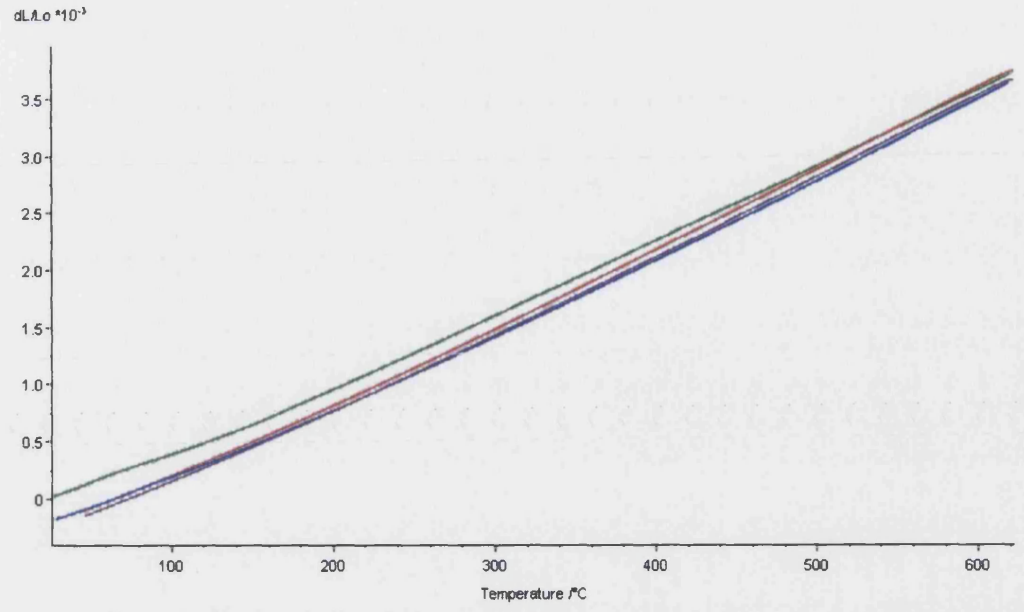

Figure B.51(b). The dilation of AGR graphite taken over two heat cycles showing a larger difference between the first heating and subsequent curves than described by Figure B.51(a).

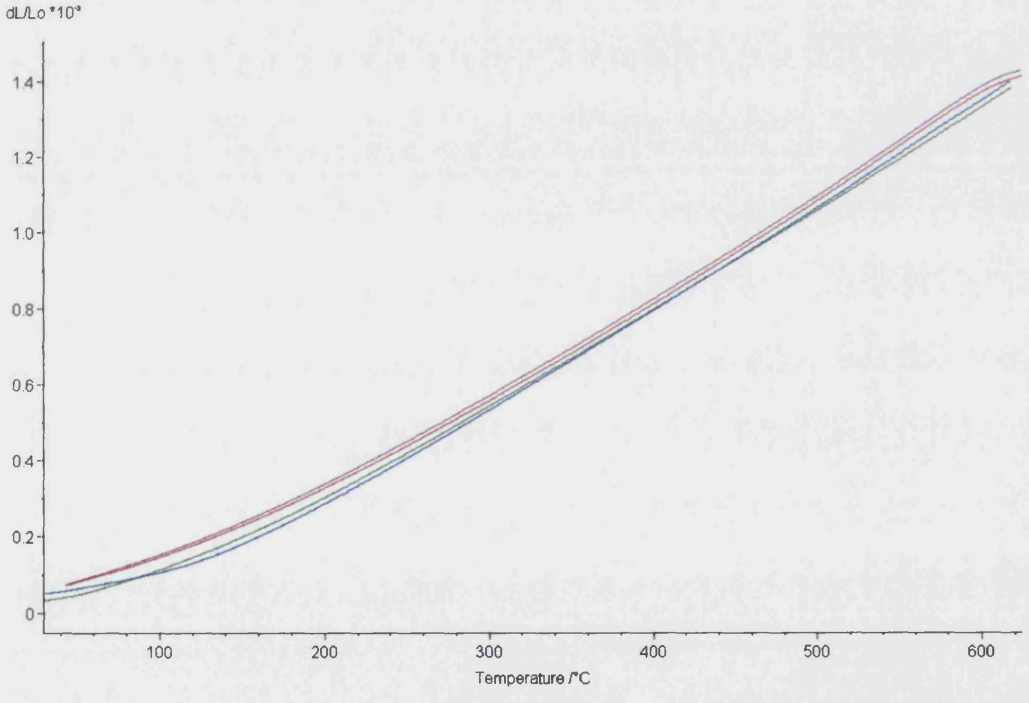

Figure B.52(a). The dilation of Magnox moderator graphite in the Parallel direction over two heat cycles.

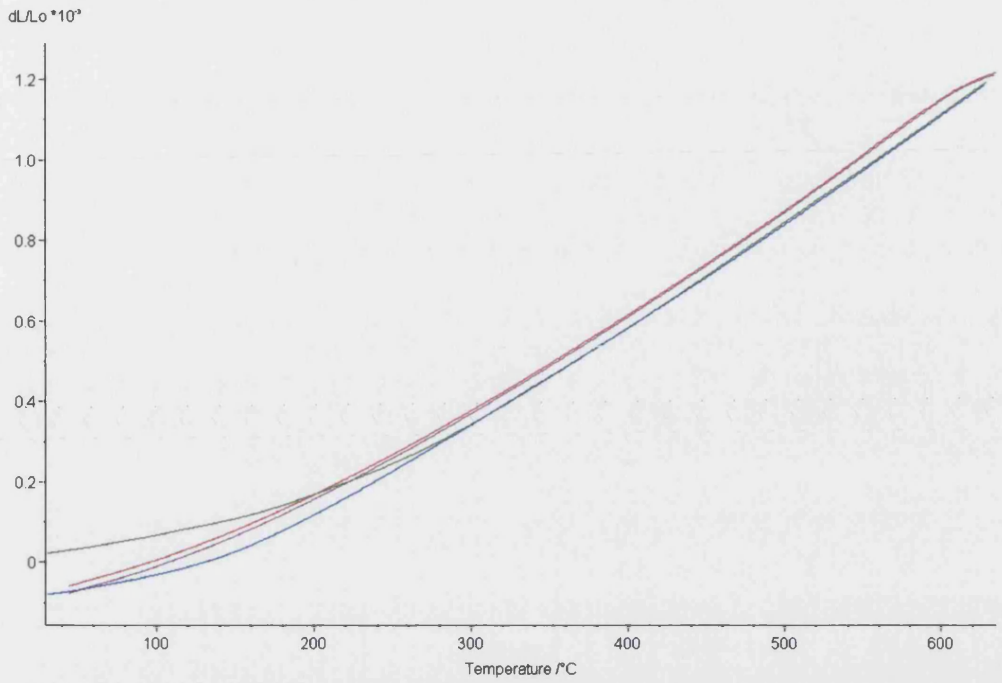

Figure B.52(b). The dilation of Magnox moderator graphite in the Parallel direction over two heat cycles showing a larger difference between the first and subsequent heating and cooling segments than in Figure 52(a).

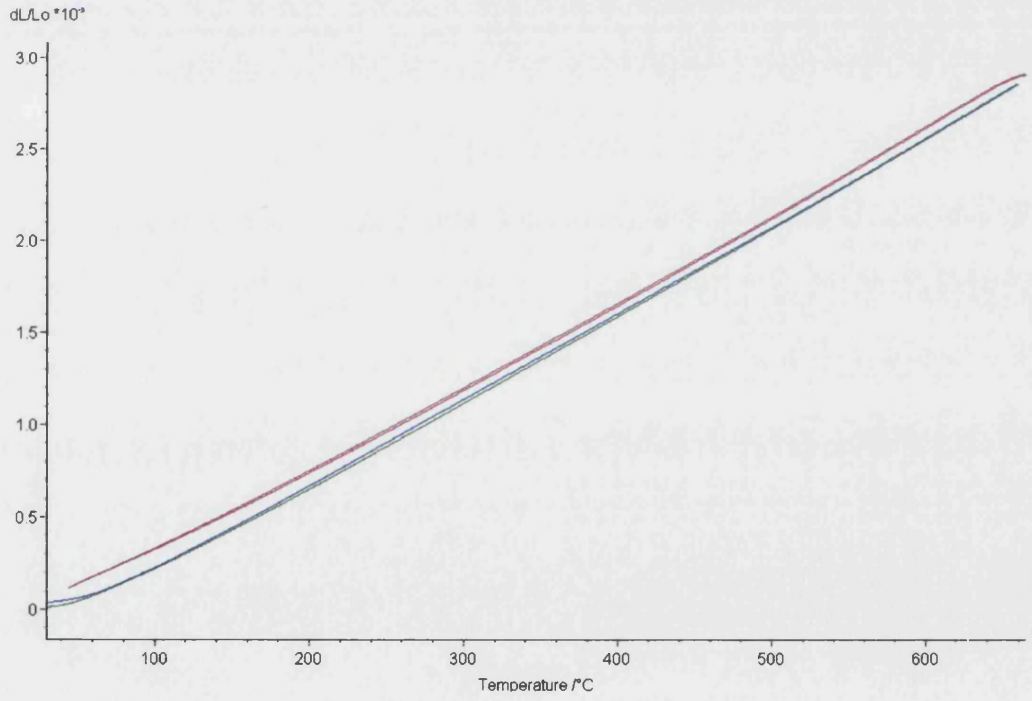

Figure B.53(a). The dilation of Magnox moderator graphite in the Perpendicular direction over two heat cycles.

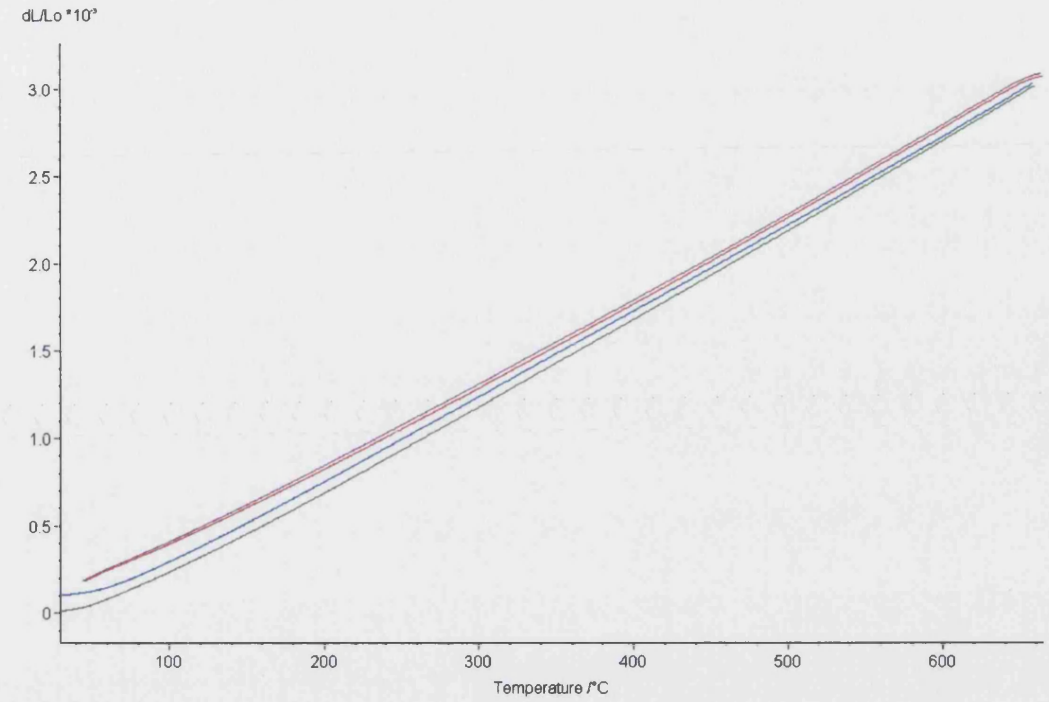

Figure B.53(b). The dilation of Magnox moderator graphite in the Perpendicular direction over two heat cycles showing a greater deviation between the first and subsequent heating cooling curves than in Figure B.53(a).

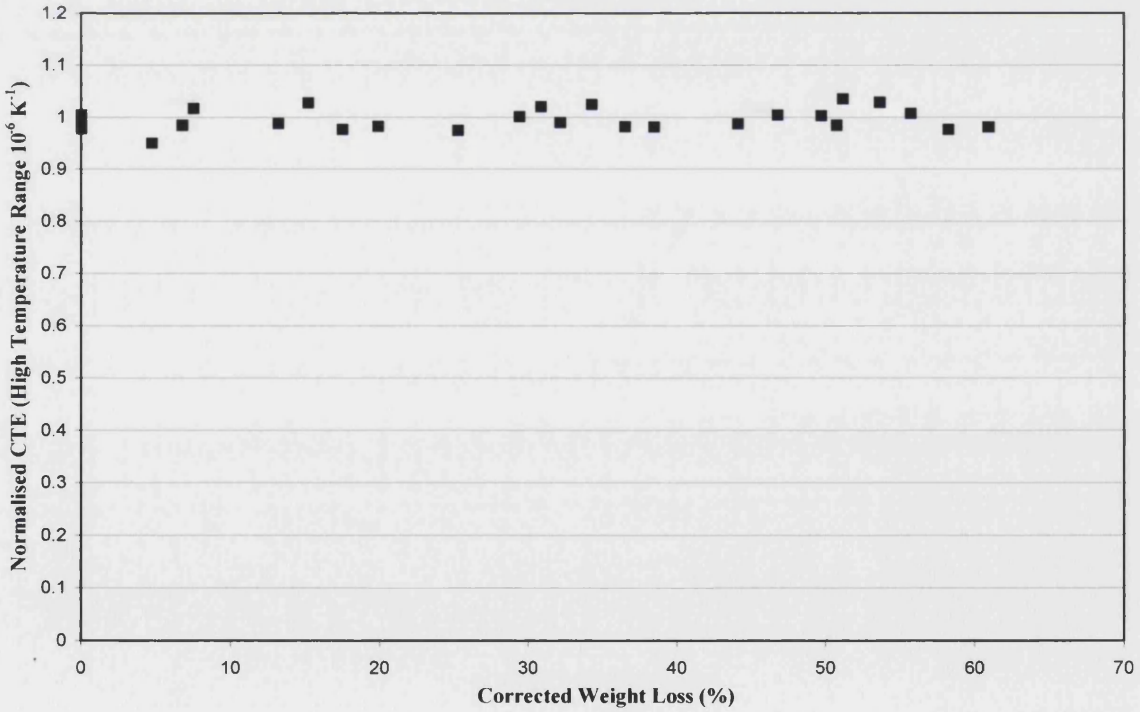

Figure B.54(a). Changes in the CTE of AGR graphite as a function of weight loss by thermal oxidation.

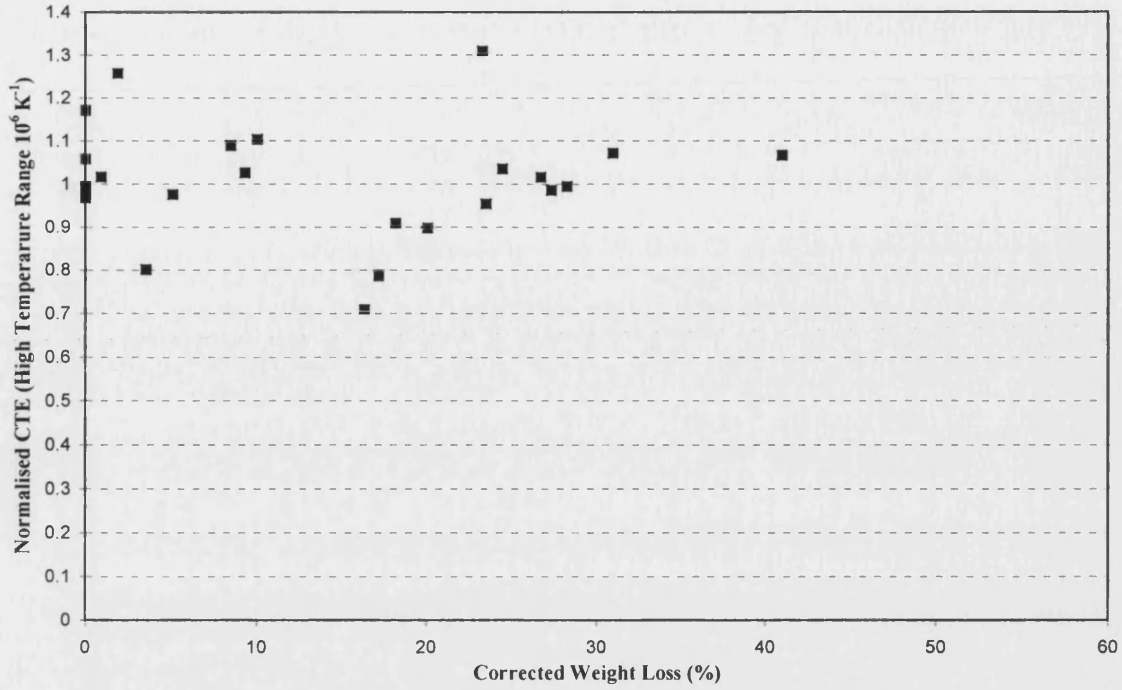

Figure B.54(b). Changes in the CTE of Magnox moderator graphite in the Parallel direction as a function of weight loss by thermal oxidation.

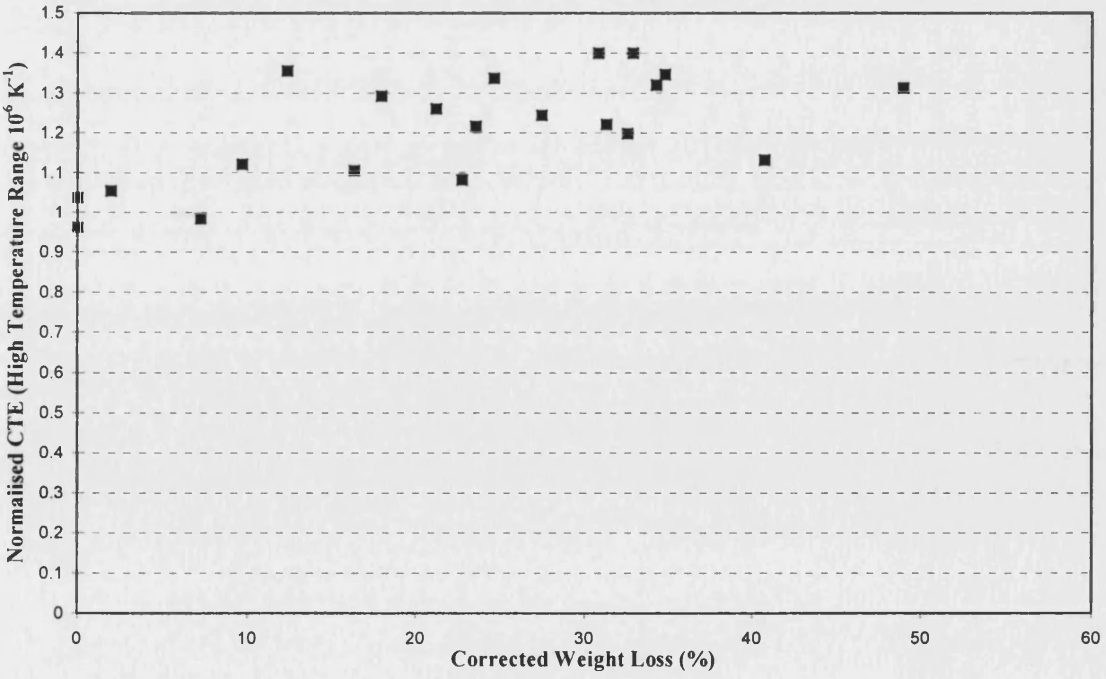

Figure B.54(c). Changes in the CTE of Magnox moderator graphite in the Perpendicular direction as a function of weight loss from thermal oxidation.

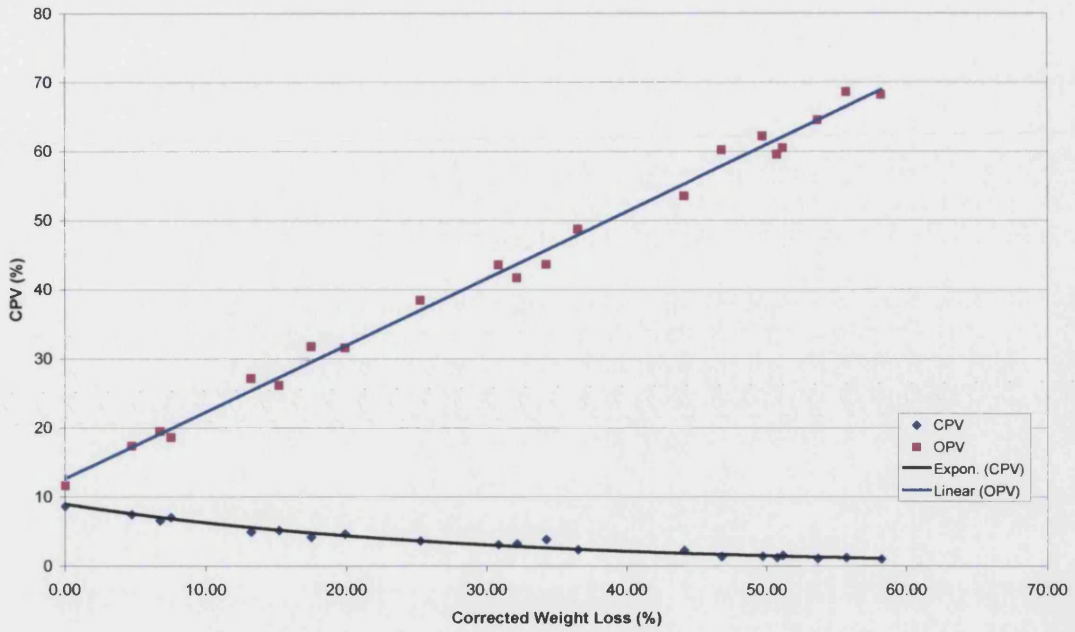

Figure B.55. The CPV and OPV of thermally oxidised AGR graphite as a function of weight loss.

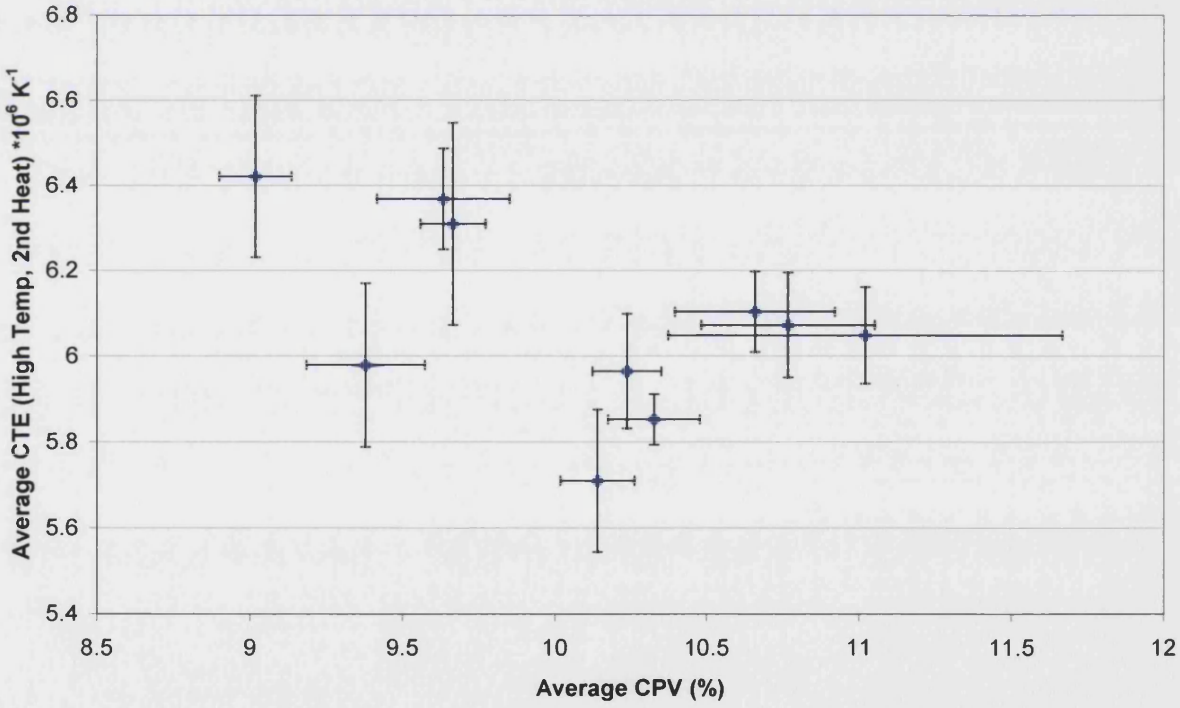

Figure B.56. The relationship between CPV and CTE for different blocks of as received AGR nuclear graphite.

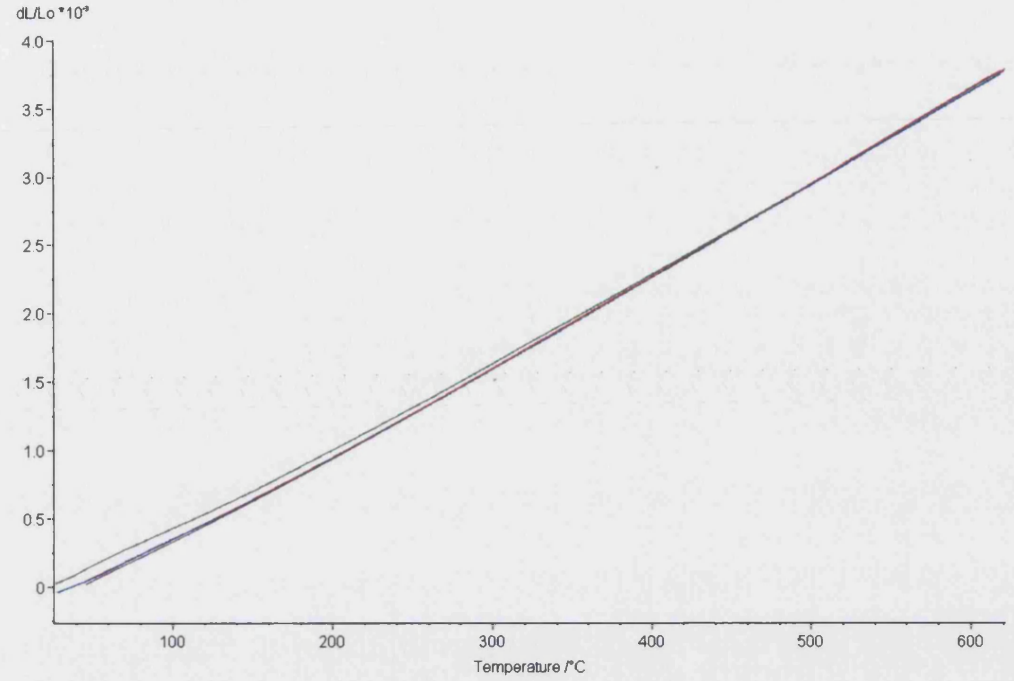

Figure B.57(a). Dilation curve of an AGR graphite sample thermally annealed at 2000°C and cooled rapidly.

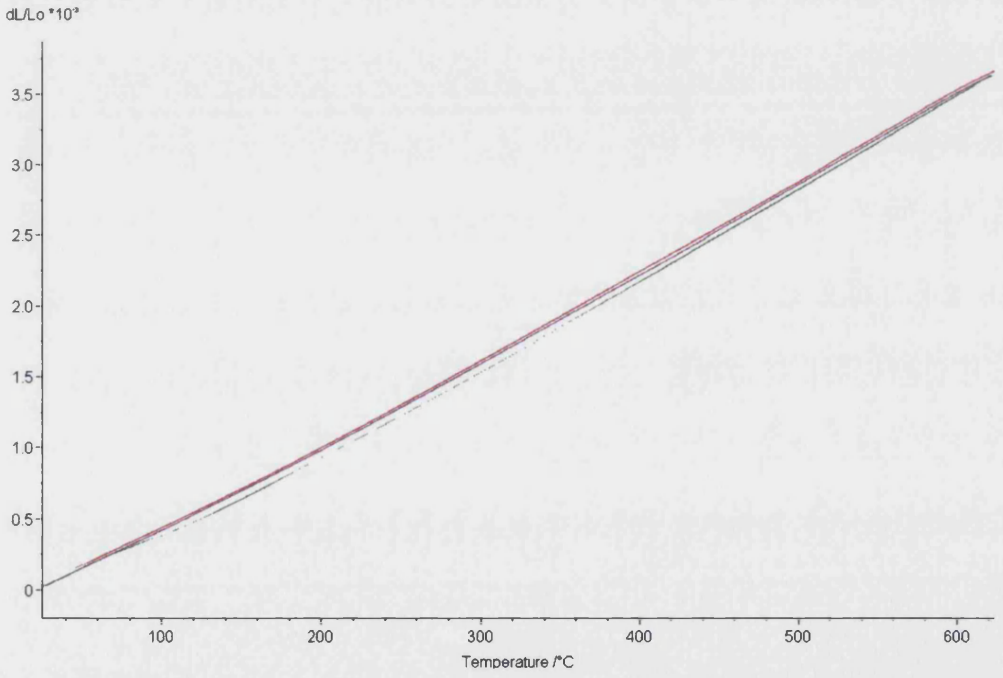

Figure B.57(b). Dilation curve of an AGR sample thermally annealed at 2000°C and cooled slowly.

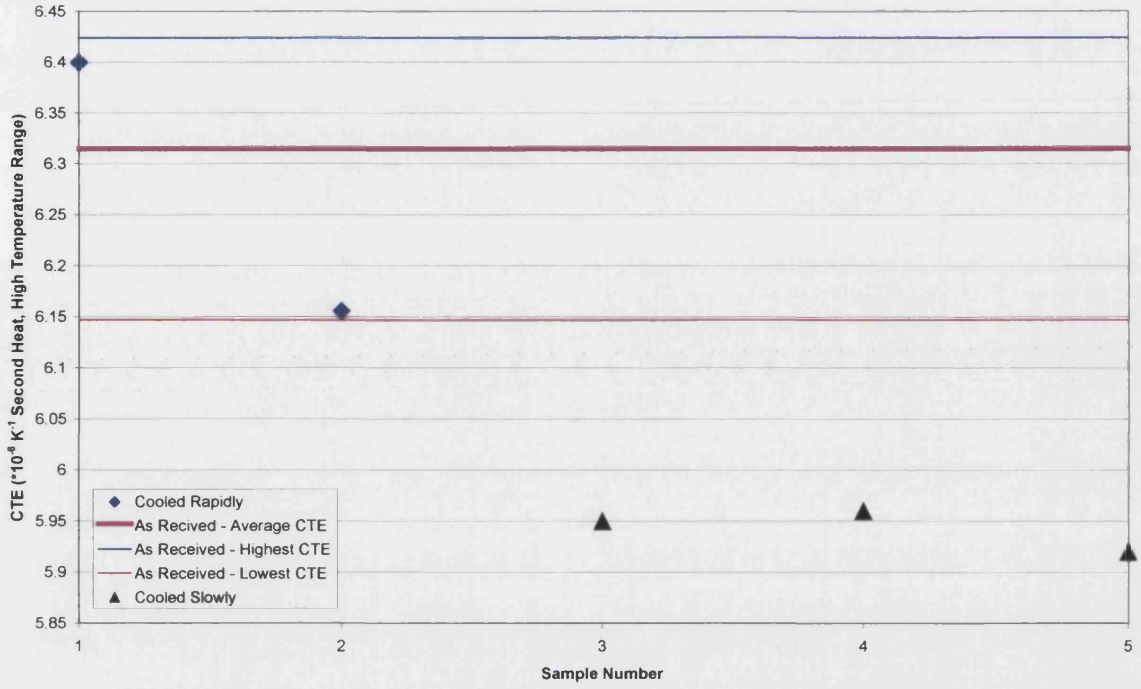

Figure B.58. The CTE of annealed samples of AGR moderator graphite.

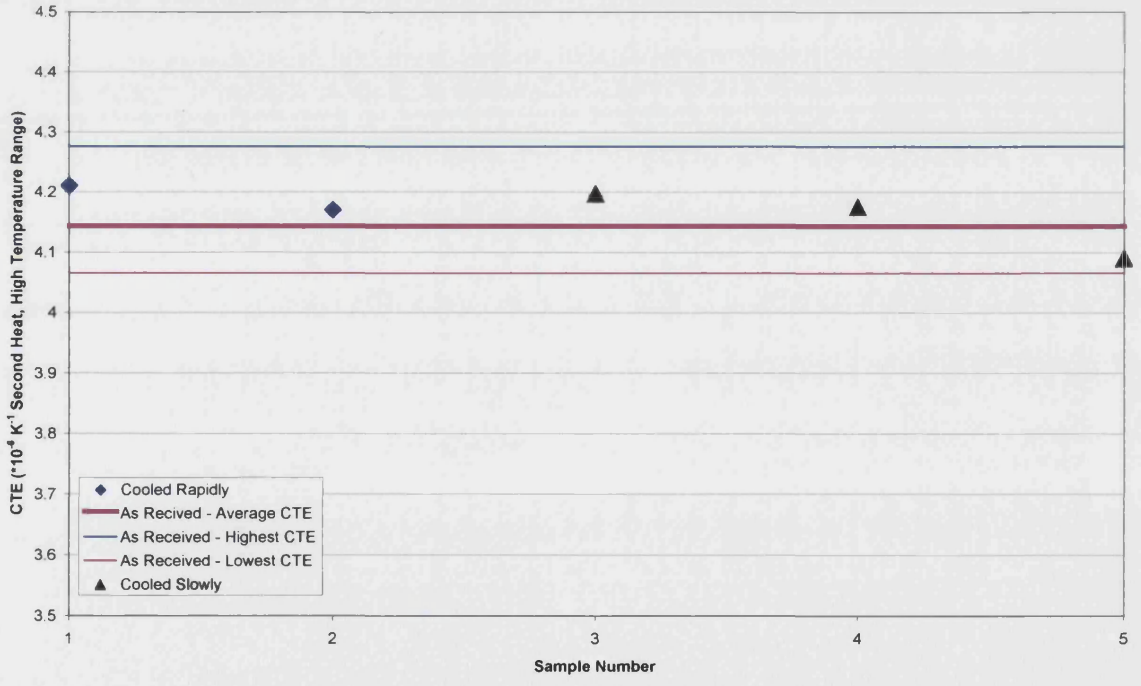

Figure B.59. The CTE of annealed samples of Magnox moderator graphite (samples measured in the Perpendicular direction).

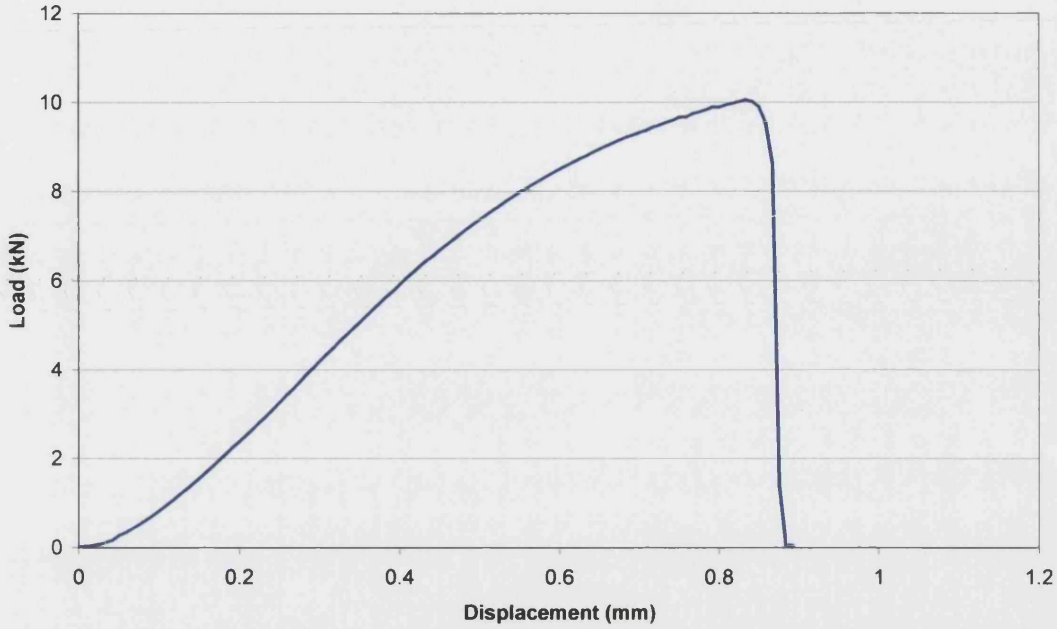

Figure B.60. Load-deflection curve for AGR moderator graphite loaded to failure in compression.

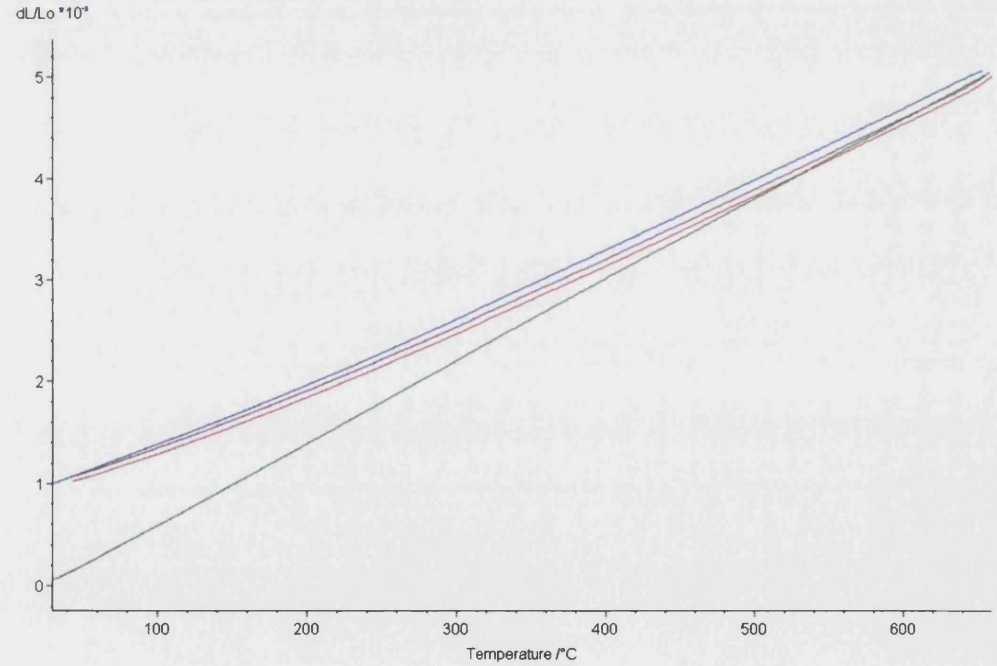

Figure B.61. The dilation curve of a pre-stressed sample (recovery time = zero minutes), showing the difference between the 1st heating segment and remaining segments.

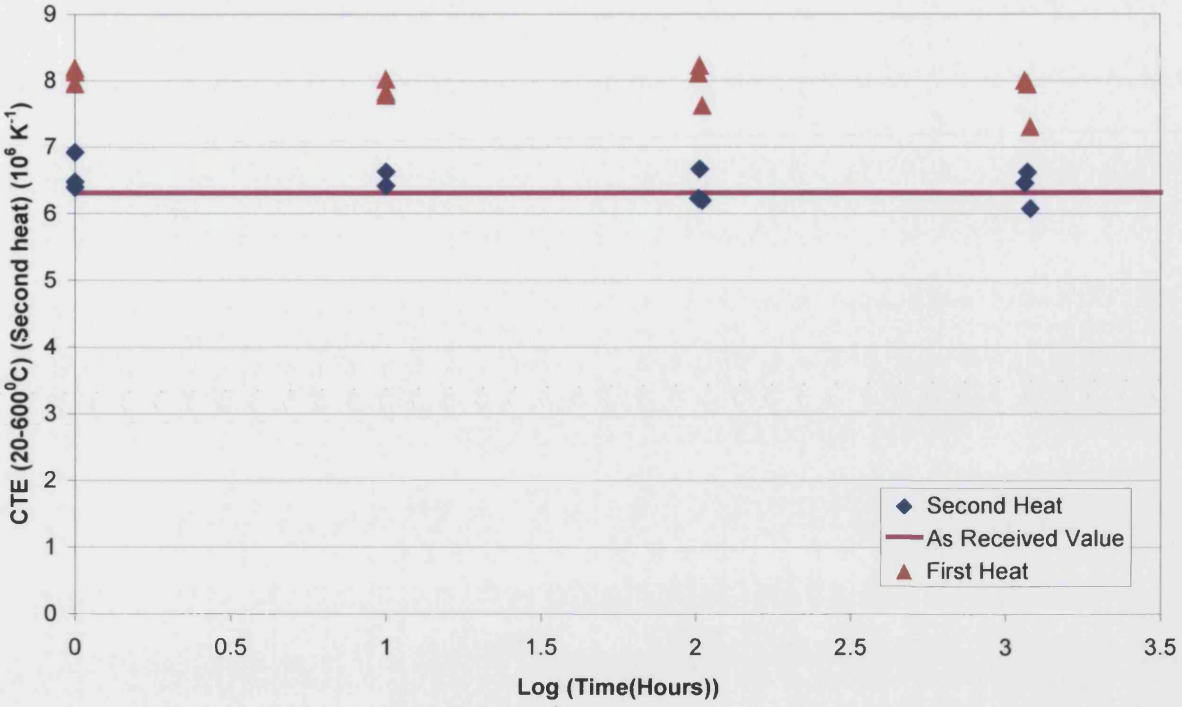

Figure B.62. The average CTE of pre-stressed samples (measured from the first and second heat) as a function of relaxation time. The solid line represents a mean CTE value from five as received samples.

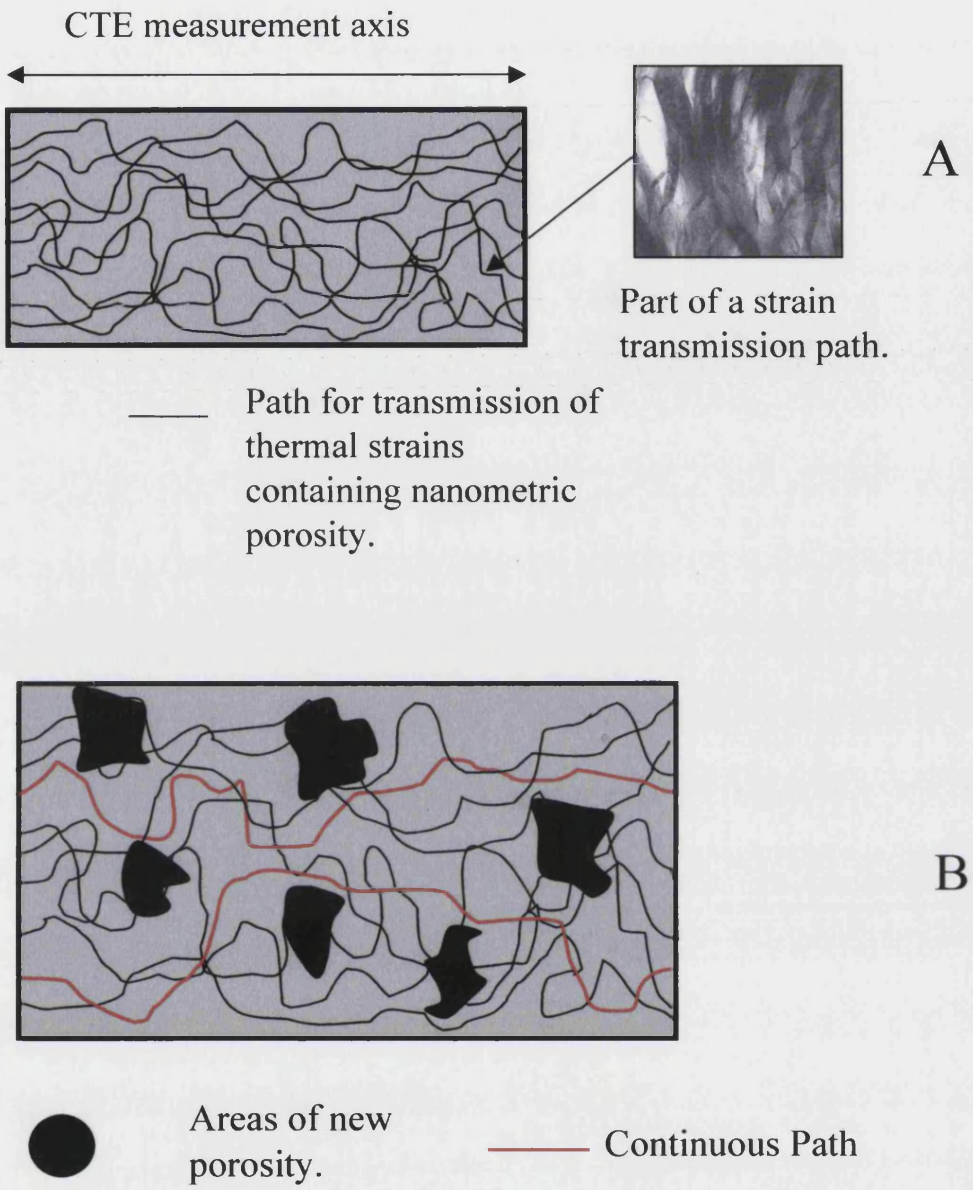

Figure B.63. Schematic illustration of the Continuous Network theory (A) before oxidation and (B) after oxidation.

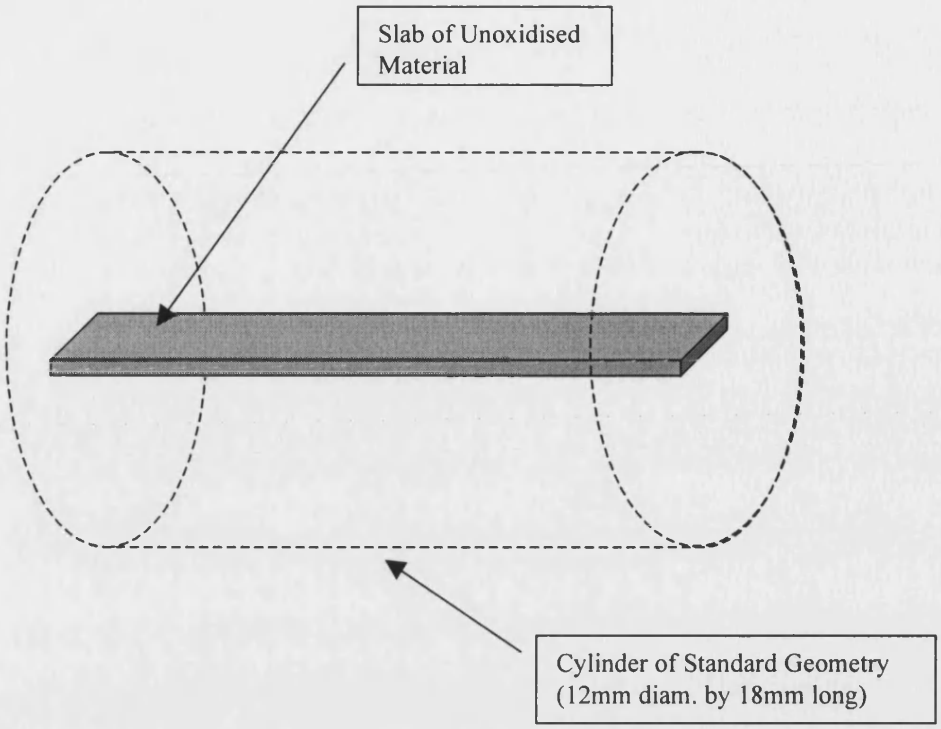

Figure B.64(a). Showing a thin slab of AGR graphite in comparison to a sample of standard dimensions.

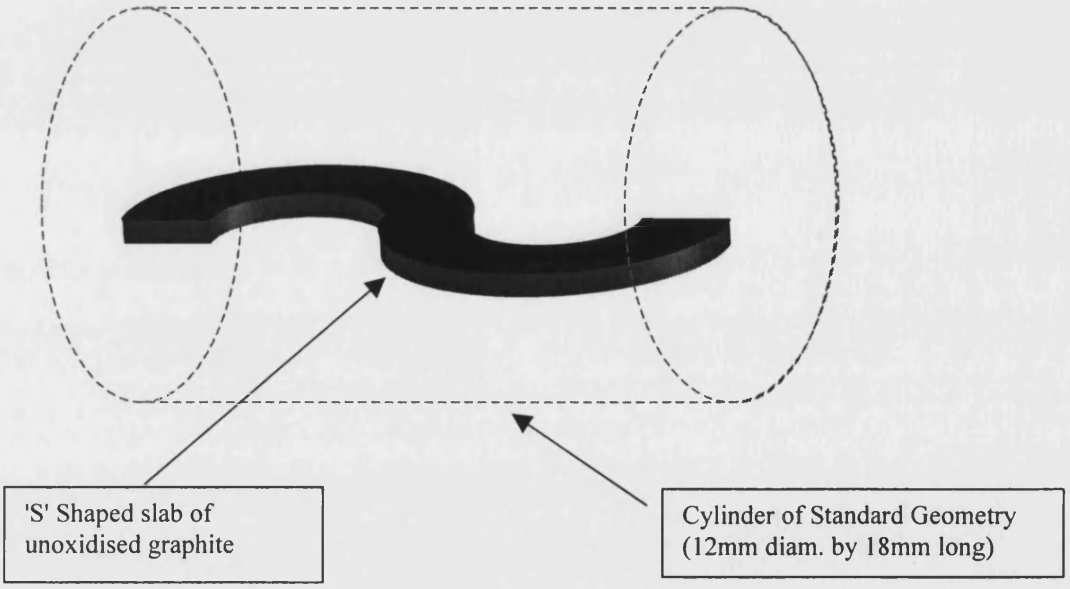

Figure B.64(b). Showing an 'S' shaped thin slab of AGR graphite in comparison to a sample of standard dimensions.

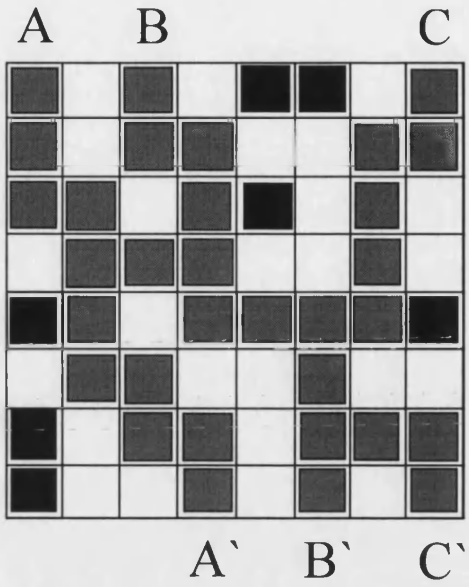

Figure B.65(a). Two dimensional representation of the oxidation of a material as a percolation process. The black cells are solid; the empty cells are pores; and the grey cells are the percolating backbone. (a) Unoxidised material showing a percolating backbone with continuity across the sample from A to A', B to B' and C to C'.

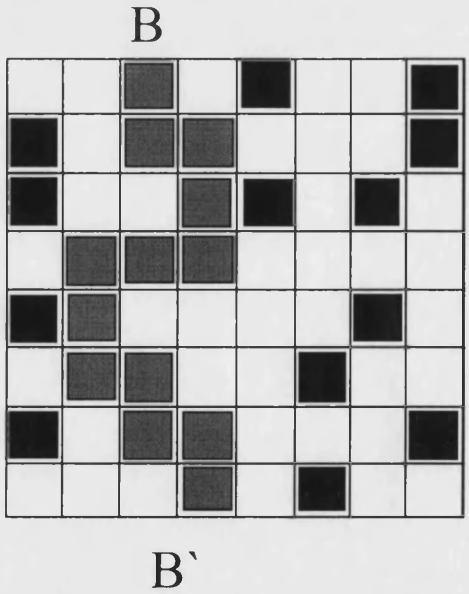

Figure B.65(b). As B.65(a) but oxidised to the percolation threshold.

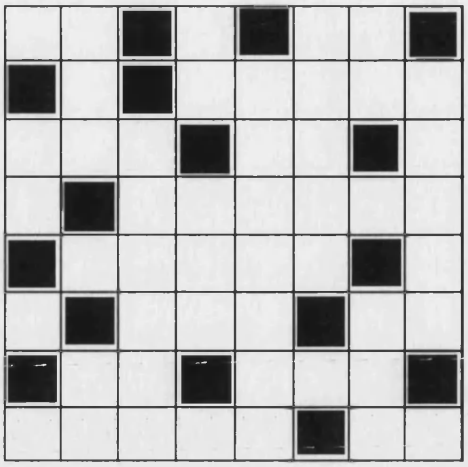

Figure B.65(c). As B.65(a) but oxidised to below the percolation threshold.

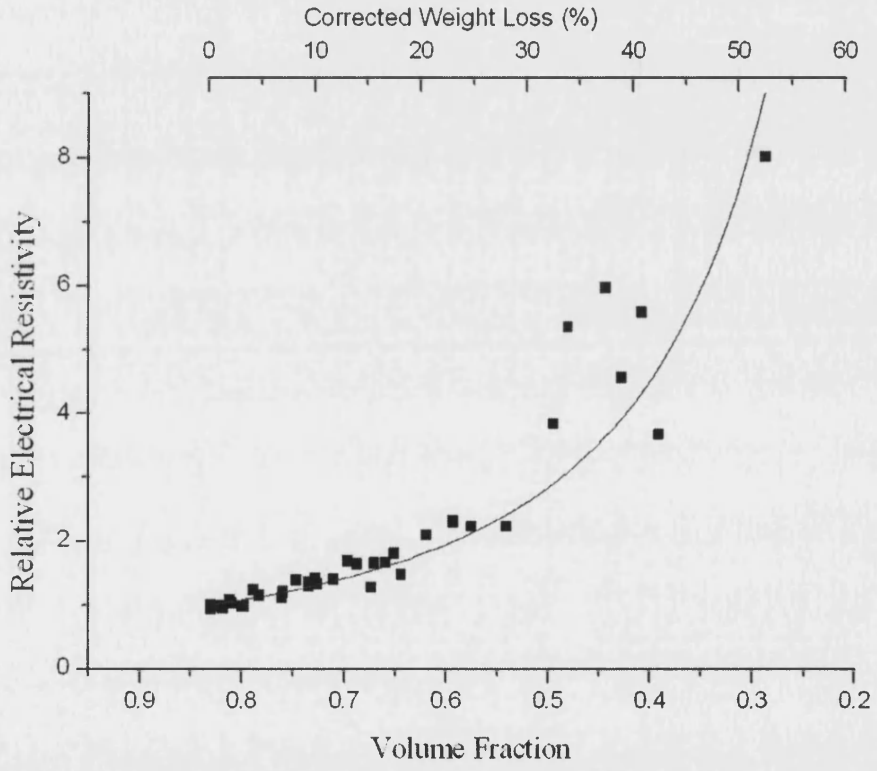

Figure B.66. A plot of the electrical resistivity of AGR graphite (GCMB grade) as a function of thermal oxidation. Resistivities are normalised to that of the unoxidised graphite (173 $m\Omega^{-1}cm^{-1}$). The curve is best fit of the data to equation B8 with p_c = 0.01674.

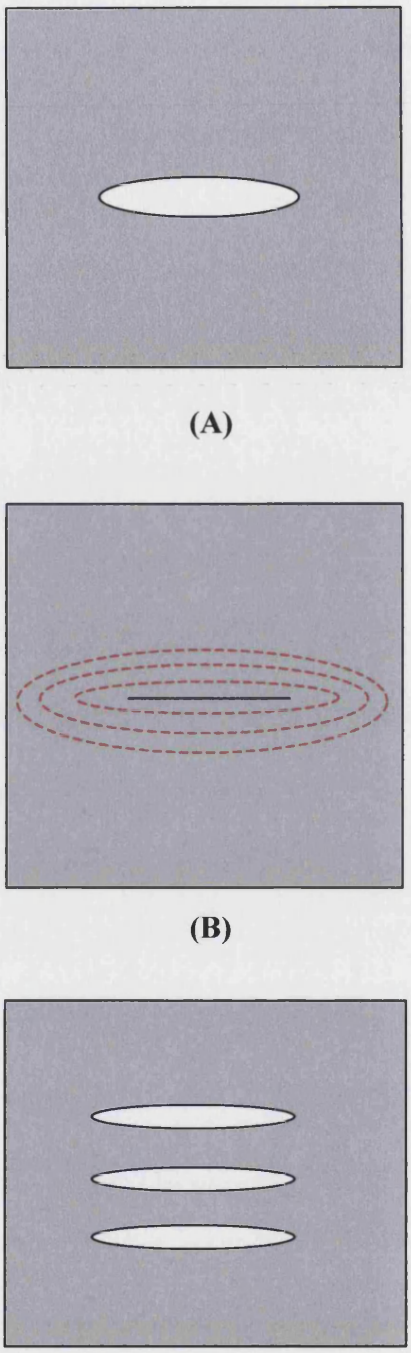

Figure B.67. A schematic of the possible effects of high heat treatment temperatures on the Mrozowski crack porosity in graphite. (A) Mrozowski crack in the graphite before heat treatment. (B) Closure of the Mrozowski crack and the generation of localised stress at high temperature. (C) Subsequent structural reorganisation and generation of additional Mrozowski cracks during cooling.

PART C: MODELLING

Parts A and B have enabled the microstructure of nuclear graphites to be better characterised. In particular the microscopy programme has shown that, at the nanometric scale, the material is continuous with continuity between crystallites. The model of a loose assembly of single crystals is a poor approximation on this scale and therefore, a poor basis for the modelling of CTE.

Another aim of this work is to produce a microstructural model, which better describes the changes in the Coefficient of Thermal Expansion (CTE) of nuclear graphites under neutron irradiation and radiolytic oxidation. Within this part of the thesis a new modelling process is described and implemented such that the important microstructural components identified in Part B are incorporated.

"The important thing in science is not so much to obtain new facts as to discover new ways of thinking about them."

Sir William Bragg

CHAPTER 10
DESCRIPTION OF THE MODELLING APPROACH

The discussions in Parts A and B have highlighted the requirement for a new approach to modelling the CTE of nuclear graphites that incorporate the key microstructural features that have been identified during the course of this work. Within this final part of the thesis a new approach to modelling the CTE of nuclear graphites is presented. The objective of the modelling process is to be able to model the dilation behaviour of AGR (and, as further work, Magnox graphite and other carbon materials) under irradiation and oxidation. This is to be achieved via a 'bottom up' process which involves the abstraction of the problem into a sequence of logical modules that increase in complexity. The modular approach also allows iteration and adjustments to be applied that can carry through the entire model in a comprehensible manner and allows investigation of particular aspects of the model.

The modelling process is described pictorially in Figure C.1 (fold out to A3). The main output at each stage of the modelling process is a dilatation curve ($\Delta L/L_0$) as a function of temperature, over the temperature range of interest for AGR and Magnox graphites (*i.e.* room temperature to 600°C). A flowchart defining the modules and associated objectives and interactions that are defined within this project are shown in Figure C.2. These include the modelling of AGR graphite behaviour under reactor conditions. The remaining modules shown in Figure C.1 (beyond the first hold point) illustrate the possibilities for further work and the wide potential applicability of this approach.

Within this Chapter, the modules shown in Figure C.2 are introduced and Module 1 is discussed. Chapter 11 discusses Module 2 in some detail, Chapter 12 considers Modules 3 and 4 and Chapter 13 presents Modules 5 and 6. A discussion chapter is also included that explores the sensitivity of the input parameters to the model and discusses the results in relation to those observed experimentally. Each module was constructed by writing computer code using Microsoft C++ and executed on an IBM compatible Personal Computer. A CD-ROM in included with this thesis that contains further information on the code generation and also contains a specially compiled version of the code for demonstration purposes.

10.1 MODULE 1: THE SEMI-INFINITE SINGLE CRYSTAL

When modelling the behaviour of polygranular graphites, a simple primary step is to model the single crystal. The simplest starting point is the dilatation of a semi-infinite (infinite in the *a*-direction) single crystal, Module 1 in Figure C1. This has been modelled as a function of temperature from 20^0C to 600^0C. This has been achieved by computing the *c*-axis single crystal expansion, as a function of temperature based upon relationships derived from experimental data. Nelson and Riley (1945) deduced such an empirical relationship between the interlayer spacing, *d*, (in Angstroms) as a function of temperature, *T*, (in degrees centigrade). This relationship was discussed in Part A and is reproduced here as Equation [C1].

$$d = 3.345 + 90.35 \times 10^{-6} T + 6.315 \times 10^{-9} T^2 \qquad [C1]$$

Module 1 generates a dilatation curve from this function. As expected, computation of CTE from this curve gives ~27 x 10^{-6} K^{-1} (between 20 and 600°C) in agreement with single crystal *c*-axis measurements.

10.2 MODULE 2: THE SPHERICAL SINGLE CRYSTAL MODEL.

The motivation for this and successive modules is based upon an extension of Engle's (1971) pictorial representation of needle coke graphite grains as discussed in chapter 2 of Part A (see Figure A.11). It is proposed that a single spherical grain, of arbitrary radius, R_0, is described as a partially ordered array of single crystals containing Mrozowski crack type microporosity (~25nm) and larger scale porosity (~1-100μm) *e.g.* calcination cracks, Figure C.3. This is also consistent with the TEM observations of AGR graphite showing spherical inclusions (*e.g.* Figure B.29) and the arcs of connected ligaments (*e.g.* Figure B.25).

The smallest and simplest element in the abstraction of this situation is the microscopic 'Single Crystal Onion Model' where the radius is of the order of the single crystal stack height (this stack height is called the L_c parameter, see Appendix 2). The concentric centre is assumed to be a point object of zero expansion resulting in the 'onion' model

as shown in Figure C.4. Thus this model represents a two-dimensional abstraction of a randomly orientated array of single crystals and incorporates connectivity in the *a*-axis direction. This abstraction can also be viewed on the granular scale, for example, if each layer within the model is taken to represent the expansion of an entire crystallite then Figure C.4 could represent a simplification of Figure C.3 excluding porosity. This issue of scale is explored as the model develops.

10.3 MODULES 3, 4, 5 AND 6: ASSEMBLIES OF SPHERICAL SINGLE CRYSTALS AND SIMULATION OF REACTOR EFFECTS.

Proceeding according to Figure C1, assemblies of Spherical Single Crystals (SSCs) are considered. The simplest case is an array of SSCs with a constant lattice pitch, Module 3 in Figure C.1. Clearly, if the SSCs are all of the same size, the dilation output will be the same as that of one SSC, however the effects of altering the sizes of individual SSC on the expansion of the bulk can be explored. After completion of this simple array the next step in the progression of the model is the generation of a more realistic assembly of SSCs, again in two dimensions, Module 4, in Figure C.1. To generate this one can consider a methodology of circular packing based upon a "particles in a box" technique (Rodriguez *et al.*, 1986). After packing is complete, another algorithm is employed to expand each SSC and then to transmit that expansion to bulk, as a function of temperature.

The effects of the reactor environment can be simulated by introducing the effects of irradiation and oxidation into the created assembly (Module 6) before modelling the thermal expansion of the modified assembly. In the case of irradiation, data for the dimensional change of single crystals, presented in Part A (Figure A.7), can be used to compute a dilation for each layer of the SSC and the dilation of the each SSC transmitted to the bulk. In the case of oxidation, individual layers of SSCs can be removed from the packed assembly before the thermal expansion is modelled.

CHAPTER 11
MODULE TWO: THE SPHERICAL SINGLE CRYSTAL

Module 2 contains the first abstraction of microstructure and is designed to incorporate structural connectivity between crystallites, by considering a randomly orientated collection of individual crystallites to behave as a fused entity. Although this construction is to be referred to as a Spherical Single Crystal (SSC) the object is modelled in two dimensions.

Within Module 2, the radial expansion of each layer, at a temperature, T, can be modelled as the result of a 'single crystal' c-axis expansion acting in the radial direction and 'single crystal like' a-axis contraction (at low temperatures), resulting in a change of circumference of the layer and hence a change in radius. The c-axis expansion is the same as that of the single crystal and can be computed directly from the previous module, giving a direct c-axis contribution to the change in radius of each layer, Δr_c.

The a-direction contraction (or expansion at temperatures >400°C) is a function of the radius of the layer but also contributes to a change in radius of Δr_a. From the single crystal experimental data for a-axis expansion, the Relative Length Change (RLC) of a single crystal, in the a-direction, as a function of T, is given by the function

$$\left(\frac{\Delta La}{La_0}\right)_T \qquad \text{[C2]}$$

where La_0 is the initial length of the single crystal in the a-direction (typically ~200Å, for AGR graphite, see Appendix 2) and ΔLa is the dilation in the a-direction. In this work, the function C2 has been obtained by first fitting a polynomial (by the least squares method) to existing CTE single crystal data (Entwisle, 1962; Bailey and Yates, 1970; Harrison, 1977) and then integrating this polynomial to obtain the a-direction RLC as a function of temperature.

Following from function [C2], in the spherical model, the change in circumference of a layer, ΔC, at a temperature T, is given by the following expression.

$$\Delta C = \frac{2\pi r_o}{La_0} \times (\Delta La)_T \qquad [C3]$$

where r_0 is the initial radius of the layer (before expansion). Now, as $\Delta r_a = \Delta C/2\pi$, it can be shown that

$$\Delta r_a = r_o \left(\frac{\Delta La}{La_0} \right)_T \qquad [C4]$$

thus, the resultant shift of the single layer, in the radial direction is given by

$$\Delta r_L = \Delta r_c + \Delta r_a \qquad [C5]$$

The RLC of the SSC consisting of n layers, at a temperature, T is therefore given by the function

$$\left(\frac{\sum_{n=1}^{n} \Delta r_L}{R_0} \right)_T \qquad [C6]$$

where R_0 is the initial radius of the SSC. The computer program described for Module 1 has been extended to compute the function [C6] (Module 2) across a temperature range for different values of n. The results are shown in Figure C.5.

Although this module represents the start of the modelling process, several interesting features are produced in the results that may indicate the behaviour of successive modules. The first point to note is the very large initial contraction and subsequent expansion for the case where n>50. This is due to the a-axis contraction, Δr_a, being a function of r_0, (Equation [C4]), whereas Δr_c is independent of r_0. Hence, the a–axis contraction becomes predominant when r_0 is large. Within the literature review presented in Part A, however, little consideration is given to this type of restraint although this work shows that it becomes important in a connected structure.

Based upon these observations, refinements to the model can be made. At present, the model allows free compression of the layers and there are no resistive forces preventing the initial shrinkage of layers, *i.e.* Equation [C5] assumes that Δr_c and Δr_a are additive. In reality, inter-atomic forces between the layers would be expected to resist the circumferential shrinkage explaining why the large initial shrinkage seen in this model are not observed in carbon and graphite materials. In order to overcome this a simple potential can be introduced to restrain the subsequent contraction of each layer onto the lower basal plane

Within this work, a Lennard-Jones type potential (Ibach and Luth (1993)) for interaction between a single carbon atom and an infinite graphene plane has been used as an approximation to that between the layers of the SSC, as given by

$$V = 4\varepsilon\left[\left(\frac{a}{r}\right)^{12} - \left(\frac{a}{r}\right)^{6}\right] \qquad [C7]$$

where V is the potential, r is the inter-atomic distance and a and ε are coefficients. As an approximation, values of a and ε (=3.416 Å and 30.14 eV respectively) were taken from a potential generated by Yin *et al.* (1999) between two carbon atoms.

For each layer of the SSC, at a given temperature, a modified change in radius, Δr_L^* can be computed from the unrestrained change in radius, Δr_L computed in Equation [C5] by the following algorithm.

1. Compute a random number, Q where $0 < Q < 1$.
3. Use Equation [C7] to compute the increase in potential required by a shift in the layer of Δr_L.
4. If $Q < (1/\Delta r_L)$ then set Δr_L^* equal to Δr_L, stop computation.
5. Decrease the magnitude of Δr_L by a small amount, δr.
6. Goto step 1

The effects of the inter-atomic potential on the model are shown in Figure C.6. The initial shrinkage has been reduced and the subsequent expansion has increased from that given previously. However, the role of the *a*-axis contraction still remains important in shaping the dilation curve. Also note the convergence of each curve in Figure C.6 at a temperature of ~450°C. This corresponds to the temperature at which the single crystal CTE in the *a*-direction, α_a, changes sign from negative to positive, *i.e.* $\Delta r_a = 0$. Therefore, at ~450°C, only the Δr_c term contributes to Δr_L.

CHAPTER 12

MODULES 3 AND 4: THE REGULAR AND RANDOM ARRAYS

The next stage in the modelling process is the generation of arrays of SSC (see Figure C.1). This begins with a simple regular array, Module 3, and continues by examining random arrays with variable lattice pitches that resemble the dropping of objects into a box, Module 4. Within this chapter these array generation processes are discussed and typical results are presented.

12.1 MODULE 3 - THE REGULAR ARRAY

The computer code constructed to model this assembly first generates an array, in two dimensions, containing the centre points of each SSC. A randomly selected number of layers, N, is given to each SSC between specified values of N_{min} and N_{max}. The spacing between each SSC (the lattice spacing) is a constant determined by the maximum number of layers, N_{max}. At a given temperature, the expansion of each SSC is computed and the resultant displacements of each neighbouring SSC is passed to the remainder of the lattice, *e.g.* Figure C.7. In this model, any contraction of a SSC will appear as additional porosity within the lattice and therefore is not transmitted to the bulk. After the total displacement of each SSC, at a given temperature, has been computed the dilation of the entire lattice is produced by measurement of the maximum relative linear displacement of a SSC on the edge of the lattice, Figure C.7.

In order to check the consistency of this model with the results generated for single SSCs, a simplified version of this model can be obtained by setting $N_{min}=N_{max}=60$ on a lattice of 10 SSCs square. Plots of the centre points of each spherical single crystal before and after expansion to 600°C are shown in Figure C.8 and the resulting expansion is shown in Figure C.9. As expected, the total expansion is only slightly less than that exhibited by the individual SSC with 60 layers in Module 2 (see Figure C.6). Also the region of zero expansion to ~200°C is also expected due to porosity created during the contraction phase of each SSC. This porosity is subsequently able to accommodate the expansion of SSCs before transmission of strain to the bulk.

This model was investigated by studying the effects of decreasing N_{min} (N_{max} being kept constant at 60 layers) and varying lattice size. The results showed that the relative expansion (at 600°C) is very sensitive to these parameters and becomes zero if the lattice size becomes greater than 100 SSCs square, or the difference between N_{min} and N_{max} is greater than 5. An example dilation curve on a 50 by 50 lattice where N_{max}-N_{min} is set to 5 is shown in Figure C.10. Thus, simply by introducing a SSC size distribution, a decrease in dilation of two orders of magnitude is observed compared to an array of SSC of constant size, Figure C.9. This demonstrates the importance of connectivity between the SSCs in enabling thermal strains to be transmitted to the bulk of the array. It also suggests that a more randomly distributed array of SSCs, as described subsequently in Module 4, is required to realistically represent such connectivity.

12.2 MODULE 4 – THE RANDOM ARRAY

In order to realistically generate a tightly packed array of SSC's, a consideration of numerical sphere packing methodologies is required. Problems concerning the packing of spheres have a long history in the field of mathematics with many simple problems still remaining unsolved. Indeed, one of the most famous, and one of the oldest, problems of discrete geometry concerns the packing of spheres. In 1611, J. L. Keplar asserted that if a number of identical spheres are stacked in a pyramid arrangement then this represents the tightest packing of spheres into the space. This so called 'Keplar conjecture' has only recently been proved (Hales, 1997). With respect to the present study, research has also been conducted on the more general problem of random packing of spheres. Torquato *et al.* (2000) suggest that the packing density of a large, random collection of spheres is dependent upon the way in which the spheres are packed and is not a universal constant.

It is not the purpose of this thesis to study the sphere packing problem *per se*. Within this work a review of approaches used in other related materials modelling problems, for example approaches to model sintered ceramics, has been made. This review suggests that two basic methodologies (Nolan and Kavanagh, 1991) can be applied to the current problem in two dimensions; a static and a dynamic approach. As both of these methods have been investigated here, Module 4 consists of two parts, Modules 4(a) and (b) the dynamic and static solutions, respectively.

Within the dynamic method (Module 4(a)), Figure C.11, SSCs of various diameters are randomly located within a square of lengths B. The value of B is computed from the square root of the number of SSCs that are to be located within the array multiplied by the mean of their diameters. For each SSC, a displacement vector is computed based upon its overlap with adjacent SSCs and gravity over a time-step Δt_1. Each SSC is then moved to the new position and the process iterates until the displacements fall below a critical value. The dilation with increasing temperature is computed in a similar fashion such that at a given temperature, the expansion of each SSC in the array is computed. Overlap then occurs with other SSCs and new displacement vectors are computed over a time-step Δt_2. Again the process iterates until the displacements fall below a critical value. As with Module 3, the dilation of the array is given by the maximum relative linear displacement of SSC on the edge of the array. An example of the results from this model are shown in Figure C.12 for an array of 1000 SSCs of random size between 1 and 60 layers. The expansion is of the same order of magnitude as that given experimentally by AGR graphite although the expansion of the graphite is under-predicted and over-predicted by the model at low and high temperatures respectively. This is encouraging as it indicates that this simple modelling methodology, combined with the graphite single crystal data, enables reasonable prediction of dilation behaviour to be made. The 'steps' in the model, Figure C.12, can be attributed to an artefact of the modelling process that results in the creation of small gaps between adjacent SSCs.

The dynamic modelling process has demonstrated that a more sophisticated solution is required to ensure that contact between each SSC is generated, especially when arrays are small, and thus to remove the 'steps' from the predicted dilation curve. To counteract this problem, a static solution, Module 4(b), to the generation of a random array problem has been generated based upon a 'particles in a box' methodology as discussed by Rodriguez *et al.* (1986), Figure C.13. In this approach, often called a 'drop and roll' algorithm (Torquato *et al.*, 2000), the position of each SSC is computed sequentially by being 'dropped' from a random location at the top of a box of length L. The first contact point, with either the base of the box or another SSC is computed before the SSC is allowed to roll to the second contact point. The stability of the SSC is then checked and if unstable the SSC 'rolls' to the next point of contact. Note that the same process can be employed even when considering SSC of different sizes.

The basics behind the operation of this improved algorithm can be given by example. Consider the situation in Figure C.14 where several SSC, of different sizes, have already been dropped and rolled to a stable position. A randomly assigned x-ordinate ($0< x < L$) has been given to the SSC awaiting placement (the red SSC in Figure C.14) together with an assigned radius, r. The first task is to locate the previously dropped SSC to which the red SSC will make 'first contact' after being dropped. This is achieved by first identifying the SSCs that have boundaries within x-min and x-max, Figure C.14. For each of these identified SSC, the corresponding y-ordinate of the dropped (red) SSC is computed as if it had made contact with that object by Pythagoras theorem, *e.g.* Figure C.15. The SSC that results in the greatest y-ordinate for the dropped object is the SSC of 'first contact' and the position of the dropped SCC is fixed at that position.

The algorithm then models the 'roll' process, in this example, Figure C.15, the dropped SSC will roll to the right. A list of possible 'second contacts' is generated by considering all SSC that overlap, at least partially, with the segment shown in Figure C.15. After the selection of a list of possible second contacts, the value of the y-ordinate of the dropped SSC is first computed as if it had rolled to each of the possible second contact SSCs in turn. An example is shown geometrically in Figure C.16. In order to calculate the co-ordinates of the centre point of the dropped SSC (D), the triangle formed between the centre points of D and the contact SSC (C) and possible second contact SSC (S) has to be considered. Within this triangle, the length of all sides (CD, DS and CD) are known such that the angle between CD and CS, marked θ in Figure C.14, is given by the 'law of cosines' (Thomas and Finney, 1988) where

$$\cos(\theta) = \frac{CD^2 + CS^2 - DS^2}{2.CD.CS} \qquad [C.8]$$

In addition to θ, the angle ϕ in Figure C.16 and hence the y-ordinate of the dropped ball (D) can be computed by basic trigonometry. After each possible second contact has been iterated through in this manner, the SSC that results in the smallest decrease in y-ordinate is chosen as the actual second contact and the dropped SSC is moved to that position. Finally, the stability of the dropped SSC is checked by comparing the x-ordinate of the dropped SSC to that of the SSC of second contact. For example, consider Figure C.17(i and ii) showing an unstable and stable condition, respectively. In

the unstable condition, the process iterates such that the next second contact is sought and terminates when either a stable condition arises or the SSC makes contact with the floor or wall of the 'box'.

After each SSC is dropped and rolled (according to a pre-set size distribution), the expansion process is conducted. This operates in a similar fashion to the dynamic expansion process described previously except that it has been simplified, such that no time step is involved. Thus, after expansion of each SSC a displacement vector is calculated for each object based upon its overlap with any other SSC. The resultant displacements are then applied to the entire array simultaneously. The advantage of this holistic method, as opposed to computing and applying displacements sequentially is that close contact is maintained, there is an instantaneous expansion of the bulk array and the interactions of the entire array on each SSC are modelled. Thus, the array of SSCs can be considered as tightly bound, rather than a loose collection of independent objects.

Following this methodology, the expansion of an array of 1000 SSCs each with a randomly assigned number of layers between 1 and 60 has been modelled, Figure C.18. The effects of the tighter packing are evident with the curve being smooth and continuous in contrast to Figure C.12. However, the under and over predictions of the model at low and high temperatures still persists. The initial period of zero expansion in Figure C.12 can be attributed to the same creation of porosity effects described in Module 3.

CHAPTER 13

MODULES 5 AND 6: SIZE DISTRIBUTIONS AND EFFECTS OF THE REACTOR ENVIRONMENT.

The results from Module 4(b), based upon an array constructed from a simple random size distribution of SSCs, has resulted in modelled dilations of the same order as those obtained experimentally for AGR graphite. Within this chapter composite optical micrographs are used to provide simple filler and binder distributions that can be used as a more refined input into the model. The role of the main phases of the optical microstructure, *i.e.* filler and binder, are considered within Module 5, as shown in Figure C.1. Further, the modelling is extended to include the effects of irradiation and oxidation upon the generated array structure, Module 6. The effects of neutron irradiation and radiolytic oxidation are simulated on each SSC and the expansion of the modified array is then computed in the same manner as that described previously.

13.1 MODULE 5 – SIZE DISTRIBUTIONS

A selection of composite micrographs of different grades of AGR graphite have been prepared by Tomlinson *et al.* (2000). One of these micrographs, reproduced here as Figure C.19 (fold out to A3), has been analysed semi-quantitativly to produce simple filler size distributions. This has been achieved by the identification of the filler particles within the image by reference to the circular distribution of calcination cracks within these regions. Subsequently, each filler particle has been characterised by the approximate measurement of the long axis of each elliptical object. Thus, an approximate distribution of filler particle size within this composite image can be made, Figure C.20. A determination of the percentage area of the image that consists of these filler particles has also been made. From this information, ~20% of the area of the image can be attributed to filler particles which have a mean diameter of ~500 μm.

Initially, the structure viewed in Figure C.19 can be modelled using a simple two-valued distribution. This distribution incorporates the mean filler particle diameter, ~500 μm, the percentage area of filler particles and the size of the image. As the image represents an area of ~ 34 μm^2, the number of filler particles of average diameter (500 μm)

CHAPTER 13

MODULES 5 AND 6: SIZE DISTRIBUTIONS AND EFFECTS OF THE REACTOR ENVIRONMENT.

The results from Module 4(b), based upon an array constructed from a simple random size distribution of SSCs, has resulted in modelled dilations of the same order as those obtained experimentally for AGR graphite. Within this chapter composite optical micrographs are used to provide simple filler and binder distributions that can be used as a more refined input into the model. The role of the main phases of the optical microstructure, *i.e.* filler and binder, are considered within Module 5, as shown in Figure C.1. Further, the modelling is extended to include the effects of irradiation and oxidation upon the generated array structure, Module 6. The effects of neutron irradiation and radiolytic oxidation are simulated on each SSC and the expansion of the modified array is then computed in the same manner as that described previously.

13.1 MODULE 5 – SIZE DISTRIBUTIONS

A selection of composite micrographs of different grades of AGR graphite have been prepared by Tomlinson *et al.* (2000). One of these micrographs, reproduced here as Figure C.19 (fold out to A3), has been analysed semi-quantitativly to produce simple filler size distributions. This has been achieved by the identification of the filler particles within the image by reference to the circular distribution of calcination cracks within these regions. Subsequently, each filler particle has been characterised by the approximate measurement of the long axis of each elliptical object. Thus, an approximate distribution of filler particle size within this composite image can be made, Figure C.20. A determination of the percentage area of the image that consists of these filler particles has also been made. From this information, ~20% of the area of the image can be attributed to filler particles which have a mean diameter of ~500 μm.

Initially, the structure viewed in Figure C.19 can be modelled using a simple two-valued distribution. This distribution incorporates the mean filler particle diameter, ~500 μm, the percentage area of filler particles and the size of the image. As the image represents an area of ~ 34 μm^2, the number of filler particles of average diameter (500 μm)

required to cover 20% of this area corresponds to ~35 SSCs. The remainder of the material (*i.e.* the binder phase) is modelled as a distribution of randomly sized SSCs with diameters up to 200μm (representing the largest iso-chromatic regions viewed on the micrograph). Therfore, approximately 3500 of such objects are required to represent the "binder" regions of the image, based upon a mean SSC size in this random distribution of 100μm in diameter. This results in an array of 3535 objects in total within which the filler particles are distributed randomly. Thus, the macroscopic scale structure of AGR graphite has been crudely approximated. The dilation curve generated from modelling this array is shown in Figure C.21(a) in comparison with the experimentally derived curve. Interestingly, Figure C.21(a) shows that even with a simple distribution, expansion behaviour at temperatures up to 600°C is of the same order as that given experimentally and well approximated as a smooth function. For comparison, the value of $\alpha(20,600)$ obtained from the model is ~40% greater than that derived experimentally.

A more refined distribution can be obtained by incorporating further information from the simple size distribution, Figure C.20. Using the mid-value, a diameter and corresponding number of filler particles can be input into the model as shown in Table C.1.

DIAMETER (μm)	NUMBER IN IMAGE
225	1
317	3
408	7
499	5
589	6
680	1
770	4
861	1

TABLE C.1: The size and number of filler particles to be distributed in the model of AGR graphite.

Incorporation of this particle size distribution with the remainder of the image being modelled as previously, results in the dilation curve shown in Figure C.21(b), showing an improved fit of the model to the experimentally obtained result. Comparison between the $\alpha(20,600)$ value obtained from the model, using the refined distribution, and that obtained experimentally differ by ~22%. Thus, a more refined (yet still simple) distribution produces results even closer to the experimentally derived curve than that shown in Figure C.21(a). Therefore, this second distribution will be used as the basis for modelling the effects of irradiation and oxidation and shall be referred to as the Standard Distribution.

13.2 MODULE 6 – THE EFFECTS OF NEUTRON IRRADIATION AND RADIOLYTIC OXIDATION

Within this section the modelling is extended to include the effects of irradiation and oxidation on the generated array structure. Each of these effects is simulated on each SSC of the Standard Distribution and the expansion of the modified array is then computed in the same manner as that described previously.

13.2.1 Irradiation Effects

The effects of irradiation can be applied to each SSC by using the data of the dimensional change of HOPG under irradiation obtained by Kelly and Brocklehurst (1971). These data have been discussed in Part A and presented in Figure A.7(a and b). For irradiation temperatures >400°C, the dimensional change, with fluence, in both the *a* and *c* directions can be well approximated by linear relationships (Neighbour, 2000)

$$\frac{\Delta X_c}{X_c} = 0.00125\gamma \qquad \text{and} \qquad \frac{\Delta X_a}{X_a} = -0.00055\gamma \qquad \text{[C.9(a,b)]}$$

where $\Delta X_c/X_c$ and $\Delta X_a/X_a$ are the fractional dimensional changes in the *c* and *a* directions respectively and γ is the fluence (in n/cm^2 x 10^{20} (EDN)). In a similar manner to the calculation of the thermal expansion of each layer within the SSC described in Module 2, the irradiation-induced change in radius of each layer is computed from each

of the a and c components. Therefore, the a-axis dilation contributes to the radial expansion by an amount Δr_a. For a given layer, at a fluence, γ, this is given by the following

$$\Delta r_a = r_o \left(\frac{\Delta X_a}{X_a} \right)_\gamma \qquad [C4]$$

where r_0 is the initial radius of the layer. As in the thermal case, the c-axis thermal expansion contributes directly to the radial expansion by an amount Δr_c such that in this case

$$\Delta r_c = \left(\frac{\Delta X_c}{X_c} \right)_\gamma L_c \qquad [C5]$$

where L_c is the crystal stack height parameter, discussed in Appendix 2. The total relative radial change of the SSC over n layers is then given by the function [C.6.]

$$\left(\frac{\sum_{n=1}^{n} (\Delta r_c + \Delta r_a)}{R_0} \right)_\gamma \qquad [C6]$$

where R_0 is the initial radius of the SSC.

After each SSC has undergone an irradiation induced expansion of this type, the array is reorganised by utilising the expansion algorithm described in the previous chapter *i.e.* displacement vectors are computed for each SSC based upon its overlap with its neighbours. This reorganised array is then subjected to the same thermal expansion process as outlined previously. The resulting dilation curves of arrays subjected to a fluence of 30 and 160 x 10^{20} n/cm^2 (EDN) are shown in Figure C.22 together with the dilation curve produced previously by the model in Module 4(b). In all cases the Standard Distribution, as shown in Table C.1, was used. These results indicate that the small increase in CTE at low fluences followed by the rapid decrease observed experimentally for AGR graphite has been simulated. In addition, the model has been

executed at a range of different fluences to 200 x 10^{20} n/cm^2 (EDN), each producing dilation curves of the same form as those in Figure C.22. The average CTE (between 20 and 120°C) has been computed for each of these curves and the results are shown in Figure C.23 in comparison with the 'accepted' curve for the CTE behaviour of AGR graphite irradiated at 600°C (previously discussed in Part A, chapter 3, section 3.3). The results of the model compare favourably with the experimentally derived curve. Interestingly, at very high fluences (beyond those obtained experimentally) the model predicts a rapid fall in CTE. This can be considered as a percolation limit and can be attributed to a loss of integrity across the sample such that thermal strains can no loner be transmitted. In comparison to the percolation limit found in Part B (see chapter 9, section 9.4) for the effects of oxidation on CTE, the percolation limit, in terms of neutron irradiation damage, also appears to be high at ~200 x 10^{20} n/cm^2 (EDN).

13.2.2 Radiolytic Oxidation Effects

Radiolytic oxidation effects can be incorporated simply by random removal of individual layers of each SSC. The studies conducted in Parts A and B have indicted that the binder phase of AGR graphite oxidises preferentially to the filler phase for both radiolytic and thermal oxidation. Thus in this modelling work, until ~20% weight loss, the effects of oxidation are incorporated such that material is only to be lost from the binder regions (those SSCs with diameters of 200μm or less). SSCs that are chosen to be "oxidised" in this manner are selected randomly in a process that iterates until the desired weight loss is achieved. The process begins with the creation of an array of SSCs according to the Standard Distribution (see section 13.1). This is then modified by "oxidation" to an arbitrary weight loss, as described. The modified array is then subjected to the same expansion process that is discussed in Chapter 12, whereby expansion into created porosity is permitted, Figure C.24. The modelled dilation curves for weight losses from 0-80% are shown in Figure C.25. In support of the experimental results presented in Part B, oxidation appears to have very little effect on CTE to high weight losses, Figures B54(a-c). However, in the model, CTE rapidly decreases to zero (*i.e.* reaches its percolation limit) above 60% weight loss whilst experimental results show that some samples can be oxidised in excess of 60% without any significant reduction in CTE. The application of percolation theory to CTE (discussed in Part B, chapter 9, section 9.3) suggests that the percolation limit for CTE may be > 90%. Also,

the dilation curves above 30% weight loss show some localised deviations from linearity. These discrepancies between modelled and experimental behaviour are likely to be an artefact of the finite size of the array and the fact that the model is not 3-dimensional. Also, the roughness of some of the modelled curves at weight losses > 40% is due to the localised expansion of elements of the array that have become detached from the bulk. Although this is a limitation of the model, these features are evidence of the severe structural disruption occurring, although the continuity of the bulk continues to be maintained.

CHAPTER 14
DISCUSSION OF THE MODELLING RESULTS

This part of the thesis has presented a new modelling methodology that describes the CTE of AGR moderator graphite both as received and under irradiation and oxidation. This has been achieved by the generation of an abstraction of the complex microstructure, based upon the observations made in Part B. By using simple filler particle size distributions obtained from composite optical microscopy of AGR graphite the results of modelling this material, both as-received and under reactor conditions, has been shown to compare reasonably with experiment.

The aim of this discussion chapter is to explore the model further. Firstly, by identification of the input parameters and the sensitivity of the output (the dilation curve) to these parameters. Secondly, the relationship between the abstracted simplification of the microstructure and the complexities of the actual microstructure are discussed.

14.1 MODEL INPUT PARAMETERS AND SENSITIVITY

The previous chapters have shown that a simple filler size distribution and the abstracted modelling approach can predict the properties of AGR graphite with a fair degree of success. Also it is encouraging that this model has been generated with a small number of input parameters each of which are presented in Table C.2 together with a brief physical description and outline of its use in the model. The generation of appropriate values for each of these parameters has been made with reference to either existing single crystal data or microstructural information, as indicated in Table C.2. In the case of the properties derived from single crystal data, these values are obtained directly and quantitatively from previous experiments. However, in the case of the parameters derived from microstructural information the need for abstraction and simplification for use in the model results in these being obtained by semi-quantitative methods and, as such, these parameters are subject to more ambiguity than those derived from single crystal data.

INPUT PARAMETER	DESCRIPTION	FUNCTION	TYPE
ΔL_c	Single crystal c-axis dilation. Given by the fit to experimental data given by Nelson and Riley (1959)	To represent the c-axis dilation contribution within each layer of an SSC	Single Crystal
$\Delta L_a/L_a$	Single crystal a-axis relative expansion. Given by a fit to various experimental data	To represent the a-axis dilation contribution within each layer of an SSC	Single Crystal
$\Delta X_c/X_c$	Irradiation induced dimensional change of the single crystal in the c-direction	To represent the c-axis irradiation induced expansion within each layer of an SSC	Single Crystal
$\Delta X_a/X_a$	Irradiation induced dimensional change of the single crystal in the a-direction	To represent the a-axis irradiation induced expansion within each layer of an SSC	Single Crystal
L_c	Nominal size of a single crystal in the c-direction (stack height)	Used to determine the number of layers in an SSC of a given size	Single Crystal
N_t	Total number of SSCs in the array	Determines the size of the modelled array	Microstructural
N_f	Number of SSCs representing filler particles	To incorporate the amount of the array representing filler particles	Microstructural
N_b	Number of SSCs representing binder particles	To model the microstructure of binder phase of the material	Microstructural
D_f	The distribution of SSCs representing filler particles	To model the microstructure of the filler phase of the material	Microstructural
D_b	The distribution of SSCs representing binder particles	To model the microstructure of the binder phase of the material	Microstructural

TABLE C.2: The model input parameters.

In addition to the parameters shown in Table C.2, particular irradiation fluences and oxidation weight losses are also input where required, however these relate to effects on the modelled array and do not affect the generation of the array itself.

14.1.1 Model Sensitivity to Changes in Single Crystal Parameters

The sensitivity of the modelled dilation of the unirradiated material was investigated first followed by an investigation of the irradiation sensitive parameters. Using the Standard Distribution, each of the Single Crystal input parameters, ΔL_c, $\Delta L_a/L_a$ and L_c (the irradiated dimensional changes are discussed subsequently) were changed by 10%. Each variable was changed in isolation and the resulting dilation curves are shown in Figures C.26 (a-c) compared to the original modelled dilation of the Standard Distribution.

The sensitivity of the dilation curve to changes in *c*-axis expansion, Figure C.26(a) are related directly to increases in the radial dilation of each SSC. A change in the *c*-axis expansion therefore results directly in a change in expansion of the array without a severe modification to the shape of the dilation curve. However, some regions showing deviations from the continuous form of the unmodified dilation curve suggest that elements of the structure may be detached from the bulk of the array.

In Figure C.26(b), decreasing the *a*-axis expansion results in an increased dilation at temperatures < 450°C and a decreased dilation at temperatures of 450°C to 600°C. Increasing the *a*-axis expansion has the opposite effect. This can be readily understood by consideration of the contribution made by the *a*-axis expansion on the dilation of individual SSCs. At low temperatures the effect of a negative value for α_a is to constrain the radial expansion. At temperatures > 450°C, α_a becomes positive and the radial expansion is enhanced. In both cases, although the shape of the dilation curve is significantly altered, the expansion to 600°C is only altered by ~10%.

In Figure C.26(c), changing the L_c parameter results in an inversely proportional change in dilation. As the L_c parameter dictates the number of layers within an SSC of a

particular size, increasing L_c decreases the number of layers and hence the *a*-axis contribution to expansion and *vice versa*. This explains why, although the expansions at a given temperature are different, Figure C.26(c) is of a similar form to Figure C.26(b).

In the case of modelling the irradiated material, the effect of increasing the irradiation induced dimensional changes by 10% is shown in Figure C.27(a and b) for the *c* and *a* directions, respectively. Each figure contains dilation curves at 30 and 160 x 10^{20} n/cm^2 (EDN) and is again compared to the unmodified dilation of the Standard Distribution, originally presented in Figure C.22. Consideration of both Figures C.27(a and b) indicates that at low fluences the expansion is insensitive to changes in the single crystal dimensional change expansion. However, at higher fluences dilation is affected. In the case of changes to the *c*-axis irradiation induced dimensional change parameter increases or decreases results in respective changes in the dilation curve as a direct result of the change in structural disruption. In the case of changes to the *a*-axis irradiation induced dimensional change parameter, the shape of the dilation curve is altered although the overall dilation at 600°C remains unchanged.

14.1.2 Model Sensitivity to Changes in Microstructural Parameters

The use of the Standard Distribution in the modelling process has resulted in expansion behaviour that is similar to that seen experimentally for as-received, irradiated and oxidised AGR graphite. The sensitivity of these input parameters can be explored in a similar manner to the single crystal parameters. However, the semi-quantitative method of generating the microstructurally based parameters results in a greater inherent uncertainty in their applicability than for the well defined single crystal parameters. Within this section, the effects of altering the Standard Distribution shall be considered.

The effects of altering the number of SSC defined by the Standard Distribution (whilst maintaining the shape of the distribution itself) is shown in Figure C.28 (note that the standard distribution dilation and those for 4000 and 3000 objects overlap) where distribution sizes above ~3000 SSCs are found to converge. As the computational time required to generate a solution increases as the square of the number of SSC it rapidly becomes impractical to compute array sizes in excess of 4000 objects (the array of 4000 objects took around five days to compute on a Pentium III system running at 500MHz).

However, these results have shown that the number of objects defined in the Standard Distribution are shown to be of a suitable number to closely approximate the behaviour of very large lattices, within the computational time constraints, at least in the absence of oxidation.

The proportion of filler/binder SSCs can also be readily altered. For example, Figure C.29 shows the effects of increasing and decreasing the filler percentage by 10% at the expense of binder SSCs. In this case the variation slightly alters the shape of the curve although the total expansions at 600°C only differ by ~3% from the Standard Distribution.

Altering the form of the standard distribution is also possible. For example, Figure C.30 shows the effects on the dilation curve of increasing the number of the largest sized SSCs (those in the diameter range 817-906 μm and 726-816 μm) by those in the smallest diameter category (180-270 and 271-363 μm). The results show the reduced dilation of the array at low temperatures, followed by a more rapid increase, and are commensurate with an increased contribution to expansion from larger SSCs.

These sensitivity studies have shown that altering both the single crystal and microstructural parameters has a comparable or reduced affect on the value of the modelled dilation at 600°C. For example, a 10% increase in the number of filler particles only results in a ~3% increase in dilation. However, changes to the single crystal parameters and the form of the standard distribution substantially alter the shape of the modelled dilation curve *e.g.* Figure C.26(b).

14.2 THE COMPARISON BETWEEN THE MODEL AND REALITY.

The modelling process described, using a small number of readily identifiable parameters, has produced results consistent with those obtained experimentally for AGR graphite. Further, the sensitivity of these input parameters has been explored. This section focuses upon a discussion of the modelling mechanisms operating during each module. In particular, these mechanisms are discussed in the context of the theoretical and experimental results described in Parts A and B of this thesis.

The microstructural study presented in Part B indicates that individual graphite crystallites exist in a complex interconnected network. Connectivity was incorporated in Module 2 with the introduction of the concept of SSCs. The mechanism generating the connectivity in the SSC has been fully described, however intuitively, connectivity in the real material would suggest that the nature of actual connectivity is likely to be much more complex. Although the current model provides close contact between SSCs even during the expansion process this only approximates the long range connectivity that has been shown to exist throughout the bulk of the material (*i.e.* the ligament structure, see Part B, chapter 9, section 9.6). Thus the degree of restraining of expansion of individual crystallites by some interaction with the bulk is likely to be greater and more complex than that modelled here, implying the generation of complex internal stresses. Indeed, the pre-stressing work conducted in Part B indicates that internal stress plays an important role in determining the thermal expansion of the aggregate (see the discussion in part B, chapter 9, section 9.5).

Consideration of the behaviour of the regular assembly of SSCs arranged on a regular lattice (Module 3) indicates the importance of connectivity between individual SSCs in the model. This agrees with the Continuous Network Theory and the percolation modelling approach discussed in Part B as methods of describing the insensitivity of CTE to oxidation. Also, these results demonstrate the importance of porosity. In particular, small scale porosity that acts to reduce connectivity, can significantly reduce the thermal expansion of the aggregate. Again, the experimental and theoretical studies have identified small-scale porosity created during cooling from graphitisation temperatures as being important in controlling thermal expansion behaviour.

The results from Module 4(a), the dynamic random array, show the importance of maintaining connectivity between SSC during the array generation stage and also during the expansion process. Apart from the "steps" in the dilation curve, which have been commented upon, the next striking observation is that the expansion is of the order of that of AGR graphite. After improvement of the array generation and expansion process, Module 4(b), the resulting dilation curve is smooth and of the same order as that found experimentally. One of the most important contributing mechanisms to the modelled dilation curve is the holistic expansion process. This process, conducted on

the entire array simultaneously, has the effect of causing the displacements of individual SSCs (comparable to an internal disruption process) to have some dependence on the displacement of the bulk. From the microscopial evidence presented in Part B, it is likely that this is also true for the real material, due to the connected ligament structure, and is likely to be another important element in influencing CTE behaviour.

In addition to structural connectivity, Parts A and B also identified the distribution and nature of Mrozowski crack porosity as being important in influencing CTE behaviour. However, it was also shown that the exact nature of this accommodating porosity and the way in which it interacts with elements of the microstructure to modify the thermal expansion of the entire aggregate is extremely complex and poorly defined. Within the modelling process, porosity has been added by virtue of the method of array construction alone *i.e.* no porosity input parameters are required. Indeed, the modelling methodology described in Module 4(b) has also enabled a complex range of porosity to be created. Consider, for example, Figure C.31 that shows the typical arrangement of SSCs generated within Module 4(b) and demonstrates the complex porosity formed between SSCs. Moreover, some of this porosity is acting to accommodate the expansion of individual SSCs, either fully or partially, analogous to Mrozowski cracks (described in Parts A and B). Further, Figure C.31 shows a 'snapshot' of an array structure that will change and evolve subtly (together with the structure of the entire array) as the expansion proceeds and SSC are shifted. Also, the dotted line in Figure C.31 demonstrates the existence of structural connectivity that exists throughout the tightly packed array that is analogous with the Continuous Network Hypothesis and percolation theory based arguments developed in Part B (see chapter 9 sections 9.3 and 9.4). Within the real material Mrozowski cracks are intra-crystalline. Within the model, however, porosity has been generated outside of individual SSCs, yet accommodation is still being provided to modify the expansion to that observed experimentally. This implies that the ability of porosity to accommodate expansion before transmission of strain to the bulk may be more important than location within the material.

The model has also been successfully applied to modelling the effects of irradiation and oxidation. In the case of the former, the irradiation-induced expansion of each SSC, followed by the use of the holistic expansion process first appears to rearrange the SSCs in a tighter configuration to that when they were originally placed, leading to a higher

thermal expansion. Increasing expansion of each SSC disrupts the connectivity between individual objects and the expansion rapidly decreases. This parallels the mechanism of porosity closure and subsequent structural disruption, described in Part A (see chapter 3, section 3.3) and is also in agreement with the thermal simulation of irradiation effects conducted in Part B (see chapter 8, section 8.1).

In summary, the modelling process has successfully approximated the behaviour of AGR graphite both as-received and under reactor conditions. It also appears that the modelling process has not only incorporated the important microstructural elements of AGR graphite in relation to CTE but has further helped to refine the understanding of some of these elements. In particular, structural rearrangement and interaction with the bulk of the material have been identified as being important additional parameters in addition to small-scale porosity and structural connectivity identified in Parts A and B. Thus, although both the real and modelled microstructures are complex these abstractions appear to have captured the most important elements with respect to CTE changes.

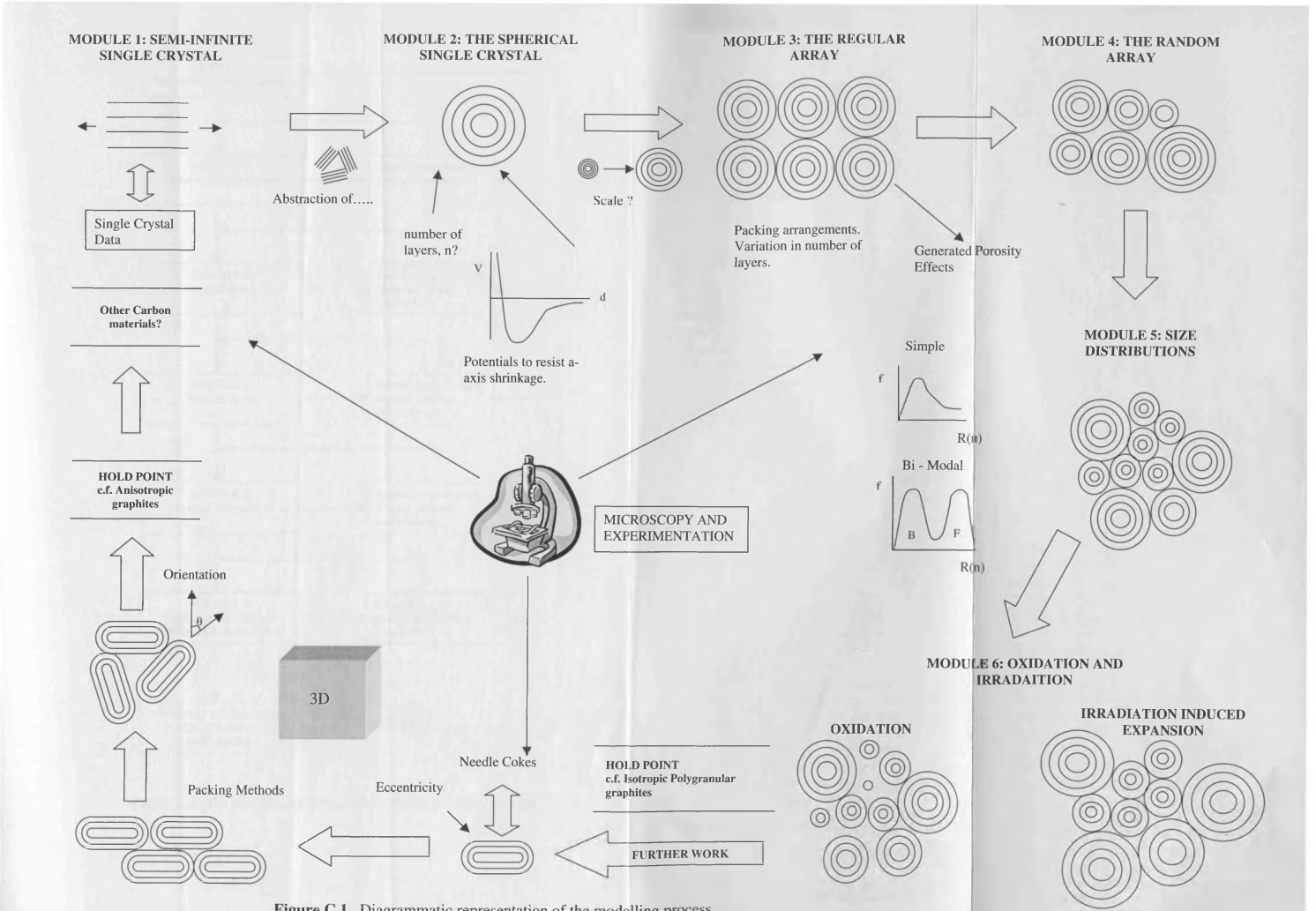

Figure C.1. Diagrammatic representation of the modelling process.

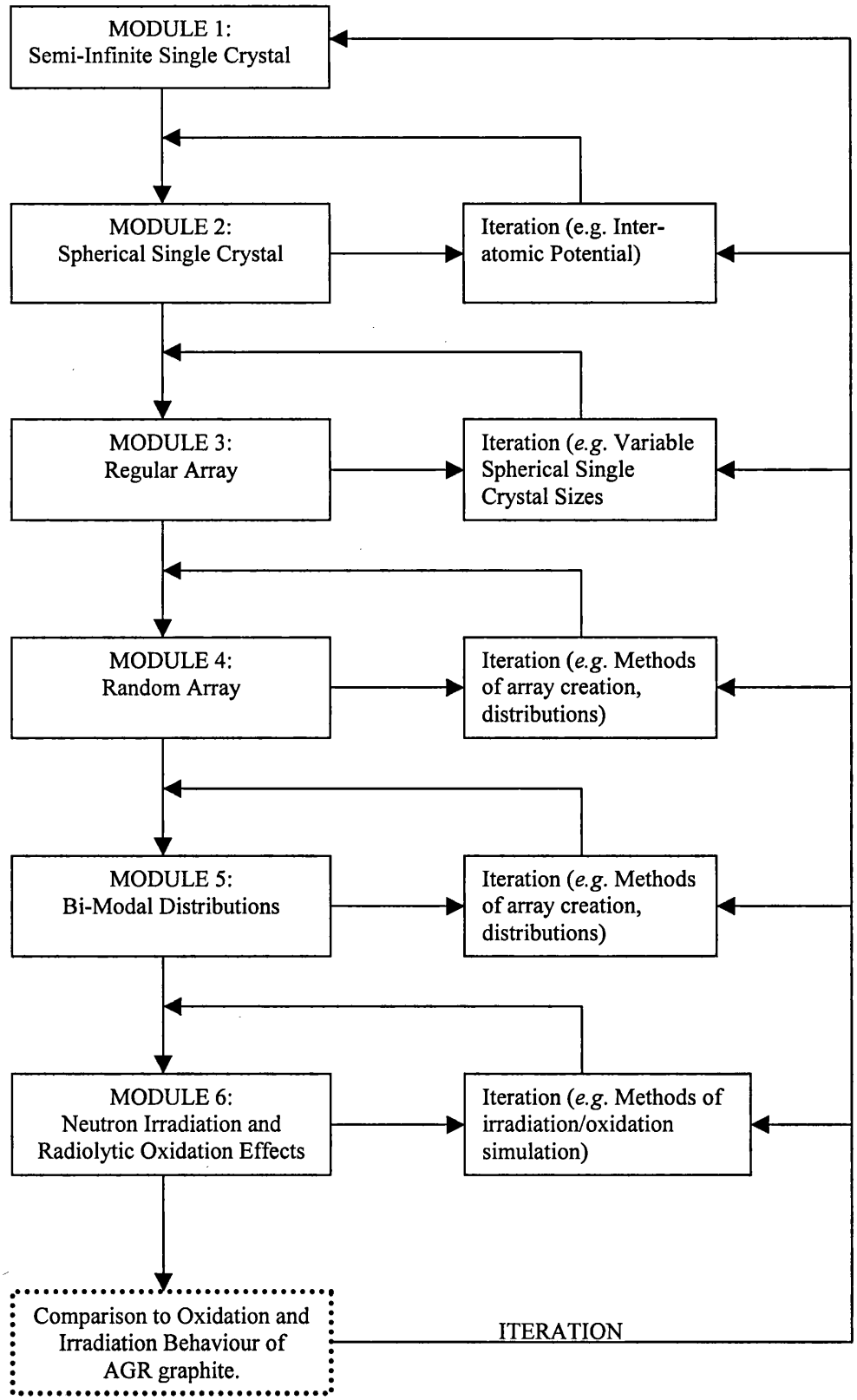

Figure C.2. The modules and interactions within the modelling process.

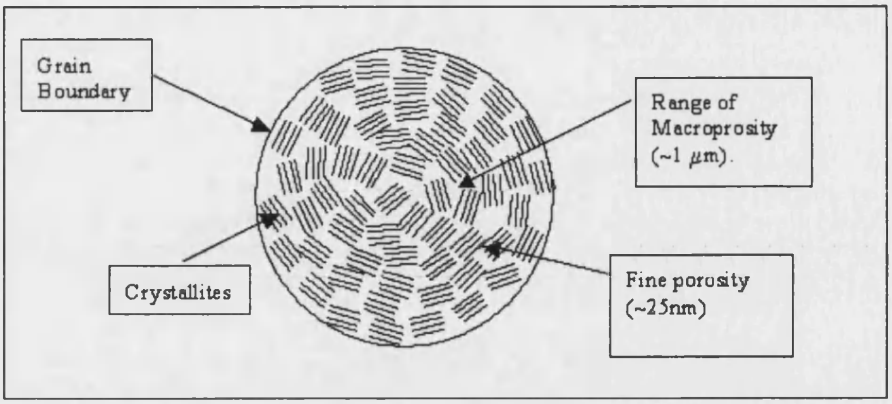

Figure C.3. A pictorial representation of a spherical grain.

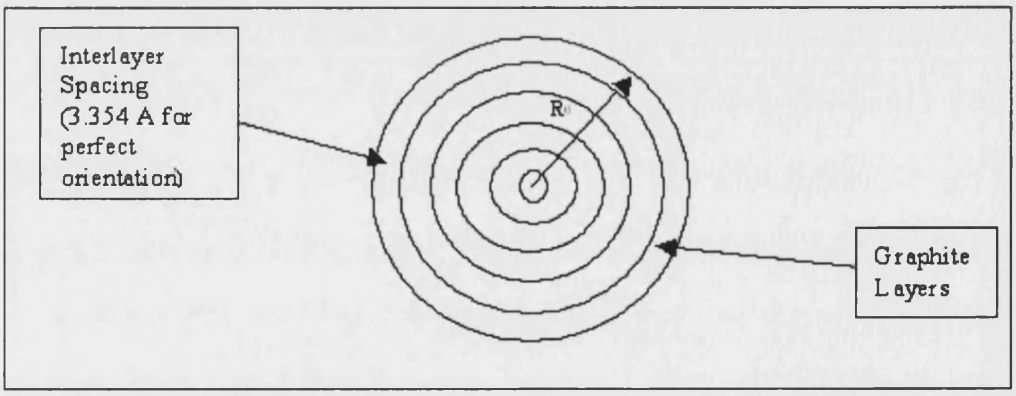

Figure C.4. The microscopic 'spherical' single crystal model.

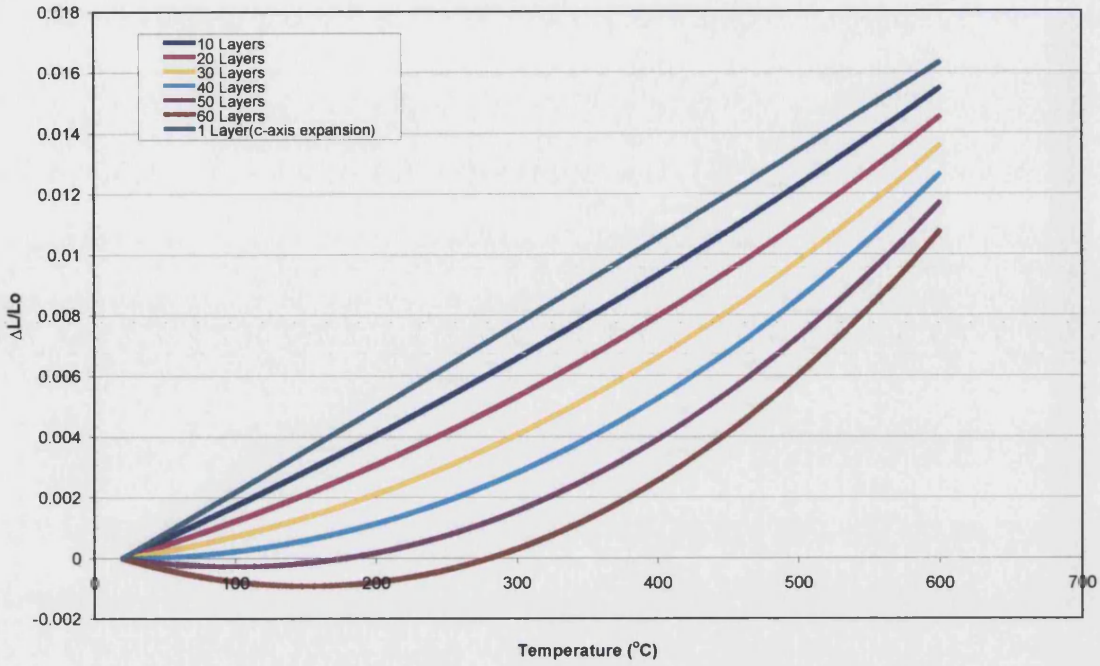

Figure C.5. The radial expansion of the "Spherical" Single Crystal (SSC) as a function of the number of concentric layers.

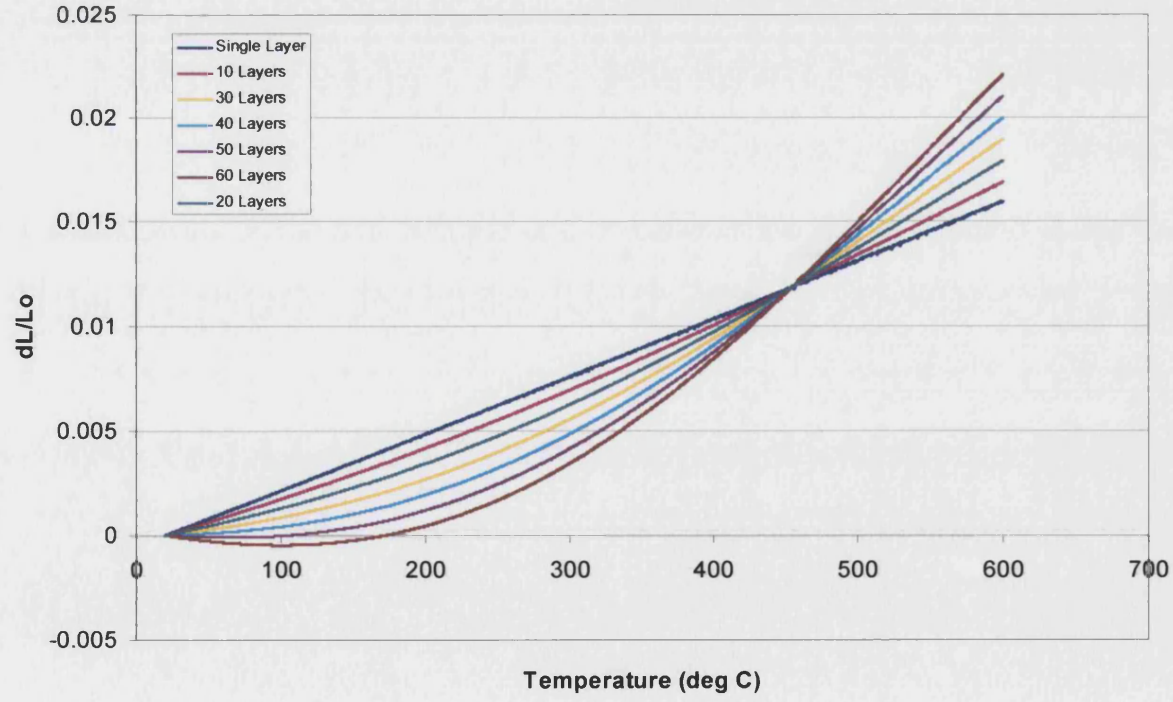

Figure C.6. The effects of introducing an inter-atomic potential to the SSC model as a function of the number of layers.

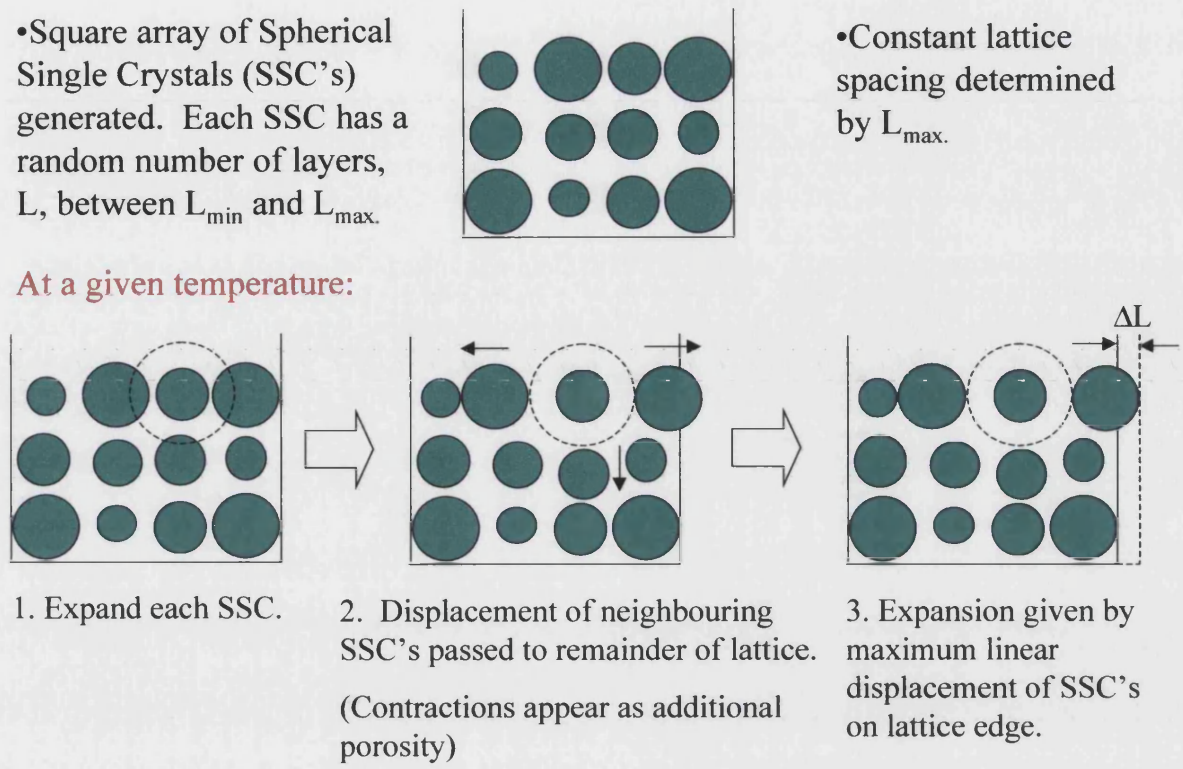

Figure C.7. Description of the modelling of the thermal expansion of a regular array of SSCs.

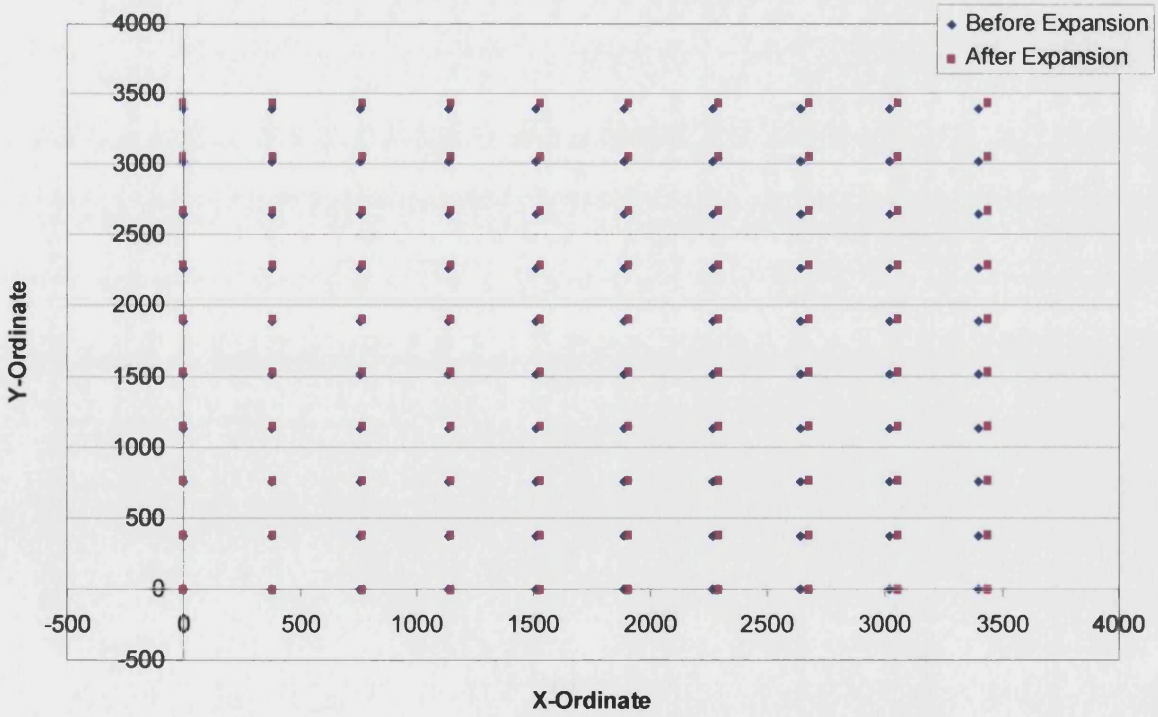

Figure C.8. Co-ordinates of the centres of an array of SSC (all of 60 layers) before and after expansion to 600°C.

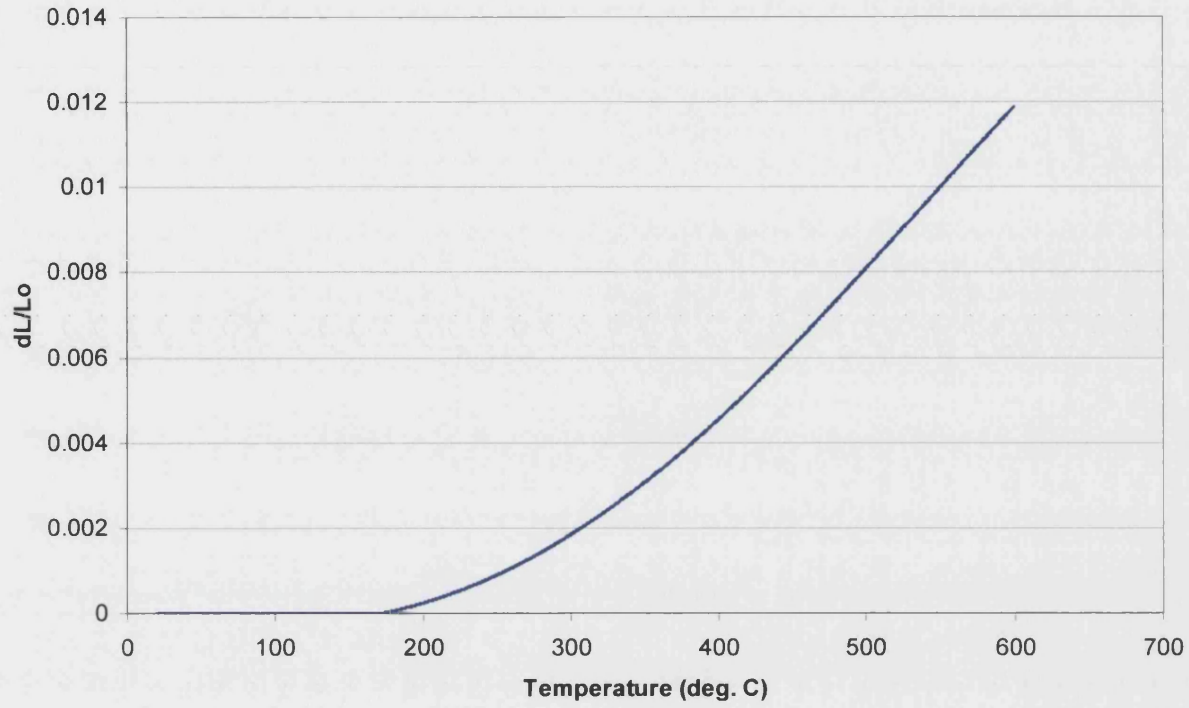

Figure C.9. Result of modelling a regular array of Spherical Single Crystals, each of 60 layers.

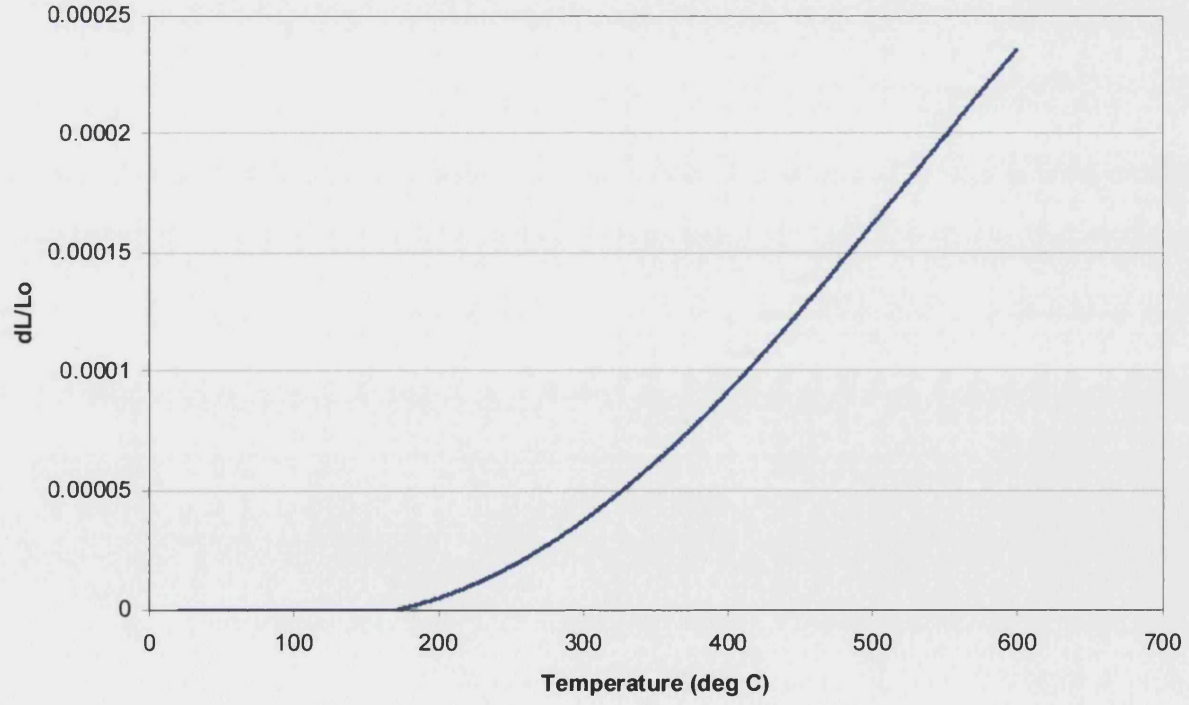

Figure C.10. Result of modelling a regular array of Spherical Single Crystals where N_{min}=55 and N_{max}=60.

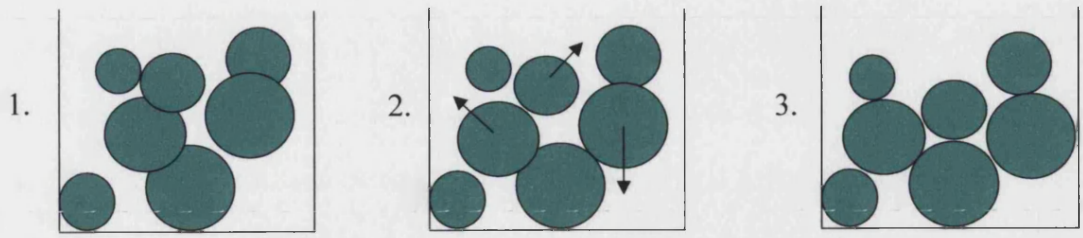

Figure C.11. A schematic of the computational steps required in the generation of a random array by the dynamic method, Module 4(a).

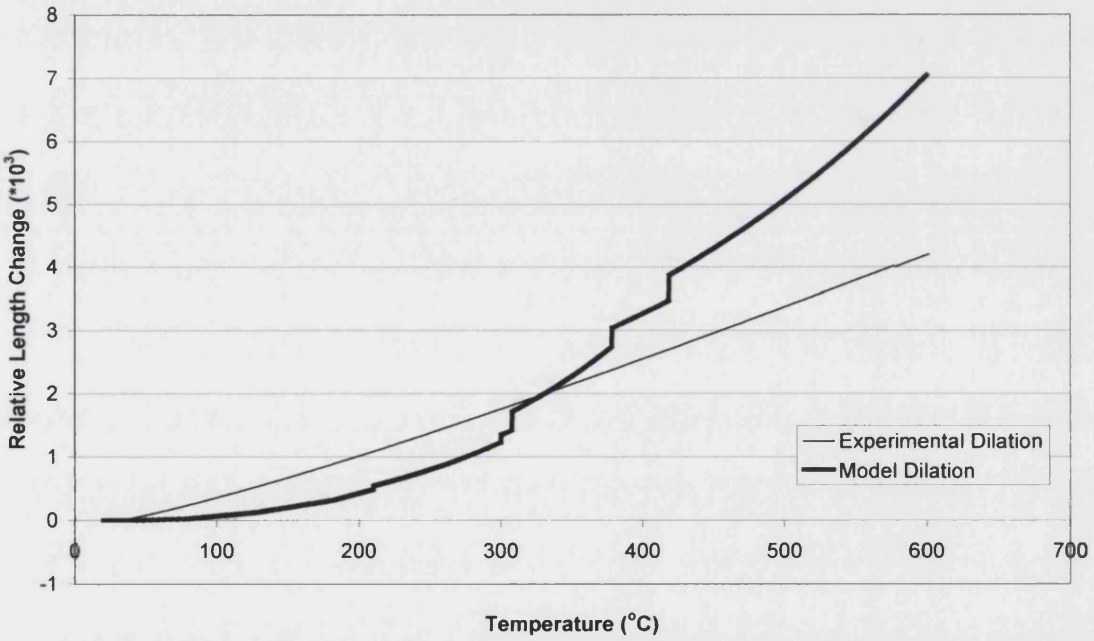

Figure C.12. Computed dilation curve generated from the dynamic random array model compared to an experimentally derived dilation curve for AGR moderator graphite.

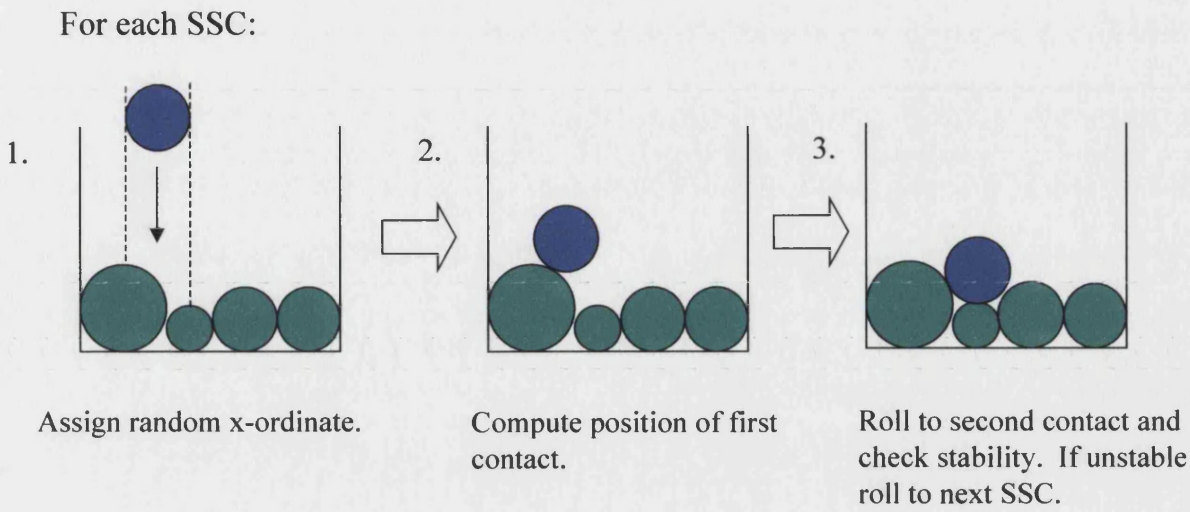

Figure C.13. The static method of generating a random array of SSCs, Module 4(b).

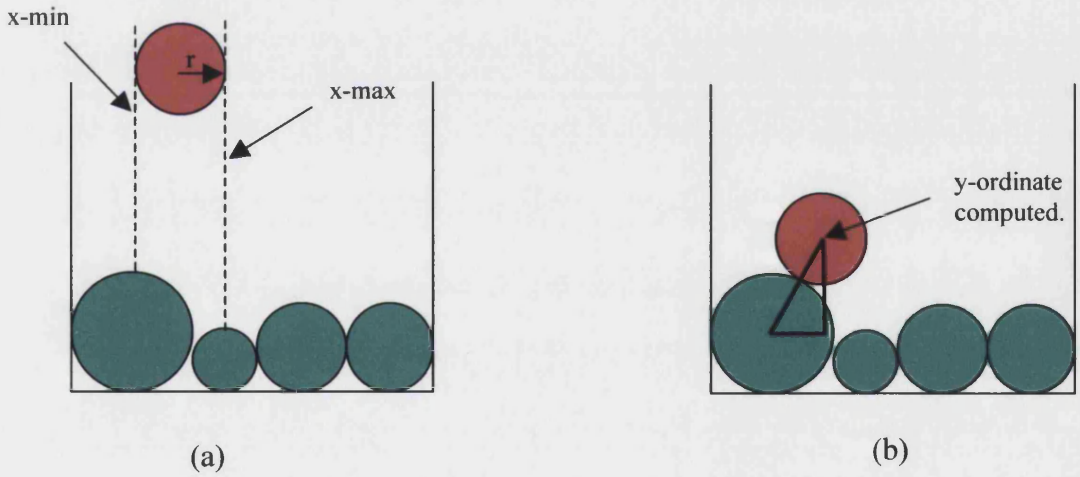

Figure C.14. The establishment of the y-ordinate of the dropped SSC for "first contact".

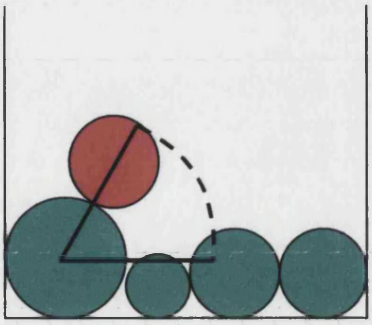

Figure C.15. The segment examined when "rolling" to second contact

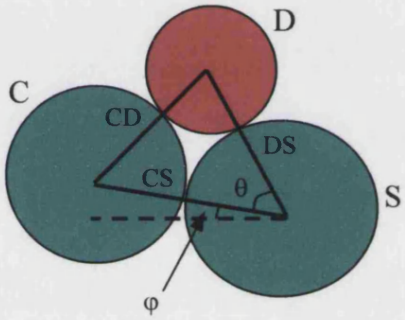

Figure C.16. The typical geometry formed on second contact between the dropped SSC (D), the first contact SSC (C) and the second contact SSC (S).

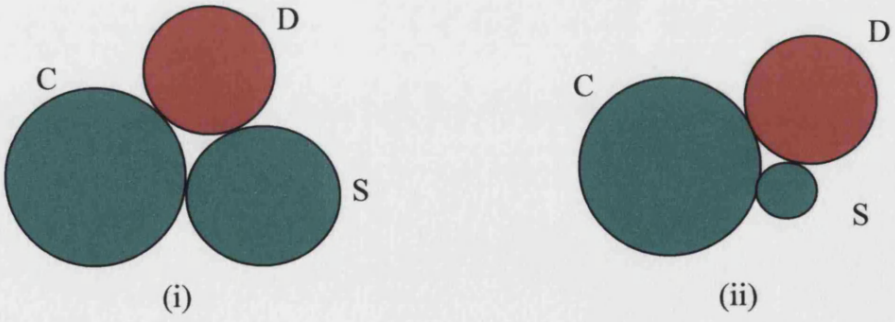

Figure C.17. Examples of second contact between dropped (D), first contact (C) and second contact (S) SSCs in positions that are (i) stable and (ii) unstable.

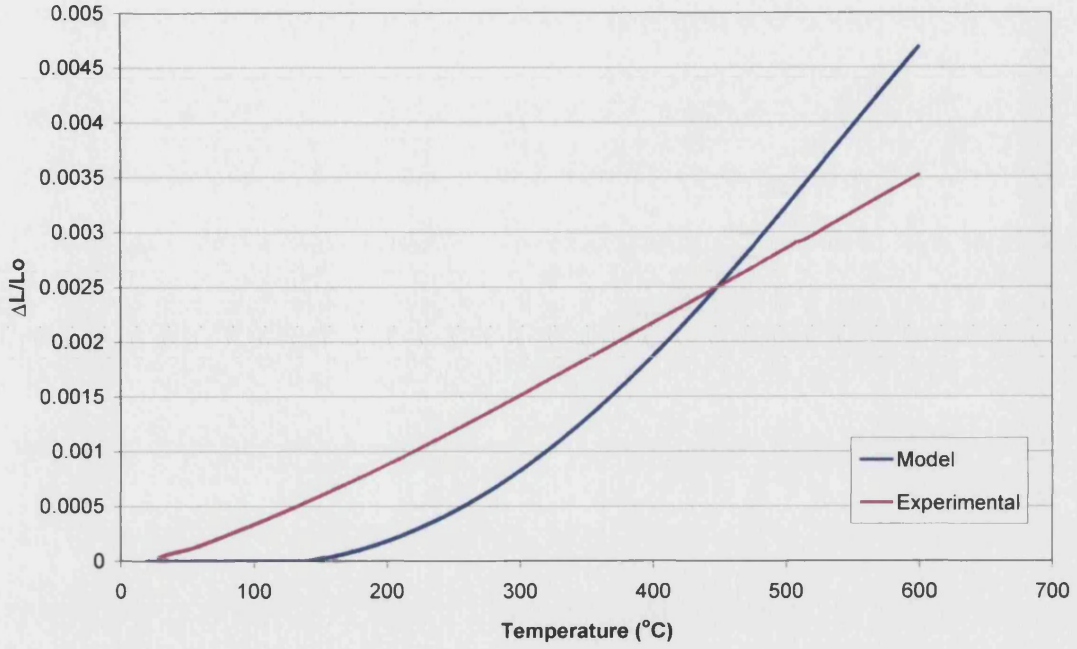

Figure C.18. Dilation curve produced from modelling a random array via the static modelling process using SSCs of a random size up to 60 layers.

Figure C.19. An polarised light composite micrograph of AGR moderator graphite (Tomlinson *et al.*, 2000).

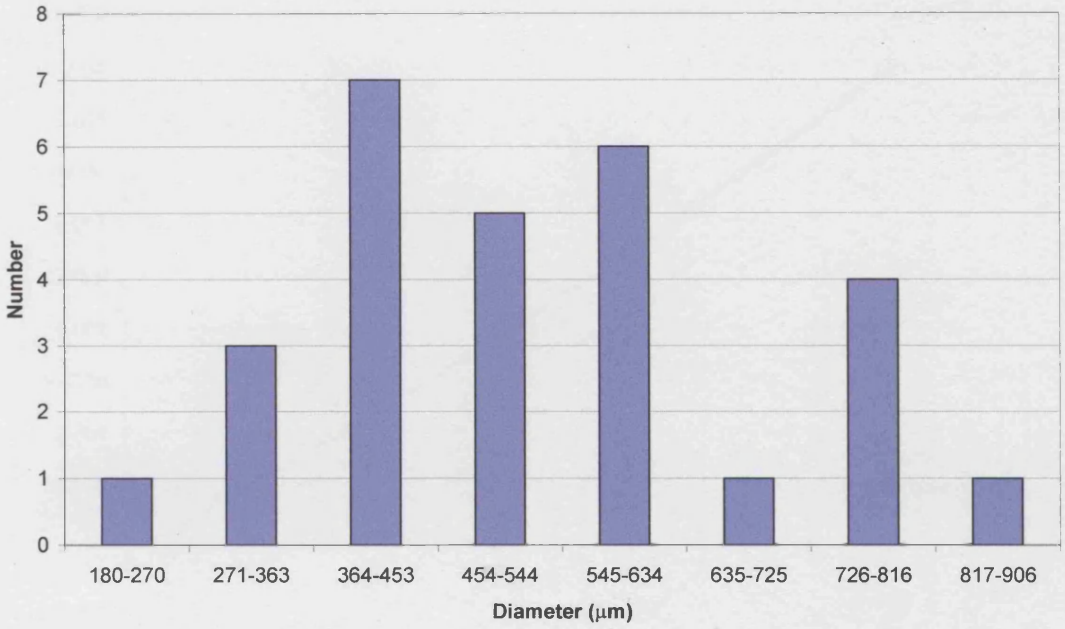

Figure C.20. A size distribution of filler particles within AGR graphite obtained semi-quantitativly from a composite optical micrograph.

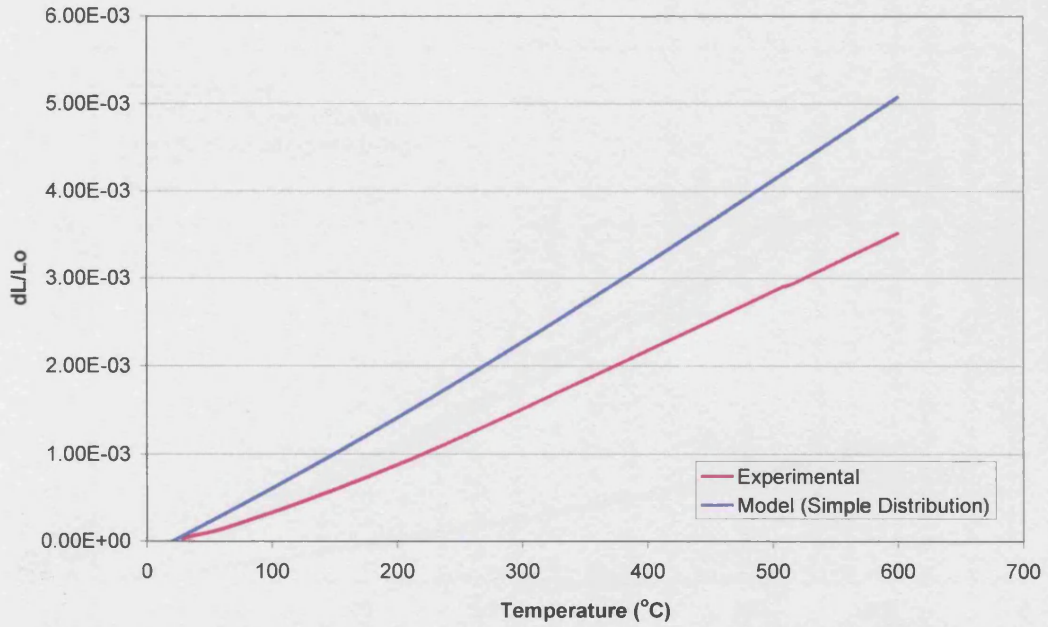

Figure C.21(a). The model output using a simple mean filler particle diameter and comparison with experiment.

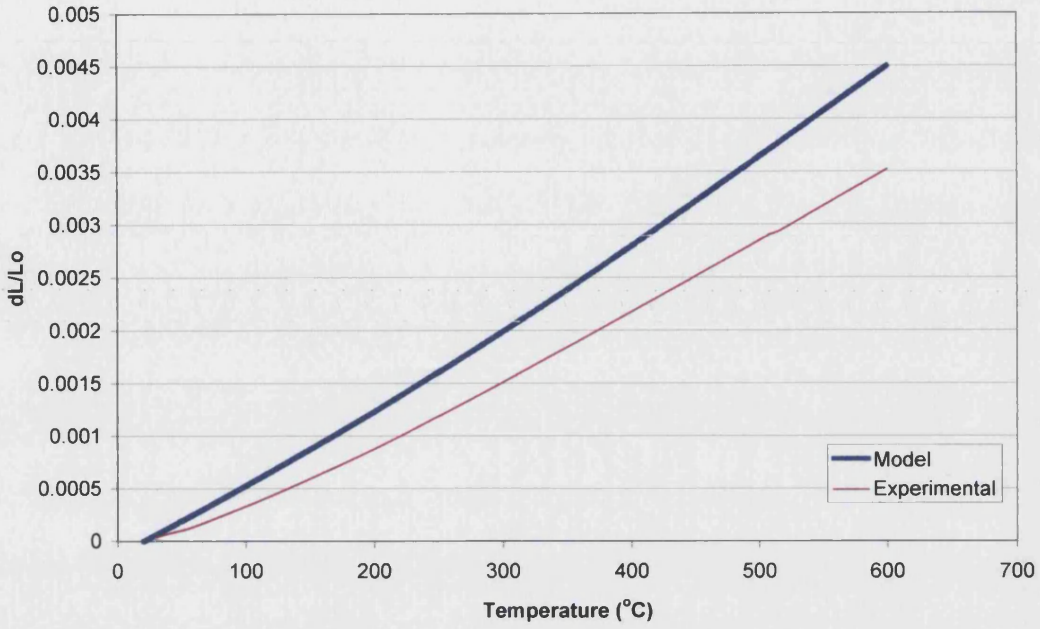

Figure C.21(b). The model output obtained from the distribution shown in figure C.18 in comparison with experiment.

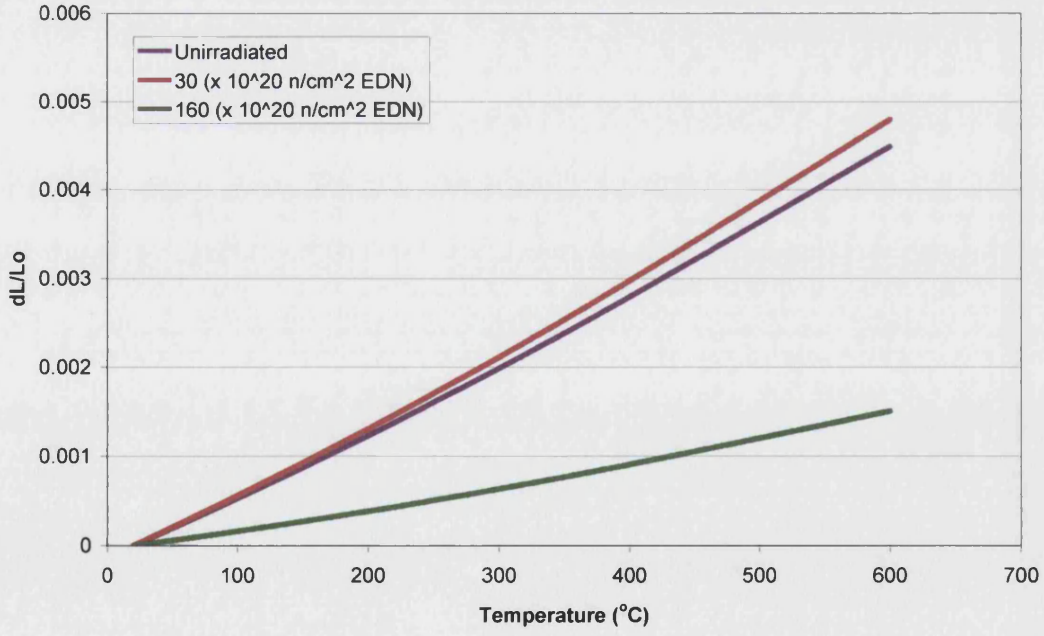

Figure C.22. The results of adding the effects of irradiation into the model at doses of 30 and 160 x 10^{20} n/cm^2 EDN.

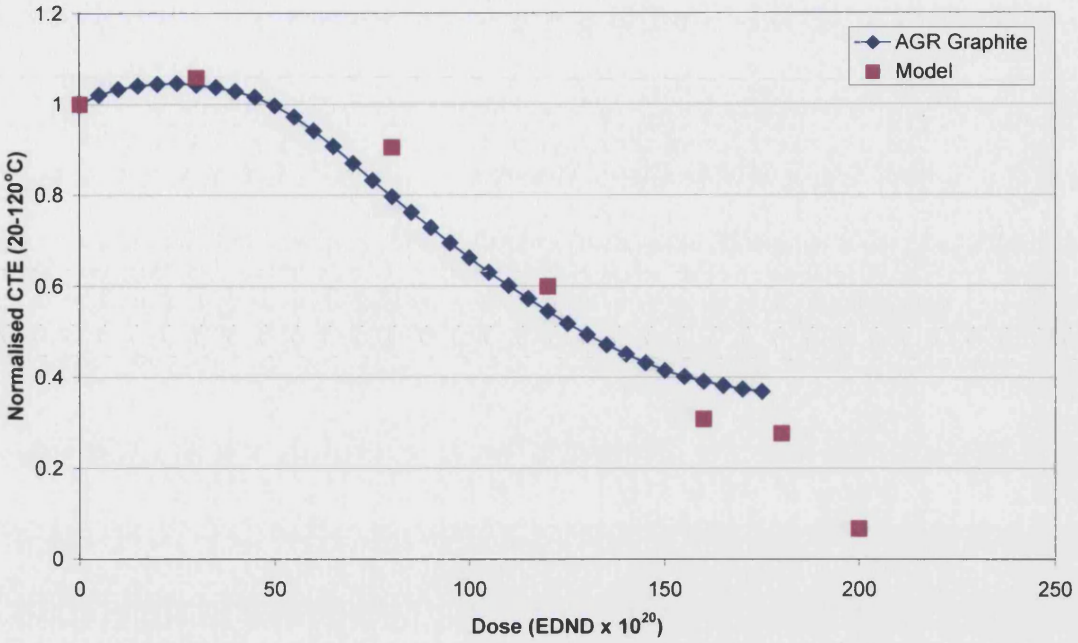

Figure C.23. Average CTE values (20-120°C) obtained from the dilation output of the model compared with the behaviour of AGR graphite under irradiation.

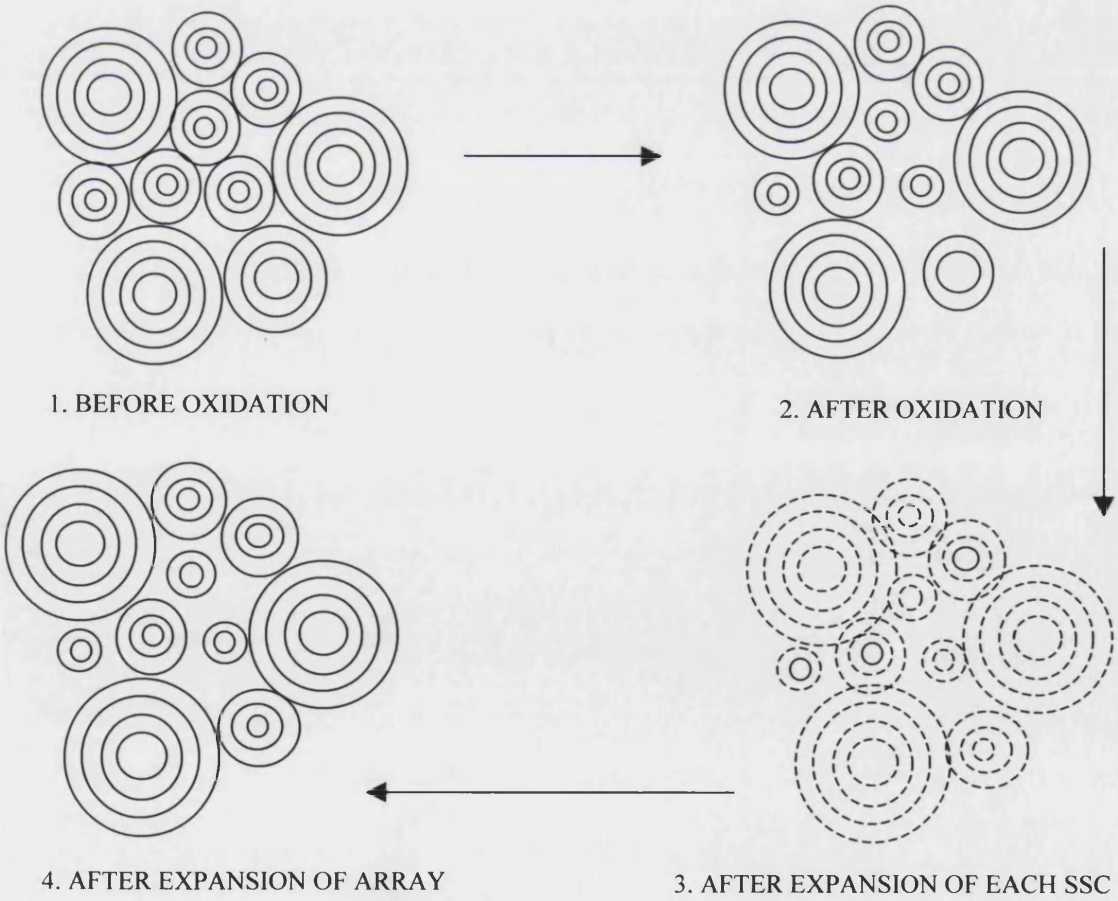

Figure C.24. Schematic showing the simulation of oxidation effects, and the subsequent expansion process, within Module 6.

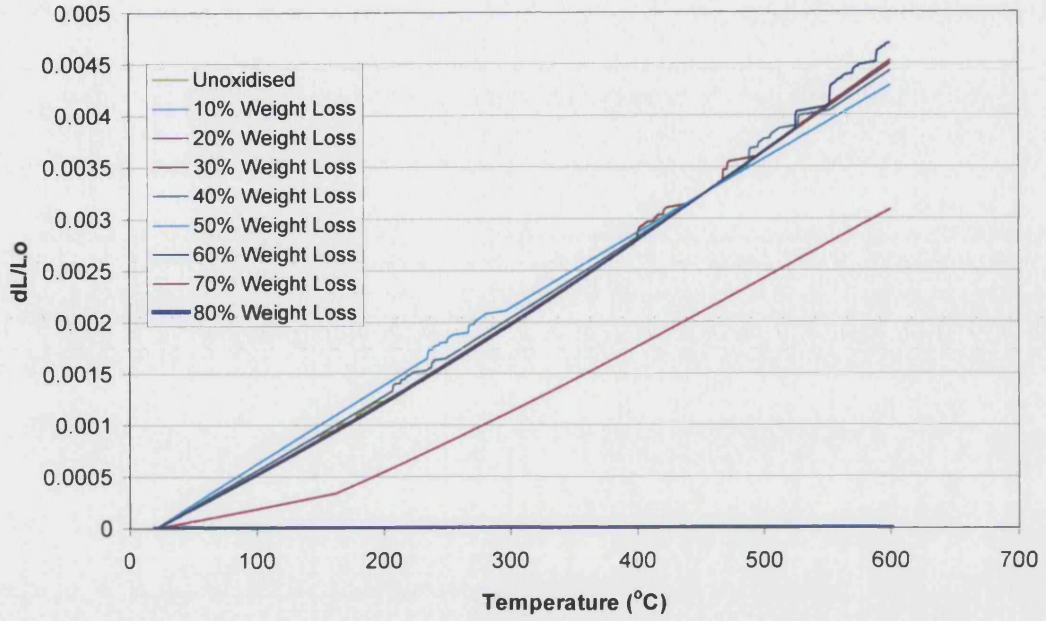

Figure C.25. The effects of oxidation on the modelled dilation curve.

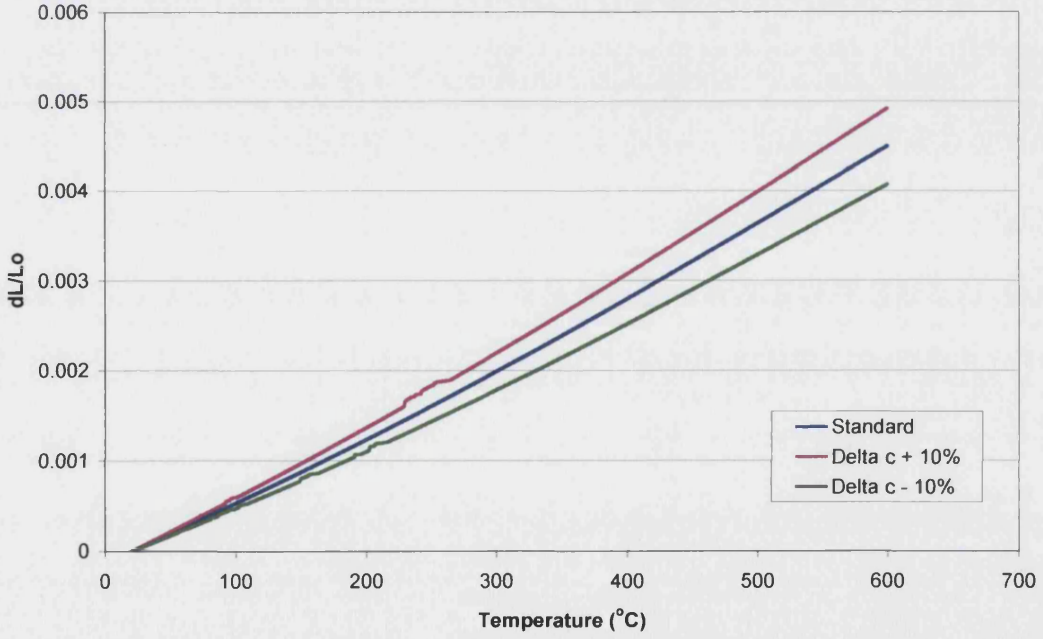

Figure C.26(a). The sensitivity of the modelled dilation curve to a 10% change in the *c*-axis single crystal expansion input parameter.

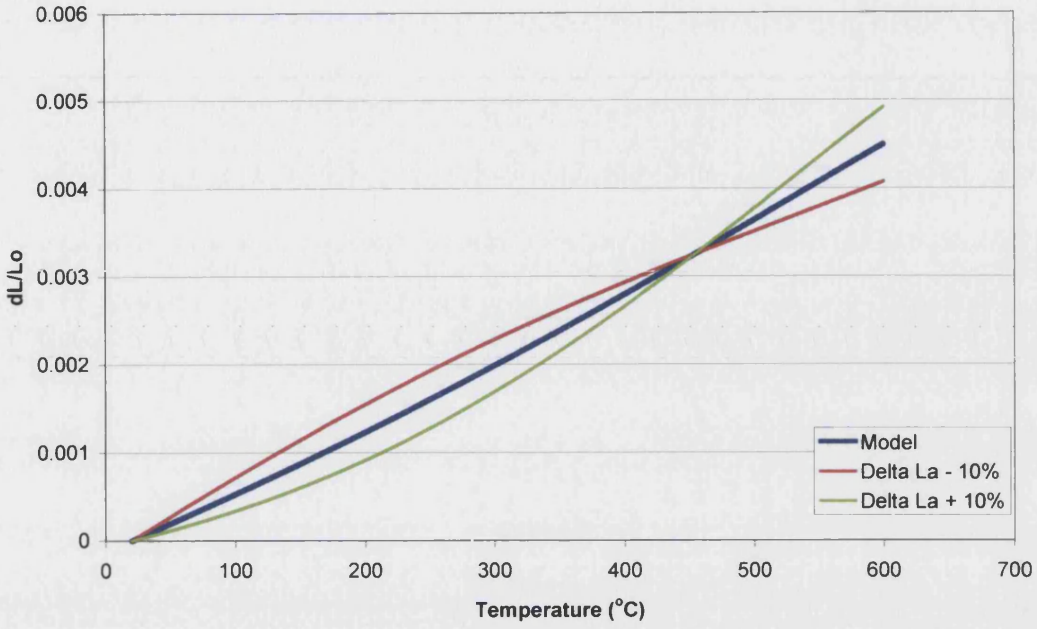

Figure C.26(b). The sensitivity of the modelled dilation curve to a 10% change in the *a*-axis single crystal expansion input parameter.

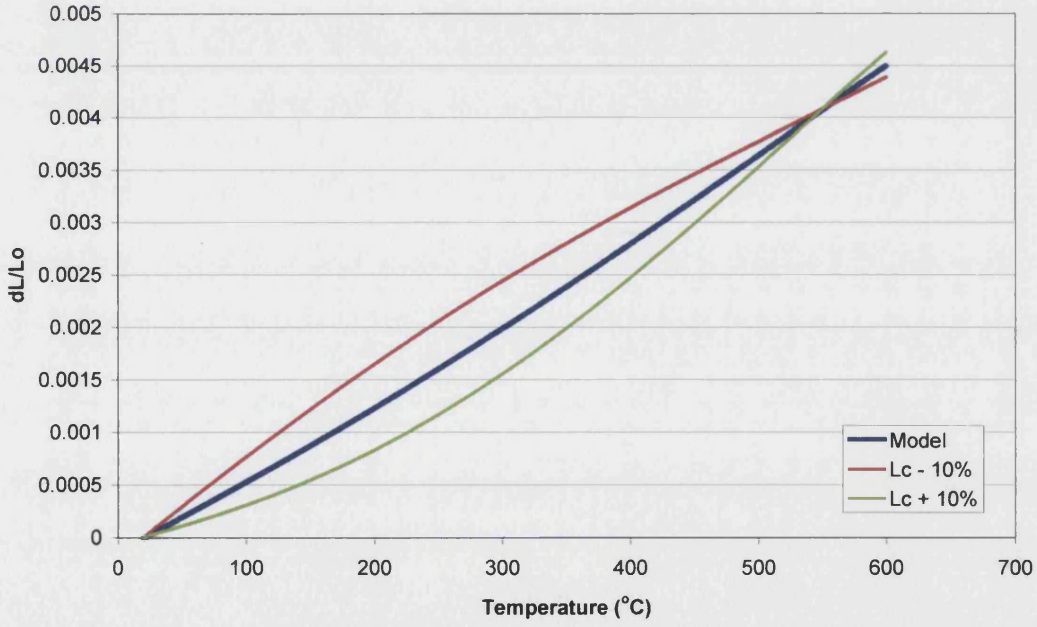

Figure C.26(c). The sensitivity of the modelled dilation curve to a 10% change in the *Lc* (stack height) single crystal expansion input parameter.

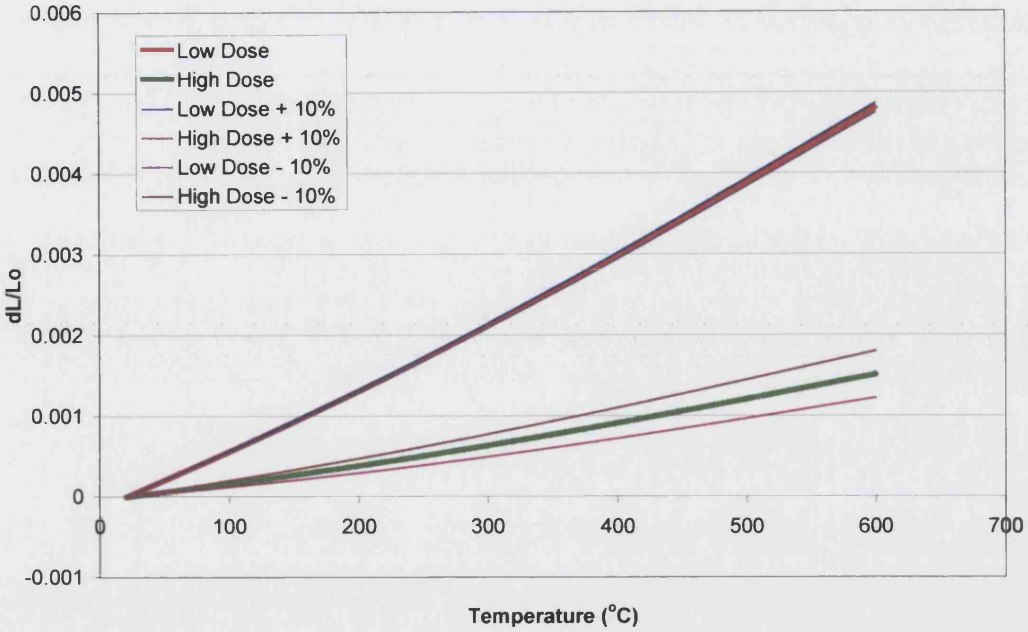

Figure C.27(a). The sensitivity of the modelled dilation curve to a 10% change in the irradiation induced dimensional change parameter in the *c*-direction compared to the unmodified dilation curves at 30 (low dose) and 160 (high dose) x 10^{20} n/cm^2 EDN.

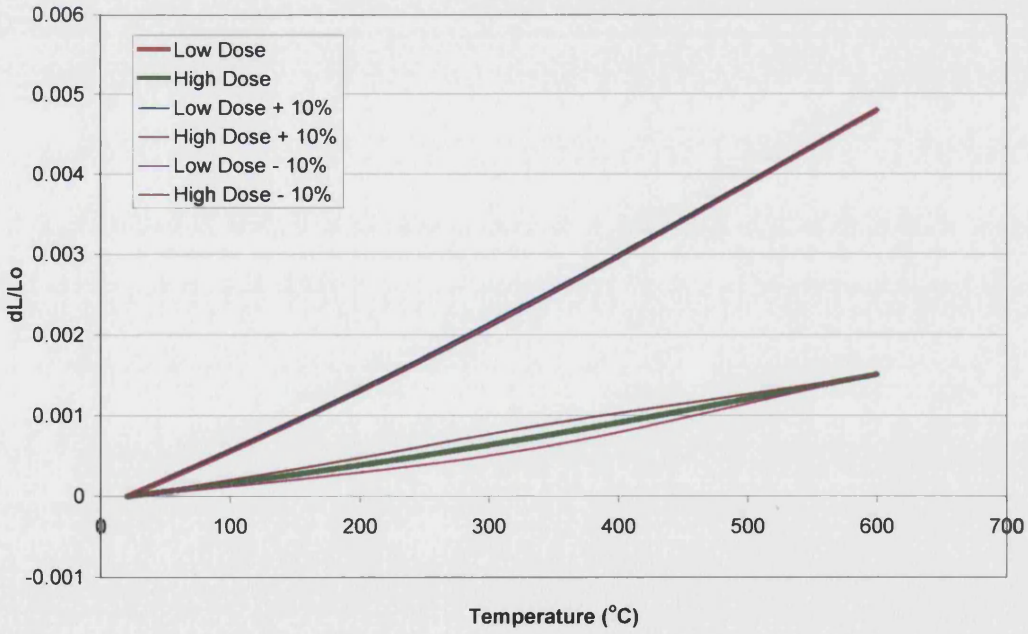

Figure C.27(b). The sensitivity of the modelled dilation curve to a 10% change in the irradiation induced dimensional change parameter in the *a*-direction compared to the unmodified dilation curves at 30 (low dose) and 160 (high dose) x 10^{20} n/cm^2 EDN.

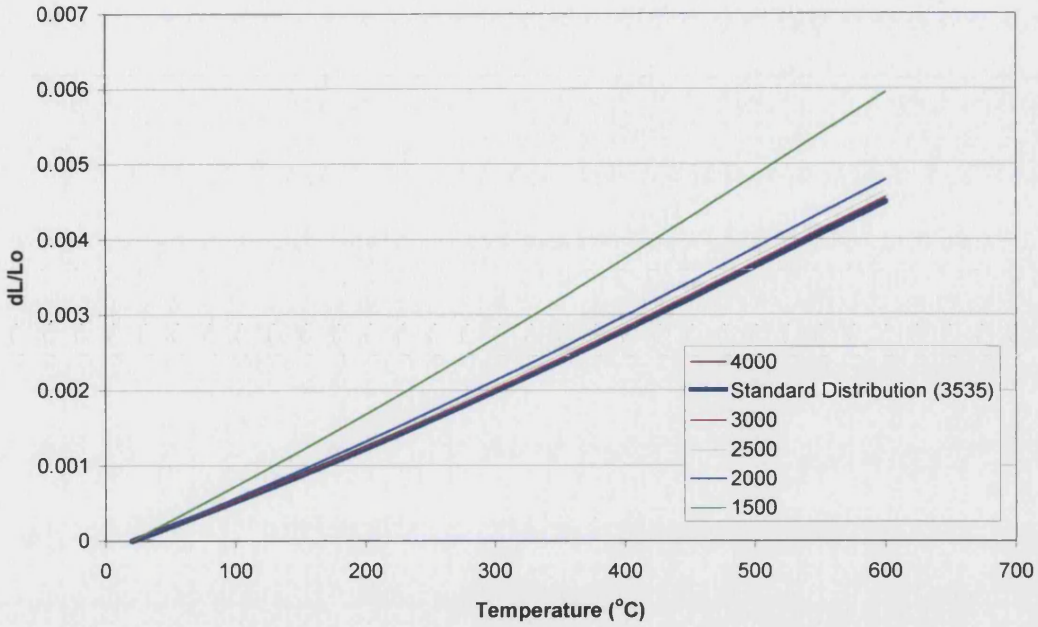

Figure C.28. The sensitivity of the modelled dilation curve to changes in the number of SSCs in the array in comparison to those in the Standard Distribution.

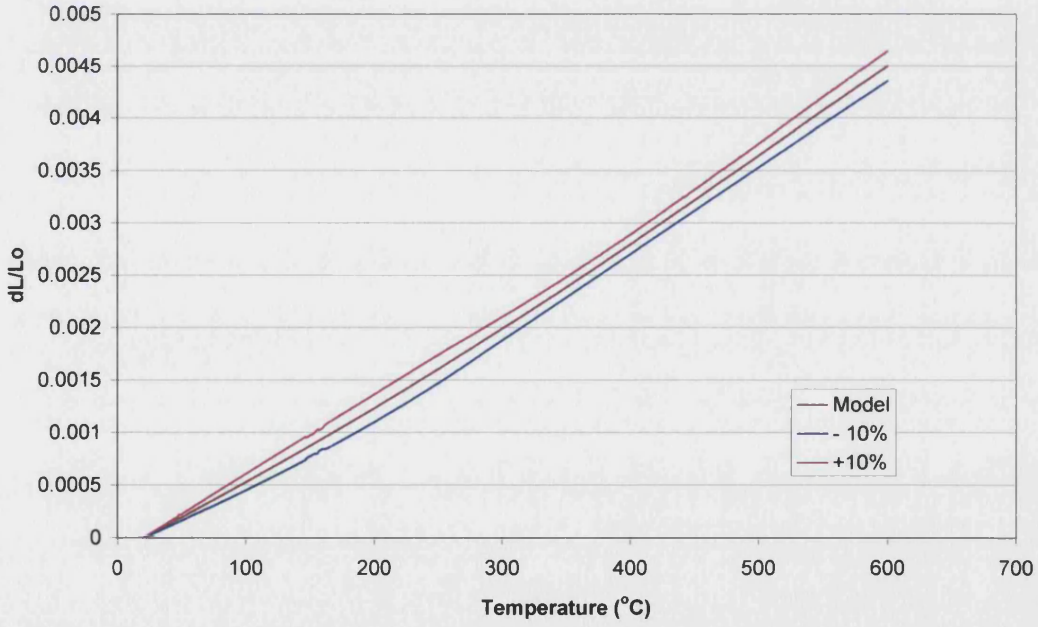

Figure C.29. The sensitivity of the modelled dilation curve to a 10% change in the number of filler particles.

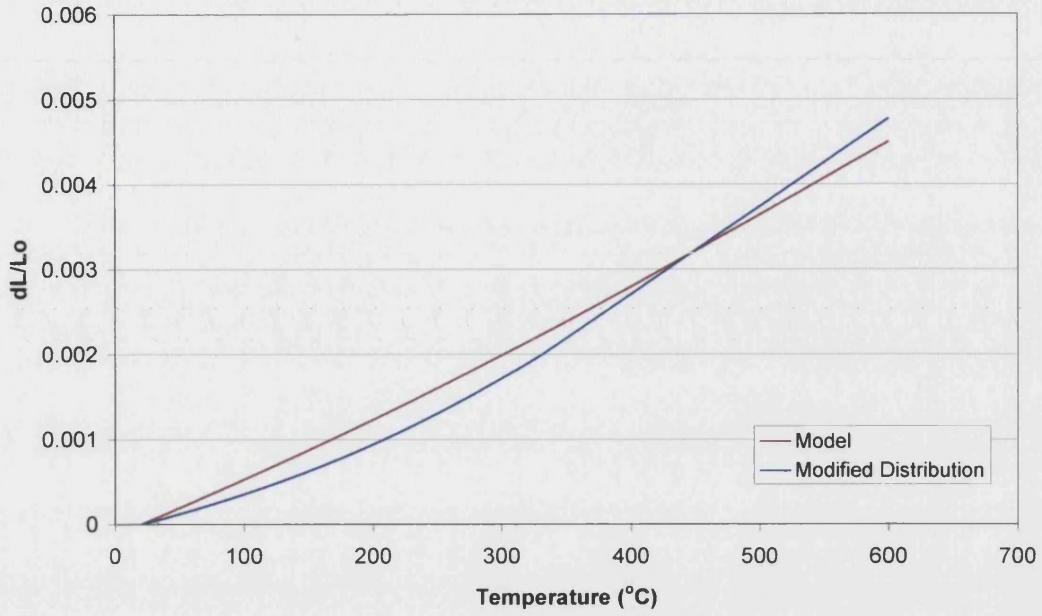

Figure C.30. The sensitivity of the modelled dilation curve to a change in the form of the Standard Distribution.

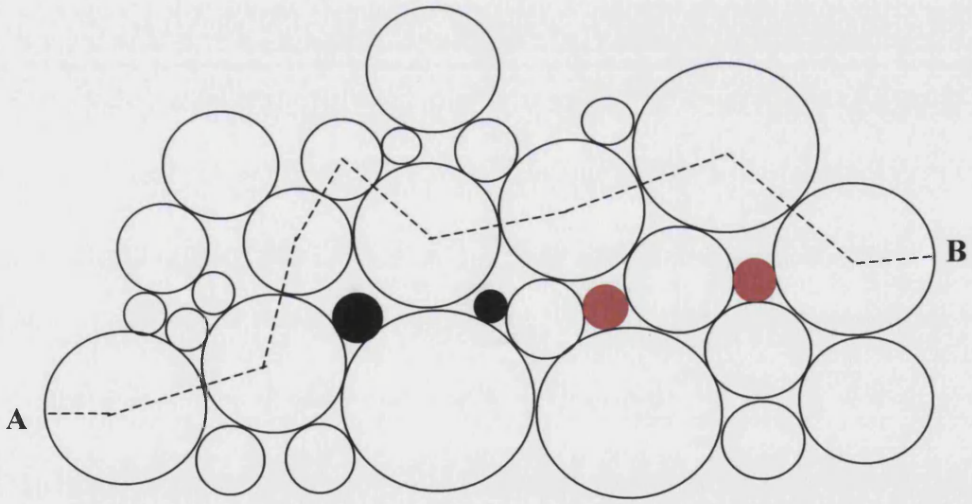

Figure C.31. The formation of regions of porosity in the random array of Module 4, that are currently providing (i) total accommodation for the expansion of the black SSC (ii) partial accommodation for the expansion of the red SSC. Note also the dotted line that represents one of many paths of structural continuity from A to B.

15. CONCLUSIONS AND FURTHER WORK

Within this final section, the main conclusions of the thesis are given with reference to the original objectives specified in the introduction. Also topics for further study are presented with specific objectives.

15.1 CONCLUSIONS

This study has two main aims; to identify and characterise those elements of the microstructure of AGR and Magnox graphites that influence thermal expansion and to develop a microstructural model that describes these changes under reactor conditions. These have been achieved by study in three interlinked areas, theoretical, experimental and modelling. Within this section the main conclusions from these sections are presented, in relation to the two primary aims, highlighting the novel aspects of the work.

15.1.1 Microstructural Characterisation and CTE Behaviour

Before this study, thermal expansion and dimensional change of nuclear graphites, under irradiation and oxidation, were considered to be controlled primarily by Mrozowski cracks defined by a specific width and periodicity. In this study, the development of a simple model of Mrozowski crack formation, together with a consideration of the effects of irradiation and oxidation on both CTE and dimensional change, concluded that CTE behaviour is controlled by such porosity and dimensional change is controlled by larger scale porosity. Therefore, small scale structure (that on the nanometric scale) is concluded as being important in determining thermal expansion behaviour.

A review of existing models of CTE and dimensional change within nuclear graphites found that all are based upon a loose assembly of single crystals. This approach results in all complex microstructural interactions being condensed into single empirical factors *e.g.* A_X.

Observation of Magnox and AGR moderator graphites under SEM and TEM microscopy have identified large amounts of small scale (nanometric sized) porosity that exists in a wide size range from ~2 to 100 nm. Under TEM the structure of the material consists of a connected ligament structure. As a result, the loose assembly of single crystals is concluded to be a poor approximation for modelling CTE in these materials.

When considering the experimental thermal response of both AGR and Magnox graphites it was concluded that, over two thermal cycles, significant differences exist between the first heating cycle and subsequent cycles. It is suggested that these differences are caused by a combination of three factors. The first is a "settling in" of the sample at the start of the experimental run that can be minimised by careful placement of the sample within the dilatometer. The second is the release of internal stress (formed during manufacture). The third, most relevant to anisotropic materials, relates to the general discussion of the thermal expansion of polycrystalline materials given by Sosman (1926) which concluded that the measurement of the expansion of such materials may, in itself, alter their small scale structure.

For the first time, this study has shown experimentally that the insensitivity of CTE to thermal oxidation extends to very high weight losses (>60% for AGR graphite). The Continuous Network Theory was developed to account for this and tested by the preparation of graphite samples with special geometries. The Continuous Network Theory was also related to percolation theory and the latter was applied to electrical conductivity data from which it was concluded that the values of electrical conductivity should not fall to zero until weight losses >95% were obtained. By implication, CTE should remain insensitive to oxidation to comparable weight losses. A discussion of the differences between thermal and radiolytic oxidation in relation to their effects on elements of microstructure that influence CTE concluded that these results were likely to also apply to the case of radiolytic oxidation.

The decrease in CTE as a function of fast neutron irradiation, for AGR graphite, at neutron fluences between ~35 to 125 n/cm^2 (EDN) has previously been attributed to "structural disruption". Magnox graphites show no change in CTE over the same dose range. By heating AGR graphite to high temperatures (2000°C) a reduction in CTE was

observed. No reduction in CTE was observed when the same process was conducted on Magnox graphite. It was concluded that, in the case of AGR graphite, subtle structural changes occur on heating that result in a decrease in CTE. These changes appear not to effect the CTE of Magnox graphite due to the coarse nature of this material.

15.1.2 Modelling CTE

A new method of modelling CTE in these materials has been presented based upon a simple abstraction of the observed microstructure that includes the elements of connectivity that are missing form the loose assembly of single crystals approach. The model is modular to allow for a traceable development that increases in complexity and also allows for the systematic inclusion of information gained from microstructural characterisation.

By carefully selecting the key input parameters, the modelling process has produced a reasonable approximation to the dilation of AGR graphite. This is especially encouraging as the number of input (or free) parameters is small and can be readily identified with well understood single crystal parameters or simple filler/binder size distributions. By using the irradiation induced dimensional change data of graphite single crystals, and by random removal of elements from the model, irradiation and oxidation effects have also been incorporated. These results also compare reasonably with those obtained experimentally on irradiated and oxidised samples of AGR graphite.

15.2 FURTHER WORK

The clearest extension to this work concerns the modelling process. In particular, the applicability of this approach appears to extend easily to anisotropic nuclear graphites (*e.g.* Magnox graphites) and the method for this extension has been described by the additional modules shown in Figure C.1. Indeed, many of the computational elements required for this extension have already been developed as a part of the current study. Attention should also be given to the wider applicability of this approach not only to other graphites but also to a wide range of materials (*e.g.* sintered ceramics) whose structure closely resemble connected packed objects. Improvements can also be made to the current modules, for example inclusion of code to monitor porosity changes

within the model would enable modelled porosity distributions to be generated. Also a more detailed understanding of the dynamics of the movement of SSCs during the expansion process (by graphical display) would be useful. Extension to three dimensions may be required to fully replicate observed behaviour. However, the availability of the computational resources required to manipulate these arrays in 3D would determine the feasibility of this approach.

Experimentally, composite TEM micrographs would enable further study of long range topography at the nanometric scale to be made. This information would help to further understand the nature of connectivity within these materials. Further microscopy studies of samples conducted after measurement of thermal expansion may also reveal differences between them and the as-received material.

REFERENCES

Alain, E. A., Neighbour, G. B. and Hacker, P. J. (2000). *Graphite single crystals and their applicability to polygranular nuclear graphites.* BNMG report for British Energy Generation Ltd., BNMG/REP/048.

Amelinckx, S., Delavignette, P. and Heerschap, M. (1965). Dislocations and stacking faults in graphite. *Chemistry and Physics of Carbon* (Ed. P. L. Walker), **1**, 1-71.

Arai, T. (1996). An analytical study on porosity changes of nuclear graphites under high temperature irradiations. *Graphite Moderator Lifecycle Behaviour, Proceedings of a Specialists Meeting*, United Kingdom, 24-27 September 1995, 255-237.

ASTM E 228-85, (1985). *Standard Test Method for Linear Thermal Expansion of Solid Materials with a Vitreous Silica Dilatometer.* American Standard Test Method.

ASTM E 289-94, (1994). *Standard Test Method for Linear Thermal Expansion of Rigid Solids with Interferometry.* American Standard Test Method.

ASTM E 831-93, (1993). *Linear Thermal Expansion of Solid Materials by Thermomechanical Analysis.* American Standard Test Method.

Atkins, P. W., (1994). *Physical Chemistry* (5th Edition), Oxford University Press, Oxford, Chapter 14.

Austin, J. B., (1952). Thermal Expansion of Nonmetallic Crystals. *Journal of the American Ceramic Society.* **35**[10], 243-253.

Bacon, G.E. (1951). The structure of graphite. *Acta Crysta*, **4**, 558-569.

Bacon, G.E. (1956). A method for determining the degree of orientation of graphite. *Journal of Applied Chemistry*, **6**, 477-481.

Bailey, A. and Yates, B. J. (1970). The CTE of graphite. *Applied Physics*, **41**, 5088-5097.

Benson, H., (1991). *University Physics*. John Wiley and Sons, Inc.

Best, J. V., Stephen, W. J. and Wickham, A. J. (1985). Radiolytic Graphite Oxidation. *Progress in Nuclear Energy*, **16**[2], 127-178.

Binning, G., Quate, C. F. and Gerber, C. (1986). The atomic force microscope, *Physical Review Letters*, **56**, 930-942.

Birch, M. and Brocklehurst, J. E. (1986). *A review of the effects of irradiation on the physical and mechanical properties of Pile Grade 'A' Graphite*. UKAEA Report, ND-R-1236(S), AGR/GCWG/P(86)4.

Bokros, J. C. (1969). In: *Chemistry and Physics of Carbon*, Vol. 5 (Ed. P. L. Walker, Jr).

Bohr, H. and Wheeler, J. A., (1939). The mechanism of fission. *Physical Review*, **56**, 426-450.

Brocklehurst, J. E. and Brown, R. G. (1969). Constant stress irradiation creep experiments on graphite in BR-2. *Carbon*, **7**, 487-497.

Brocklehurst, J. E., Brown, R. G., Gilchrist, K. E. and Labton, V. Y. (1970). The effect of radiolytic oxidation on the physical properties of graphite. *Journal of Nuclear Materials*, **35**, 183-194.

Brocklehurst, J. E. (1984). *Irradiation damage in AGR moderator graphite*. UKAEA Report ND-R-1117(S).

Brown, A. R. G. and Watt, W. (1958). The pyrolytic deposition of graphite. *Proceedings of the First SCI Conference on Industrial Carbons and Graphites*, SCI, London (1958), 55-58.

Brown, M. E. (1988) *Introduction to thermal analysis techniques and applications*, Chapman and Hall, London.

Burchell, T. D. and Eatherly, W. P. (1991). The effects of radiation damage on the properties of GraphNOL N3M. *Journal of Nuclear Materials*, **179**, 205-208.

Burchell, T. D. and Oku, T (1994). Material properties data for fusion reactor plasma facing carbon-carbon composites. *Atomic and Plasma-Material Interaction Data For Fusion (supplement to the journal Nuclear Fusion)*. International Atomic Energy Agency, **5**, 77-128.

Carpenter, E. W. and Norfolk, D. J. (1984). Lattice of power: graphite core life. *Nuclear Energy*, **23**[2], 83-96.

Charsley, E. L. and Warrington, S. B. (eds.) (1992) *Thermal analysis: techniques and applications*, Royal Society of Chemistry, London.

Coble, R. L. and Kingery, W. D. (1956). Effect of porosity on physical properties of sintered alumina. *Journal of the American Ceramic Society*, **39**[11], 377-385.

Cohen, S. H. (1993). *Atomic Force Microscopy and Scanning Tunnelling Microscopy.* Plenum Press, New York.

Cullity, B. D. (1990). *Elements of x-ray diffraction.* (2^{nd} edition). Addison-Wesley Publishing Compnay, Inc, London.

Davies, M. W. (1996). Graphite core design in UK reactors. Graphite Moderator Lifecycle Behaviour, *Proceedings of a Specialists Meeting held in Bath*, United Kingdom, 245-259.

Derrida, B, Zabolitzky, J. G., Vannimenus, J. and Stauffer, D. (1984). Numerical percolation models. *Journal of Statistical Physics*, **36**, 31-43.

Diez, M. A. and Marsh, H. (2000). The penetration of potassium, sodium and lithium into graphitic and non-graphitic carbons - a commentary. *Proceedings of the 1st World Conference on Carbon*, Berlin, Germany, 927-928.

Engle, G. B. (1971). Irradiation behaviour of nuclear graphites at elevated temperatures. *Carbon*, **9**, 539-554.

Engle, G. B. (1974). Relationship between crystal structure and properties and irradiation behaviour of reactor graphites. *Carbon*, **12**, 291-306.

Euler, P. (1957). Simple Geometric Model for the Effect of Porosity on Material Constants. *Journal of Applied Physics*, **28**[11], 1342-1345.

Entwisle, F. (1962). Thermal expansion of pyrolytic graphite. *Physics Letters*, **2**[5], 236-238.

Essam, J. W., Gaunt, D. S. and Guttmann, A. J. (1983). Percolation limits in different lattice types. *Journal of Physics A*, **11**, 233-246.

Family, F. and Landau, D. P. (1984). (eds) International Conference on Kinetics of Aggregation and Gelation, Athens, USA.

Feates, F. S. (1970). Topographical studies of oxidation of single crystal graphite. *3rd Conference on Industrial Carbons and Graphite*, 233-237.

Feng, B. and Bhatia, S. K. (1999). The electrical resistivity of oxidised coal chars. *Extended Abstracts 24th Biennial Conference on Carbon*, Charleston, South Carolina, USA, 228-229.

Gazda, I. W. (1970). The effects of compressive pre-stress on the CTE of graphties. *Carbon*, **8**, 511-522.

Geurin, F. (1998). *The effects of pre-stress on the thermal expansion of graphite*. Final Year Degree Report, University of Bath.

Glenda-Hughes, E. E. and Thomas, J. M. (1962). Topography of oxidised graphite crystals. *Nature,* **193**, 838-845.

Goutfer-Wurmser, F., Herold, C., Mareche, J-F. and Lagrange, P. (1998). On the intercalation into graphite of phosphorous with potassium. *Proceedings of Eurocarbon '98*, Strasbourg, France, 35-36.

Gray, W. J. (1973). Constant stress irradiation-induced compressive creep of graphite at high fluences. *Carbon*, **11**, 383-392.

Gray, B. S., Brocklehurst, J. E. and McFarlane, A. A. (1967). The irradiation induced plasticity in graphite under constant stress. *Carbon,* **5**, 173-180.

Grisedale, R. O., Pfister, A. C. and van Roosbroek, W. (1951). The formation of graphite by pyrolitic deposition. *Bell Systems Technology Journal*, **30**, 271-281

Grisdale, R. O. (1963). The oxidation of single crystal graphite. *Journal of Applied Physics*, **24**, 1291-1303

Hacker, P. J., Neighbour, G. B., McEnaney, B. and Wickham, A. J. (1998). An International Database on Irradiated Nuclear Graphite Properties. *Extended Abstracts, Eurocarbon '98*, Strasbourg, France, 715-716.

Hacker, P. J and Neighbour, G. B. (1999). *Method statement for the determination of the thermal expansion of AGR moderator graphite*. BNMG Report, BNMG/REP/052.

Hacker P. J., Neighbour, G. B and McEnaney, B. (1999a). *The coefficient of thermal expansion of graphite*. BNMG Report for the Health and Safety Executive, FC/GNSR/44, BNMG/REP/024.

Hacker, P. J., Neighbour, G. B. and McEnaney, B. (1999b). The Thermal Expansion Behaviour of AGR Moderator Graphite. *The Nuclear Engineer*, 40[6], 229-235.

Hacker, P. J., Neighbour, G. B. and McEnaney, B. (2000). The coefficient of thermal expansion of nuclear graphite with increasing thermal oxidation. *Journal of Physics D: Applied Physics*, **33**, 991-998.

Hales, T. C. (1997). Sphere Packings, II. *Discrete and Computational Geometry*, **18**, 135-149.

Hammond, G. P. (1996). Nuclear Energy into the Twenty-first Century. *Applied Energy*, **54**[4], 327-344.

Harrison, J. W. (1977). Absolute measurements of the coefficient of thermal expansion of pyrolytic graphite from room temperature to 1200 K and a comparison with current theory. *High Temperatures – High Pressures*, **9**, 221-229.

Hart, P. E. (1972). The CTE of pre-stressed nuclear graphites. *Carbon*, **10**, 234.

Hennig, G. R. (1956). Review of radiation damage to graphite. In: *Progress in Nuclear Energy, Series V Metallurgy and Fuels*. Eds. Finniston, H. W. and Howe, J. P., Pergamon Press.

Hennig, G. R. (1959). Electron microscope studies of graphite single crystals. *Proceedings of the 4th Carbon Concerences*, Buffalo, USA, 145-154.

Hennig, G. R. (1960). Surface reactions of single crystals of graphite. *Journal de Chimie Physique*, **58**, 12-19.

Hennig, G. R. (1961). Surface oxides on graphite single crystals. *Proceedings of the 5th Carbon Conference*, Pennsylvania State University, **1**, 143-146.

Hennig, G. R. (1966). Electron microscopy of reactivity changes near lattice defects in graphite. *Chemistry and Physics of Carbon*, Ed. P. L. Walker Jr., **2**, 1-49.

Hennig, G. R. and Kanter, M. A. (1960). Effect of lattice defects on the reactivity of graphite. *Proc. 4th Intern. Symp. Reactivity Solids.* Amsterdam, 649-660.

Ibach, H and Luth, H. (1993). *Solid State Physics*. Spinger-Verlag Publishers.

Jenkins, G. M. (1964). The Thermal Expansion of Polygranular graphite. *Journal of Nuclear Materials*, **13**[1], 33-39.

Jones, S. S. and Woodruff, E. M. (1970). Microstructure of Carbon Blacks in Pitch-Bonded Graphites and Structural Changes Produced by Gas-Graphite Oxidation Reactions. *Carbon*, **9**, 259-264.

Kelly, B. T. (1979). Prediction of the dimensional changes of AGR moderator graphite subjected to simultaneous radiolytic oxidation and irradiation. UKAEA Report ND-M-830(S), sub-ref: AGR/GCWG/P(79)25.

Kelly, B. T. (1981). *Physics of graphite*. Applied Science Publishers.

Kelly, B. T. (1982). Graphite – the most fascinating nuclear material. *Carbon*, **20**, 3-11.

Kelly, B. T. (1985). The radiolytic corrosion of Advanced Gas-Cooled Reactor graphite. *Progress in Nuclear Energy*, **16**[1], 73-96.

Kelly, B. T. (1992a). Irradiation damage and radiolytic oxidation in nuclear reactor graphite. AEA-Report RS-5193.

Kelly, B. T. (1992b). Irradiation creep in graphite - some new considerations and observations. *Carbon*, **30**[3], 379-383.

Kelly, B. T. (1994). Nuclear reactor moderator materials. In: *Materials Science and Technology, A Comprehensive Treatment*, Eds. Cahn, R. W, Haasen, P. and Kramer, E. J., 10A[1], 365-417.

Kelly, B. T. and Burchell, T. D. (1994). The analysis of irradiation creep experiments on nuclear reactor graphite. *Carbon*, **32**, [1], 119-125.

Kelly, B. T. and Brocklehurst, J. E. (1971). High dose fast neutron irradiation of highly oriented pyrolytic graphite. *Carbon*, **9**, 783-789.

Kelly, B. T., Brocklehurst, J. E. and Ashton, B. W. (1974). *The interaction of radiolytic oxidation and fast neutron irradiation in the moderators of CO_2 cooled reactors.* TRG Report 2589(S), RPC/CGC/M2/P(74)26, RPC(GP)P(74)20.

Kelly, B. T. and Foreman, B. (1986). The Theory of Irradiation Creep in Reactor Graphite - The Dislocation Pinning-Unpinning Model. *Carbon,* **12**, 151-158.

Kelly, B. T., Martin, W. H. and Nettley, P. T. (1966a). Dimensional changes in pyrolytic graphite under fast-neutron irradiation. *Philosophical Transactions A*, **260**, 37-49.

Kelly, B. T., Martin, W. H. and Nettley, P. T. (1966b). Dimensional changes in polygranular graphites under fast-neutron irradiation. *Philosophical Transactions A*, **260**, 51-71.

King, C. D. G. (1964). *Nuclear power systems.* The Macmillan Publishing Company, New York.

Knudsen, F. P. (1959). Dependance of Mechanical Strength of Brittle Polycrystalline Specimens on Porosity and Grain size. *Journal of the American Ceramic Society*, **42**[8], 376-387.

Kochling, B., McEnaney, B., Rozploch, F. and Fitzer, E. (1982). International Committee for Characterisation and Terminology of Carbon: First Publication of 30 Tentative Definitions. *Carbon*, **20**[5], 445-449.

Lobb, C. J. and Frank, D. J. (1984). Percolation in large numerically derived lattices. Physical Review B, **30**, 4090-4111.

Lyons, L. *Data Analysis for physical science students*, Cambridge University Press.

Mantell, C. L. (1968). *Carbon and graphite handbook*, Interscience, New York.

Martin, D. G. and Caisley, J. (1977). Some studies of the effect of irradiation on the neutron small angle scattering from graphite. *Carbon*, **15**, 251-255.

Martin, D. G. and Caisley, J. (1978). Some studies of the effect of thermal and radiolytic oxidation on the neutron small angle scattering from nuclear graphites. *Carbon*, **16**, 199-203.

Martin, W. H. and Entwisle, F. (1963). Thermal expansion of graphite over different temperature ranges. *Journal of Nuclear Materials*, **10**, 1-7.

Mason, I. B. and Knibbs, R. H. (1964). The thermal expansion of polycrystalline carbon and graphite from –196°C to 2000°C. *Journal of Nuclear Energy*, **18**, 311-329.

Matsuo, H. and Sasaki, Y. (1981a). Thermal expansion of nuclear graphite under compressive stress at high temperatures. *Journal of Nuclear Materials,* **101**, 232-234.

Matsuo, H., Saito, T. and Sasaki, Y. (1981b). Effects of high temperature neutron irradiation on dimension and thermal expansion coefficient of nuclear grade graphites. *Journal of Nuclear Science and Technology*, **18** [1], 863-869.

Matsuo, H. and Sasaki, Y. (1982). Thermal expansion of nuclear graphite under a tensile pre-stress. *Journal of Nuclear Materials*, **102**, 176-198.

Matsuo, H. and Sasaki, Y. (1985). Thermal expansion of some pre-stressed nuclear grade graphites. *Carbon*, **23**[1], 51-57.

Matuyama, E. (1955). A High Temperature X-ray Diffraction Powder Camera. *Journal of Scientific Instruments*, **32**, 229-231.

Mendez, R., Granda, M. and Bermejo, J. (1997). In *'Introduction to Carbon Technologies'*, eds. Marsh, H., Heintz, E. A. and Rodriguez-Reinoso, F., Universidad de Alicante, Alicante, Spain, 461-490.

Morgan, W. C. (1967). CTE in nuclear graphites. *Journal of Applied Physics*, **38**, 1996-2006

Mrozowski, S. (1956). Mechanical strength, thermal expansion and structure of cokes and carbons. *Proc. of the 1st and 2nd Conference on Carbon*, 31-45.

Murdie, N., Edwards, I. And Marsh, H. (1986). Changes in porosity of graphite caused by radiolytic gasification by carbon dioxide. *Carbon*, **24**[3], 267-275.

Neighbour, G. B. (1993). Microstructural processes leading to fracture in nuclear graphites. PhD Thesis, University of Bath.

Neighbour, G. B. (1998). The performance of reactor core materials. *Proceedings of the Bath Royal Literary and Scientific Institution*, 51-52. ISSN 1465-8496.

Neighbour, G. B. (1999). *Using MTR data to predict materials properties in an AGR.* BNMG Report for British Energy Generation Ltd., BB/E/41248, BNMG/REP/025.

Neighbour, G. B. (2000). Modelling of dimensional change in irradiated nuclear graphites. *Journal of Physics D. Applied Physics*, **33**, 2966-2972.

Neighbour, G. B. and McEnaney, B. (1997). *Channel brick durability studies - Brush Tests (Schedule C).* BNMG Report for the Industry Management Committee, GRA/GNSR/5012, GCDMC/A/P(97)41, RACSC/P48, BNMG/REP/006.

Neighbour, G. B., Hartley, M. S. and McEnaney, B. (1997). *CTE variation with thermal oxidation and pre-stress.* BNMG Report for Nuclear Electric Plc., BNMG/REP/003, GCDMC/A/P(97)39, RACSC/P49.

Neighbour, G. B., Hacker, P. J. and McEnaney, B. (1998a). *The relationship between the microstructure of polygranular graphite and the coefficient of thermal expansion.* BNMG Report for Nuclear Electric Ltd., GCDMC/A/P(98)67, BNMG/REP/011.

Neighbour, G. B., Deven, M. J., Hacker, P. J., Wickham, A. J. and McEnaney, B. (1998b). *Thermal oxidation of reactor graphites*, BNMG Report for the Industry Management Committee, GRA/GNSR/5012A, GCDMC/A/P(98)87, BNMG/REP/013.

Neighbour, G. B., Hacker, P. J., Luo, J. and McEnaney, B. (1999). *Graphite properties with weight loss.* BNMG Report for Nuclear Electric Ltd, BB/E/40935, BNMG/REP/017.

Nelson, J. B. and Riley, D. P. (1945). The thermal expansion of graphite from 15 °C to 800 °C: Part 1. Experimental. *Proceedings of the Royal Society*, **A57**, 477.

Nightingale, R. E. (1962). *Nuclear graphite.* Academic Press Inc. Ltd. London.

Nolan, G. T. and Kavanagh, P. E. (1991). Computer Simulation of Random Packing of Hard Spheres. *Powder Technology*, **72**, 149-155.

Norfolk, D. J., Johnston, G. O. and Tucker, M. O. (1986). Achieving optimum graphite performance in AGR core and fuel. *IAEA specialists meeting on graphite component structural design*, Tokai Mura, Japan, 176-181 (JAERA summary report).

Oberlin, A. (1989) TEM studies of carbon and graphite. In 'Chemistry and Physics of Carbon' ed. Thrower, P. A., New York, **22**, 1-144.

Okada, J. (1960). Thermal expansion of pitch bonded carbons. *Proceedings of the Fourth Conference on Carbon*, University of Buffalo, Buffalo, New York. Pergamon Press. 547-552.

Perks, A. and Simmons, J. H. W. (1964). Properties of nuclear graphites. *Carbon*, **1**, 441-453.

Pickup, I. M., McEnaney, B. and Cooke, R. G. (1996). The thermal corrosion of nuclear graphite. *Carbon*, **21**, 535-339.

Pierson, H. O. (1993). *Handbook of Carbon, Graphite, Diamond and Fullerenes*, Noyes Publications, New Jersey, USA.

Pitner, A. L. (1971). Irradiation behaviour of POCO graphites. *Carbon*, **8**, 637-644.

Platonov, P.A., Chugunov, O. K., Karpukhin, V. I., Kuznetsov, V. N., Alekseev, S. I. And Golovin, V. P. (1979). Linear coefficient of thermal expansion of graphitic materials. *Soviet Atomic Energy*, **47**[6], 992-997.

Platonov, P.A., Novobratskaya, I. F., Tumanov, Y. P., Karpukhin, V. I. and Alekseyev, S. I. (1981). Effect of neutron irradiation on the dimensional stability of graphite pre-treated at different temperatures. *Radiation Effects*, **54**, 91-98.

Price, R. J. and Bokros, J. C. (1965). The CTE of graphites and carbons. *Journal of Applied Physics*, **36**, 1897-1912.

Rice, R. W. (1993). Comparison of stress concentration versus minimum solid area based mechanical property-porosity relations. *Journal of the American Ceramic Society,* **76**[7] 1801-1811

Riga, A. T. and Neag, C. M. (eds.). (1991). *Materials characterization by thermomechanical analysis.* ASTM Special Technical Publication, STP 1136.

Riley, D. P. (1945). The Thermal Expansion of Graphite: Part II. Theoretical. *Proceedings of the Royal Society Part A.*, **57**[6], 486-502.

Rodriguez, J. Allibert, C. H and Chaix, J. M. (1986). A computer method for random packing of spheres of unequal size. *Powder Technology*, **47**, 25-33.

Seehra, M. S. and Pavlovic, A. S. (1992). The structural characterisation of powdered carbons and graphites. *Carbon,* **31**[4], 557-564.

Sahimi, M. (1983). In *Percolation, Random Walks, Modelling and Simulation* (p.314). Springer Verlag Publishers.

Simmons, J. H. W. (1959). The effects of irradiation on the mechanical properties of graphite. *Proceedings of the Third Biennial Conference on Carbon*, Pergamon Press, New York, 132-135.

Shtrombakh, Y. I., Platonov, P. A., Gurovich, B. A. and Alekseev, V. M. (1996). Radiation behaviour of graphite for HTGR. *Graphite Moderator Lifecycle Behaviour, Proceedings of a Specialists Meeting*, United Kingdom, 24-27 September, 251-262.

Slagle, O. D. (1968). Averaging Techniques in Polycrystalline Graphites, *Carbon*, **6**, 111-121.

Slagle, O. D. (1969). Thermal Expansion Hysteresis in Polycrystalline Graphites. *Carbon,* **7**, 337-344.

Stauffer, D. (1984). *Introduction to percolation theory.* Taylor and Francis Publishers, London.

Stewart, E. G., Cook, B. P., Kellet, E. A. (1960). Dependence on temperature of the interlayer spacing in carbons of different graphitic perfection. *Nature*, **4742**, 1015-1016.

Strange, J. F. and Walker, P. L. (1976). Carbon-carbon dioxide reaction: Langmuir-Hinshelwood kinetics at intermediate pressures. *Carbon*, **14**, 345-350.

Sutton, A. L. and Howard, V. C. (1962). The role of porosity in the accommodation of thermal expansion in graphite. *Journal of Nuclear Materials*, **7**[1], 58-71.

Sosman, S. (1928). *The properties of Silica.* Cambridge Academic Press.

Thomas, J. M. (1965). Topographical studies of oxidised graphite surfaces: a summary of the present position. *Carbon*, **7**, 359-364.

Thomas, G. B. and Finney, R. L. (1988). *Calculus and Analytic Geometry*. Addison-Wesley Publishing Company, USA.

Thrower, P. A. and Reynolds, W. N. (1963). Microstructural changes in neutron irradiated graphite. *Journal of Nuclear Materials*, **8**[2], 221-226.

Tomlinson, A., Mays, T. J. and Neighbour, G. B. (2000). *AGL/BAEL/UCAR attack rates*. BNMG report for British Energy Generation Ltd. BB/G/41240, BNMG/REP/043.

Torquato, S., Truskett, T. M. and Debenedetti, P. G. (2000). Is random close packing of spheres well defined? *Physical Review Letters,* **84**[10], 2064-2067.

Tucker, M. O. and Wickham, A. J. (1990). Graphite core performance and integrity assessment, In: *The commissioning and operation of AGRs*, a seminar organised by the Nuclear Energy Committee of the Power Industries Division at I. Mech. E. HQ, Westminster, SW1H 9JJ.

Virgilev, Y. S. (1981). Effect of neutron irradiation on the thermal expansion of polygranular graphite. *Inorganic Materials*, **17**[8], 1108-1111.

Virgilev, Y. S. and Grigoreva K. V. (1986). Effect of radiation of the thermal expansion coefficient of reactor graphite. *Physics and Chemistry of Materials Treatment*, **20**[3], 289-290.

White J. L. (1975). The formation of microstructure in graphitisable materials. *Progress in Solid State Chemistry*, **9**, 59-104.

Wilets, L., (1964). *Theories of Nuclear Fission*, Clarendon Press, Oxford.

Wood, J. L., Bradt, R. C. and Walker, J. L. (1980). Oxidation effects on toughness and slow crack growth in polycrystalline graphites. *Carbon*, **18**, 179-189.

Yin Y. F., Mays, T. J and McEnaney, B. (1999). Adsorption of nitrogen in carbon nanotube arrays. *Langmuir*, **15**, 8714-8718.

Yoda, S. and Fujiaki, K. (1983). Thermo-physical properties in nuclear graphite. *Journal of Nuclear Materials*, **113**, 263-267.

Zabolitzky, J. G. (1984). The numerical computation of the percolation threshold for large lattices. *Physical Review B*, **30**, 4077-4097.

Zhao, J. X., Wood, J. L., Bradt, R. C. and Walker, P. L. (1981) Changes in coefficients of thermal expansion of polycrystalline graphites upon oxidation. *15th Biennial Conference on Carbon*, 522-523.

APPENDICES

APPENDIX 1

NOTES ON THE CORRECTION OF DILATION CURVES OBTAINED USING MECHANICAL DILATOMETRY.

The method of mechanical dilatometry uses the signal generated from the thermomechanical analyser to compute the relative length change (ΔL) of the sample. In practice however, the measured signal encompasses the vectorial sums of the length changes of the sample, pushrod and sample holder and these need to be corrected for in order to extract the sample expansion

The method of calibration of mechanical dilatometers for the accurate determination of average CTE measurements[1] has been addressed in an ASTM standard (Riga *et al.*, 1991). In this work it is shown that the total error on an average CTE value, δα, can be expressed as follows

$$\frac{\delta\alpha}{\alpha} = -\frac{\delta L_0}{L_0} + \frac{\delta(\Delta L)}{\Delta L} - \frac{\delta(\Delta T)}{\Delta T} \qquad [1.1]$$

where α is the actual average CTE, L_0 is the initial specimen length, and ΔT is the temperature difference. The error on each variable is associated with the δ prefix. Here, the error associated with the mechanical length measurement is discussed, δ(ΔL), as this is generally the largest source of error, provided samples are well prepared and thermocouple used for measurement are calibrated and reliable.

Riga *et al.* (1991) state that in the mechanical dilatometer, when the temperature of the specimen is changed by ΔT, the expansion of the specimen, ΔL_s, is expressed as follows

$$\Delta L_s = \Delta X_s - \Delta(L_a - L_b) + \Delta L_h \qquad [1.2]$$

where ΔX_s is the measured expansion, L_a is the length of the pushrod, L_b is the length of the sample holder beyond the specimen and L_h is the length of the holder in the

[1] That is, a CTE coefficient computed over a temperature range $T_0 + \Delta T$

specimen region. Expressed as a relative length change equation [1.2] can be simply rewritten as follows:

$$\frac{\Delta L_s}{L_{s0}} = \frac{\Delta X_s}{X_{s0}} - \frac{\Delta(L_a - L_b)}{(L_{a0} + L_{b0})} + \frac{\Delta L_h}{L_{h0}} \qquad [1.3]$$

Similarly, if a reference material, R, with a known relative expansion ($\Delta L_r/L_{r0}$) is measured this expansion can be expressed as

$$\frac{\Delta L_r}{L_{r0}} = \frac{\Delta X_r}{X_{r0}} - \frac{\Delta(L_a - L_b)}{(L_a + L_b)} + \frac{\Delta L_h}{L_{h0}} \qquad [1.4]$$

where ΔX_r is the expansion of standard with initial length X_{r0}. Providing the sample and reference material are measured under the same conditions, and as the expansions are expressed as relative quantities, Equations [1.3] and [1.4] can be combined to remove the sample holder terms to give the following

$$\frac{\Delta L_s}{L_{s0}} = \frac{\Delta X_s}{X_{s0}} - \frac{\Delta X_r}{X_{r0}} + \frac{\Delta L_r}{L_{r0}} \qquad [1.5]$$

It is important to note that even if the sample length (L_o) and the standard length (L_{r0}) differ, Equation [1.5] still remains valid as the correction is made based upon relative length changes and not absolute expansion data. Although, to an extent, very small sample lengths in relation to the standard remain undesirable as this increases the sensitivity of the corrected result to errors in expansion measurement and uncertainties in determination of temperatures and initial lengths. Of importance is the requirement that the samples be measured under identical conditions. Equation [1.5] is used to generate the correction term in the Netzsch control software supplied with the dilatometer used in this work and, via the method outlined, can thus be related directly to the ASTM standard.

APPENDIX 2

X-RAY DIFFRACTION MEASUREMENTS OF AGR GRAPHITE

X-ray diffraction is a commonly used method of analysing the crystal structure of a solid or powdered material and is reviewed in many standard textbooks (*e.g.* Cullity, 1990). The method uses the principle that as the angle of incidence between incident x-rays and the crystal changes, peaks in diffraction intensity are produced each corresponding to a series of parallel planes orientated throughout the regular atomic structure. The planar spacing, d, the angle of incidence, θ, and the wavelength of the x-rays are related by the Bragg Law as follows, where n is the order of the reflection.

$$n\lambda = 2d\sin(\theta) \qquad [2.1]$$

Thus, providing the correct diffraction peaks are chosen, the crystallographic parameters (a and c, in the case of graphite) can be determined. The results of x-ray diffraction from a standard sample of AGR graphite, over a wide-angle range, are shown in Figure 2.1. The important diffraction peaks for the measurement of crystallographic properties are identified by reference to their corresponding planes (in the Miller notation). In particular, the 'a' parameter can be derived using the (100) diffraction peak and the (002) peak gives half the 'c' parameter. The use for the (101) peak is discussed later.

In addition to the a and c parameters, x-ray diffraction can also provide information on the average crystallite size in the material from the broadening of the appropriate diffraction peaks. Within graphite these crystallite sizes are denoted L_c and L_a in the directions perpendicular and parallel to the basal planes respectively. In this work, these parameters are important as they are used as inputs into the microstructural model of CTE. These crystallite sizes are often estimated using the Scherrer equation (Seehra and Pavlovic, 1992) as follows

$$L_c = \frac{(0.91)\lambda}{\beta\cos\phi} \qquad L_a = \frac{(1.84)\lambda}{\beta\cos\phi} \qquad [2.2]$$

where λ is the wavelength of the incident x-rays and β (in radians) is the width of an appropriate diffraction peak at half the maximum intensity. However, the measured line width does not correspond directly to β due to broadening by the instrument. This can be corrected for by using the following equation

$$\beta^2 = B^2 - b^2 \qquad [2.3]$$

where B is the experimentally measured line width and b is determined from a diffraction peak in a standard material (*e.g.* silica, Figure 2.2.) whose diffraction angle, θ, is close to that of the peak being corrected in the graphite. In order to determine the L_c parameter the (002) line can again be used, whereas for L_a the (101) peak can be used (Seehra and Pavlovic, 1992). Following this method the L_a and L_c parameters were determined for two grades of AGR graphite (four samples of each) manufactured by BAEL and UCAR, using a Philips Analytical Diffractometer PW1820. The results of the measurement of the crystallite size parameters are shown in Table 2.1. The mean and standard deviation of each grade and of both grades together are shown in Table 2.2

GRAPHITE GRADE AND SAMPLE NUMBER	L_a(Å)	L_c(Å)
BAEL Sample 1	201	475
BAEL Sample 2	200	482
BAEL Sample 3	151	489
BAEL Sample 4	179	408
UCAR Sample 1	171	591
UCAR Sample 2	190	521
UCAR Sample 3	172	402
UCAR Sample 4	177	578

TABLE 2.1: L_a and L_c parameters for two grades of AGR graphite.

	L_a(Å)	L_c(Å)
Mean (BAEL)	183	464
Standard Deviation (BAEL)	23	37
Mean (UCAR)	178	523
Standard Deviation (UCAR)	9	86
Mean (Total)	**180**	**493**
Standard Deviation (Total)	**17**	**69**

TABLE 2.2: Mean values and Standard Deviations of the measurement of L_a and L_c parameters for two grades of AGR graphite.

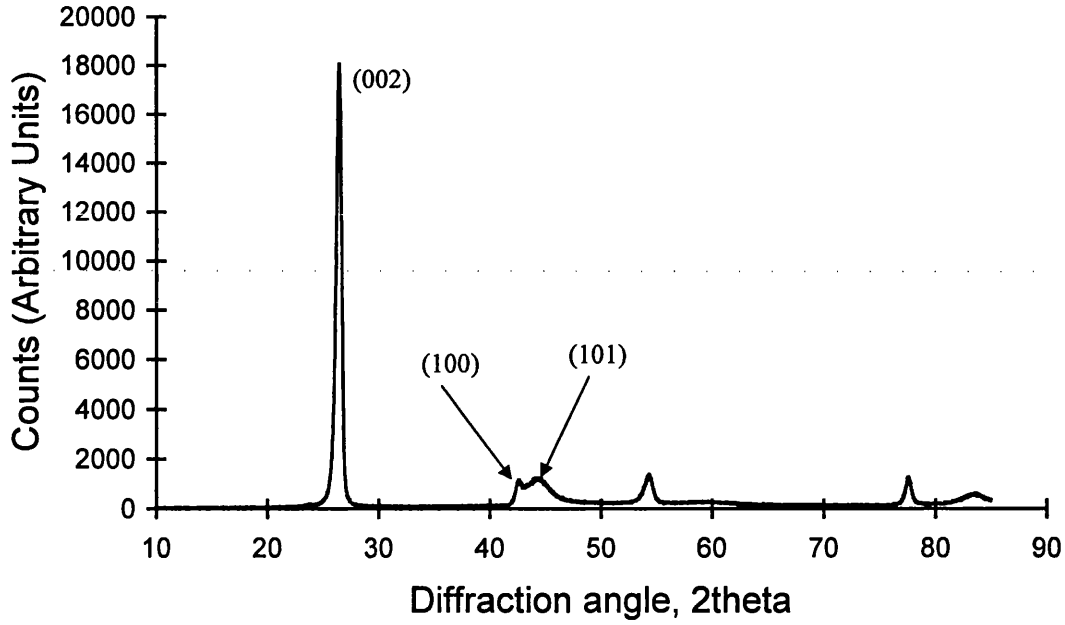

Figure 2.1. Typical XRD curve for a sample of AGR graphite.

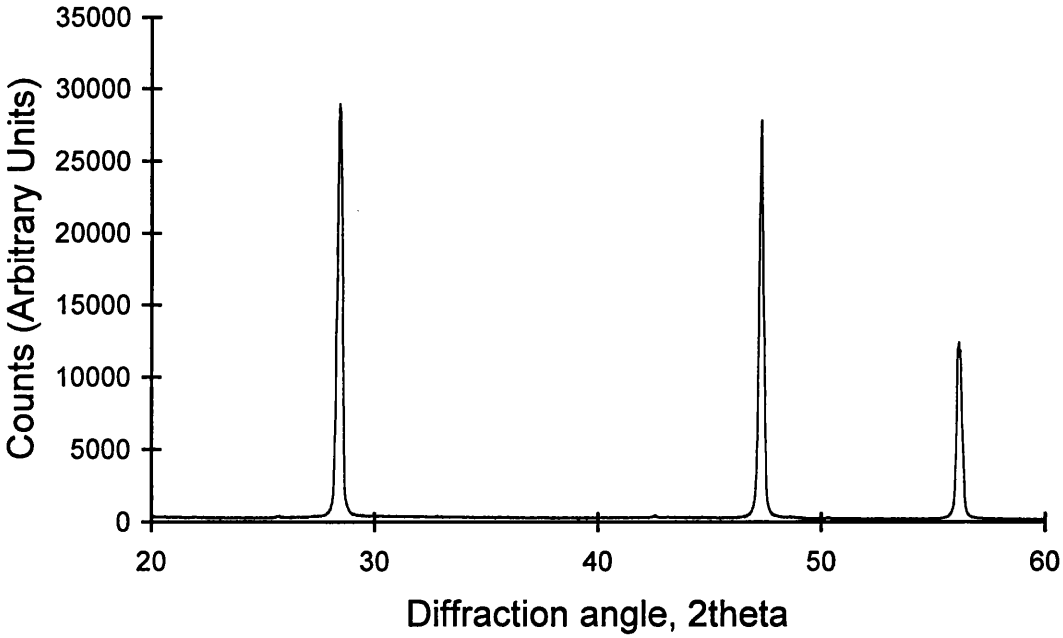

Figure 2.2. XRD curve of silicon used as a calibration curve to correct for instrumental peak broadening effects.

APPENDIX 3
HYPOTHESIS TESTING

Hypothesis testing allows two populations to be compared. For this work, the objective is to ascertain, to a certain degree of significance, if both populations can be described as belonging to the same dataset. This is achieved by using a Students *t*-test, described below.

A Null hypothesis is first derived as follows

$$H_0: \ \mu_1 = \mu_2 \qquad [3.1]$$

Where μ_1 and μ_2 are the means of the first and second populations respectively. That is, the Null hypothesis assumes there is no difference in the population means *i.e.* both populations are from the same dataset. The Alternative hypothesis is as follows

$$H_1: \ \mu_1 \neq \mu_2 \qquad [3.2]$$

A *t*-value (t_c) can now be calculated from Equation [3.3] as follows

$$t_c = \frac{\mu_1 - \mu_2}{S \times \sqrt{\frac{1}{n_1} + \frac{1}{n_2}}} \qquad [3.3]$$

Where n_1 and n_2 are the number of samples in populations 1 and 2 respectively and S is given by Equation [3.4] as follows

$$S^2 = \frac{(n_1 - 1)S_1^2 + (n_2 - 1)S_2^2}{n_1 + n_2 - 2} \qquad [3.4]$$

A tabulated *t*-value (t_t) is obtained from statistical tables for the value of the Students-*t* distribution that corresponds to the degree of significance required. For a 5% significance level, a fractional area 0.025 is used (corresponding to a two-tailed test)

where the number of degrees of freedom is given by n_1+n_2-2. If $t_c < t_t$, H_0 is accepted at the 5% confidence level, *i.e.* it the likelihood of each population being a part of the same dataset is 95%. If $t_c > t_t$ H_1 is accepted at the 5% confidence level, *i.e.* the likelihood of each population being a part of the same dataset is only 5%.

NOTES ON THE USE OF THE CD-ROM

Supplied with this thesis is a CD-ROM that should operate on any Personal Computer running the Microsoft Windows 95 operating system or higher and contains a demonstration copy of the model and further information on the construction of the computer code. Full details are available when running the application. If the application does not 'autostart' when the disc is inserted into the drive, please run the 'start' application on the CD. Note that running the code may take some time. A typical run on an Intel Pentium III based computer, running at 500 MHz, takes around 15-20 minutes.

Please note that this software is supplied 'as is' for information purposes only. In particular, the author cannot be held responsible for any loss or damage that may arise from its use. Also, attention is drawn to the fact that the copyright of the software remains with the author.